



Transmetteurs photoniques sur silicium pour la prochaine génération de réseaux optiques

Thèse

Omid Jafari

Doctorat en génie électrique
Philosophiæ doctor (Ph. D.)

Québec, Canada

Transmetteurs photoniques sur silicium pour la prochaine génération de réseaux optiques

Thèse

Omid Jafari

Sous la direction de:

Sophie LaRoche, directrice de recherche
Wei Shi, codirecteur de recherche

Résumé

Les dernières décennies ont été témoins d'une flambée sans précédent du trafic de données, nécessitant un besoin urgent de liaisons optiques ultra-rapides. Cela a donné l'impulsion aux systèmes de transmission optique à haute capacité de nouvelle génération. Dans ces systèmes, des modulateurs optiques intégrés ayant une bande passante élevée, économe énergétiquement, compacts, stables et adaptés à une intégration à grande échelle sont très demandés.

La plate-forme de photonique sur silicium (SiP), bien qu'elle souffre de l'absence d'effets électro-optiques inhérents dans la silice, s'est néanmoins avéré être une solution rentable pour les transmetteurs de haute capacité puisqu'elle tire parti du processus CMOS mature. Par conséquent, un effort considérable a été consacré au développement d'appareils de haute performance sur cette plate-forme. Cette thèse se concentre sur les transmetteurs SiP pour la prochaine génération de réseaux optiques où l'espace, en tant que dernière dimension physique, est proposé pour surmonter le « manque de capacité » associé à la technologie actuelle.

Pour construire de tels transmetteurs, il faut intégrer un ensemble de modulateurs optiques dans une seule puce. Ces modulateurs doivent simultanément se caractériser par un fonctionnement à grande vitesse, une faible consommation d'énergie, un encombrement réduit et une grande stabilité. Les modulateurs SiP bien connus, tels que les modulateurs à micro-anneaux (MRM) et les modulateurs Mach-Zehnder (MZM), ne répondent pas à tous les critères susmentionnés. Les MRM présentent une faible performance en termes de stabilité et les MZM sont gourmands en énergie. C'est pourquoi nous étudions des modulateurs SiP nouveaux et avancés dans deux chapitres de cette thèse. Pour la première fois, nous faisons la démonstration de modulateurs SiP basés sur la conversion de mode. Lorsqu'opérés en réflexion, les modulateurs de Bragg offrent un rendement élevé ainsi qu'un fonctionnement à grande vitesse. Cependant, les modulateurs fonctionnant en réflexion sont gênés par le manque de circulateurs sur puce. Nous abordons cette question et présentons expérimentalement un modulateur SiP basé sur des guides d'ondes asymétriques à réseau de Bragg suivis d'un coupleur directionnel asymétrique (ou jonction Y asymétrique), offrant des opérations en réflexion sans avoir besoin de circulateurs et avec de faibles pertes sur la puce. Dans notre deuxième contribution, nous faisons la démonstration du premier modulateur à lumière lente basé sur des résonateurs à réseau de Bragg couplés (BGR), un MZM assisté par des BGR couplés. Les BGR, composés de cavités à faible facteur Q en série, ralentissent les ondes optiques dans une large bande

passante optique (quelques nanomètres). Cela permet au modulateur d'améliorer la modulation de phase sur une gamme de longueurs d'onde de fonctionnement relativement large, ce qui se traduit par des performances plus stables par rapport aux modulateurs à résonance unique (p. ex., les MRM). Atteignant un bon équilibre dans les indicateurs de performance, le MZM assisté par les BGR peut être reconnu comme un choix potentiel pour les futurs systèmes de multiplexage par répartition en longueur d'onde/espace (SDM/WDM).

Suite à notre démonstration pionnière, nous étudions, comme troisième contribution, l'impact de l'effet de lumière lente sur la performance des modulateurs SiP, le compromis existant entre efficacité et vitesse en particulier. Lorsque l'efficacité est améliorée dans des modulateurs SiP typiques, soit en augmentant la capacité de la jonction PN (dans les MZM), soit en introduisant des structures hautement résonantes (dans les MRM), cela entraîne également une augmentation de la constante de temps RC ou de la durée de vie des photons, respectivement, et donc une diminution de la largeur de bande électro-optique (EO). Dans ce chapitre, nous proposons de remettre en question ce compromis pour les modulateurs à lumière lente et d'étudier s'ils sont capables de surpasser les modulateurs SiP typiques. À cette fin, il est nécessaire de disposer de modèles complets de la réponse EO de ces modulateurs, intégrés soit avec des électrodes en bloc, soit avec des électrodes mobiles. À l'aide de ces modèles, nous comparons les modulateurs à lumière lente avec les MZM convectifs. Nous examinons également différentes méthodes de conception pour réduire les V_π des modulateurs SiP afin qu'ils puissent répondre aux exigences des pilotes COMS et des interfaces électriques pour la prochaine génération de transmetteurs SiP.

Dans notre quatrième contribution, nous faisons état d'un modulateur tout silicium à lumière lente qui permet un fonctionnement à grande vitesse du PAM sans utiliser de convertisseur numérique-analogique (CNA) électrique. Les BGR sont intégrés dans chaque bras d'un MZM afin de ralentir les ondes optiques, ce qui améliore la modulation de phase sur une bande passante optique relativement importante. Le signal optique PAM à 4 niveaux est généré par une conception segmentée dans des déphaseurs à lumière lente avec deux signaux de commande binaires, ce qui élimine le besoin d'un CNA à grande vitesse. Ce modulateur combine les avantages d'un encombrement ultra-compact, d'une faible consommation d'énergie, d'une large bande passante électro-optique et d'un fonctionnement stable en présence de variations de température. Les guides d'ondes à lumière lente présentent de bonnes performances avec de faibles variations de la longueur d'onde centrale et de la largeur de bande sur la plaquette. Ce modulateur devrait être singulièrement intéressant pour les applications qui nécessitent un groupe de modulateurs compacts sur une seule puce.

Enfin, pour notre cinquième contribution, nous poursuivons l'objectif de développer des transmetteurs optiques SDM à haute performance adaptés aux systèmes de transmission optique à haute capacité de la prochaine génération. Nous proposons des transmetteurs optiques présentant un rendement énergétique élevé, une densité de bande passante élevée, une stabilité relativement élevée et entièrement intégrés dans la plateforme SiP (une solution rentable). Nous discutons des méthodologies de conception et des exigences de ces transmetteurs SDM qui consistent en des modulateurs

à lumière lente (MZMs assistés par des BGRs) suivis d'un multiplexeur modal sur puce. Nous citons les systèmes à courte et longue portée en concevant respectivement des modulateurs PAM à électrodes groupées et des modulateurs IQ à électrodes à ondes progressives. Afin de multiplexer spatialement les signaux provenant des modulateurs, nous faisons la démonstration d'une conception de multiplexeurs modaux sur puce basée sur des coupleurs directionnels asymétriques. Nous mettons en cascade trois de ces coupleurs pour créer quatre canaux spatiaux (TE0, TE1, TE2 et TE3). Pour réaliser une transmission MDS complète. Cette sortie multiplexée spatialement doit être injectée dans une fibre à noyau elliptique faiblement multimode supportant les mêmes modes.

Abstract

Recent decades have witnessed an unprecedented surge in data traffic, necessitating an urgent need for ultra-fast optical links. This has provided the impetus for the next-generation high-capacity optical transmission systems. In these systems, integrated optical modulators that are high-bandwidth, power efficient, compact, stable, and suited-for-large-scale-integration are highly demanded.

The silicon photonics (SiP) platform, although it suffers from the lack of inherent electro-optic effects in silicon, has nevertheless offered a cost-effective solution for high-capacity transmitters leveraging the mature CMOS process. Hence, a tremendous effort has been dedicated to developing high-performance devices in this platform. This thesis focuses on SiP transmitters for the next generation of optical networks where space, as the last physical dimension, is offered to overcome the “capacity crunch” associated with the current technology.

To build such transmitters, a set of optical modulators is required to be integrated into a single chip. These modulators should simultaneously feature high-speed operation, low energy consumption, compact footprint, and stability. Well-known SiP modulators, such as micro-ring modulators (MRMs) and Mach-Zehnder modulators (MZMs), do not meet all the aforementioned criteria. MRMs present a poor performance in terms of stability and MZMs are energy-hungry. Hence, we investigate novel and advanced SiP modulators in two chapters of this thesis. As our first contribution, for the first time, we demonstrate mode-conversion based SiP modulators. If operated in reflection, Bragg modulators offer high efficiency as well as high-speed operation. However, modulators operating in reflection are hindered by the lack of on-chip circulators. We address this issue and experimentally present a SiP modulator based on asymmetric Bragg grating waveguides followed by an asymmetric directional coupler (or asymmetric Y-junction), offering operation in reflection without the need for circulators and with low on-chip loss. In our second contribution, we demonstrate the first slow-light modulator based on coupled Bragg-grating resonators (BGRs), an MZM assisted by coupled BGRs. BGRs, composed of low-Q-factor cavities in series, slow down optical waves in a broad (a few nanometers) optical bandwidth. This enables the modulator to enhance phase modulation across a relatively wide operating wavelength range, resulting in more stable performance compared to single-resonance-based modulators (*e.g.*, MRMs). Achieving a good balance in the performance indicators, the MZM assisted by BGRs can be recognized as a potential choice for future space/wavelength division multiplexing (SDM/WDM) systems.

Following our pioneering demonstration, as the third contribution, we study the impact of the slow-light effect on the performance of SiP modulators, the existing trade-off between efficiency and speed in particular. When efficiency is enhanced in typical SiP modulators, either by increasing PN junction capacitance (in MZMs) or by introducing highly resonant structures (in MRMs), it also leads to increasing the RC time constant or the photon lifetime, respectively; thus, spoiling the electro-optic (EO) bandwidth. In this chapter, we aim to challenge this tradeoff in slow-light modulators and investigate whether they are capable of outperforming typical SiP modulators. To this end, comprehensive models for the EO response of these modulators integrated either with lumped electrodes or with travelling-wave electrodes are required. Using these models, we compare slow-light modulators with conventional MZMs. We also examine different design methodologies for reducing V_π of SiP modulators so that they can meet the requirements of CMOS drivers and electrical interfaces for the next generation of SiP transmitters.

In our fourth contribution, we report a slow-light all-silicon modulator that enables high-speed PAM operation without using an electrical digital-to-analog converter (DAC). BGRs are integrated into each arm of a MZM in order to slow down optical waves, enhancing the phase modulation over a relatively large optical bandwidth. Optical 4-level PAM signal is generated using a segmented design in slow-light phase shifters with two binary driving signals, eliminating the need for a high-speed DAC. This modulator combines advantages of ultra-compact footprint, low energy consumption, large electro-optic bandwidth, and stable operation in the presence of temperature variations. The slow-light waveguides show good performance with small variances in center wavelength and bandwidth across the wafer. This modulator should be singularly interesting for applications that require a group of compact modulators on a single chip.

Finally as our fifth contribution, we pursue the goal of developing high-performance optical SDM transmitters suited for next-generation high-capacity optical transmission systems. We propose optical transmitters featuring high power efficiency, high bandwidth density, relatively high stability, and fully integrated in the SiP platform (a cost-effective solution). We discuss design methodologies and requirements of these SDM transmitters which consist of slow-light modulators (MZMs assisted by BGRs) followed by an on-chip mode multiplexer. We target both short-reach and long-haul systems in designing PAM modulators with lumped electrodes and IQ modulators with travelling-wave electrodes, respectively. In order to spatially multiplex the signals coming from the modulators, we demonstrate a design of on-chip mode multiplexers based on asymmetric directional couplers. We cascade three of these couplers to create four spatial channels (TE0, TE1, TE2, and TE3). To realize a full SDM transmission, this spatially multiplexed output should be injected into a few-mode elliptical-core fiber supporting the same modes.

Contents

Résumé	iii
Abstract	vi
Contents	viii
List of Tables	x
List of Figures	xi
Abbreviations	xviii
Variables	xxi
Acknowledgement	xxv
Foreword	xxvi
I Introduction	1
I.1 Silicon photonic technology	2
I.2 Silicon photonic modulators	6
I.3 Segmented silicon photonic modulators	8
I.4 Space division multiplexing	11
I.5 Thesis structure	12
1 Mode-conversion-based silicon photonic modulator loaded with different PN junction profiles	17
1.1 Introduction	19
1.2 Mode-conversion modulator loaded with lateral PN junctions	20
1.3 Mode-conversion modulator loaded by a combination of lateral and interleaved p-n junctions	26
1.4 Conclusion	34
2 Slow-light silicon photonic modulators: a Mach-Zehnder modulator assisted by coupled Bragg grating resonators	36
2.1 Introduction	38
2.2 Modulator operating principle	39
2.3 Design and optimization	40
2.4 Dynamic response	50

2.5	Characterization of MZM assisted by Bragg grating resonators	55
2.6	Conclusion	61
3	Efficiency-speed tradeoff in slow-light silicon photonic modulators	63
3.1	Introduction	65
3.2	SL-MZMs with lumped electrodes	67
3.3	SL-MZMs with TW electrodes	75
3.4	V_π reduction in silicon photonic modulators	80
3.5	Conclusion	83
4	DAC-less PAM-4 slow-light silicon photonic modulator providing high efficiency and stability	85
4.1	Introduction	87
4.2	Modulator design	88
4.3	Modulator characterization	90
4.4	Conclusion	97
5	Fully integrated designs of SDM transmitters with compact footprint and power-efficient operation	99
5.1	Introduction	102
5.2	Mode multiplexer	103
5.3	Silicon photonic modulator designs	105
5.4	SDM transmitter designs	110
5.5	Transmission power penalty of slow-light modulators	113
5.6	Conclusion	120
	Conclusion and future works	122
	Publication list	126
	Bibliography	128

List of Tables

3.1	A list of the parameters used in the simulation of lumped-electrode SL-MZM	70
3.2	A list of the parameters used in the simulation of TW SL-MZM	77
3.3	Comparing different design strategies based on their operating parameters	82
5.1	The parameters of the designed directional couplers	105

List of Figures

I.1	SiP applications, Silicon Photonics 2018 report, Yole Développement, January 2018, http://www.yole.fr	2
I.2	SiP ecosystems, Silicon Photonics 2018 report, Yole Développement, January 2018, http://www.yole.fr	3
I.3	Trend in SiP transceiver [45]	3
I.4	Cross-section of typical SiP CMOS process [47]	4
I.5	Schematic of the coherent transceiver demonstrated by Infinera, its cross section, and its flip-chip assembly [56]	5
I.6	Cross-sections of carrier depletion, carrier injection, and carrier accumulation [24] . .	6
I.7	Schematic of a single-drive push-pull SiP MZM combined with TW electrodes and its cross-sections [65]	6
I.8	Schematic of an vertical PN junction in different reverse voltages [68]	7
I.9	Schematic of a U-shaped PN junction in different reverse voltages [69]	7
I.10	Schematic of SISCAP device and SEM image of fabricated device [70]	7
I.11	Schematic of an MRM and its cross-section [21]	8
I.12	Schematic of an Bragg grating modulator and it operational wavelength in transmis- sion and reflection [73]	8
I.13	Schematic of a SL modulator based on photonic crystal waveguides [76]	9
I.14	Schematic of a SL modulator based on micro-ring resonators [23]	9
I.15	Schematic of a SL modulator based on Bragg grating waveguides [25]	9
I.16	Schematic of our work on SL modulator based on Bragg grating resonators presented in [80]	9
I.17	Schematic and micrograph of a segmented MZM [82]	10
I.18	Schematic of segmented MRM, its cross-section and its micrograph [40]	10
I.19	Schematic of segmented Bragg grating modulator and its cross-section [20]	11
I.20	System capacity trends per fiber in optical communications in research and commer- cialization [86]	11
I.21	The five physical multiplexing dimensions and their contribution in enhancing the link capacity [87]	12
1.1	a) Schematic of the modulator, b) design and SEM picture of the asymmetric Y-branch and its SEM picture, c) schematic and SEM picture of asymmetric Bragg grating waveguide. All dimensions are in μm	20
1.2	a) Transmission in TE ₀ and TE ₁ mode when the TE ₀ mode is excited in the input port, b) Transmission to the input port and the drop port when the power in TE ₁ mode is excited in through port. Insets show the field distribution.	21

1.3	a) Schematic of the ASBG, b) transmission and reflection of ASBG in different modes. In (a), black curve shows the lithography effect simulated by Pyxis. Note that the simulation was performed considering $\Lambda = 310$ nm, while in the demonstrated design, Λ is 320 nm. All dimensions are in μm . T: Transmission, R: Reflection	22
1.4	Refractive index variations for TE0 and TE1 modes, and the Bragg wavelength shift as a function of the PN junction offset at a reverse bias of 2 V for lateral PN junctions.	23
1.5	a) Design of back-to-back asymmetric Y-branch, b) the spectrum of Y-branch for different output and input ports.	24
1.6	a) Optical spectrum of the modulator, b) the operating point of the modulator at the edge of the stop band.	24
1.7	Measured EO scattering parameter S21 as a function of the applied reverse bias.	25
1.8	Experimental setup used to measure BER and eye diagram.	25
1.9	a) Eye diagram for a bit rate of 20 Gb/s, b) BER as a function of received power for different bitrates. Both measured at a bias of -2 V.	26
1.10	Schematic of (a) the full modulator structure, (b) the asymmetric directional coupler, (c) the taper between the asymmetric directional coupler and the asymmetric Bragg structure, (d) the asymmetric Bragg grating waveguide loaded by a C-LI PN junction and its cross-section. The parameter values are in μm	27
1.11	Spectral response of the asymmetric directional coupler simulated in Lumerical-FDTD showing the transmission of the input TE0 mode to the through port (blue) and the transmission of the reflected TE1 mode to the drop port (red).	28
1.12	Schematic of (a) lateral, (b) interleaved, and (c) C-LI PN junctions. (d) Sum of refractive index modulation for TE0 and TE1 modes ($\Delta n_0 + \Delta n_1$) as function of reverse bias for different PN junction profiles.	29
1.13	Refractive index variations for TE0 (blue line) and TE1 (red line) modes as well as sum of them ($\Delta n_0 + \Delta n_1$) as a function of junction offset.	30
1.14	SEM picture of (a) the directional coupler, (b) the asymmetric Bragg grating waveguide.	30
1.15	Measured spectra of the asymmetric directional coupler when (a) the power is input in port 1 and coupled to the TE0 mode in the multimode waveguide, and (b) the power is input in port 4 and coupled to the TE1 mode in the multimode waveguide.	31
1.16	Reflective index variation of asymmetric Bragg grating modulators with different PN junction profiles as a function of the reverse voltage.	32
1.17	Zoom on the edge of the optical spectra, where the modulator is operated, of the asymmetric Bragg grating waveguide for reverse bias voltages of 0 V and 2 V.	32
1.18	Small-signal measurement of the asymmetric Bragg grating modulator for different reverse voltages.	33
1.19	Block diagram of the experimental setup.	33
1.20	BER as a function of the received power for different modulation speeds.	34
1.21	a) Measured BER as a function of bitrate without and with applying DD-MMSE equalizer, b) Histograms of detected bits (one sample per symbol) used for BER calculation at bitrate of 45 Gb/s and c) 55 Gb/s. The dashed lines show the Gaussian distributions in (b) and (c).	35

2.1	Schematic of the BGR-MZM showing a) the configuration of the BGR-MZM, b) the phase-shifted IBG present in each arm, c) the cross-section showing the p-n junction and the three doping levels, and d) the phase-shifted IBG cavity. TH: Thermal element, PS: Phase-shifted cavity, M1: Metal 1, M2: Metal 2, NOP: Number of periods of the resonator mirrors on each side, NOR: number of resonators. All dimensions are shown in micrometers.	40
2.2	Simulated photonic band-structure of the IBG.	42
2.3	Power transmission (black line) and phase response (colored lines) of an IBG with multiple phase shifts. The transmission is calculated for NOP = 15 and NOR = 6. Phase shifts are plotted for NOP = 15 and different values of NORs. NOR: number of resonators, NOP: number of periods.	42
2.4	Variation of the rib waveguide effective refractive index and absorption loss of p-n junction as a function of reverse voltage for simple phase shifters.	43
2.5	Phase variation as a function of applied reverse voltage for NOP = 15 and various NORs. RPS: a reference phase-shifter (waveguide with p-n junction that has a length equal to the length of the IBG with NOR = 6 and NOP = 15. NOR: number of resonators, NOP: number of periods.	44
2.6	Group index (solid line) and transmission (dashed line) versus wavelength for NOP = 15 and NOR = 6. NOR: number of resonators, NOP: number of periods.	44
2.7	a) Enhancement factor, b) 3-dB optical bandwidth of the transmission peak, c) Efficiency factor, and d) FOM; all as functions of NOR and NOP. Star and dot markers show two designs chosen for long- and short-distance applications, respectively. . . .	45
2.8	Delay-bandwidth product as a function of NOP for various NORs.	46
2.9	a) OMA and b) 3-dB OMA bandwidth as functions of NOR and NOP. Star and dot markers are the designs chosen for long- and short-distance applications respectively as in Fig. 2.7.	47
2.10	Design process flowchart of Bragg grating resonators.	47
2.11	a) OMA and b) ER as functions of V_{pp} and $\Delta\varphi_0$ for NOP = 17 and NOR = 15. c) OMA and d) ER as functions of V_{pp} and $\Delta\varphi_0$ for NOP = 15 and NOR = 6. Star and dot markers are the designs chosen for long- and short-distance applications respectively (as in Fig. 2.7 and Fig. 2.9).	49
2.12	a) Static optical modulation calculations for NOR = 6 and NOP = 15 (blue curves); and for NOR = 15 and NOP = 17 (black curves), b) OMA as a function of voltage for these two designs. In (a), dashed-line and solid-line show off and on states, respectively.	50
2.13	OMA spectra calculated for a) NOR = 15 and NOP = 17 (black line), and b) NOR = 6 and NOP = 15 (black line). In (a), OMA calculated with temperature variations of $\Delta T = -12.5^\circ\text{C}$ (blue line) and $\Delta T = 12.5^\circ\text{C}$ (red line) are also plotted. In (b), OMA calculated with temperature variations of $\Delta T = -25^\circ\text{C}$ (blue line) and $\Delta T = 25^\circ\text{C}$ (red line) are also plotted.	51
2.14	a) Transient time of the FDTD model at λ_0 normalized to E_0 , b) normalized steady state value of each node for the forward and backward fields at λ_0	53
2.15	Time response of BRG-MZM for a) 30 Gb/s, b) 70 Gb/s, and c) 110 Gb/s when applying RF voltage of 4 V_{pp} on each arm at the reverse voltage of -2 V and at λ_0	53
2.16	Eye diagrams calculated for BGR-MZM operated at (a) 30 Gb/s, (b) 70 Gb/s (c) 110 Gb/s.	54
2.17	Capacitance (blue) and resistance (red) of p-n junction as a function of reverse voltage. The resulting electrical cut-off frequency (black) is also shown.	54
2.18	Normalized EO impulse response.	55
2.19	Small-signal EO response of BGR-MZM.	55

2.20	OMA as a function of bitrate.	56
2.21	a) Modulator schematic, b) modulator cross-section, c) SEM picture of the two arms with their resonators. (Dimensions in a) and b) are in μm).	56
2.22	a) Simulated transmission amplitude and phase responses of the IBGR b) Transmission amplitude and phase responses of the IBGR measured with a LUNA OVA.	57
2.23	Measured EO scattering parameter S21 for different operational wavelengths at a reverse bias of 1V.	59
2.24	OMA spectra measured for bitrates of 10 Gb/s (black curve), 20 Gb/s (blue curve), and 30 Gb/s (red curve) at a V_{bias} of -1.5 V. Symbols are experimental measurements, the curves are guides for the eye. The inset is the eye diagram for a bitrate of 20 Gb/s.	60
2.25	Setup used to measure OMA, BER, and eye diagram.	60
2.26	BER as a function of the received power for different bitrates. Results are measured at V_{bias} of -1.5 V and λ_0 of 1570 nm.	61
2.27	BER vs. wavelength for different bitrates at V_{bias} of -1.5 V.	61
3.1	Schematic of a SL-MZM based on Bragg grating resonators and a) lumped electrodes, and b) TW electrodes. A C-MZM with TW electrodes is shown in c).	66
3.2	a) Schematic of a single-drive push-pull MZM with lumped electrodes. b) Equivalent RF circuit model.	67
3.3	The changes in the refractive index and the p-n junction absorption loss as a function of reverse voltage for a simple waveguide.	68
3.4	Normalized S21 of SL-MZM with lumped electrodes ($\gamma = 7$, $V_{bias} = -1$ V and $L_{SL-MZM} = 162 \mu\text{m}$). Dash-colored lines are measurement results for different operational wavelengths. The solid black line is the EO response predicted by the model.	71
3.5	Eye diagram of SL-MZM with lumped electrodes at 20 Gb/s a) simulation b) measurement with $V_{pp} = 3.5$ V on each arm, $V_{bias} = 1.5$ V and $\lambda_0 = 1570$ nm.	71
3.6	The EO bandwidth as a function of reverse voltage for different enhancement factors and $L_{SL-MZM} = 162 \mu\text{m}$	72
3.7	Normalized S21 for SL-MZMs with lumped electrodes and the C-MZM. $L_{C-MZM} = 4.8$ mm, $L_{SL-MZM} = 4.8/\gamma$ mm, and $V_{bias} = -1$ V.	73
3.8	FOM for OOK modulation format ($M = 2$), without considering loss ($\alpha = 1$ dB/cm for both cases), as a function of baudrate for lumped-electrode SL-MZMs and the C-MZM. $L_{C-MZM} = 4.8$ mm, $L_{SL-MZM} = 4.8/\gamma$ mm, and $V_{bias} = -1$ V.	74
3.9	FOM for OOK modulation format ($M = 2$), considering loss ($\alpha_{C-MZM} = 12.5$ dB/cm for C-MZM and $\alpha_{SL-MZM} = 17.5 \times \gamma$ dB/cm), as a function of baudrate for lumped-electrode SL-MZMs and the C-MZM. $L_{C-MZM} = 4.8$ mm, $L_{SL-MZM} = 4.8/\gamma$ mm, and $V_{bias} = -1$ V.	75
3.10	EO response of SL-MZMs combined with TW electrodes with $L_{SL-MZM} = 1$ mm at a reverse bias of 1 V.	77
3.11	The EO bandwidth as a function of enhancement factor at the reverse voltages of 1 V. $L_{C-MZM} = 4.8$ mm and $L_{SL-MZM} = 4.8/\gamma$ mm.	78
3.12	EO bandwidth of SL-MZMs with TW electrodes as a function of the enhancement factor for different V_{bias} . $L_{C-MZM} = 4.8$ mm and $L_{SL-MZM} = 4.8/\gamma$ mm.	78
3.13	FOM for OOK modulation format ($M = 2$) a) without b) with considering loss of the SL waveguides as a function of baudrate for TW SL-MZM and the C-MZM. $L_{C-MZM} = 4.8$ mm, $L_{SL-MZM} = 4.8/\gamma$ mm, and $V_{bias} = -1$ V.	79

3.14	Phase modulation multiplication factor, total loss, and RC constant of a simple p-n junction as a function of the normalized doping density factor (a normalized doping density factor of 5 means doping concentrations of $5 \times N_A$ and $5 \times N_D$ with $N_A = 5 \times 10^{17} \text{ cm}^{-3}$ and $N_D = 3 \times 10^{17} \text{ cm}^{-3}$).	81
3.15	FOM of the different approaches for V_π reduction through phase modulation enhancement as a function of baudrate.	83
4.1	a) Schematic of the DAC-less PAM-4 SL-MZM, b) cross-section of the modulator (the labeled parameters are in μm), c) close view of the fabricated modulator, d) SEM picture of a part of the fabricated modulator (inset is a zoom on the Bragg grating), and e) modulator under the test.	89
4.2	a) and b) are respectively schematics of the test configuration used to measure transmission and reflection of each arms in the test structure; c) and d) are respectively the transmission and reflection spectra of the test structure for different input/output ports.	91
4.3	a) Bragg wavelength and b) optical bandwidth of measured on chips from different wafer locations.	92
4.4	a) Transmission and reflection spectra of the SL-MZM, b) transmission of the two ports of the adiabatic coupler (located at the end of the modulator for recombining optical wave) as a function of the heater power. T1: output power from port1 of the adiabatic coupler, T2: output power from port2 of the adiabatic coupler, T1@QP: Transmission of the port 1 at the quadrature point.	92
4.5	Transmission spectra for different combination of applied voltages (see inset table) to generate four levels (in linear scale in the inset figure).	93
4.6	a) S11 of LSB and MSB segments. RF crosstalk between LSB and MSB segments (black) also is shown b) EO responses of MSB and LSB segments for different reverse voltages, c) 3-dB EO bandwidth spectra of MSB and LSB segments.	94
4.7	Block diagram of the experimental setup.	95
4.8	BER spectral measurement when modulating either the a) MSB and b) LSB segments, for OOK modulation at different bitrates. Dashed and dotted lines show 7% and 20% FEC thresholds, respectively.	96
4.9	BER spectral measurement of DAC-less SL-MZM for PAM-4 format. Dotted and dash-dotted lines show 7% and 20% FEC thresholds, respectively.	97
4.10	Histograms of detected bits (one sample per symbol) used for BER calculation at different bitrates (30, 50, 70 and 90 Gb/s) and operational wavelengths (1561, 1562 and 1563 nm).	97
5.1	TE and TM modes supported by in the highly-elliptical-core fiber.	103
5.2	a) Schematic of an asymmetric directional coupler b) effective refractive indices of TE0-TE4 as a function of width of the waveguide (W) c) mode coupling as a function of waveguide width (or super-mode simulation). The inset in (c) shows the simulation area in Lumerical-mode where the simulation area is defined on the cross-section of the coupling area (<i>i.e.</i> , including bus waveguide with width of W and the waveguide with width of 500 nm).	104

5.3	Simulation results of asymmetric directional coupler when designed for coupling a) TE0 into TE1 b) TE0 into TE2 c) TE0 into TE3. The insets show the mode propagation for coupling of each design to desired mode in the bus waveguide as well as their cross-sections. In the simulations, the power monitors are placed after the coupling area plus 20 μm	106
5.4	Schematic of the mode multiplexer based on cascaded asymmetric directional couplers.	107
5.5	Schematic of PAM SL modulators based on Bragg grating resonators with two segments and four DC elements to set the operating point and bias the modulator	107
5.6	a) Layout of PAM SL modulators designed in Pyxis b) a close view of Bragg grating structure.	107
5.7	Schematic of IQ SL modulators based on Bragg grating resonators	108
5.8	a) Layout of IQ SL modulators designed in Pyxis b) a close view of Bragg grating structure.	109
5.9	Loaded TW electrode with "T" shaped extensions to increase the RF index	109
5.10	a) Four-channel SDM transmitter based on PAM4 SL modulators, b) a close view of on-chip mode multiplexers, c) a close view of a back-to-back configuration of mode multiplexers	110
5.11	Simulation results of the cross-section of the mode multiplexer output a) index profile, b) TE0 mode profile, c) TE1 mode profile, d) TE2 mode profile, e) TE3 mode profile. The capital letters show the same information for the highly-elliptical-core fiber in [95]	112
5.12	Lens-based coupling scheme between the on-chip mode multiplexer and the highly elliptical core fiber	112
5.13	a) Four-channel SDM transmitter based on IQ SL modulators, b) a close view of on-chip mode multiplexers, c) a close view of a back-to-back configuration of mode multiplexers	113
5.14	a) Schematic of our model to calculate the total TPP of PAM SL modulators with lumped electrodes at baudrate of 50 GBaud, b) eye diagram of generated data, c) eye diagram of electrical signal after pulse shaping, d) eye diagram of electrical signal after applying bandwidth limitation of DAC, e) eye diagram of electrical signal after pre-compensating the DAC, f) EO response of the MSB segment, g) eye diagram of the pre-distorted signal due to the finite bandwidth of modulator, h) eye diagram of electrical signal after RF amplifier, i) eye diagram of applied signal to the modulator, k) eye diagram of optical modulated signal.	115
5.15	Total transmission power penalty as a function of length of SL phase shifters for different enhancement factors (γ) at baudrate of 50 GBaud for PAM4 format.	116
5.16	Total transmission power penalty as a function of baudrate for the designed PAM SL modulator introduced in section 5.3.1.	117
5.17	a) Schematic of our model to calculate the total TPP of IQ SL modulators with TW electrodes at a baudrate of 100 GBaud, b) eye diagram of generated data, c) eye diagram of electrical signal after pulse shaping, d) eye diagram of electrical signal after applying bandwidth limitation of DAC, e) eye diagram of electrical signal after pre-compensating the DAC, f) EO response of the modulator, g) eye diagram of the pre-distorted signal due to the finite bandwidth of modulator, h) eye diagram of electrical signal after RF amplifier, i) eye diagram of applied signal to the modulator, k) constellation diagram of optical modulated signal	118
5.18	Constellation diagram of modulated IQ signal for different scenarios at a baudrate of 100 GBaud for a) 16 QAM and b) 64 QAM.	119

5.19	Total transmission power penalty as a function of length of SL phase shifters for different enhancement factors (γ) for the 16 QAM format at a baudrate of 50 GBaud. .	119
5.20	a) Total transmission power penalty and b) probability error factor of the designed IQ SL modulator introduced in section 5.3.2 as a function of baudrate for different modulation formats.	120
5.21	Total transmission power penalty of IQ SL modulators with a γ of 6 (red line) and conventional MZMs (blue line) as a function of phase shifter length at 50 GBaud. The red dash line shows the TPP of an SL-MZM that presents less loss. The dot on the blue line shows the TPP of the reference conventional IQ MZM presented in [61], the dot on the red line represents the TPP of the designed IQ SL MZM, and finally the dot on the red dash line shows the better TPP of the structurally improved IQ SL MZM.	120

Abbreviations

A-IBG	Asymmetric Integrated Bragg Grating
ASBG	Asymmetric Sidewall Bragg Grating
BER	Bit Error Rate
BOX	Buried Oxide
EDFA	Erbium-Doped Fiber Amplifier
EO	Electro-Optic
C-LI	Combination of Lateral and Interleaved
CMOS	Complementary Metal Oxide Semiconductor
CPS	Coplanar Strip line
CPW	Coplanar Waveguide
DSP	Digital Signal Processing
EAM	Electro Absorption Modulator
ER	Extinction Ratio
FOM	Figure Of Merit
HPC	High-Performance Computing
IBG	Integrated Bragg grating
IBGR	Integrated Bragg grating resonator
InP	Indium Phosphide
IQ	In phase Quadrature Modulator
ISI	Inter Symbol Interference

LiNbO3	Lithium Niobate
LSB	Least Significant Bit
MMSE	Minimum Mean Square Error
MOSCAP	Metal Oxide Semiconductor Capacitor
MSB	Most Significant Bit
MUX	Multiplexer
MWP	Multi Project Wafer
MZM	Mach-Zehnder Modulator
MRM	Micro-ring Modulator
NRZ	Non Return to Zero
OBPF	Optical Band-Pass Filter
OFDM	Orthogonal Frequency-Division Multiplexing
OOK	On-Off Keying
OSNR	Optical Signal to Noise Ratio
PAM-4	Four-level Pulse Amplitude Modulation
PRBS	Pseudo Random Bit Sequence
QAM	Quadrature Amplitude Modulation
OMA	Optical Modulation Amplitude
RF	Radio Frequency
RTO	Real Time Oscilloscope
SDM	Space Division Multiplexing
SiP	Silicon Photonics
SISCAP	Semiconductor Insulator Semiconductor Capacitor
SOI	Silicon On Insulator
TDM	Time Division Multiplexing
TPP	Transmission Power Penalty

TW	Travelling-wave
WDM	Wavelength Division Multiplexing
3D	Three Dimension

Variables and Symbols

C_i	Capacitance
D	Distance between two adjacent points in constellation diagram when there is no impairment from IQ SL modulators
d	Distance between two adjacent points in constellation diagram in the presence of impairments from IQ SL modulators
Gbaud	Giga baud
Gb	Giga bit
GHz	Giga hertz
L	Inductance of traveling wave electrodes
L_{SL-MZM}	Length of the phase shifter in an SL modulator
L_{C-MZM}	Length of the phase shifter in a conventional MZM
M	Modulation order in PAM modulation
n	Dopant type n
n_g	Group index of the optical signal
n_{RF}	RF effective index of the loaded transmission line
p	Dopant type p
pJ	Pico joule
ps	Pico second
P_{in}	Input optical power
P_{out}	Output optical power
R	Resistance
V_{in}	Input voltage
V_{pp}	Peak to peak voltage

V_b	Bias voltage
V_{RF}	RF voltage
V_{DC}	DC voltage
V_{bias}	Bias voltage
V_π	Half wave voltage of the modulator
α	Optical attenuation constant
$\Delta\varphi$	Phase shift from a pn doped optical waveguide due to applied reverse voltage
$\Delta\varphi_0$	Initial phase deference between two arms of a MZM
ΔT	Operating temperature range
$\Delta\lambda_{BW}$	Operating wavelength range
Ω	Ohm
γ	Enhancement factor in phase modulation
λ_0	Operational wavelength
$^{\circ}\mathbf{C}$	Centigrade

*To my darling better half, Rizan
my beloved mother, Shahla
my inspiring father, Gholam Ali
and my adorable brother, Saeed*

“A goal without a plan is just a wish.”

Antoine de Saint-Exupéry

Acknowledgement

I would like to express my sincere gratitude to Professor Sophie LaRochelle and Professor Wei Shi for giving me this unique opportunity to study in an outstanding research center. I cannot thank them enough for their continued support of my research. I encountered many challenges during my Ph.D. studies but never felt alone in this way. Their constant supports and encouragements greatly motivated me to accomplish my tasks. Sophie is someone you definitely love to work with because of her ambitious in science, leadership, and great professionalism. She is an excellent example of a professor who manages projects and guide students in the best manner possible. I enjoyed every discussions we had on our projects and I truly learn a lot from her. Wei is someone who grabs your attention instantly as he makes science fun and exciting for you. He supports your ideas, gives you freedom and encourages you to pursue your goals. I like how we engaged in our discussions and couldn't notice the time pass.

Next, I cannot thank Hassan Sepehrian enough who kindly helped me in many aspects at the beginning of my studies. I would also like to thank my colleague Sasan Zhalehpour who helped me in processing the captured data in the lab. Furthermore, I would love to thank all of my friends at COPL for all their helps and interesting discussions. And a special thanks to my officemate for all their supports from the beginning of my study: Charles, Antoine, Alessandro, Gabriel, and Long.

Last but not least, a special thanks to my family. Words cannot express how grateful I am to my mother, father, brother and fiancée for all of the sacrifices that they have made on my behalf. Their prayer for me was what sustained me thus far. Especially, throughout my academic studies, my beloved fiancée has always been the one who inspired and motivated me to overcome obstacles along the way. She helped me to find out my courage, strengths, weaknesses, and faith. I cannot imagine myself to get along in this bumpy path **without her SUPPORTS**.

Foreword

Four chapters of this thesis (chapter 1, 2, 3, and 4) are based on materials published in conference and journal papers. Most of the contents in these four chapters are the same as the journal papers; however, some modifications are made for better coherency. I was the first author and the main contributor of these papers. I designed, simulated, and experimentally characterized the devices presented in the following chapters. Professor LaRochelle and Professor Shi helped me in developing ideas and debugging the lab issues. We had many scientific discussions to accomplish each task. My co-author, Sasan Zhalehpour, also helped me in the offline digital processing during measurement of devices presented in chapter 1 and 4. Moreover, the other co-author, Hassan Sepehrian, helped me with the typeout of devices presented in chapter 2. The other co-author, Jiachuan Lin, also helped me with BER measurement results presented in our ECOC paper, which is a part of chapter 1.

Chapter 1: O. Jafari, W. Shi, and S. LaRochelle, “Silicon Photonic Modulator using Mode Conversion with Asymmetric Sidewall Bragg Gratings”, 2018 IEEE International Conference on Group IV Photonics (GFP). IEEE, 2018.

O. Jafari, J. Lin, W. Shi, and S. LaRochelle, “Mode-conversion-based silicon photonic modulator using asymmetric Bragg grating and Y-branch”, European Conference on Optical Communication (ECOC), 2019.

O. Jafari, S. Zhalehpour, W. Shi, and S. LaRochelle, “Silicon photonic modulator loaded by a combination of lateral and interleaved p-n junctions”, OSA Advanced Photonics Congress (APC), 2020.

O. Jafari, S. Zhalehpour, W. Shi, and S. LaRochelle, “Mode-conversion-based Silicon photonic modulator loaded by a combination of lateral and interleaved p-n junctions”, OSA Photonic Research, 9 (4), 2021.

These papers demonstrate a novel design of silicon photonic modulators based on the mode conversion in the active area. This mode conversion enables the modulator to operate in reflection without adding significant on-chip loss. The mode conversion is achieved by an asymmetric Bragg grating waveguide, realized by introducing a half-period offset between sidewall gratings. Using an asymmetric Y-branch or asymmetric directional coupler as a mode splitter, we retrieve the reflected

modulated light at the input of the modulator. This design allows avoiding the need for an external circulator and reducing the on-chip loss introduced by the on-chip coupler from 6 dB to 1 dB. We also manipulate PN junction shape to enhance the phase modulation.

Chapter 2: O. Jafari, H. Sepehrian, W. Shi, and S. LaRochelle, “High-Efficiency Silicon Photonic Modulator Using Coupled Bragg Grating Resonators”, *Journal of Lightwave Technology*, 37(9), 2065-2075, 2019.

O. Jafari, W. Shi, and S. LaRochelle, “Mach-Zehnder Silicon Photonic Modulator Assisted by Phase-Shifted Bragg Gratings”, *IEEE Photonics Technology Letters*, 32(8), 445-448, 2020.

O. Jafari, H. Sepehrian, W. Shi, and S. LaRochelle, “Silicon Photonic Modulator based on Coupled Bragg Grating Resonators used as Phase Shifters”, *Optical Fiber Communications Conference (OFC)*, 2018.

O. Jafari, W. Shi, and S. LaRochelle, “Silicon Photonic Modulator Using Coupled Bragg Grating Resonators in a Mach-Zehnder structure”, *Conference on Lasers and Electro-Optics (CLEO)*, 2019.

These papers aim to demonstrate the first slow-light silicon photonic modulators based on coupled Bragg grating resonators. We propose a Mach-Zehnder modulator (MZM) assisted by low-Q-factor resonators. When operated in the low-dispersion-slow-light regime, the resonators can significantly enhance the modulation efficiency of MZMs. Also, these structures can be engineered to have a relatively larger optical bandwidth than MRMs in order to increase modulation stability and robustness with respect to temperature variations. Therefore, the modulator combines the advantage of compact footprint, low power consumption, large electro-optic bandwidth and relatively stable operation.

Chapter 3: O. Jafari, W. Shi, and S. LaRochelle, “Efficiency-speed tradeoff in slow-light silicon photonic modulators”, *IEEE Journal of Selected Topics in Quantum Electronics*, 27(3), pp. 1-10, 2021.

O. Jafari, W. Shi, and S. LaRochelle, “A model for electro-optic response of slow-light silicon photonic modulators with lumped electrodes”, *IEEE Photonics conference (IPC)*, 2020.

In this work, we investigate the impact of the SL effect on the fundamental tradeoffs in silicon photonic modulators (efficiency-stability tradeoff, efficiency-speed tradeoff, and efficiency-loss tradeoff). To this end, we first derive a comprehensive model for the dynamic response of slow-light modulators. Next, we compare slow-light modulators with conventional MZMs considering key parameters: efficiency, speed and loss. The second objective of this chapter is to assess different design strategies to reduce V_π and meet the requirement of CMOS drivers: 1) a longer phase shifter, 2) higher doping

densities, and 3) the SL effect.

Chapter 4: O. Jafari, S. Zhalepour, W. Shi, and S. LaRochelle, “Highly efficient DAC-less PAM-4 silicon photonic modulator with stable operation”, *Journal of Lightwave Technology*, accepted.

O. Jafari, S. Zhalepour, W. Shi, and S. LaRochelle, “DAC-Less PAM-4 Slow-Light Silicon Photonic Modulator Assisted by Coupled Bragg Grating Resonators”, *Optical Fiber Communications Conference (OFC)*, 2021.

This chapter aims to demonstrate a silicon photonic modulator which is well-suited for the next-generation optical transmission systems. We report a SL modulator that simultaneously achieves all desired features, especially power efficiency, compact footprint, and stability. It enables a high-speed PAM operation without the need for a DAC. Bragg grating resonators are loaded into each arm of an MZM in order to slow down optical waves, enhancing the phase modulation over a relatively wide bandwidth. Optical PAM-4 signal is generated employing a segmented design in the SL phase shifters.

Introduction

Last decades have seen a boom in using stream video, online games, sensor networks, financial transactions, and cloud communication. This results in a dramatic increase in Internet traffic, introducing a rapidly growing demand for storing, transferring, and manipulating "Big Data" in data centers. Studies show that on-chip, chip-to-chip, board-to-board, and rack-to-rack data transmission is the main constraint of data centers' performance [1, 2]. These heavy interactions necessitate the need for a data center featuring high bandwidth, low latency, and low energy consumption [3, 4].

Optical interconnect leveraging optical components is a promising technology to meet the aforementioned criteria, specifically energy efficiency [5–7]. Three figures of merit (FOMs) have been defined to evaluate optical networks [6]:

- I. $Gbps/mm^3$: bandwidth density per volume of transceivers
- II. pJ/bit or $mW/Gbps$: energy consumption of links
- III. $\$/Gbps$: cost per speed

Different techniques for multiplexing data are combined to enable optical interconnects offering high bandwidth density: time division multiplexing (TDM), wavelength division multiplexing (WDM), orthogonal frequency-division multiplexing (OFDM), and space division multiplexing (SDM). Therefore, with all-optical networks, data centers save energy up to 75% due to the unique properties of optical components and the above techniques [8, 9].

Nevertheless, at the beginning, such data centers were not as cost-effective as traditional ones [10]. Indeed, cost and scaling were the important impediments to widely implement optics in data centers. The new technology should be able to offer optics as ubiquitous as copper, but at a similar cost [10]. To this end, the best solution is to leverage the large investment made in the mature CMOS process and use this technology to fabricate optical chips [11, 12].

Silicon photonic (SiP) technology has demonstrated a great potential to bridge this chasm. Indeed, since silicon is a compatible material with the CMOS technology, silicon-based components fabricated with standard CMOS processes have been widely reported for generating [13–16], mod-

ulating [17–26], manipulating [27–31], and detecting [32–36] light. Therefore, reusing the CMOS manufacturing process paves the path for the SiP technology to reach large-scale productions.

I.1 Silicon photonic technology

SiP technology emerged in 1980s where Soref and Lorenzo demonstrated the first all-silicon integrated-optical components [37]. Following this pioneering work, tremendous efforts have been dedicated to delivering today’s SiP integrated circuits, for example 112 Gb/s PAM-4 SiP transmitter based on micro-ring modulators (MRMs) [38–40] and 1.6 Tb/s SiP integrated circuit using 16-channel 50-Gbaud PAM-4 MRMs [41] both presented by Intel, 400 Gb/s SiP transceiver demonstrated by Analog Photonics [42], and 400 Gb/s SiP coherent transceiver exhibited by Ciena [43].

Nowadays, SiP technology plays a crucial role not only in data centers but also in high performance computing (HPC), telecom, aeronautics aerospace, sensors, medical, and autonomous cars as shown in Fig. I.1 [44]. The key driving force behind SiP technology is the compatibility with mature CMOS manufacturing processes, leading to a cost reduction in R&D process and mass production. Hence, many companies are in the SiP’s value chain, resulting in day-by-day breakthroughs and progresses in this technology. Fig. I.2 shows ecosystems of the SiP technology.

Figure I.3 refers to the evolutionary trend in SiP transceivers considering industry form factors. The trend indicates a path towards not only higher bandwidth (or speed) but also high-density integration, low power consumption, and large operating temperature range. Scaling performance is expected to be a bumpy path because of some intrinsic limitations related to integrated laser, CMOS-photonics co-design, and electro-optic (EO) efficiency of SiP modulators.

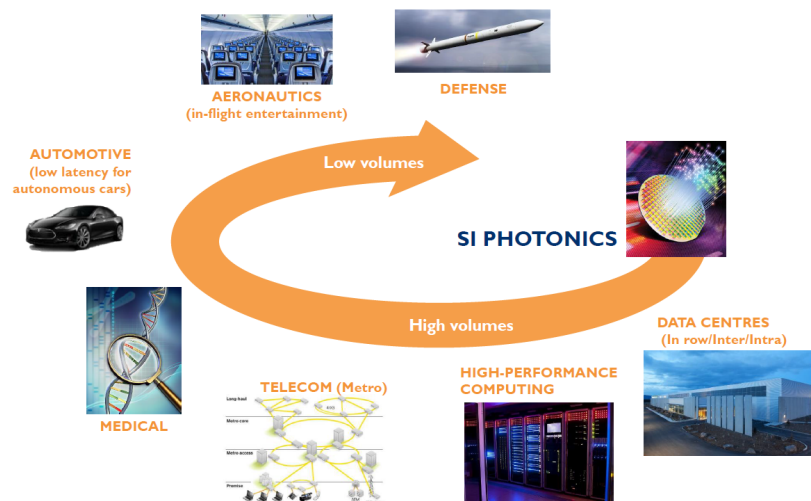


Figure I.1 – SiP applications, Silicon Photonics 2018 report, Yole Développement, January 2018, <http://www.yole.fr>

- **Integrated laser.** Figure I.4 displays a typical cross-section of SiP CMOS process. As shown, current SiP CMOS processes offer all key optical components for EO integration except laser source due to the low emission efficiency in silicon. Hence, an extensive research effort is undergoing to find promising solutions based on porous silicon, silicon nanocrystals, silicon Raman laser, etc. [46]. An ideal on-chip laser source should allow significant reduction in energy consumption and high density in integration. Nevertheless, thermal stabilization is a challenging issue in this case. On the contrary, off-chip laser sources show good efficiency and stability; however, they suffer from a large chip-to-chip coupling loss and costly packaging.

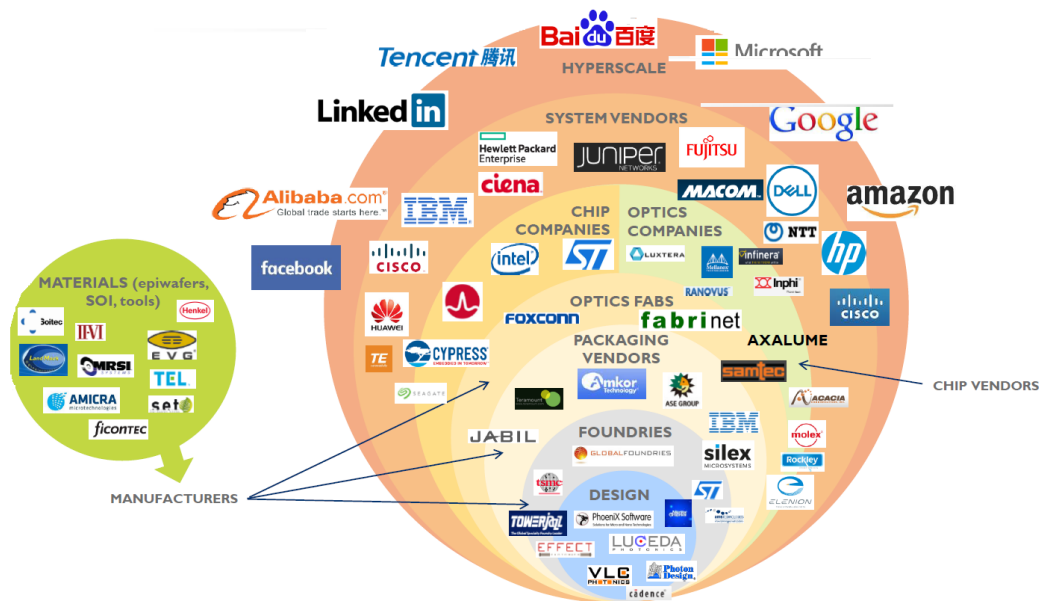


Figure I.2 – SiP ecosystems, Silicon Photonics 2018 report, Yole Développement, January 2018, <http://www.yole.fr>



Figure I.3 – Trend in SiP transceiver [45]

- CMOS-photonics co-design.** Monolithic integration of CMOS drivers with SiP modulators has been recognized as a promising technology, offering a cost-efficient and power-efficient electrical connection to the transceiver circuit chip [48]. The main advantage of monolithic SiP integration lies in minimizing the parasitic capacitance induced by the interconnection of SiP and CMOS dies. Also, this technology provides a shorter RF path from CMOS drivers to SiP modulators, resulting in reduced RF loss especially in higher frequencies. It thus becomes necessary for bandwidth scaling for the next generation of optical transceivers (expected to be 106 Gb/lane [42]). To achieve these substantial advantages, this process requires simultaneous optimization of photonic and electronic devices. This means that transistors in the monolithic process should tolerate modifications of the fabrication process due to optical components [48]. To this end, these transistors are usually fabricated using older CMOS processes (for example, 90nm SOI CMOS demonstrated by IBM [49] or 45nm SOI CMOS presented by Ayar Lab [48]). In contrast, non-monolithic platforms, also called hybrid integration, offer independent optimization of photonic and electronic devices. This means that fabricating optical components imposes no restrictions on the electronic process and offers full flexibility in choosing technologies. Therefore, hybrid integration makes it possible to target the full potential of CMOS process from both electronic and photonic perspectives. However, the additional parasitic capacitance and inductance introduced by micro-bumps or wire-bondings at the interfaces between SiP and CMOS dies increase the required optical and electrical power budgets [48]. Moreover, at future target speeds, *i.e.*, >100 Gb/lane, RF propagation loss dramatically increases in a way leading to RF transmission lines inside the package becoming critically energy-hungry [42].
- EO efficiency of SiP modulators.** Sensitivity of optical properties of materials to the applied electrical field determines EO efficiency of modulators. Some materials such as lithium niobate (LiNbO₃) [50–52] and III-V semiconductor [53–55] provide a strong EO efficiency. These materials are not, however, compatible with standard CMOS process, leading to a significantly costly integration. Nevertheless, Infinera has recently demonstrated a 1.6 Tb/s coherent transceiver based on InP modulators as shown in Fig. I.5 [56]. There are also some companies doing thin-film LiNbO₃ on silicon.

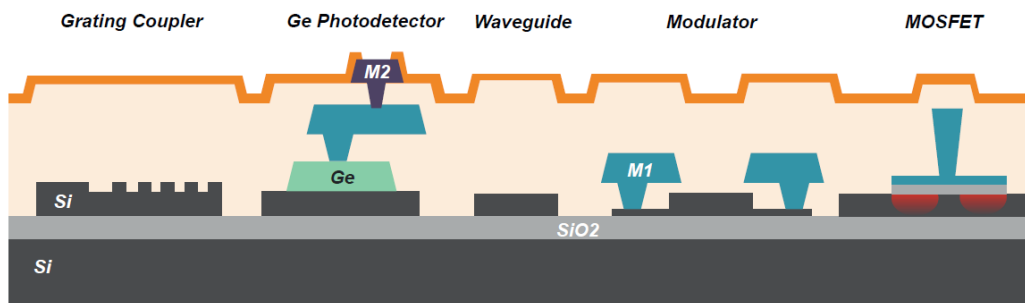


Figure I.4 – Cross-section of typical SiP CMOS process [47]

On the other hand, silicon shows a poor EO sensitivity. Indeed, pure silicon presents extremely weak Pockels effect, Kerr effect, and Franz–Keldysh effect at the telecommunication wavelengths [24, 57]. Hence, there is on-going research on how to add these effects to the silicon platform. For example, IBM has recently demonstrated a hybrid BTO/silicon technology—combining Barium titanate (BTO) with SiP platform—that is capable of considerably enhancing Pockels effect in silicon-based devices [58].

The common method to gain EO modulation in silicon has been the plasma dispersion effect wherein refractive index variation is achieved by modulating carrier concentrations [57]. In 1987, Soref and Bennett reported an experimentally derived model for refractive index variation as a function of the change in free carrier concentrations, presented in Eq. I.1-I.3 [59].

$$\Delta n = - \left[8.8 \times 10^{-22} \times \Delta n_e + 8.5 \times 10^{-18} \times \Delta n_h^{0.8} \right] \quad @ \lambda = 1.55 \mu m \quad (I.1)$$

$$\Delta n = - \left[6.2 \times 10^{-22} \times \Delta n_e + 6.0 \times 10^{-18} \times \Delta n_h^{0.8} \right] \quad @ \lambda = 1.3 \mu m \quad (I.2)$$

$$\Delta n_{eff} = \frac{\iint_S E^* \Delta n E \, ds}{\iint_S E^* E \, ds} \quad (I.3)$$

where Δn_e and Δn_h are the changes in electron and hole carrier concentrations, respectively; and E is the electrical field of optical modes. As indicated, the effective refractive index variation depends on the changes in free carrier concentrations and the overlap between electrical and optical modes [47]. Three mechanisms have been widely used for manipulating electrical charge distribution as shown in Fig. I.6: carrier depletion, carrier injection, and carrier accumulation [24]. Among these mechanisms, SiP modulators based on the carrier depletion

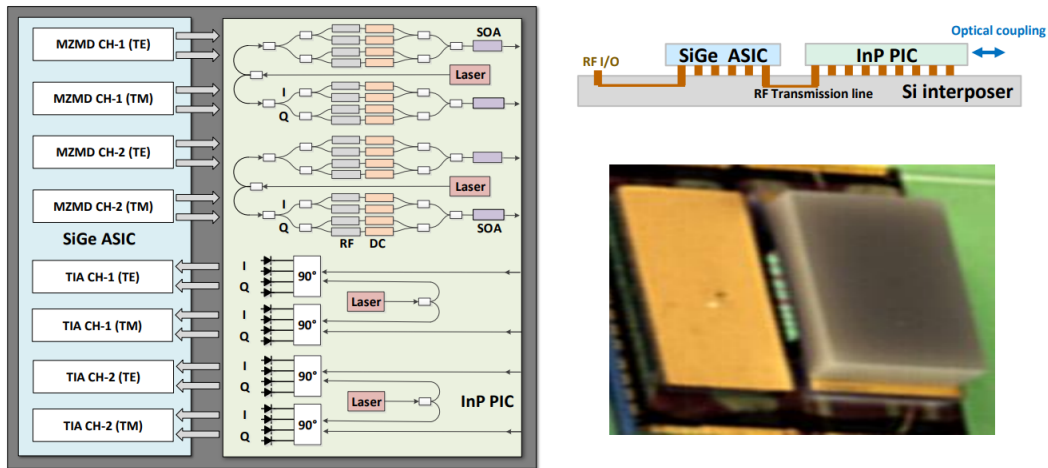


Figure I.5 – Schematic of the coherent transceiver demonstrated by Infinera, its cross section, and its flip-chip assembly [56]

have demonstrated a large EO bandwidth and been extensively utilized for high-speed applications [60–64]. Despite this advantage, the carrier depletion introduces less modulation efficiency compared to the two others, leading to longer and energy-hungry phase shifters.

I.2 Silicon photonic modulators

MZMs combined with traveling wave (TW) electrodes have been the most commonly-used SiP modulators in industry so far because of their reliability and speed. Fig. I.7 displays a single-drive push-pull SiP MZM integrated with TW electrodes and its cross-section [65]. These modulators present a broad thermal operating range due to their wide optical bandwidth and offer a chirp-free operation if driven under a push-pull configuration. Nevertheless, nowadays, high-density integration and low power consumption are two determining performance criteria in next-generation optical transmitters. Considering these criteria, MZMs lose their popularity. This is because RF crosstalk between adjacent TW electrodes does not allow to place MZMs very close to each other, depriving optical transmitters of high-density integration [66, 67]. In Ref. [66], a minimum distance of 600 μm is suggested between two adjacent TW electrodes with a length of 4 mm to keep crosstalk lower than 30 dB. In addition, dissipating RF power at 50- Ω terminations, as well as losing RF power along loaded TW electrodes, make MZMs energy-hungry.

Enhancement in modulation efficiency is required in order to shorten phase shifters and combine MZMs with lumped electrodes. To do so, one approach is to reconfigure PN junctions in the way that the overlap between the depletion region and optical modes is enhanced. Vertical PN junctions (see Fig. I.8 [68]) and U-shaped PN junctions (see Fig. I.9 [69]) increase the overlap, however, at the cost of reducing EO bandwidth. Silicon Insulator Silicon CAPAcitor–SISCAP (see Fig. I.10 [70])–demonstrated by Cisco is another promising candidate to address low efficiency of the

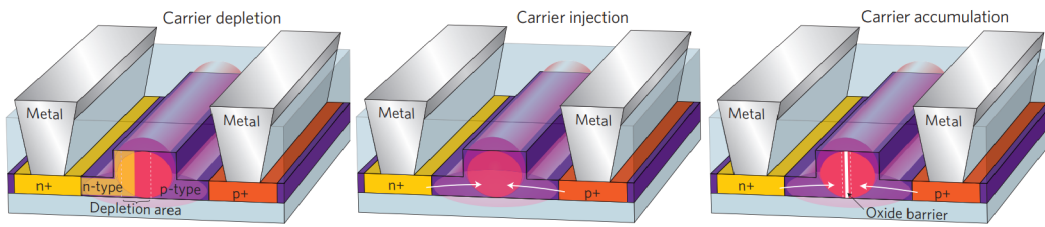


Figure I.6 – Cross-sections of carrier depletion, carrier injection, and carrier accumulation [24]

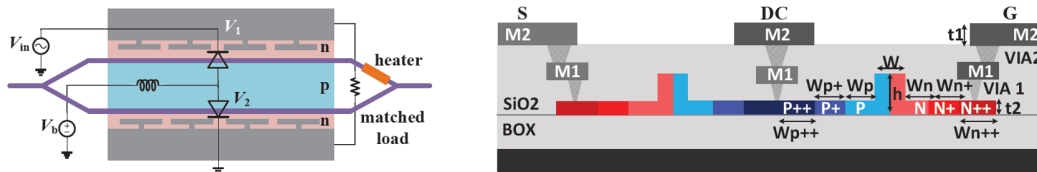


Figure I.7 – Schematic of a single-drive push-pull SiP MZM combined with TW electrodes and its cross-sections [65]

plasma dispersion effect [70,71]. SISCAP is formed by poly-silicon layer at the middle of waveguide (like a metal gate in CMOS capacitor). However, high insertion loss and complicated fabrication process become the biggest impediments for further development of this technology.

Resonance based modulators, usually known as micro-ring modulators (MRMs), are recognized as the leading candidate to achieve power-efficient and ultra-compact transmitters. Fig. I.11 illustrates a schematic of MRMs [21]. Formed by a high-Q-factor resonator, MRMs are characterized by low energy consumption (a few femto joules per bit [21]) and compact footprint. Furthermore, due to their short phase shifters, MRMs are loaded with lumped electrodes, making them a perfect solution for high-density integration. Nevertheless, their resonance nature creates a narrow wavelength range wherein MRMs can operate. This results in unstable operation and limited speed. MRMs have an operating wavelength range of < 0.1 nm, corresponding to < 10 °C operating temperature range. Therefore, a temperature stabilizer circuit to find and lock the resonance wavelength is a vital part of MRM-based transmitters, which in turn consumes more power than MRMs themselves. In addition to this, high photon lifetime restricts EO bandwidth, resulting in a sharper roll-off in EO response of MRMs compared to that of MZMs. Hence, MRMs cannot operate at a baudrate that is much larger than their 3-dB bandwidth. Furthermore, when modulating optical signal amplitude, MRMs also

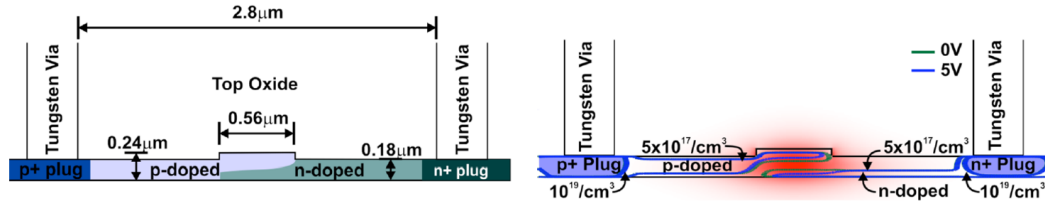


Figure I.8 – Schematic of an vertical PN junction in different reverse voltages [68]

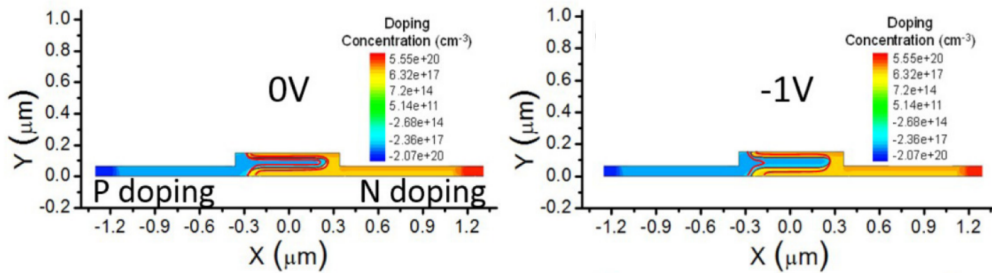


Figure I.9 – Schematic of a U-shaped PN junction in different reverse voltages [69]

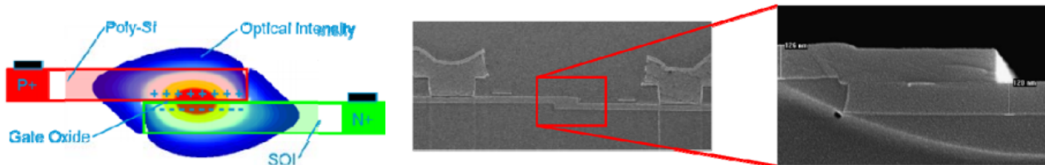


Figure I.10 – Schematic of SISCAP device and SEM image of fabricated device [70]

manipulate output phase, resulting in chirpy pulses.

When operated at the edge of the stop band, Bragg grating waveguides can also be exploited for modulating optical waves, as shown in Fig. I.12 [18, 25, 72, 73]. Bragg grating modulators are versatile because their performance, depending on their designs, can be tuned to provide features close to those of MZMs [25] or MRMs [18]. This means that these modulators can reach a compromise between speed and energy consumption.

Slow-light (SL) SiP modulators recently received extensive attention because of their unique performance in improving the intrinsic tradeoff between stability and efficiency [23, 25, 74–80]. Indeed, slowing down optical waves inside phase shifters enables SL modulators to enhance the modulation efficiency in a relatively large optical bandwidth. These modulators combine advantages of low energy consumption, compact footprint, stable operation (nm-scale operating wavelength range), and chirp-free modulation if operated with a push-pull configuration. Different structures have been proposed to slow down optical waves such as photonic crystal waveguide (see Fig. I.13 [76]), micro-ring resonators (see Fig. I.14 [23]), Bragg grating waveguide (see Fig. I.15 [25]), and our work on Bragg grating resonators (see Fig. I.16 [80]). These modulators will be discussed in detail in chapters 2 and 3.

I.3 Segmented silicon photonic modulators

Increasing the number of bits per symbol is a viable approach to meet the growing speed requirement. Providing a compromise between data rate and complexity, pulse amplitude modulation (PAM) is a great means to increase the speed in short-reach systems where power efficiency and cost are important criteria. PAM only requires the direct detection, without the need for a complex digital

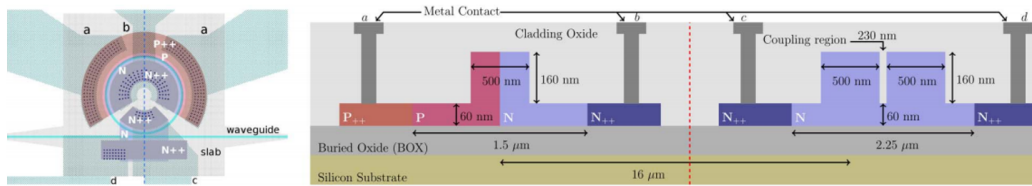


Figure I.11 – Schematic of an MRM and its cross-section [21]

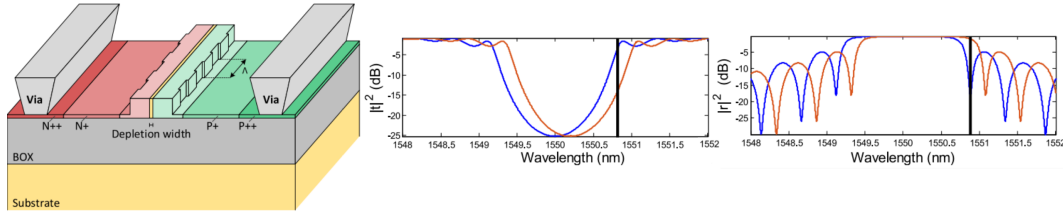


Figure I.12 – Schematic of an Bragg grating modulator and it operational wavelength in transmission and reflection [73]

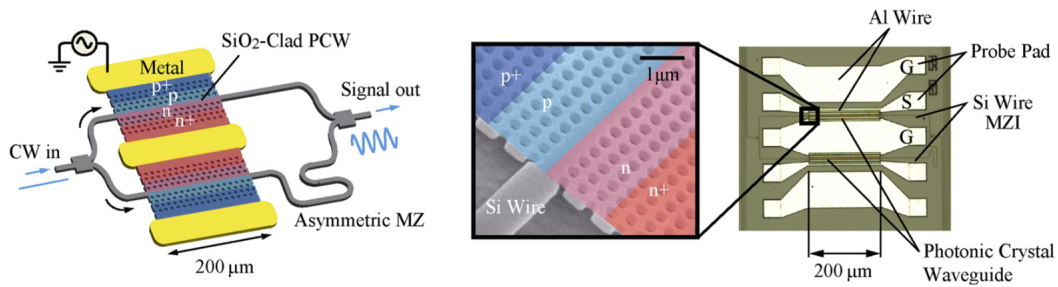


Figure I.13 – Schematic of a SL modulator based on photonic crystal waveguides [76]

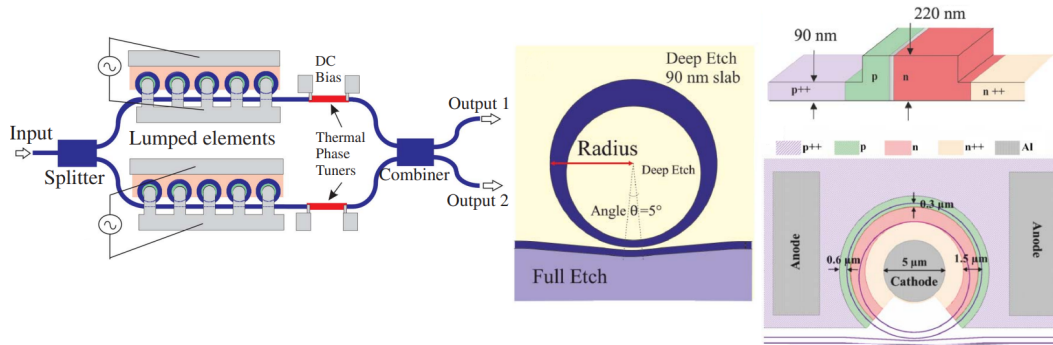


Figure I.14 – Schematic of a SL modulator based on micro-ring resonators [23]

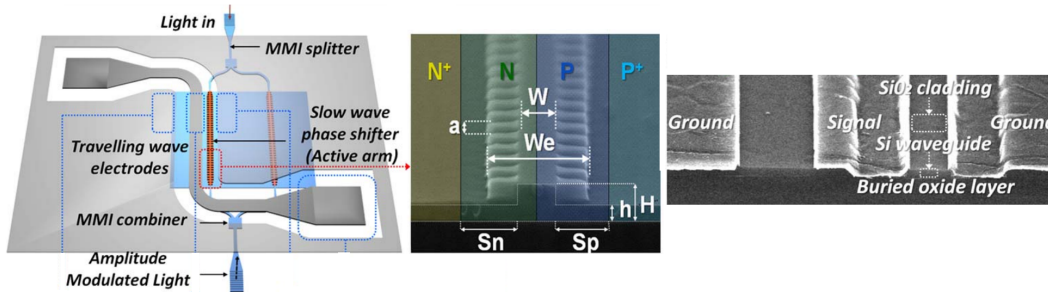


Figure I.15 – Schematic of a SL modulator based on Bragg grating waveguides [25]

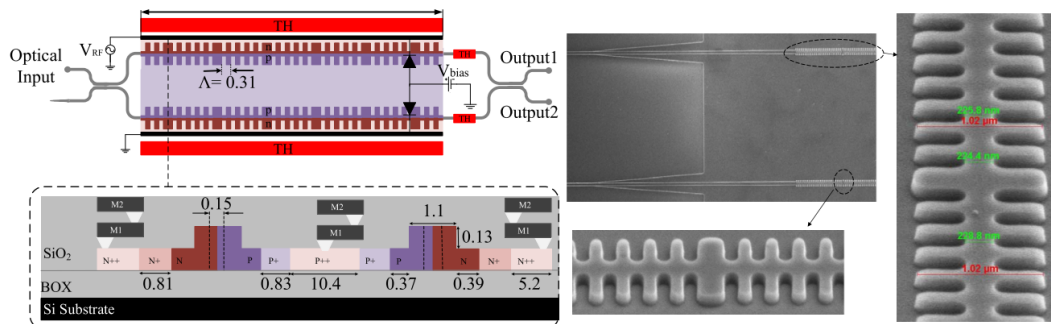


Figure I.16 – Schematic of our work on SL modulator based on Bragg grating resonators presented in [80]

signal processing (DSP), resulting in reduced complexity and cost in comparison to the quadrature amplitude modulation (QAM) [65]. This motivates targeting 4-level PAM (PAM-4) to reach the IEEE 400 Gb/s Ethernet standard as reported by its task force [38–42, 81]. This speed can be achieved by 25 Gbaud PAM-4 using 8 wavelength channels or 50 Gbaud PAM-4 using 4 wavelength channels. PAM is generated either by multi-level CMOS drivers (digital-to-analog converters (DACs)), resulting in added complexity to CMOS circuits, or by on-chip segmented modulators. Segmented SiP modulators have been demonstrated based on different structures, such as MZMs [63, 64, 82–84], MRMs [21, 38–40, 85], and Bragg grating modulators [20].

MZMs with several series segments, shown in Fig. I.17 [82], have been probably the most common configurations to generate the DAC-less PAM-4 format because they offer high-speed operation (>100 Gb/s) and have a wide band response, resulting in no need for temperature stabilization. Moreover, they do not require any customized manufacturing process due to their simple structure [63, 64, 82, 83]. Also, since segmented MZMs are composed of several shorter phase shifters instead of one long phase shifter, their EO bandwidth is enhanced due to the reduction in the RF loss.

A novel design of MRMs with two segments has been recently demonstrated (see Fig. I.18) [40]. With an optimized PN junction profile and a reshaped PN junction (a lateral-vertical PN junction), the modulator improves the tradeoff between bandwidth and efficiency. This modulator features high-speed operation of 128 Gb/s, compact footprint, low energy consumption (18 fJ/bit for PAM-4), and large electro-optic (EO) bandwidth of 50 GHz. This remarkable enhancement in EO bandwidth compared to other MRM demonstrations is achieved by using high doping levels. This leads to significantly increasing the absorption loss of PN junctions, resulting in reduced photon lifetime (or Q factor) [38–40].

A dual phase-shifted Bragg grating modulator has been also reported for generating PAM-4 sig-

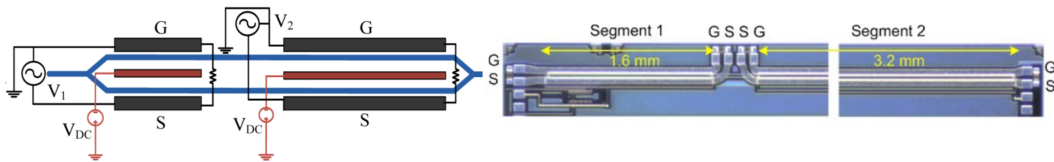


Figure I.17 – Schematic and micrograph of a segmented MZM [82]

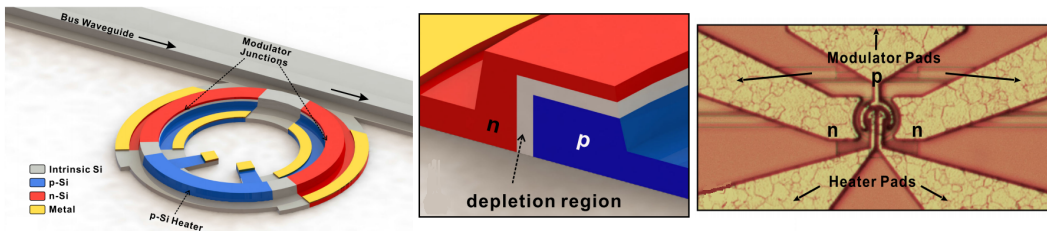


Figure I.18 – Schematic of segmented MRM, its cross-section and its micrograph [40]

nals as shown in Fig. I.19 [20]. In this demonstration, two cascaded resonators are driven with a push-pull configuration, reducing modulation chirp. Furthermore, the modulator provides larger optical bandwidth, resulting in decreased temperature sensitivity compared to that of single-resonance-based modulators [20, 65]. A modulation speed up to 60 Gb/s was achieved using this segmented modulator [20].

I.4 Space division multiplexing

In 1948, Claude Shannon showed that the maximum information-carrying capacity in any additive white Gaussian noise communication channel is dictated by its available bandwidth (BW) and signal-to-noise ratio (SNR), $C = BW \log_2(1 + SNR)$, known as Shannon limit. In practice, parameters such as performance margin, component quality, and nonlinear impairments, reduce the achievable capacity. Fig. I.20 [86] projects the evolution of the capacity per fiber in research and commercialization. During the last decade, TDM, OFDM, WDM, and coherent techniques have enabled optical communication systems to keep up with growing demand. Nevertheless, nowadays, exploiting these techniques pushes the capacity of single mode fibers (SMFs) to its maximum, *i.e.*,

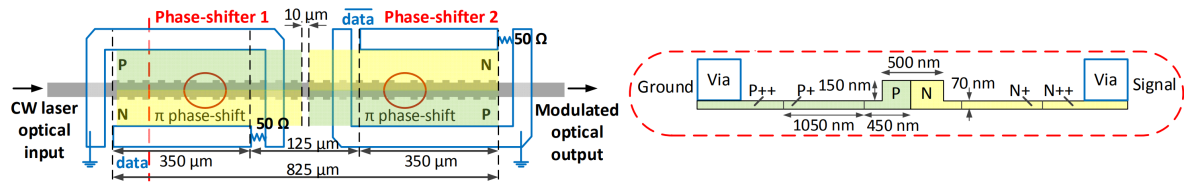


Figure I.19 – Schematic of segmented Bragg grating modulator and its cross-section [20]

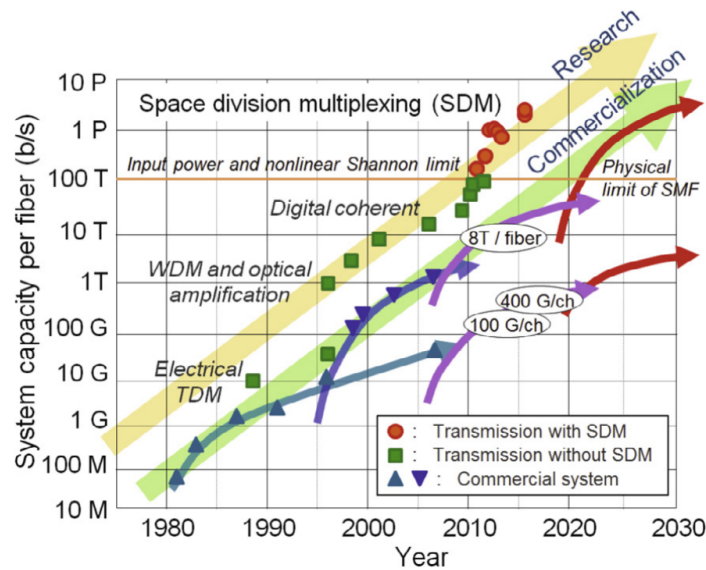


Figure I.20 – System capacity trends per fiber in optical communications in research and commercialization [86]

we are reaching the Shannon limit and optical networks are faced with a "capacity crunch" [87,88] .

As predicted in Fig. I.20, a potential solution to tackle the capacity shortage lies in exploiting the space as the last physical dimension for orthogonally multiplexing data [86–91]. Fig. I.21 displays the five physical dimensions and their contributions in enhancing the fiber capacity. It is shown that the SDM technique is capable of making a leap in the capacity by introducing spatial channels. These channels can be realized by multi-core fibers (MCFs) [92,93], few-mode fibers (FMFs) [94–96], or even a combination of them [90].

The trend toward utilizing SDM/WDM systems necessitates the need for optical transmitters built by a large set of SiP modulators. Hence, all features including footprint, power consumption, modulation speed, and reliability are crucial in choosing the best SiP modulator candidate for EO integration. Indeed, none of these features should be sacrificed to improve another. Thus, a desirable option is a candidate providing a good balance in all features.

I.5 Thesis structure

I.5.1 Motivation

SDM/WDM transmitters enable future optical interconnects to leverage spatially parallel data paths through a single fiber to answer growing bandwidth demands. Harnessing the full potential of these transmitters demands high-density integration as well as low-crosstalk and compact mode multiplexers. To this end, a new design of SiP modulators is needed to provide a compromise in performance considering power efficiency, bandwidth density, stability, scalability, and cost. Below, we list these properties and the requirements they place on the design.

- **Power efficiency** → highly efficient phase shifters and low energy dissipation in the driving scheme

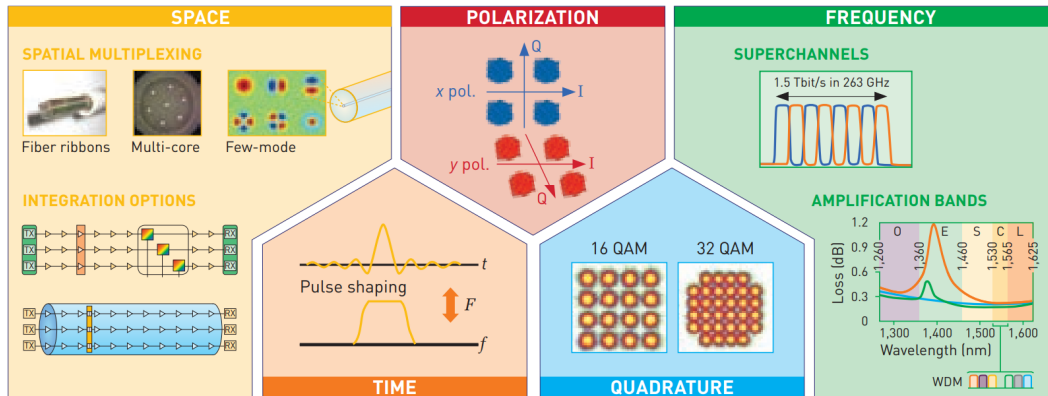


Figure I.21 – The five physical multiplexing dimensions and their contribution in enhancing the link capacity [87]

- **Bandwidth density** → compact footprint, large EO bandwidth, and ability to perform higher order modulation formats
- **Stability** → insensitive to operational wavelength
- **Scalability** → ultra-low RF crosstalk between TW electrodes or capable of being loaded by lumped electrodes, compact footprint, and low power consumption
- **Cost** → compatible with generic SiP manufacturing process

Next, from the integration perspective, an on-chip mode multiplexer featuring low crosstalk, broad-band response, compact footprint and mode selectivity is a key component. This thesis aims to explore novel SiP modulators and on-chip mode multiplexers that make it possible to bridge the existing gap between SDM efforts and SiP integration. It is divided into five chapters as described in the following paragraphs. Chapters 1 and 2 examine novel modulators, chapters 3 and 4 evaluate system impacts, and the final chapter provides a vision for future SDM transmitters.

I.5.2 Chapter 1: Mode-conversion-based silicon photonic modulator loaded with different PN junction profiles

Analysis of Bragg grating dynamics reveals that faster modulation can be achieved in reflection [73]. However, this operating mode is precluded by the lack of on-chip circulator that inevitably leads to a 6-dB insertion loss when a 3-dB coupler or Y-branch is used. In this chapter, for the first time, we report a SiP modulator operated in reflection employing an asymmetric Bragg grating structure followed a mode splitter. The asymmetric Bragg grating can be realized by a half-period offset between the two-sidewall gratings, leading to a contra-directional coupling between two orthogonal modes. This mode conversion enables us to design another component at the modulator input that will guide the incident signal, in the TE₀ mode, into the asymmetric Bragg grating. Whereas, the reflected modulated signal in the TE₁ mode is directed to the drop port in the TE₀ mode. Asymmetric Y-junction and asymmetric directional couplers are components giving this functionality.

Main contributions:

- a) Demonstrate the first mode-conversion-based SiP modulator operating in reflection without the need for circulators
- b) Design and characterize asymmetric Bragg grating waveguide to convert incident TE₀ mode into reflected TE₁ mode
- c) Design and characterize mode-splitters component using asymmetric Y-junctions and asymmetric directional couplers
- d) Optimize the position of lateral PN junction to enhance the phase modulation
- e) Design and characterize an asymmetric Bragg grating modulator loaded with a novel PN junction, named lateral-interleaved PN junction, to enhance the phase modulation

I.5.3 Chapter 2: Slow-light silicon photonic modulators: an MZM assisted by Bragg grating resonators

SiP modulators use the plasma dispersion effect as the principal means to achieve electro-optic (EO) modulation, which results in a relatively low modulation efficiency. Conventional MZMs are thus characterized by large device footprint and high power consumption, requiring travelling-wave electrodes to reach high speed. Modulation enhancement through the use of optical resonators is a promising solution to overcome these limitations. MRMs offer a very compact footprint and low-power-consumption operation. However, these beneficial attributes are associated to important drawbacks such as significant chirp and a narrow optical bandwidth that makes them highly temperature and wavelength sensitive. In this chapter, we demonstrate the first SL SiP modulators based on Bragg grating resonators that is capable of achieving a compromise between the high modulation efficiency of MRMs and the stable operation of MZMs. We use low-Q-factor resonators to enhance optical bandwidth. Then, to reach a sufficient phase modulation, we cascade several of these resonators along the waveguide, each resonator generating a part of the total required phase shift. The modulator thus reduces power consumption and footprint compared to conventional MZMs and provides larger operating temperature range than MRMs. This design is based on coupled resonators rather than cascaded ones, which leads to further performance improvement, easier development for generating advanced modulation formats (PAM and QAM), and significantly relaxed measurement setup because there is no need to fine-tune each cavity individually.

Main contributions:

- a) Demonstrate the first SL MZM based on Bragg grating resonators
- b) Develop a model for simulating photonic band-structure of Bragg gratings
- c) Simulate superstructured integrated Bragg gratings using transfer matrix method
- d) Develop a methodology for designing SL MZMs based on phase shifted Bragg gratings
- e) Develop a dynamic model for MZMs assisted by Bragg grating resonators by solving time-dependent coupled-mode equations using FDTD
- f) Optimize the lateral PN junctions to reach a compromise between optical loss and EO bandwidth

I.5.4 Chapter 3: Efficiency-speed tradeoff in slow-light silicon photonic modulators

In this chapter, we reveal the impact of SL effect on modulation speed and examine the efficiency-speed tradeoff in SL modulators. To do so, we require a model for EO response of these modulators. Hence, we will derive complete models for SL modulator integrated either with lumped electrodes or with traveling-wave electrodes. Next, we compare them with conventional MZMs considering the transmission power penalty (TPP). At the end of this chapter, we also discuss different design strategies to reduce V_π as well.

Main contributions:

- a) Study the speed-efficiency tradeoff in SL SiP modulators
- b) Introduce the EO interaction time as a limiting factor leading to bandwidth reduction in SL MZMs with lumped electrodes
- c) Derive a comprehensive model for EO response of SL MZMs integrated with lumped electrodes
- d) Develop a comprehensive time-domain model for SL MZMs with TW electrodes by solving coupled equations of the forward and backward RF waves using FDTD
- e) Perform a system-oriented comparison between SL MZMs and conventional MZMs considering the TPP including propagation loss, modulation loss, and finite bandwidth
- f) Examine and compare different design strategies to decrease V_π : 1) longer phase shifters, 2) higher doping densities, and 3) the SL effect

I.5.5 Chapter 4: DAC-less PAM-4 slow-light silicon photonic modulator: high efficiency and stability in operation

To meet the IEEE 400 Gb/s Ethernet standard, four-level pulse amplitude modulation (PAM-4) has been recognized as a standard modulation format in short-reach systems. Given that electrically generating multi-level signal increases the cost and power consumption of CMOS drivers, SiP modulators with multi-series electrodes have emerged as an enabling solution, acting as an optical DAC. Segmented modulators are widely reported based on MZMs and MRMs. Despite their attractive properties, they are not able to meet all performance requirements: power efficiency and bandwidth density (speed per unit footprint [Gb/s/m²]) in the former case and stability and cost efficiency in the latter case. In this chapter, we present a novel design of segmented MZMs that is capable of providing a balance in the performance. After proposing SL MZMs in chapter 2 and analysing the SL effect in chapter 3, in this chapter, We use this concept to report the first DAC-less PAM-4 SL MZM based on Bragg grating resonators. What makes this design unique is employing cascaded coupled cavities, which leads to resonating almost all resonators in a same wavelength. Therefore, the mechanism for tuning cavities separately is not necessary, resulting in highly relaxed measurement process. Also, since Bragg gratings are 1-D photonic crystals, instead of 2-D, they are inherently less sensitive to fabrication errors compared to photonic crystal waveguides and are routinely fabricated with CMOS compatible fabrication process using UV lithography. The modulator experimentally shows that is an enabling candidate for accomplishing IEEE Ethernet task force with featuring simultaneously high power efficiency, high bandwidth density, large operating wavelength range (stable operation), and compatibility with standard CMOS manufacturing process (cost-effective design).

Main contributions:

- a) Demonstrate the first DAC-less PAM-4 SL MZM based on Bragg grating resonators
- b) Design and optimize super-structured integrated Bragg grating with a large number of resonators

- c) Experimentally study the reliability and uniformity of the design on whole wafer
- d) Experimentally examine the similarity of the two super-structured Bragg gratings that are integrated into the two arms of the MZM
- e) Experimentally investigate the RF crosstalk between the two series lumped electrodes

I.5.6 Chapter 5: Fully integrated designs of SDM transmitters with compact footprint and power-efficient operation

As a discussion of all results presented in previous chapters, this chapter aims to propose a vision of four-channel SDM transmitters using SL SiP modulators combined with an on-chip mode multiplexer. We target both short-reach systems in designing PAM modulators and long-haul transmissions in designing IQ modulators. Instead of using conventional MZMs and MRMs, we employ MZMs assisted by cascaded Bragg grating resonators (MZM-BGRs). In these modulators, BGRs slow down optical waves in a broad (a few nanometers) optical bandwidth, enhancing phase modulation across a relatively wide operating wavelength range to achieve more stable operation compared to MRMs. For short-reach applications, we design MZM-BGRs with two series lumped electrodes for PAM-4 formats without the need for DACs. We placed four of these modulators in parallel with a careful RF engineering to suppress inter-channel crosstalk. We also design IQ modulators based on MZM-BGRs integrated with travelling-wave electrodes to generate QAM signals. We discuss the TPP of SDM transmitters presenting complete models. The models include the dynamic power penalty coming from the DAC compensation and pre-distortion of signal due to finite bandwidth of SiP modulators. Also, the models take into account the static power penalty caused by the propagation loss and the modulation loss. These modulators are multiplexed by a mode multiplexer that generate TE₀, TE₁, TE₂, and TE₃ modes.

Main contributions:

- a) Propose all-silicon designs for SDM transmitters based on IQ SL modulators and PAM SL modulators followed by an on-chip mode multiplexer
- b) Develop a model to estimate the TPP of the SDM transmitter composed of IQ SL modulators with travelling wave electrodes
- c) Simulate and predict the TPP of the SDM transmitter consisting of PAM SL modulators with lumped electrodes
- d) Propose a new design of mode multiplexers

Chapter 1

Mode-conversion-based silicon photonic modulator loaded with different PN junction profiles

Résumé — Dans ce chapitre, nous présentons une nouvelle conception de modulateurs SiP basée sur le guide d'ondes à réseaux de Bragg asymétrique qui introduit la conversion de mode dans la zone active, permettant au modulateur d'opérer en réflexion sans générer de perte supplémentaire sur la puce. Nous introduisons un décalage d'une demi-période entre les réseaux à parois latérales afin de réaliser la conversion de mode, en convertissant le mode TE₀ se propageant vers l'avant en un mode TE₁ se propageant vers l'arrière. En plaçant une branche Y asymétrique à l'entrée des réseaux de Bragg intégrés (IBG), le signal modulé peut être récupéré avec une faible perte et sans avoir besoin d'un circulateur. Avec un encombrement réduit de 240 μm , le modulateur chargé de jonctions PN latérales peut opérer en modulation de type OOK jusqu'à 30 Gb/s avec une énergie de commutation estimée à 150 fJ/bit. Ensuite, nous améliorons la conception pour obtenir l'augmentation de la modulation de phase en utilisant une nouvelle forme de jonction PN : la jonction PN à intercalation latérale. Nous montrons expérimentalement que la combinaison de la jonction PN latérale et entrelacée (C-LI) augmente la modulation de phase de 67% par rapport à la jonction PN latérale, avec des caractéristiques de conception qui respectent les exigences des procédés de fabrication standards. Le modulateur amélioré démontre une vitesse de modulation allant jusqu'à 45 Gb/s avec un taux d'erreurs (BER) inférieur du seuil de 7 % de correction d'erreur directe (FEC) (et jusqu'à 55 Gb/s avec un seuil FEC de 20 %) ainsi qu'une faible consommation d'énergie de 226 fJ/bit.

Abstract — In this chapter, we present a novel design of SiP modulators based on the asymmetric Bragg grating waveguide that introduces mode conversion in the active area, allowing the modulator to operate in reflection without generating additional on-chip loss. We introduce a half-period offset between sidewall gratings in order to achieve mode conversion, converting forward TE₀ mode into backward TE₁ mode. By placing an asymmetric Y-branch at the input of the inte-

grated Bragg gratings (IBGs), the modulated signal can be retrieved with low loss and without the need for a circulator. With a compact footprint of $240\ \mu\text{m}$, the modulator loaded with lateral PN junctions operates OOK up to 30 Gb/s with an estimated switching energy of 150 fJ/bit.

Next, we upgrade the design to gain the phase modulation enhancement using a novel PN junction shape: lateral-interleaved PN junction. We experimentally show that the combination of lateral and interleaved (C-LI) PN junction increases the phase modulation by 67 %, compared to the lateral PN junction, with design features that respect the requirements of standard fabrication processes. The upgraded modulator demonstrates a modulation speed up to 45 Gb/s with a bit error rate (BER) below the 7 % forward-error-correction (FEC) threshold (up to 55 Gb/s with 20 % FEC) and a low power consumption of 226 fJ/bit.

1.1 Introduction

Photonic integration leverages design kits of silicon photonic (SiP) components to achieve high yield and reduced costs using the mature complementary metal oxide-semiconductor (CMOS) manufacturing process. A key element of integrated transceivers are SiP modulators that have received considerable attention during the last decade. SiP Mach-Zehnder modulators (MZMs) and micro-ring modulators (MRMs) have thus been demonstrated with high-speed operation and high stability in the former case, and low energy per bit with ultra-compact footprint in the latter case [21, 40, 61, 97]. Despite these attractive properties, the narrow optical bandwidth of MRMs makes them difficult to stabilize, while the long phase shifters MZMs are energy-hungry. Bragg grating modulators, through careful optimization of their structure, offer the potential to improve this performance trade-off, *i.e.* offering a compact solution with reduced stabilization requirements [25, 80, 98].

Analysis of Bragg grating modulators reveals that operating the device in reflection is more efficient than using it in transmission [73]. More specifically, when operated in reflection, the grating strength can be lower for a given optical modulation amplitude, thereby introducing less time delay and improving modulation speed [73]. However, operation in reflection is typically characterized by higher loss due to the lack of on-chip circulators. Therefore, the signal from Bragg grating modulators operated in reflection is typically retrieved by either an external circulator, adding complexity and cost, or by an on-chip splitter, *e.g.*, a Y-junction that introduces an additional loss of 6 dB.

In this chapter, we propose a novel IBG-based modulator that can operate in reflection with low loss and without a circulator. The modulator configuration is composed of two main parts: an asymmetric integrated Bragg grating (A-IBG) in a multi-mode waveguide and an asymmetric Y-branch. The A-IBG performs mode conversion by introducing contra-directional coupling between the forward TE₀ and the backward TE₁ modes. It is formed by introducing a half-period offset between the two sidewall gratings. Because of this mode conversion upon reflection, the reflected power can be directed towards the drop port of the asymmetric Y-branch, eliminating the need for a circulator. We experimentally characterize, for the first time, the operation of the A-IBG as a modulator. The structure has a short phase-shifter length of only 240 μm and shows a low power consumption of 150 fJ/bit at a bias of -2V. The asymmetric Y-branch has a 1 dB insertion loss, which is a significant reduction compared to the 6 dB of standard Y-branch.

Following our pioneering demonstration, to optimize the phase modulation, we introduce a novel design of an asymmetric Bragg grating modulator loaded with the combination of lateral and interleaved (C-LI) p-n junctions. In our initial work presented at ECOC, we used an asymmetric Y-branch to filter the reflected mode and phase modulation was achieved by a standard lateral PN junction. We experimentally show that in our upgraded design, the C-LI p-n junction increases the phase modulation by 67 %, compared to the lateral p-n junction, with design features that respect the requirements of standard fabrication processes. We further propose an asymmetric directional coupler, instead of an asymmetric Y-branch, to reduce insertion loss and crosstalk. This optimized

design, with a phase shifter length of $290\ \mu\text{m}$, demonstrates modulation speed up to $55\ \text{Gb/s}$ with an estimated power consumption of $226\ \text{fJ/bit}$.

1.2 Mode-conversion modulator loaded with lateral PN junctions

1.2.1 Design and Modulator Structure

Figure 1.1 shows a schematic of the modulator (Fig. 1.1 (a)) and of its two main parts: the asymmetric Y-junction (Fig. 1.1 (b)), and the asymmetric Bragg grating waveguide (Fig. 1.1 (c)).

Asymmetric Y-junction. An ideal asymmetric Y-branch (Fig. 1.1 (b)) should operate as follows: when the TE₀ mode is excited in the input arm, all the power couples to the TE₀ mode of the multi-mode waveguide (MMW). On the other hand, when the power is reflected in the TE₁ mode, all of the reflected power goes to the drop arm of Y-branch. The proposed Y-branch consists of two single mode arms with different widths, a multi-mode interference (MMI) section, and an output MMW. The width of the input and drop arms are $650\ \text{nm}$ and $490\ \text{nm}$, respectively. the width and length of the MMI are $1.38\ \mu\text{m}$ and $4.3\ \mu\text{m}$, respectively, with a $50\ \text{nm}$ distance before the start of the MMI. The width of the MMW is $1.14\ \mu\text{m}$. Fig. 1.2 (a) shows the electrical field distribution and transmission spectra in the TE₀ and TE₁ modes of the MMW (TE₀ mode is excited at the input port, simulations are done in Lumerical FDTD). Transmission into the TE₀ mode is around 85%. Fig. 1.2 (b) shows

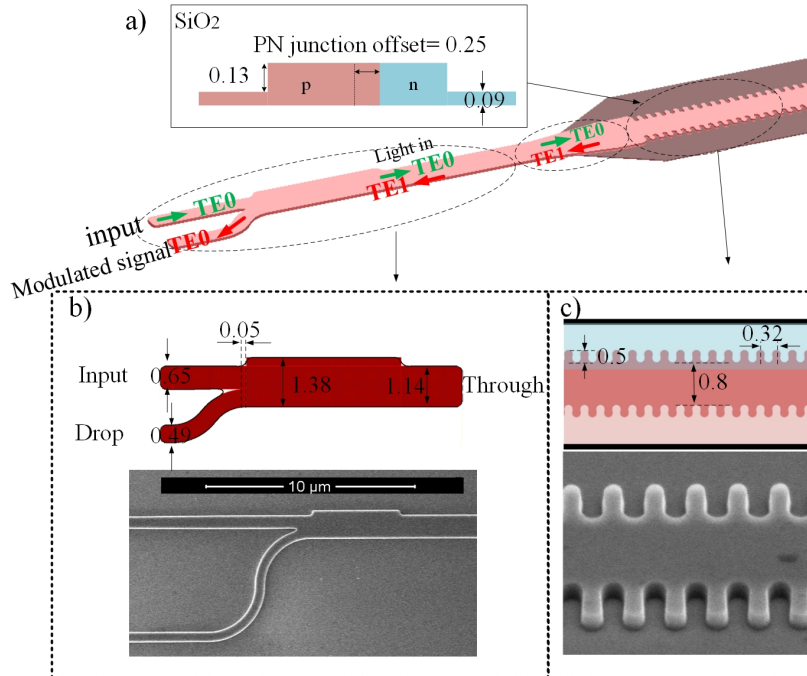


Figure 1.1 – a) Schematic of the modulator, b) design and SEM picture of the asymmetric Y-branch and its SEM picture, c) schematic and SEM picture of asymmetric Bragg grating waveguide. All dimensions are in μm .

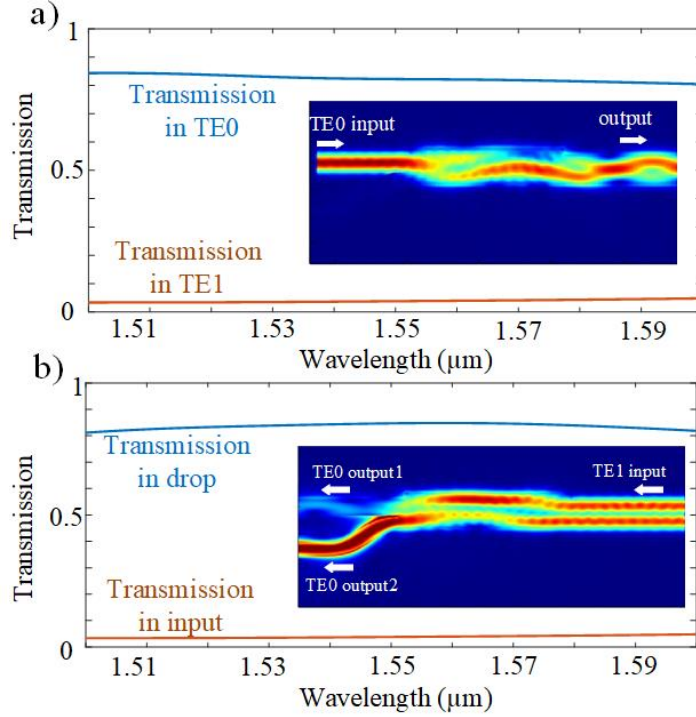


Figure 1.2 – a) Transmission in TE0 and TE1 mode when the TE0 mode is excited in the input port, b) Transmission to the input port and the drop port when the power in TE1 mode is excited in through port. Insets show the field distribution.

the power transmitted into the input and drop ports when the reflected TE1 mode is excited at the through port. It shows that more than 83% of the reflected power is coupled to the TE0 mode in the drop port, while only 4% goes to the input port. Therefore, the use of the asymmetric Y-branch also avoids strong optical feedback to the input port. A taper length with a length of $10\ \mu\text{m}$ (Fig. 1.1 (a)) is used to convert the modes of the $1.14\ \mu\text{m}$ strip waveguide to the ridge waveguide.

Asymmetric Bragg grating waveguide. In an asymmetric sidewall Bragg grating (ASBG) with π phase shift between the two gratings, unlike symmetric gratings, the coupling coefficient between the fundamental forward and backward modes is zero. On the other hand, the coupling between an odd mode and an even mode can be efficient if the phase matching condition is satisfied; in the present case this is $\lambda_B = (n_0 + n_1)\Lambda$, where n_0 and n_1 are the effective indices of the TE0 and TE1 modes, respectively, and Λ is the grating period. The asymmetric grating, shown in Fig. 1.3 (a), is designed with 50% duty cycle corrugations and $\Lambda = 320\ \text{nm}$ in a ridge waveguide with a width of $800\ \text{nm}$, a height of $220\ \text{nm}$ and a slab height of $90\ \text{nm}$. The lateral corrugation is $500\ \text{nm}$. A simulation of the UV lithography effect on the proposed design (black curve in Fig. 1.3 (a)) shows that when the $800\ \text{nm}$ width is increased to $1.018\ \mu\text{m}$, the corrugation acquires a sinusoidal shape with a depth of $300\ \text{nm}$. We simulated the spectral response of the ASBG with the lithography effect. Because of memory limitation, we simulated only 50 periods. Fig. 1.3 (b) shows the simulated transmission and

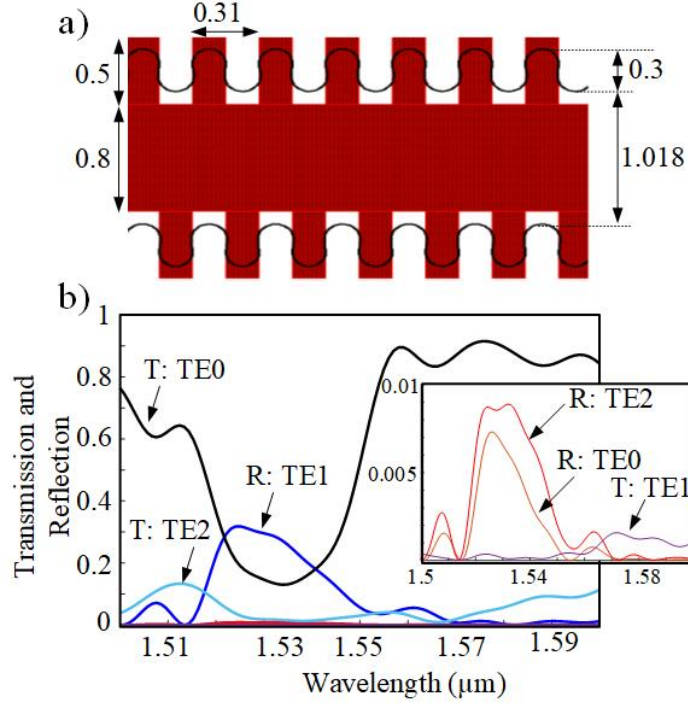


Figure 1.3 – a) Schematic of the ASBG, b) transmission and reflection of ASBG in different modes. In (a), black curve shows the lithography effect simulated by Pyxis. Note that the simulation was performed considering $\Lambda = 310$ nm, while in the demonstrated design, Λ is 320 nm. All dimensions are in μm . T: Transmission, R: Reflection

reflection spectrum for the various modes (incident power in the TE0 mode). It is seen that most of the reflection occurs in the TE1 mode (note that the reflectivity would be much larger if we simulated a large number of periods).

PN junction position. The modulation efficiency of this modulator strongly depends on the PN junction position. For example, if a lateral PN junction (shown in Fig. 1.1 (a)) is placed at the middle of the waveguide, the overlap between the optical TE0 mode and the depletion region will be maximum. However, in this case, a low overlap between the optical TE1 mode and the depletion region will occur because the optical power for TE1 mode field is close to zero in this region. Therefore, the total phase modulation, which depends on the refractive index change of both TE1 and TE0 modes, will not be maximized. In Fig. 1.4, we examine the Bragg wavelength shift (*i.e.*, $\Delta\lambda_B = (\Delta n_0 + \Delta n_1)\Lambda$, where Δn_0 and Δn_1 are the refractive index change for TE0 and TE1 modes, respectively) as a function of the PN junction offset. It is seen that Δn_0 is maximum when the PN junction is located at the middle of the waveguide, while Δn_1 becomes maximum when the offset is 320 nm. The Bragg wavelength shift therefore peaks at an offset of 250 nm where Δn_0 and Δn_1 reach a compromise.

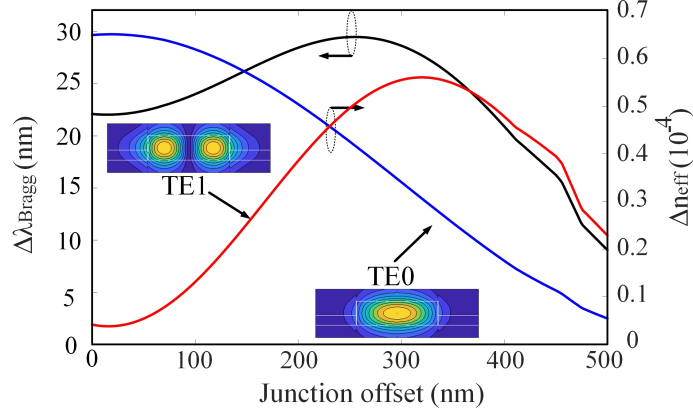


Figure 1.4 – Refractive index variations for TE0 and TE1 modes, and the Bragg wavelength shift as a function of the PN junction offset at a reverse bias of 2 V for lateral PN junctions.

1.2.2 Modulator characterization

The modulator was fabricated in a multi-project wafer run (CMC Microsystems) using a standard-193-nm-lithography process at the IME (AMF) A*STAR. The thickness of the silicon layer is 220 nm and the thickness of buried oxide 2 μm . Fig. 1.1 (b) and (c) show the SEM picture of fabricated asymmetric Y-junction and the ASBG waveguide, respectively. The phase shifter has a length of 240 μm (750 grating periods). The PN junction has three doping levels.

Asymmetric Y-branch. The asymmetric Y-branch should operate in such a way that when light is reflected in the TE1 mode, it is coupled to the drop port, while light reflected in the TE0 mode is coupled back to the input port. In our layout, we placed two Y-branches back-to-back to measure its performance as shown in Fig. 1.5 (a). Fig. 1.5 (b) shows the measured transmission spectra for different output and input ports. From S_{31} spectrum (input port 1 and output port 3), it is seen that the power in TE1 mode in MMW is directed to the port 3 (or the drop port in Fig. 1.1 (b)). In addition, S_{42} measurement indicates that the incident power in TE0 mode at the port 2 (or the input port in Fig. 1.1 (b)) couples almost completely to the TE0 mode in MMW. Therefore, the results show that the total on-chip loss of the asymmetric Y-junction is around 1.5 dB at the operational wavelength.

DC and EO characterization. Figure 1.6 (a) shows the optical spectrum of the modulator. It is seen that the ASBG provides a stop band of approximately 30 nm where the TE0 mode is reflected in TE1 mode before being coupled to the TE0 mode of the Y-branch drop port. For modulation, we operate the device at the edge of the stop band; in the present case at an operational wavelength of $\lambda_0 = 1533.55$ nm as shown in Fig. 1.6 (b).

The total insertion loss of the modulator is 23 dB, including the coupling loss of 17 dB between the fiber and the chip (two un-optimized grating couplers with 8.5 dB loss). There is also a loss of 6 dB coming from the optimization of the operating point at the edge of the stop band as shown in Fig. 1.6 (b). Moving the operating point towards higher transmission would result in a lower extinction

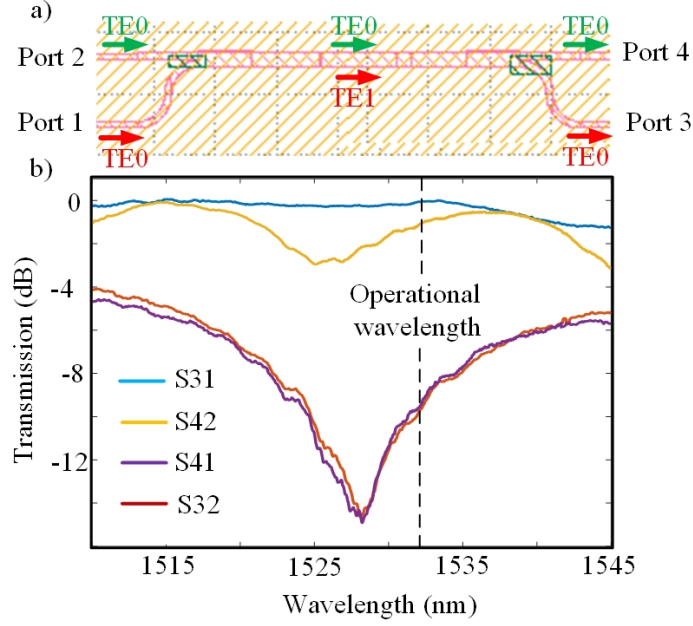


Figure 1.5 – a) Design of back-to-back asymmetric Y-branch, b) the spectrum of Y-branch for different output and input ports.

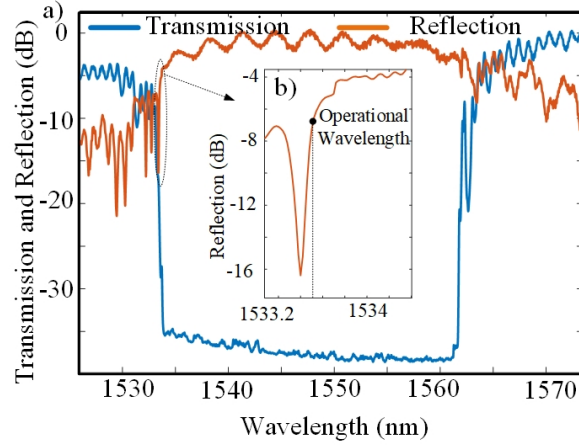


Figure 1.6 – a) Optical spectrum of the modulator, b) the operating point of the modulator at the edge of the stop band.

ratio.

We measured the EO bandwidth of the modulator at different bias voltages using a PNA Network Analyzer (Agilent N5227A 10 MHz-67 GHz). Fig. 1.7 shows the S21 measurement, indicating that the modulator has a 3-dB EO bandwidth of 22 GHz at a bias of -2 V. The energy consumption per bit of the modulator for OOK is calculated from $E_b = CV_{pp}^2/4$. The p-n junction capacitance at a bias of 2 V is 1 pF/C. Considering a 240 μm phase shifter length, the total capacitance is estimated at 24 fF. We use a RF signal with a peak-to-peak voltage of 5 V and, as a result, the power consumption

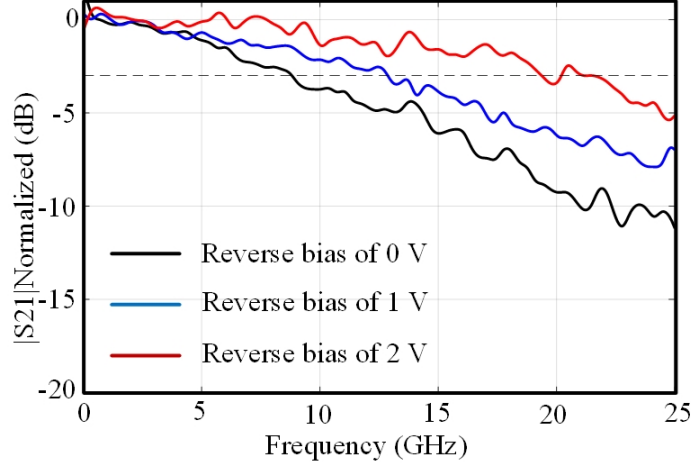


Figure 1.7 – Measured EO scattering parameter S21 as a function of the applied reverse bias.

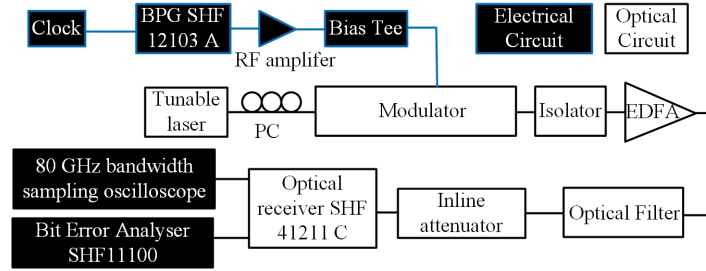


Figure 1.8 – Experimental setup used to measure BER and eye diagram.

is estimated to be 150 fJ/bit.

Large signal response. We measured the modulator performance with OOK using the experimental setup shown in Fig. 1.8. We first generated a pseudo-random bit sequence with a length of $2^{31}-1$ using a bit pattern generator (BPG) (SHF 12103 A) and then amplified the RF signal to a peak-to-peak voltage of 5 V (RF amplifier bandwidth of 50 GHz). The DC and RF signals were combined by a bias-T and applied to the modulator. The laser power was 15 dBm before coupling to the chip and a polarization controller (PC) was adjusted to maximize the coupling into the fundamental TE mode. The modulated optical signal was amplified by an erbium-doped fiber amplifier (EDFA) followed by a tunable optical bandpass filter (TOBP, 0.5 nm 3-dB bandwidth). Finally, an inline attenuator controlled the received power. To capture the eye-diagrams and measure the BER, we used an 80 GHz bandwidth sampling oscilloscope (SO) and a bit-error-rate analyzer (SHF 11100 B with 32 GHz SHF 41211 optical receiver), respectively. The wavelength was fine-tuned by ± 0.025 nm around $\lambda_0 = 1533.55$ nm. Fig. 1.9 (a) shows the eye diagram of the modulated signal having an extinction ratio (ER) of 4 dB at a bit rate of 20 Gb/s with a bias of -2 V. The BER curves measured as a function of the received power and at a bias of 2 V are shown in Fig. 1.9 (b). Assuming 7 % FEC threshold, the modulator can operate up to 30 Gb/s without additional digital signal processing.

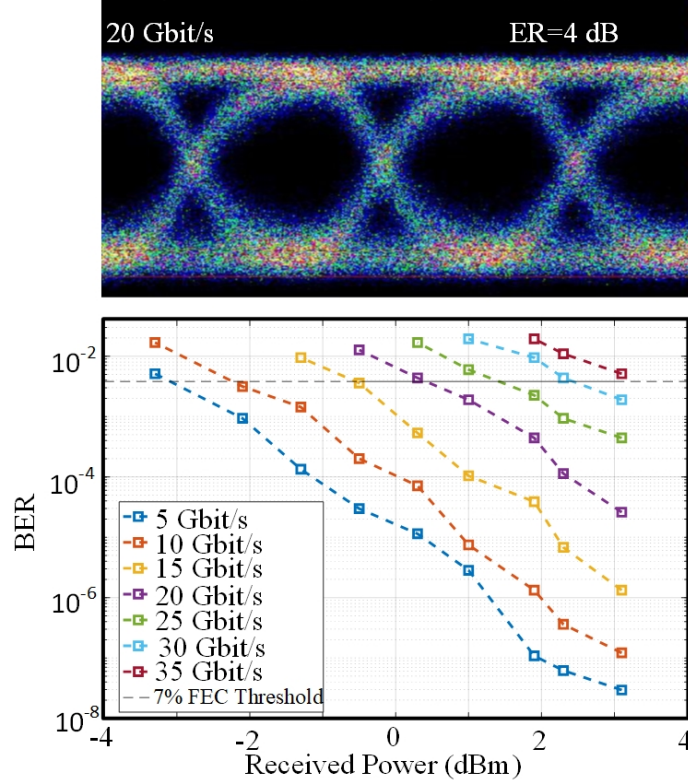


Figure 1.9 – a) Eye diagram for a bit rate of 20 Gb/s, b) BER as a function of received power for different bitrates. Both measured at a bias of -2 V.

1.3 Mode-conversion modulator loaded by a combination of lateral and interleaved p-n junctions

In this section, we examine an improved version of the modulator in which 1) the refractive index variation is increased by using a combination of lateral and interleaved p-n junctions and 2) asymmetric directional coupler is used as a mode splitter which offers less crosstalk, less loss and more broadband response compared to the asymmetric Y-branch.

1.3.1 Design and modulator structure

Figure 1.10 (a) presents the modulator schematic and operating principle. It shows that the launched TE₀ mode is guided into the asymmetric Bragg grating waveguide using a directional coupler and a taper. Thereafter, due to half period offset between two side-wall gratings, contra-directional coupling converts the incident TE₀ mode into a reflected TE₁ mode. Then, the reflected signal is directed to the drop port using the asymmetric directional coupler, shown in Fig. 1.10 (b), that converts the TE₁ mode to TE₀ mode at the output. The combination of asymmetric Bragg grating and asymmetric directional coupler thus overcomes the need for an on-chip circulator.

Asymmetric directional coupler. Ideally, the asymmetric directional coupler should transmit all

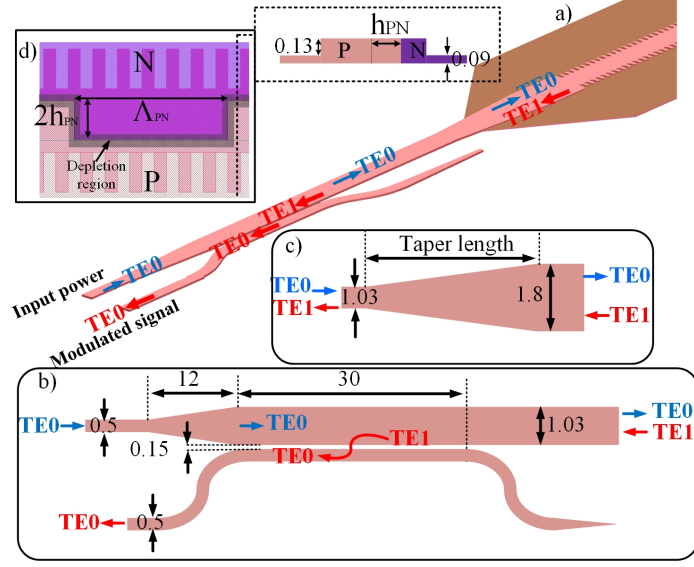


Figure 1.10 – Schematic of (a) the full modulator structure, (b) the asymmetric directional coupler, (c) the taper between the asymmetric directional coupler and the asymmetric Bragg structure, (d) the asymmetric Bragg grating waveguide loaded by a C-LI PN junction and its cross-section. The parameter values are in μm .

of the incident power, launched in the TE0 mode, to the TE0 mode of the multimode waveguide output; while all of the reflected power in the TE1 mode should be coupled to the TE0 mode of the drop port. Fig. 1.10 (b) shows the design of the asymmetric directional coupler consisting of a 500-nm-width input waveguide and a taper with a length of 12 μm followed by bus and drop waveguides with respective widths of 1.03 μm and 500 nm. The coupling section has a length of 30 μm and a gap 150 nm. Design and simulations of the asymmetric coupler were performed using Lumerical-Mode and Lumerical-FDTD. Fig. 1.11 shows the simulation results, showing negligible insertion loss for transmission of the TE0 through the device (see blue arrows in Fig. 1.10 (b), blue line and left inset in Fig. 1.11) and less than 0.5 dB loss when coupling the reflected TE1 to TE0 modes (see red arrows in Fig. 1.10 (b), red line and right inset in Fig. 1.11).

Finally, note that a taper, shown in Fig. 1.10 (c), is placed between the directional coupler multimode output and the multimode waveguide with the asymmetric Bragg grating in order to insure mode-matching. Simulations showed that a taper length of at least 10 μm was required to guarantee low loss for both modes. We chose a 20 μm taper length.

Asymmetric Bragg grating waveguide. The asymmetric Bragg grating consists of a waveguide whose sidewall grating are placed with a π phase shift, as shown in Fig 1.10 (d). This π phase shift suppresses the Bragg reflection of the fundamental TE0 mode but allows contra-directional coupling between the two TE0 and TE1 modes if the phase-matching condition is satisfied. The asymmetric grating is designed with a 50% duty cycle, lateral corrugations of 500 nm on each side, and a pitch of $\Lambda = 325$ nm in a ridge waveguide with a 800 nm width.

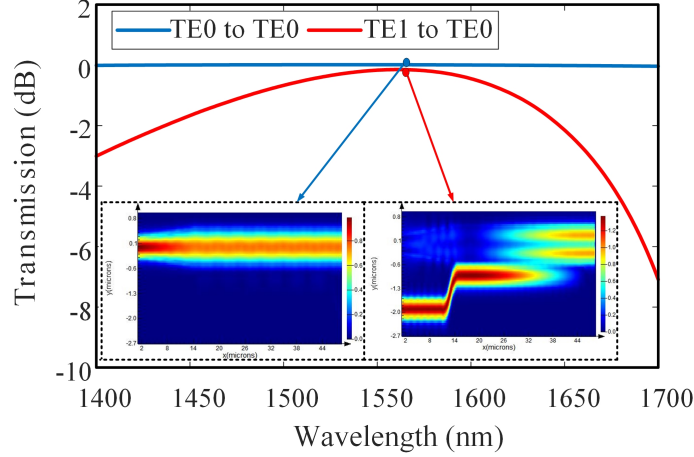


Figure 1.11 – Spectral response of the asymmetric directional coupler simulated in Lumerical-FDTD showing the transmission of the input TE0 mode to the through port (blue) and the transmission of the reflected TE1 mode to the drop port (red).

In Fig. 1.13, we examine the modulation of refractive indices for positive and negative junction offsets. As indicated, although the optical modes are symmetric with respect to the middle of the waveguide, index modulations for TE0 (blue line) and for TE1 (red line) are not due to unequal index modulations introduced by holes and electrons. Nevertheless, their sum values for optimum junction offset ($h_{PN} = 250$ nm) and its negative value ($h_{PN} = -250$ nm) are almost identical (see the blue dots marked on the black line in the figure 1.13). Given that the sum of them (*i.e.*, $\Delta n_0 + \Delta n_1$) determines the Bragg wavelength modulation, we assume that the lateral p-n junctions can offer the same phase modulation if placed in one section with a positive optimum offset and in the next section with a negative optimum offset. Such a doping profile, with a half-period Λ_{PN} , is shown in Fig. 1.10 (d). This doping profile helps to gain modulation enhancement because, in addition to the lateral PN junction, it creates an additional phase modulation resulting from the presence of the interleaved section. In Fig. 1.12 (d), we examine the refractive index variations of TE0 and TE1 modes ($\Delta n_0 + \Delta n_1$) as a function of the reverse voltage for the three doping shapes: lateral PN junction with $h_{PN} = 250$ nm (Fig. 1.12 (a)), interleaved PN junction with $\Lambda_{PN} = 1$ μ m (Fig. 1.12 (b)), C-LI PN junction with $h_{PN} = 250$ nm and $\Lambda_{PN} = 1$ μ m (Fig. 1.12 (c)). For the interleaved and C-LI, the refractive index change is averaged over one doping period and simulations were done in Matlab. Fig. 1.12 (e) shows that C-LI PN junction introduces significantly more phase modulation than a lateral PN junction but less than the sum of interleaved and lateral.

1.3.2 Device characterization

Modulators and test structures were fabricated in a multi-project wafer run (CMC Microsystems) using a standard-193-nm-lithography process at the Advanced Micro Foundry (AMF). The thickness of the silicon layer is 220 nm and the thickness of buried oxide 2 μ m. The modulator phase shifters have a length of 290 μ m (900 grating periods). Fig. 1.14 (a) and (b) show the SEM pictures of the

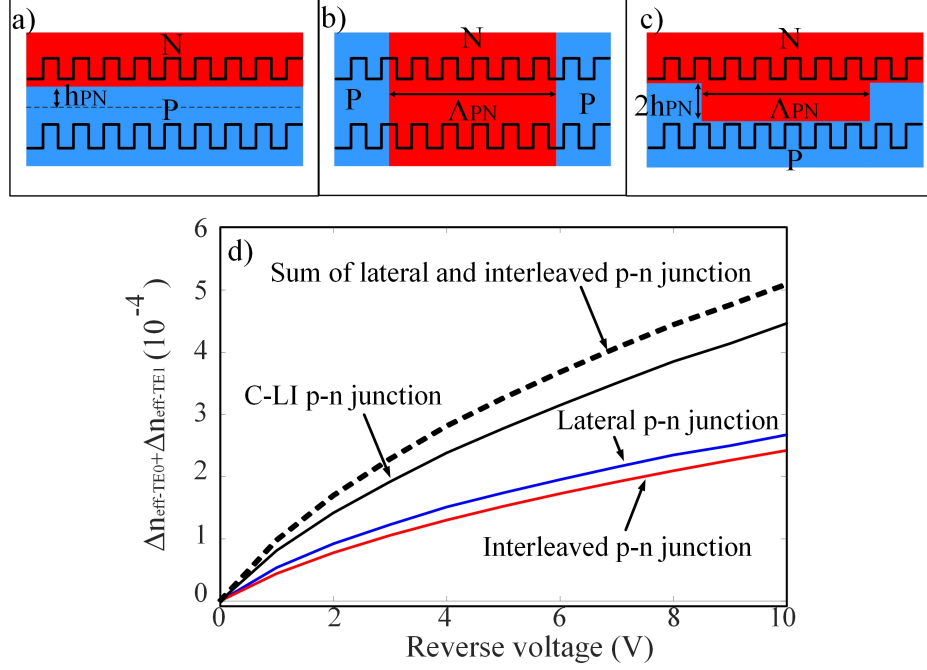


Figure 1.12 – Schematic of (a) lateral, (b) interleaved, and (c) C-LI PN junctions. (d) Sum of refractive index modulation for TE0 and TE1 modes ($\Delta n_0 + \Delta n_1$) as function of reverse bias for different PN junction profiles.

fabricated directional coupler and asymmetric Bragg grating waveguide, respectively.

Asymmetric directional coupler

We experimentally evaluate the performance of the directional coupler using a four-port back-to-back test structure shown in the inset of Fig. 1.15. Fig. 1.15 (a) shows the spectra when the power is launched from port 1. As expected, most power is captured from port 2. The crosstalk, *i.e.* the power from port 3, is lower than 30 dB over the C-band. Also, the reflected power captured from port 4 is negligible. In this case, there is no mode conversion, *i.e.* the TE0 mode is transmitted through the device (input waveguide, bus waveguide, and output waveguide). Fig. 1.15 (b) illustrates the results when the power is launched from the port 4. In this case, the mode conversion occurs at both directional couplers (*i.e.* the TE1 mode propagates in the bus waveguide) and most power exit from the port 3. The insertion loss is lower than 2 dB and the crosstalk (S24) is less than 30 dB in the C-band. Finally, the reflected power detected at port 1 is very small, close to the noise floor of the measurement.

Compared to the asymmetric Y-branch in the previous case, the directional coupler has a broader spectral response, lower loss over the C-band, and significantly less crosstalk. The asymmetric Y-branch was characterized by an operating bandwidth of 15 nm, an insertion loss of 1.5 dB, and a crosstalk of 7 dB, while the directional couple improves these parameters to 35 nm, 1 dB, and 30 dB respectively.

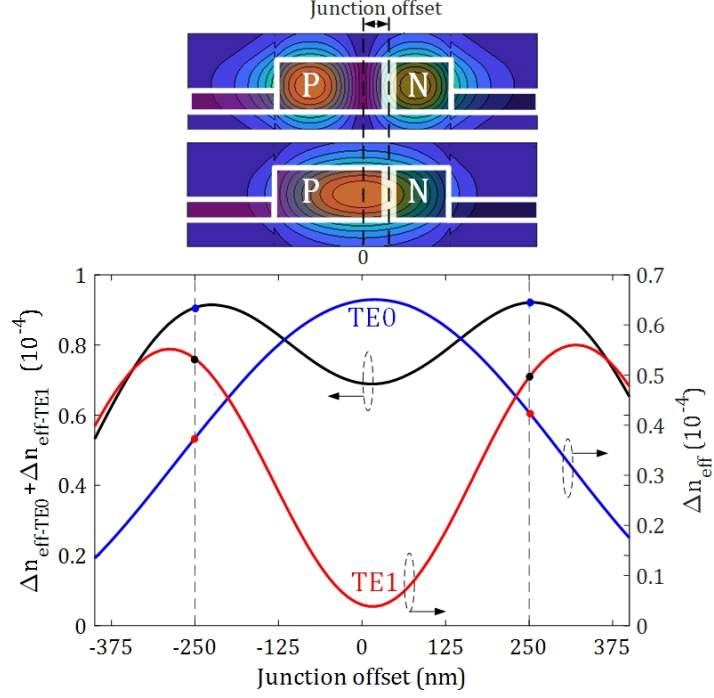


Figure 1.13 – Refractive index variations for TE0 (blue line) and TE1 (red line) modes as well as sum of them ($\Delta n_0 + \Delta n_1$) as a function of junction offset.

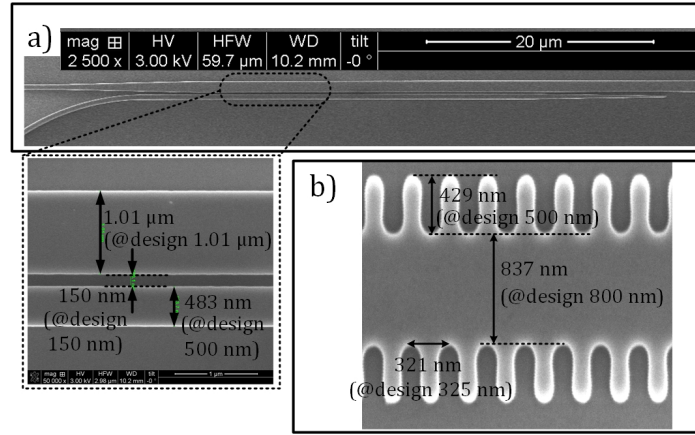


Figure 1.14 – SEM picture of (a) the directional coupler, (b) the asymmetric Bragg grating waveguide.

Modulator characterization.

We first evaluate the phase modulation enhancement using several modulators, with the five different doping profiles but with the same passive structure, fabricated on the same die. Fig. 1.16 shows the refractive index variations measured from the shift in Bragg wavelength when applying reverse voltage for a lateral PN junction with a h_{PN} of 250 nm, an interleaved PN junction with a Λ_{PN} of 2 μm , and three C-LI junctions with a same h_{PN} of 250 nm and Λ_{PN} of 1, 2, and 10 μm . During measurement, the device slightly heats as the bias voltage is applied. We estimate that the

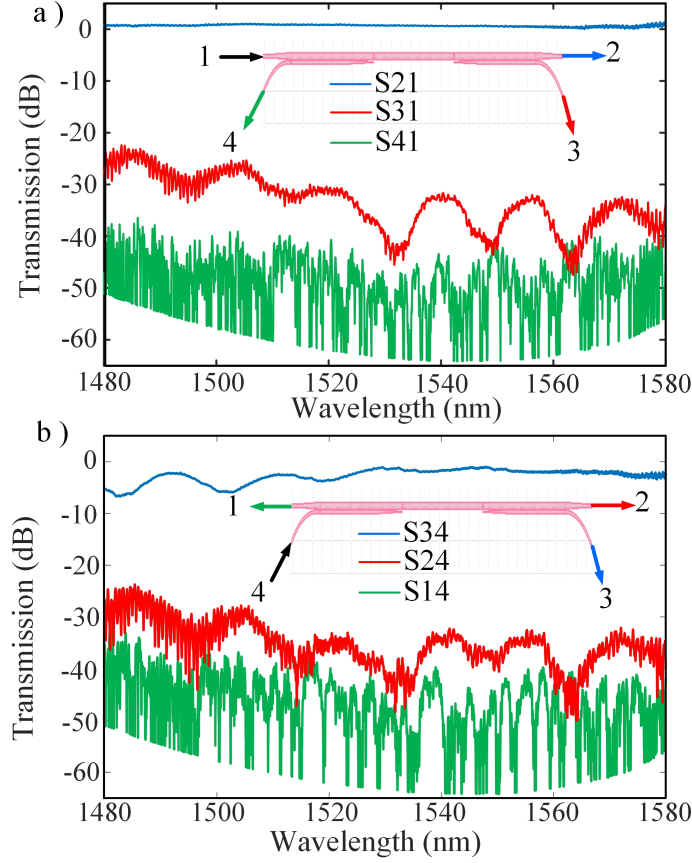


Figure 1.15 – Measured spectra of the asymmetric directional coupler when (a) the power is input in port 1 and coupled to the TE₀ mode in the multimode waveguide, and (b) the power is input in port 4 and coupled to the TE₁ mode in the multimode waveguide.

temperature increase depends quadratically on the applied DC voltage with a maximum change of 1.3 °C at a reverse voltage of 6 V. Note that the wavelength shift due to the change in the temperature is equal to 82 pm/°C [99]. This contribution was subtracted from all curves on Fig. 1.16. In terms of the phase modulation, the C-LI PN junction outperforms the lateral PN junction as well as the interleaved PN junction. In addition, Fig. 1.16 illustrates that the C-LI junction with 2 μm pitch demonstrates the best performance, with 67% enhancement in phase modulation in comparison to the lateral PN junction. The reason is that smaller pitch Λ_{PN} for the PN junction increases the number of interleaved sections, enhancing phase modulation. However, the pitch size is also limited by the fabrication process. Consequently, the C-LI junction with the smaller pitch (*i.e.*, $\Lambda_{PN} = 1 \mu\text{m}$) shows a poorer phase modulation since it corresponds to the minimum feature size of the standard implantation process at AMF. Therefore, for the transmission experiment, we selected the modulator having a C-LI PN junction with a pitch of $\Lambda_{PN} = 2 \mu\text{m}$.

Figure 1.17 zooms on the reflected spectral response, at edge of the stop band, where this modulator is operated. The sharp response at the edge comes from employing strong corrugations in our

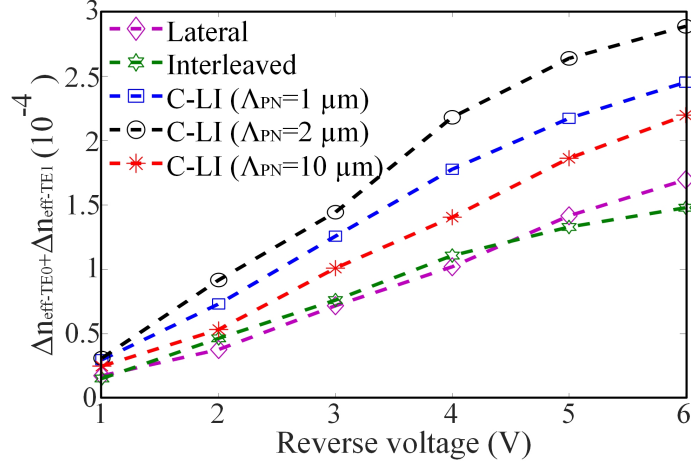


Figure 1.16 – Reflective index variation of asymmetric Bragg grating modulators with different PN junction profiles as a function of the reverse voltage.

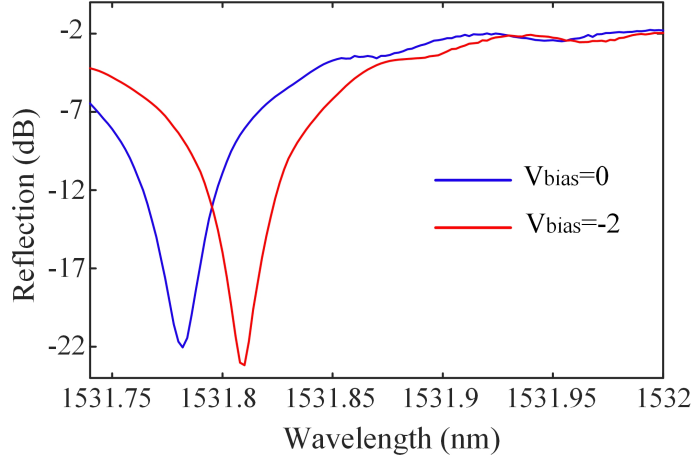


Figure 1.17 – Zoom on the edge of the optical spectra, where the modulator is operated, of the asymmetric Bragg grating waveguide for reverse bias voltages of 0 V and 2 V.

design ($\Delta W = 500$ nm). However, the strong corrugations also lead to a high insertion loss of 2 dB.

Figure 1.18 shows the EO response of the modulator measured with a PNA Network Analyzer (Agilent N5227A 10MHz-67GHz). Note that we used a 50- Ω -terminated RF probe because of the lack of on-chip termination. It is seen that 3-dB EO bandwidth is 7.9 GHz for a reverse bias of 2 V. The EO bandwidth is limited not only by the RC time constant of the lumped electrode, but also by the response time of the strong grating structure characterized by an increased group velocity near the band edge. Slow light has the benefit of increasing the interaction time between the optical wave and the uniform RF voltage along the lumped electrode.

We tested the large signal response of the modulator by measuring the bit error rate (BER) using the setup shown in Fig. 1.19. We first generated a PRBS with a length of $2^{15}-1$ using a bit pattern

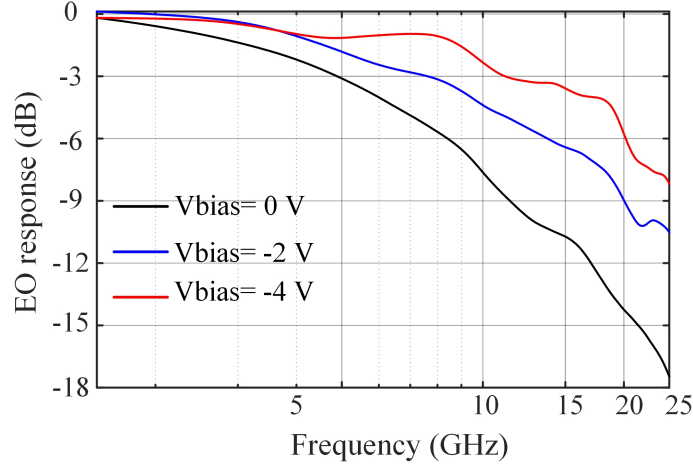


Figure 1.18 – Small-signal measurement of the asymmetric Bragg grating modulator for different reverse voltages.

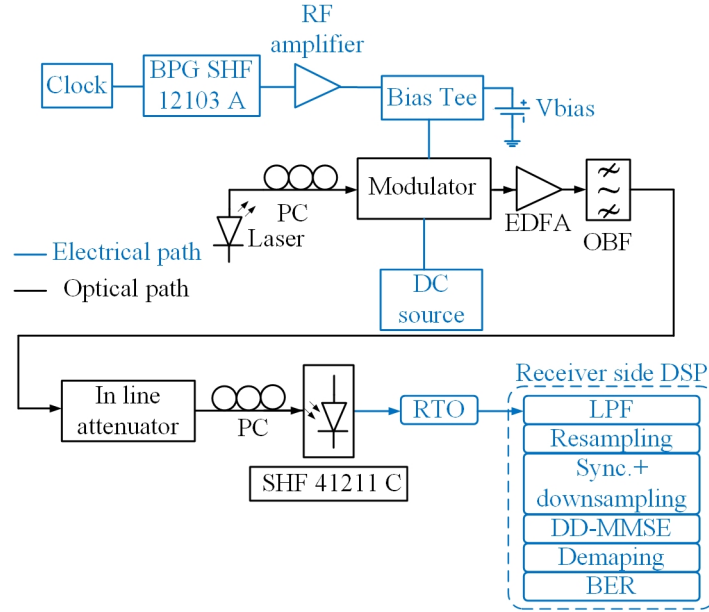


Figure 1.19 – Block diagram of the experimental setup.

generator (SHF 12103 A), the signal was amplified with a RF amplifier (bandwidth of 50 GHz and V_{pp} of 5 V) and applied to the modulator using a bias-T (bandwidth of 50 GHz) that combined the RF signal and DC bias voltage ($V_{bias} = -2$ V). Considering a lumped electrode with a length of $290 \mu\text{m}$, the total capacitance is estimated to be 36.25 fF at the reverse bias of 2 V [98]. The energy consumption per bit is thus calculated as $E_b = CV_{pp}^2/4 = 226 \text{ fJ/bit}$.

In the optical part, we set the laser power to 15 dBm and adjusted the polarization with a polarization controller before coupling the light into the chip. After modulation, the signal was amplified by an EDFA followed by a tunable optical bandpass filter with a fixed bandwidth of 0.7 nm. The

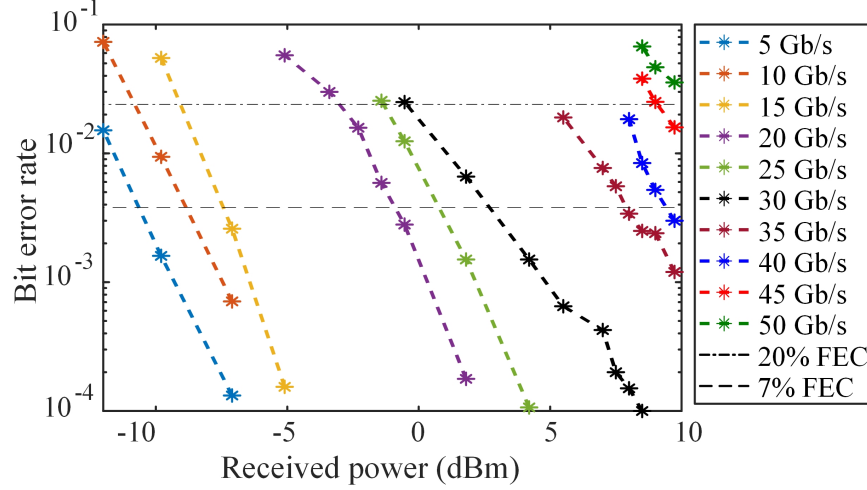


Figure 1.20 – BER as a function of the received power for different modulation speeds.

output optical signal was converted to an electrical signal using a photodetector (SHF 41211 with a 32 GHz bandwidth) and then digitalized by a real-time oscilloscope (RTO) with a sampling rate of 80GSa/s and bandwidth of 60 GHz. At the receiver side (Fig. 1.19), the digital signal processing consisted of filtering (10th order super Gaussian low pass filter (LPF)), resampling, time synchronized, and downsampling. The bit error rate (BER) is calculated with and without using a decision-directed minimum mean square error (DD-MMSE) equalizer with 2^4 taps. The signal is demapped for BER calculation. Fig. 1.20 presents the BER measurement results as a function of the received power showing that the modulator can reach a speed of 45 Gb/s with 20% FEC without DD-MMSE. The large degradation between 15 Gb/s to 20 Gb/s comes from the modulator bandwidth. Also, the second degradation between 30 Gb/s to 35 Gb/s is imposed by the setup due to the bandwidth limitation of some equipment, photo-detector in particular. 1.21 (a) also displays BER after applying a DD-MMSE equalizer at the maximum received power. Using a blind equalizer, transmission speeds up to 55 Gb/s can be reached with 20% FEC. Fig. 1.21 (b) and (c) show histograms of the detected bits at modulation speeds of 45 Gb/s and 55 Gb/s, respectively, presenting the quality of eye-openings.

1.4 Conclusion

We have demonstrated the first mode-conversion-based modulator with a half-period offset between sidewall gratings. We employed asymmetric Bragg grating waveguide to convert the incident TE0 mode to a reflected TE1 mode in order to direct the modulated signal to a drop port either by using an asymmetric Y-junction or by using an asymmetric directional coupler. The whole structure therefore acts similarly to an on-chip circulator and avoids the usually high insertion loss of Bragg grating modulators. The modulator in the first demonstration had a compact structure, which results in a low power consumption of 150 fJ/bit. The BER measurement showed that the modulator can be operated below the 7% FEC threshold up to 30 Gb/s.

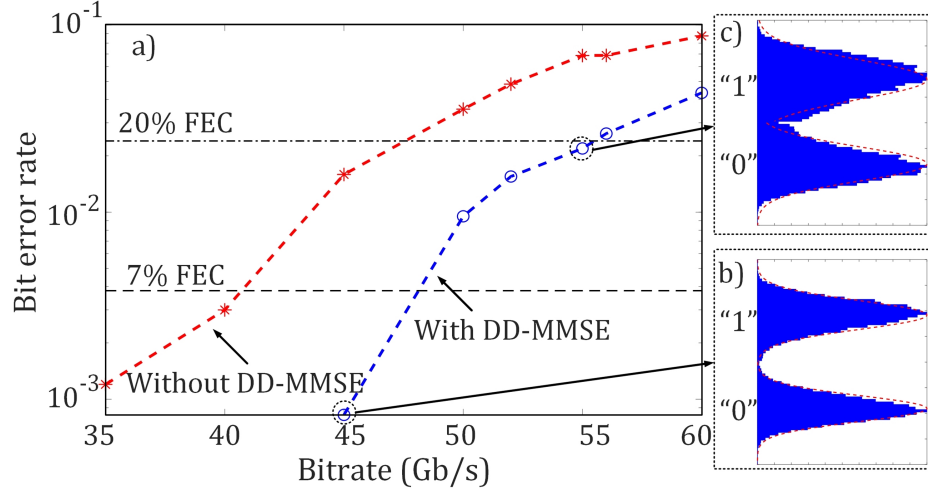


Figure 1.21 – a) Measured BER as a function of bitrate without and with applying DD-MMSE equalizer, b) Histograms of detected bits (one sample per symbol) used for BER calculation at bitrate of 45 Gb/s and c) 55 Gb/s. The dashed lines show the Gaussian distributions in (b) and (c).

Thereafter, we presented a mode-conversion based SiP modulator that takes advantage of lateral and interleaved p-n junctions, simultaneously, to enhance phase modulation. The modulator gains a 67% improvement in the phase modulation when loaded by the C-LI p-n junction compared to the lateral one. The experimentally demonstrated modulator had a phase shifter length of 290 μm , an insertion loss of 2 dB, and the power consumption of 226 fJ/bit. The modulator operated up to 45 Gb/s (55 Gb/s) with BER below the 7 % (20 %) FEC threshold showing great potential for high speed, low cost, power efficient transmissions.

Chapter 2

Slow-light silicon photonic modulators: a Mach-Zehnder modulator assisted by coupled Bragg grating resonators

Résumé — Nous proposons une nouvelle conception d’un modulateur SiP qui a une grande efficacité de modulation et qui est tolérant aux variations de température. Une série de réseaux de Bragg déphasés est placée dans chaque bras d’un interféromètre Mach-Zehnder afin de fournir une modulation de phase améliorée. L’effet de lumière lente dans ces résonateurs couplés ultra-compacts améliore l’efficacité de la modulation de phase par rapport aux déphaseurs conventionnels en silicium. Ces cavités de réseaux de Bragg sont conçues de telle sorte que la bande passante optique est supérieure par rapport à d’autres modulateurs basés sur la résonance, tels que les modulateurs en anneau. Cette bande passante supérieure réduit la sensibilité des appareils à la température. Nous présentons en détail comment optimiser ces modulateurs en tenant compte de propriétés telles que l’efficacité de modulation ($V_\pi \times L$), l’amplitude de modulation optique (OMA) et la largeur de bande optique ($\Delta\lambda_{BW}$); cette dernière propriété déterminant la plage de température d’opération (ΔT). À titre d’exemples, nous présentons deux conceptions qui répondent à des cibles de spécifications différentes pour les applications à courte et à longue portée. Nous fournissons également un modèle, basé sur la théorie des modes couplés, pour étudier la réponse dynamique du modulateur proposé. Une analyse des grands signaux est effectuée en utilisant la méthode du domaine temporel à différence finie (FDTD) afin de simuler la modulation en tout ou rien (OOK) et le diagramme de l’œil.

Ensuite, nous faisons la démonstration expérimentale d’un modulateur sur SiP de type Mach-Zehnder (MZM) assisté par des réseaux de Bragg déphasés. Fabriqué selon un procédé de fonderie compatible au CMOS, le dispositif a obtenu un petit signal $V_\pi \times L$ de 0.18 V.cm, ce qui est sept fois moins qu’un MZM classique en silicium fabriqué selon le même procédé. Le dispositif a un

encombrement réduit, avec une longueur de $162\ \mu\text{m}$ seulement, et présente une largeur de bande de modulation de 28 GHz avec une polarisation inverse de 1 V. La modulation de non-retour à zéro est démontrée à 30 Gb/s avec un taux d'erreur sur les bits (BER) inférieur au seuil de correction d'erreur directe (FEC) de 7% sur une largeur de bande de $\Delta\lambda_{BW} = 3.5\ \text{nm}$. Cette largeur de bande devrait se traduire par une plage de température d'opération supérieure à $\Delta T > 40\ ^\circ\text{C}$.

Abstract- We propose a novel design of a SiP modulator that has a high modulation efficiency and is tolerant to temperature variations. A series of phase-shifted Bragg gratings are placed in each arm of a Mach-Zehnder interferometer in order to provide enhanced phase modulation. The slow light effect in these ultra-compact coupled resonators improves phase modulation efficiency compared to conventional silicon phase shifters. These Bragg grating cavities are designed such that the optical bandwidth increases compared to other resonance-based modulators such as micro-rings. This improved bandwidth reduces the temperature sensitivity of the devices. We present in detail how to optimize these modulators considering properties such as modulation efficiency ($V_\pi \times L$), optical modulation amplitude (OMA), and optical bandwidth ($\Delta\lambda_{BW}$); the latter property determining the operating temperature range (ΔT). As examples, we present two designs that meet different target specifications for short-reach and long-haul applications. We further provide a model, based on coupled mode theory, to investigate the dynamic response of the proposed modulator. A large signal analysis is performed using finite difference time domain (FDTD) in order to simulate on/off keying (OOK) modulation and eye diagrams.

Next, we experimentally demonstrate a SiP Mach-Zehnder modulator (MZM) assisted by phase-shifted Bragg gratings. Fabricated using a CMOS-compatible foundry process, the device achieved a small-signal $V_\pi \times L$ of 0.18 V.cm, which is seven times lower than a conventional silicon MZM fabricated with the same process. The device has a compact footprint, with a length of only $162\ \mu\text{m}$, and shows a modulation bandwidth of 28 GHz at a reverse bias of 1 V. Non-return-to-zero modulation is demonstrated at 30 Gb/s with a bit-error-rate (BER) below the 7%-overhead forward error correction (FEC, 3.8×10^{-3}) threshold over a bandwidth of $\Delta\lambda_{BW} = 3.5\ \text{nm}$. This bandwidth should translate into an operating temperature range greater than $\Delta T > 40\ ^\circ\text{C}$.

2.1 Introduction

Optical communications are the backbone of modern communication systems that provide high-speed access and exchange of data stored around the world. Research in electro-optic (EO) modulators is currently playing a critical role in the ongoing development of future optical interconnects needed to improve the performance of data communication networks [57, 100]. SiP modulators are currently being considered as a key technology because of their compatibility with complementary metal oxide semiconductor (CMOS) fabrication processes, which ensures low-cost large-scale production. However, the performance of SiP modulators is impaired by the lack of significant EO or electro-absorption effects [57]. Plasma dispersion, therefore, becomes the preferred means to modulate the refractive index of silicon.

Conventional silicon Mach-Zehnder modulators (MZM) require long phase shifters combined to travelling RF waveguides to achieve the required phase modulation. These MZMs are typically characterized by low efficiency and high power consumption [62, 97, 101–103]. Notwithstanding, conventional MZM have a wide optical bandwidth, which also translates into a large temperature operating range. MZMs further present the significant advantage of small chirp when operated in a push-pull configuration. Resonator-based SiP modulators (RBMs) [18, 20–22, 104], in contrast to conventional MZMs, have a more compact footprint and lower power consumption. This results from the resonance phenomenon, and its associated cavity lifetime, that leads to phase-shifts that are much more sensitive to the applied voltage, resulting in sharply increased modulation efficiency. However, RBMs generate chirped pulses and are very sensitive to temperature variations due to their narrow optical bandwidth. It is worth pointing out that the active stabilization of micro-ring modulators (MRMs) consumes significantly more energy than the modulator driver [21].

Combining resonators and a Mach-Zehnder interferometer (MZI) structure can improve modulator performance. In [105, 106], ring resonators are introduced into the arm of an MZI to increase modulation efficiency. This further makes the device more compact, but is achieved at the expense of a reduced optical bandwidth, which raises its temperature sensitivity significantly. Cascaded rings have been inserted in each arm of a MZI to overcome optical bandwidth limitations; however, this design also suffers from uncoupled resonators [23]. In another approach, photonic crystal waveguides (PCWs) were proposed for phase modulation enhancement that achieve high delay-bandwidth product [74, 75, 107]. However, PCW-based designs are very challenging for large-wafer fabrication processes with UV lithography and their performance is highly sensitive to parameter variations. In [108], it is reported that fluctuation of the hole radius by only 1% results in a propagation loss of 150 dB/cm. Consequently, most PCW-based devices typically require highly accurate fabrication process such e-beam lithography [109]. Bragg grating devices, which are 1-D photonic crystals, are less sensitive to fabrication errors and are routinely fabricated with CMOS compatible fabrication process using UV lithography [18, 20, 110–114].

In this chapter, we propose and characterize a novel SiP modulator design based on phase mod-

ulation enhancement in a MZI using coupled Bragg grating resonators (BGRs). This modulator exhibits properties that achieve a compromise between the high modulation efficiency of MRM and the wide optical bandwidth of conventional MZM. The coupled BGRs are used in low-dispersion slow light (LDSL) regime and, compared to other RBMs, they show an improved delay-bandwidth product, which is the fundamental limitation of slow-light-based devices. High time delay, corresponding to large group index, offers modulation enhancement. Wider optical bandwidth results in lower sensitivity to temperature. Consequently, the proposed design is more stable and has a broader operating temperature range than the MRM. In comparison to conventional MZMs, it requires a lower peak-to-peak voltage and offers a much more compact footprint. Furthermore, due to its short length, the modulator can be operated with lumped electrodes, even at high speed.

2.2 Modulator operating principle

In silicon waveguides, light propagates with a group velocity equal to c/ng where c is the speed of light in vacuum and the group index, ng , is typically equal to about 3.8 for rib-waveguides. The group index depends on the first-order dispersion that can be sharply enhanced by the presence of a resonance [115]. Ring resonators [116–118], photonic crystals [119, 120], and Bragg gratings [121–123] are all resonating structures that can result in slow-light behavior for optical frequencies close to their band gap. The cost associated with the beneficial attributes of slow light is that the second-order dispersion also increases, consequently making the optical bandwidth narrower [115, 124]. Therefore, using slow light to improve the efficiency of modulators could have important benefits for optical interconnects by offering a solution with high speed, small size, and low energy consumption. However, optical structures providing wider optical bandwidth and improved stability must first be demonstrated.

Figure 2.1 (a) shows the configuration of the proposed modulator that we will refer to as a Bragg grating resonator assisted MZM (BGR-MZM). To take advantage of slow light, one superstructured IBG with a uniform period is inserted in each arm. These IBGs have coupled resonators created by introducing π -phase shifts as shown in Fig. 2.1 (b). The coupled resonators are designed with a low-quality factor to make the optical bandwidth wider while maintaining a large phase enhancement. In other words, each resonator operates in the LDSL regime to achieve a wide optical bandwidth; thereafter, the large enhancement in phase modulation is achieved by placing a series of coupled resonators. Therefore, the modulation efficiency is similar to other RBMs but with a higher optical bandwidth, conferring a larger achievable temperature operating range without thermal stabilization. Lastly, the whole IBG length (L) remains quite small, even when a large number of resonators are inserted, because the IBGs are designed with a strong coupling coefficient that is obtained by large sidewall corrugations.

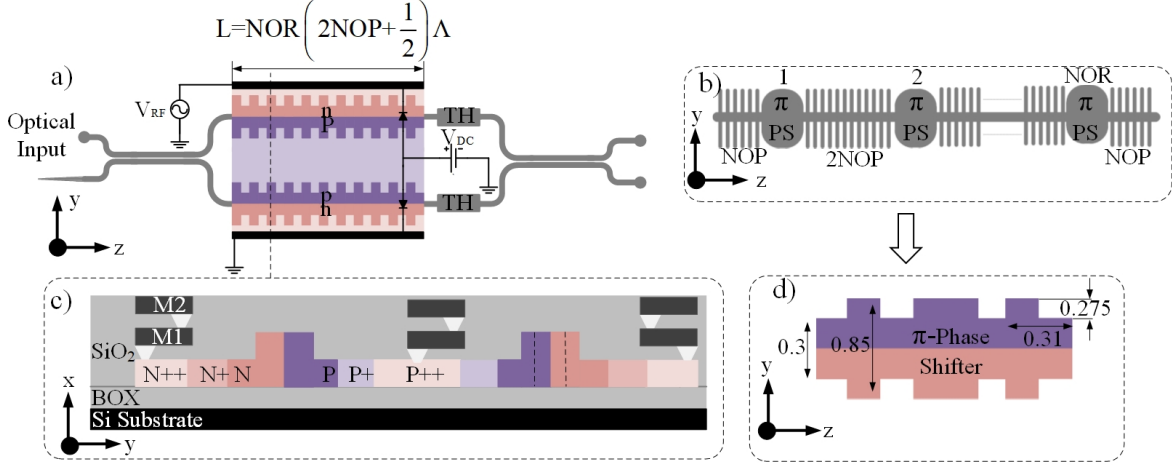


Figure 2.1 – Schematic of the BGR-MZM showing a) the configuration of the BGR-MZM, b) the phase-shifted IBG present in each arm, c) the cross-section showing the p-n junction and the three doping levels, and d) the phase-shifted IBG cavity. TH: Thermal element, PS: Phase-shifted cavity, M1: Metal 1, M2: Metal 2, NOP: Number of periods of the resonator mirrors on each side, NOR: number of resonators. All dimensions are shown in micrometers.

2.3 Design and optimization

In this section, we first calculate the static response of the BGR-MZM and then optimize the IBG design through numerical simulations. We consider IBGs with a uniform period of $\Lambda = 310$ nm in each arm. As can be seen in Fig. 2.1 (c) and (d), the gratings are designed using sidewall corrugations with a duty cycle of 50% in a ridge waveguide having a maximum width of 850 nm, minimum width of 300 nm, ridge height of 220 nm, and slab height of 90 nm. Each resonator of the Bragg grating structure is composed of two mirrors with NOP periods and a phase shift of half a period, resulting in a total length for the structure that scales with NOR as indicated in Fig. 2.1 (a). The NOP and the NOR are varied to obtain the desired modulator properties. The total corrugation amplitude and average waveguide width are 550 nm and 575 nm, respectively. The aforementioned parameters are considered constant during the optimization of the NOR and NOP. Under the application of the driving voltage, we assume that the modulator is operated in a single drive push-pull configuration. Thermal elements are placed in both arms in order to adjust the modulator phase bias. The p-n junctions are formed over the entire IBG length.

2.3.1 Spectral response

After the 3-dB adiabatic coupler, the input light goes through an IBG in each arm of the MZI. To determine the transmission power and phase responses of the IBGs, we use the transfer-matrix implementation of the solutions to the coupled-mode equations. Propagation through an IBG can be

calculated using [124],

$$\begin{bmatrix} F(0) \\ B(0) \end{bmatrix} = T \begin{bmatrix} F(L) \\ B(L) \end{bmatrix}, \quad T = (APA)^M \quad (2.1)$$

where F is the slowly varying envelope of the forward propagating mode, B is the backward propagating one, M is the number of phase-shifts in the IBG, A is transfer matrix that represents the IBGs on each side of the phase-shift resonators, and P is the matrix representing propagation through the phase-shift region. These matrices are defined as,

$$A = \begin{bmatrix} A_{11} & A_{12} \\ A_{21} & A_{22} \end{bmatrix} \quad (2.2)$$

$$A_{11} = A_{22}^* = \cosh \left(l \sqrt{\kappa^2 - \Delta\beta^2} \right) + j \frac{\Delta\beta}{\sqrt{\kappa^2 - \Delta\beta^2}} \sinh \left(l \sqrt{\kappa^2 - \Delta\beta^2} \right) \quad (2.3)$$

$$A_{12} = -A_{21} = j \frac{\kappa}{\sqrt{\kappa^2 - \Delta\beta^2}} \sinh \left(l \sqrt{\kappa^2 - \Delta\beta^2} \right) \quad (2.4)$$

$$P = \begin{bmatrix} P_{11} & P_{12} \\ P_{21} & P_{22} \end{bmatrix} \quad (2.5)$$

$$P_{11} = P_{22}^* = \exp \left(i\beta \frac{\Lambda}{2} \right) \quad (2.6)$$

$$P_{12} = P_{21} = 0 \quad (2.7)$$

where l is the length of grating on one side of a resonator which is $l = N_{(1or2)} \times \Lambda$, where $N_1 = N_2$ is the number of periods on each side of the cavities and Λ is the grating period. Also, κ is the coupling coefficient, and $\Delta\beta$ represents the wavenumber detuning (or momentum mismatch [124]), which is defined as $\Delta\beta = \beta - \pi/\Lambda$, where β is the propagation constant.

To estimate the grating coupling coefficient, κ , we first calculate the IBG photonic band gap, $\Delta\lambda_{PBG}$, using a commercial software (FDTD-Lumerical). Then, the coupling coefficient for IBG modeling is extracted using [47],

$$\kappa = \frac{\pi n g \Delta\lambda_{PBG}}{\lambda_c^2} \quad (2.8)$$

where λ_c is the central wavelength of $\Delta\lambda_{PBG}$ and ng is the average group index. Fig. 2.2 shows the band-structure of the IBG. The photonic bandgap, $\Delta\lambda_{PBG} = 82$ nm, corresponds to a coupling coefficient of $\kappa = 402370 \text{ m}^{-1}$.

The goal of using an IBG with a large photonic band gap is that a lower number of periods is needed to achieve the required 3-dB optical bandwidth, resulting in an extremely short IBG length that translates into a low modulation power. In other words, we keep grating strength ($\kappa \times L$) high but grating length small. Note that an IBG with strong corrugation is likely to exhibit significant radiation loss, and consequently a higher attenuation coefficient per unit length but the total average loss remains in reasonable range as will be discussed in the section 2.3.5.

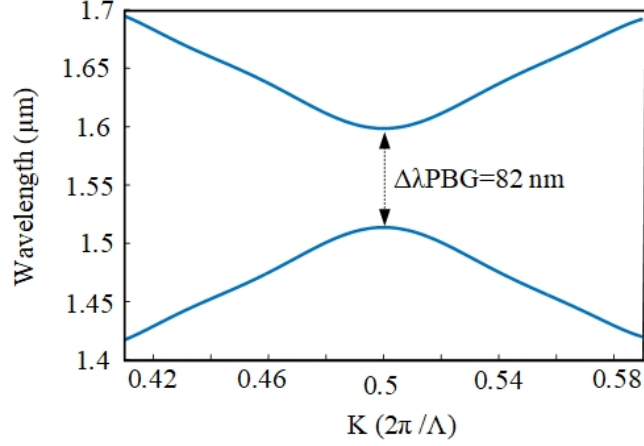


Figure 2.2 – Simulated photonic band-structure of the IBG.

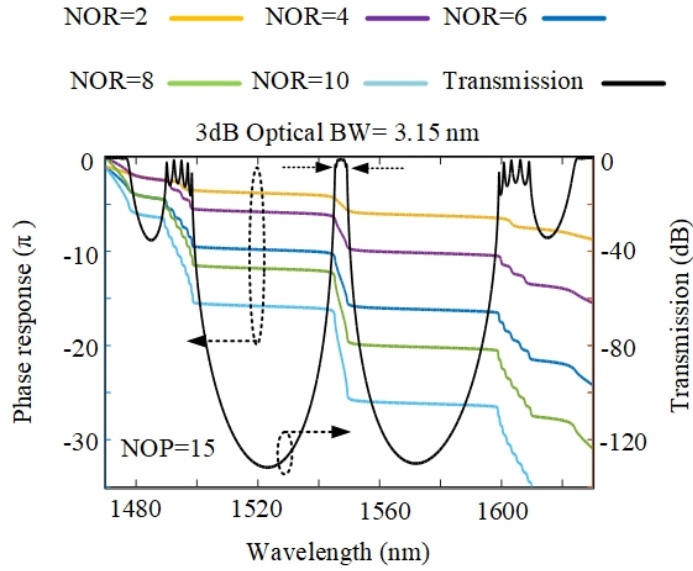


Figure 2.3 – Power transmission (black line) and phase response (colored lines) of an IBG with multiple phase shifts. The transmission is calculated for $NOP = 15$ and $NOR = 6$. Phase shifts are plotted for $NOP = 15$ and different values of NORs. NOR: number of resonators, NOP: number of periods.

Figure 2.3 (solid black line) shows the spectral response of an IBG with multiple phase shifts. The transmission amplitude is plotted for $NOP = 15$ and $NOR = 6$. The 3-dB optical bandwidth is $\Delta\lambda_{BW} = 3.15$ nm, confirming that the proposed modulator will have improved thermal stability compared to usual RBMs.

2.3.2 Phase response

When voltage is applied to the IBGs, modification of the width of the depletion region causes a variation of the waveguide refractive index. For high-speed operation, the p-n junction is operated

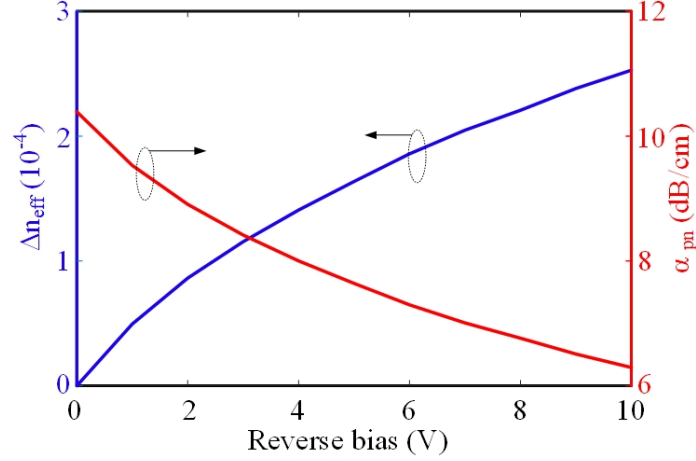


Figure 2.4 – Variation of the rib waveguide effective refractive index and absorption loss of p-n junction as a function of reverse voltage for simple phase shifters.

in a carrier depletion mode using a reverse bias. Fig. 2.4 plots the variation of the effective refractive index, Δn_{eff} , as a function of reverse bias voltage modeled in [125]. As can be seen, Δn_{eff} remains below 2.5×10^{-4} due to the weak plasma dispersion effect in silicon and to the small overlap between the optical mode and the depletion region in the lateral-junction configuration.

Figure 2.3 shows how resonators can improve the phase modulation. The colored lines represent the phase of the transmitted signal for $NOP = 15$ and different values of NOR . The phase response is becoming steeper with increasing NOR for wavelengths transmitted through the transmission peak created by the resonating cavities. We define the operational wavelength, λ_0 , as the central peak wavelength, which is, in the present case, $\lambda_0 = 1547.3$ nm. Therefore, phase modulation enhancement is achieved, which means that a lower V_{pp} is needed to reach the required phase modulation. Fig. 2.5 shows the absolute value of the transmitted phase modulation as a function of voltage for a NOP of 15 and various NOR s. Comparison to the reference phase shifter in the conventional rib waveguide (solid blue line with square marker) shows a substantially increased slope in the phase response.

2.3.3 Phase modulation enhancement

To further investigate the LDSL regime, we examine Fig. 2.6 that shows the spectral dependence of the calculated ng for $NOR = 6$ and $NOP = 15$ on each side of the resonators. The group index curve shows a plateau near the peak wavelength with $ng \simeq 20$, which is several times larger than the ng of a rib waveguide. On the edge of the passband, ng reaches values near 60, but over a narrow optical bandwidth, which makes the operation of the modulator at these wavelengths unstable, similar to RBMs.

To quantify the slow light effect, we introduce an enhancement factor, γ , which is defined as

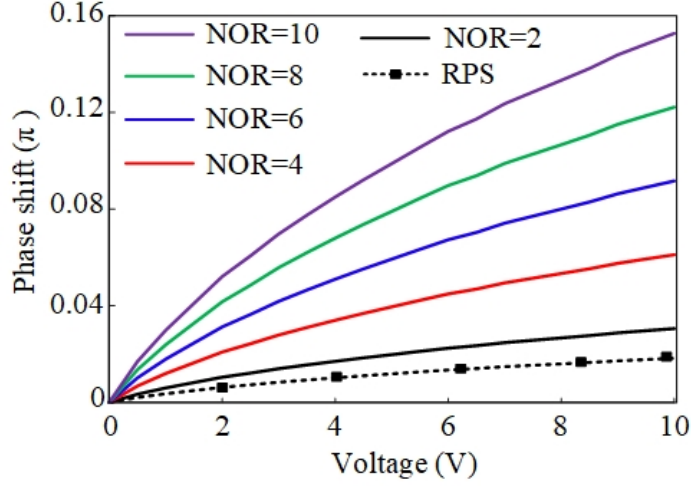


Figure 2.5 – Phase variation as a function of applied reverse voltage for $NOP = 15$ and various NOR s. RPS: a reference phase-shifter (waveguide with p-n junction that has a length equal to the length of the IBG with $NOR = 6$ and $NOP = 15$). NOR : number of resonators, NOP : number of periods.

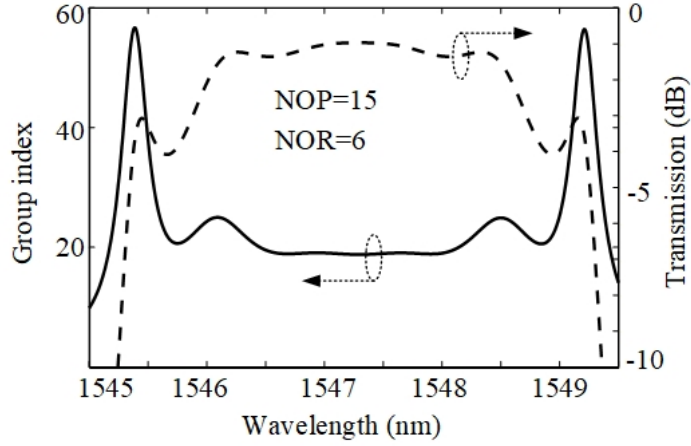


Figure 2.6 – Group index (solid line) and transmission (dashed line) versus wavelength for $NOP = 15$ and $NOR = 6$. NOR : number of resonators, NOP : number of periods.

the ratio between the values of the derivative of the transmitted phase with respect to the applied voltage for an IBG with multiple resonators to the derivative calculated for a conventional phase shifter (waveguide with p-n junction) of the same length. We write

$$\gamma = \frac{\partial \varphi / \partial V}{\partial \varphi_w / \partial V} \quad (2.9)$$

where V is the applied voltage, and φ and φ_w are the transmitted phase of the IBG and of a simple rib waveguide, respectively. Fig. 2.7 (a) shows γ as functions of both NOP and NOR . As can be seen, a larger NOP results in a more efficient modulator. However, as shown in Fig. 2.7 (b), this enhancement comes at the cost of reduced 3-dB optical bandwidth because of the increased quality

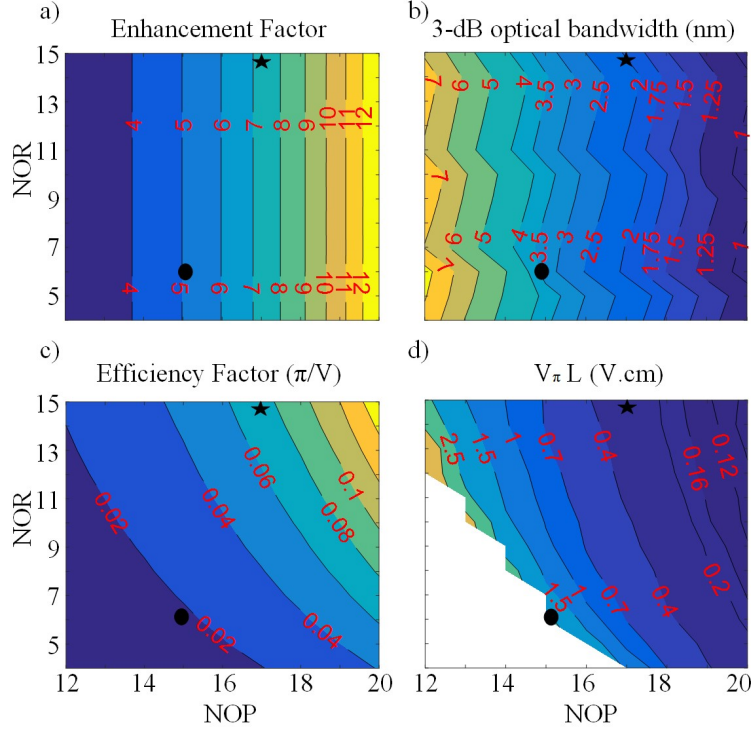


Figure 2.7 – a) Enhancement factor, b) 3-dB optical bandwidth of the transmission peak, c) Efficiency factor, and d) FOM; all as functions of NOR and NOP. Star and dot markers show two designs chosen for long- and short-distance applications, respectively.

factor of the resonators. Therefore, the choice of NOP is a compromise between the operational temperature range and modulation efficiency, *i.e.*, delay-bandwidth product. Fig. 2.8 shows the aforementioned tradeoff between bandwidth and time delay with respect to NOP for various NORs. From Fig. 2.7 (a) and (b), we also see that the enhancement factor and 3-dB optical bandwidth remain almost constant as the number of cavities is increased. More precisely, when the NOR is increased, some small ripples appear in the amplitude response, but the changes in the 3-dB optical bandwidth are negligible.

To examine modulation efficiency, we also plot in Fig. 2.7 (c) the value of the derivative of the transmitted phase with respect to the applied voltage at λ_0 . We refer to this quantity as the efficiency factor. Fig. 2.7 (c) shows the variation of the efficiency factor with respect to both NOP and NOR. From Fig. 2.7 (b) and (c), it is clear that adding resonators improves phase modulation (larger time delay) while the 3-dB optical bandwidth remains almost constant, leading to an enhanced delay-bandwidth product. Fig. 2.8 confirms the product enhancement. However, a larger NOR results in a higher optical loss that will be considered in the discussion of OMA.

The FOM defined as $V_\pi \times L$ is often used to characterize the efficiency of a modulator. Fig. 2.7 (d) shows the FOM calculated as functions of NOR and NOP; note that NOP is directly linked to the enhancement factor (Fig. 2.7 (a)) and the NOR is mostly related to the IBG length (L). A given FOM

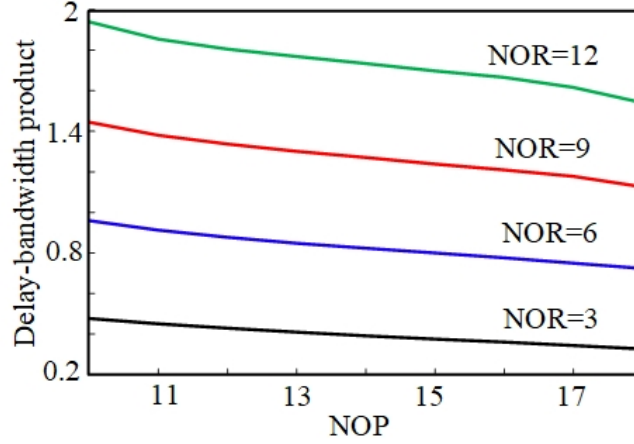


Figure 2.8 – Delay-bandwidth product as a function of NOP for various NORs.

can therefore be achieved with different sets of NOR and NOP. For example, to design a modulator with a FOM of 1 V.cm, we can choose NOR = 13 and NOP = 15 ($L = 121 \mu\text{m}$, $\gamma = 5$), NOR = 10 and NOP = 16 ($L = 100 \mu\text{m}$, $\gamma = 6$), or NOR = 7 and NOP = 17 ($L = 74 \mu\text{m}$, $\gamma = 7.2$). From Fig. 2.7 (b), their 3-dB bandwidths are approximately 4 nm, 3 nm, and 2 nm, respectively. If we target a smaller enhancement factor (corresponding to lower NOP), the 3-dB optical bandwidth will be larger resulting in a more stable operation of the device. In this case however, the NOR will have to be increased in order to achieve a specific phase modulation.

2.3.4 Optical modulation amplitude (OMA)

These IBGs are phase modulators that need to be inserted in a MZI to produce amplitude modulation. The quality of the amplitude-modulated signal is thus examined by calculating the OMA of the BGR-MZM at λ_0 . In this section, we calculate the OMA from the static response, *i.e.*, as a function of DC voltage. The dynamic response will be examined in section 2.4. The output power of the MZI is calculated assuming ideal input and output 3-dB power splitters,

$$P_{out} = P_{in} \exp(-\alpha L) \cos^2(\Delta\varphi_v) \quad (2.10)$$

$$\Delta\varphi_v = \frac{k_0 \Delta n_{eff}(V) \gamma L + \Delta\varphi_0}{2} \quad (2.11)$$

where P_{in} is the input power and α is the propagation loss coefficient. The total phase difference between the two MZI arms is $\Delta\varphi_v$. $\Delta\varphi_0$ represents the initial phase difference between the two arms. The phase modulation is calculated from the variation of the waveguide refractive index, Δn_{eff} multiplied by γ . Finally, k_0 is the wavenumber equal to $2\pi/\lambda_0$. At the BGR-MZM output, the OMA is calculated using

$$OMA = 10 \log \left(\frac{Output Power_{on} - Output Power_{off}}{Input Power} \right) \quad (2.12)$$

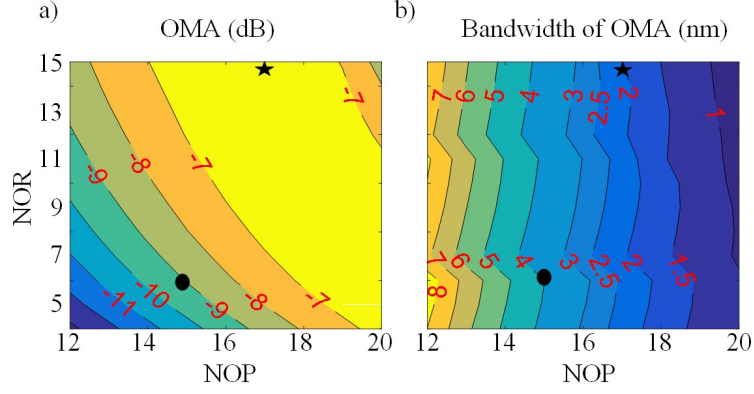


Figure 2.9 – a) OMA and b) 3-dB OMA bandwidth as functions of NOR and NOP. Star and dot markers are the designs chosen for long- and short-distance applications respectively as in Fig. 2.7.

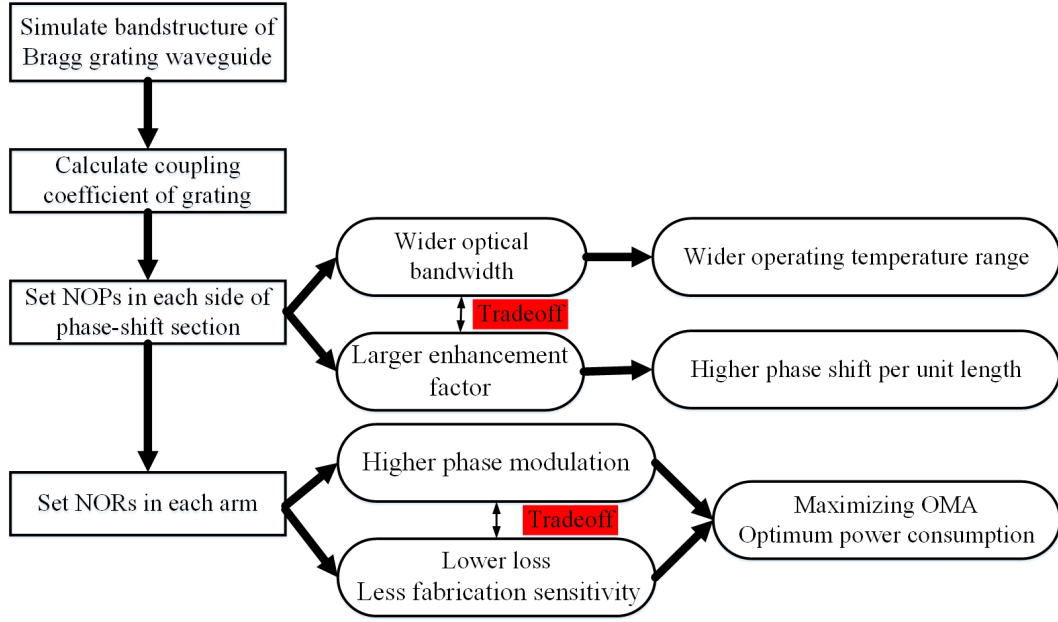


Figure 2.10 – Design process flowchart of Bragg grating resonators.

Figure 2.9 (a) shows the OMA at λ_0 as functions of NOR and NOP with V_{pp} of 4 V on each arm, V_{bias} is -2 V, and $\Delta\varphi_0$ is $\pi/2$. The lower OMA (the bottom-left corner) comes from the lower efficiency factor, which results in a closed eye. The opposite corner (*i.e.*, the top-right corner) also shows a lower OMA although this corresponds to a region with a high-efficiency factor. In this case, it is the long IBG length that induces high loss, which reduces the power level of bits “1”. Consequently, there are some IBG parameter sets (NOR and NOP) that maximize the OMA (yellow color in Fig. 2.9 (a)). High OMA is a key parameter in long-distance applications. In Fig. 2.10, we summarize the whole design flow of Bragg grating resonators.

The 3-dB OMA spectral bandwidth (BW-OMA) can be used to examine the stability of the modulator operation with respect to temperature variations, *i.e.*, a larger BW-OMA corresponds to a

lower thermal sensitivity. Fig. 2.9 (b) shows the BW-OMA versus NOR and NOP for a $V_{pp} = 4$ V on each arm, $V_{bias} = -2$ V, and $\Delta\varphi_0 = \pi/2$. From Fig. 2.9 (b) and Fig. 2.7 (b), it can be seen that the BW-OMA variations follow the 3-dB optical bandwidth of the transmission peak.

2.3.5 Loss

The on-chip loss of the modulator comes mostly from the absorption due to the carriers in the pn-junction and the scattering loss produced by the IBG with strong corrugations. The simulated absorption loss of the pn junction for a simple phase shifter is plotted in Fig. 2.4, showing 9 dB/cm absorption loss for bias voltage of -2 V. Assuming that the absorption loss increases linearly with the enhancement factor and considering an average enhancement factor of 8 (see Fig. 2.7 (a)), the absorption loss of our structure is 72 dB/cm. Furthermore, according to Xu. *et al.* [126], at up to 160 nm corrugation, no significant excess loss in IBGs is observed compared to simple waveguides. Since the corrugations of the IBGs in our proposed modulator structure are significantly larger, we performed 3D FDTD simulations to estimate loss. Due to memory limitations, we simulated a uniform IBG with a length of about 15.5 μm (50 periods) and corrugations of 550 nm (275 nm on each side). The simulated device was surrounded by perfectly matched layer (PML) boundaries and power monitors were placed at the IBG output and the input to calculate the transmission (T) and reflection (R). The IBG excess loss calculated as $1 - (T + R)$ was negligible (< 0.003) both outside its bandgap and in its stopband over the spectral bandwidth where it is operated as a modulator. As a best estimate, we therefore assume that the results reported in [126] are also valid in the case of our device and set the loss of the IBG structure of our modulator at 2.5 dB/cm, similarly to the scattering loss of a simple waveguide as in [126]. Now, considering an average enhancement factor of 8, and assuming a linear relationship between the enhancement factor and the scattering loss, our best estimate for the scattering loss of the modulator is 20 dB/cm. Despite this large loss, the total loss of our modulator remains reasonable because of the very small lengths involved. Considering a typical phase shifter length of 100 μm , the loss of the modulator structure is of the order of 1 dB.

2.3.6 Examples of modulator designs

We now examine two specific modulator designs: [NOR = 15, NOP = 17] and [NOR = 6, NOP = 15]. Their characteristics are marked as a black-star and a black-dot respectively in Fig. 2.7 and Fig. 2.9. The first design, with a larger number of resonators and grating period, achieves higher OMA but requires higher driving power due to the longer IBG length ($L = 160$ μm). The second design is a compact modulator ($L = 56$ μm) that compromises on the OMA to reduce driving power requirement. The longer design would, therefore, be appropriate for systems requiring higher performance, such as high-order modulation formats, while the shorter one would be of interest for short-reach data links.

When optimizing the electrical bias, both OMA and energy consumption should be considered. Energy consumption is a function of V_{pp} and is written as $E_b = CV_{pp}^2/4$ for OOK modulation. The

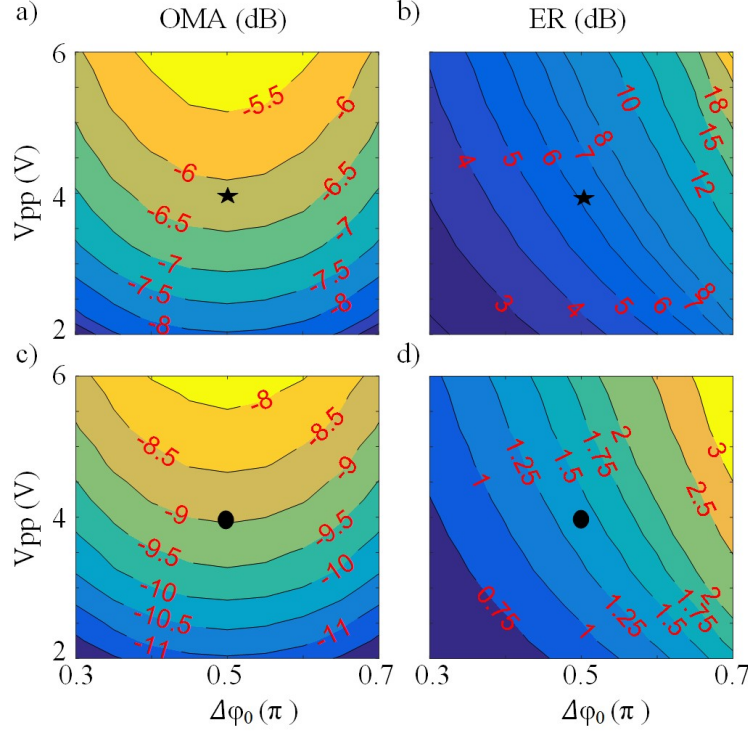


Figure 2.11 – a) OMA and b) ER as functions of V_{pp} and $\Delta\varphi_0$ for NOP = 17 and NOR = 15. c) OMA and d) ER as functions of V_{pp} and $\Delta\varphi_0$ for NOP = 15 and NOR = 6. Star and dot markers are the designs chosen for long- and short-distance applications respectively (as in Fig. 2.7 and Fig. 2.9).

driving voltage, V_{pp} , decreases when the NOR increases but this increase in L also results in a larger capacitance. Nonetheless, to lower energy consumption, it is beneficial to choose V_{pp} as low as possible. Fig. 2.11 (a) and (b) show OMA and extinction ratios (ER) at λ_0 as functions of $\Delta\varphi_0$ and V_{pp} on each arm. We consider that V_{bias} is $-V_{pp}/2$. Unsurprisingly, Fig. 2.11 (a) demonstrates that the highest OMA is reached when $\Delta\varphi_0 = \pi/2$, called the quadrature point. Therefore, biasing the modulator at the quadrature point ensures that the lowest V_{pp} will be needed to reach a given OMA, and will result in the lowest energy consumption. Note that the ER increases as functions of both $\Delta\varphi_0$ and V_{pp} as indicated in Fig. 2.11 (b). We consider $\Delta\varphi_0 = \pi/2$ and $V_{pp} = 4$ V in all the simulation results presented below. This corresponds to the black-star markers in Fig. 2.11 (a) and (b) for NOP = 17 and NOR = 15. Fig. 2.11 (c) and (d) demonstrate similar results for the second design. In Fig. 2.7, Fig. 2.9, and Fig. 2.11, simulations are performed with NOP and NOR that are integer numbers which would result in block type graphs. To aid in identifying the trends, we smoothed the block type color graph using the Contourf command in MatLab.

Figure 2.12 (a) shows the modulation of the transmission for these two designs using $V_{pp} = 4$ V on each arm, $V_{bias} = -2$ V, and $\Delta\varphi_0 = \pi/2$. As can be seen, the ON/OFF ERs are 6.1 dB and 1.4 dB. Fig. 2.12 (b) shows how OMA is improved when increasing V_{pp} . Furthermore, in Fig. 2.12 (a), note that the BW-OMA is reduced, from approximately 4 nm to 2 nm, when increasing the enhancement

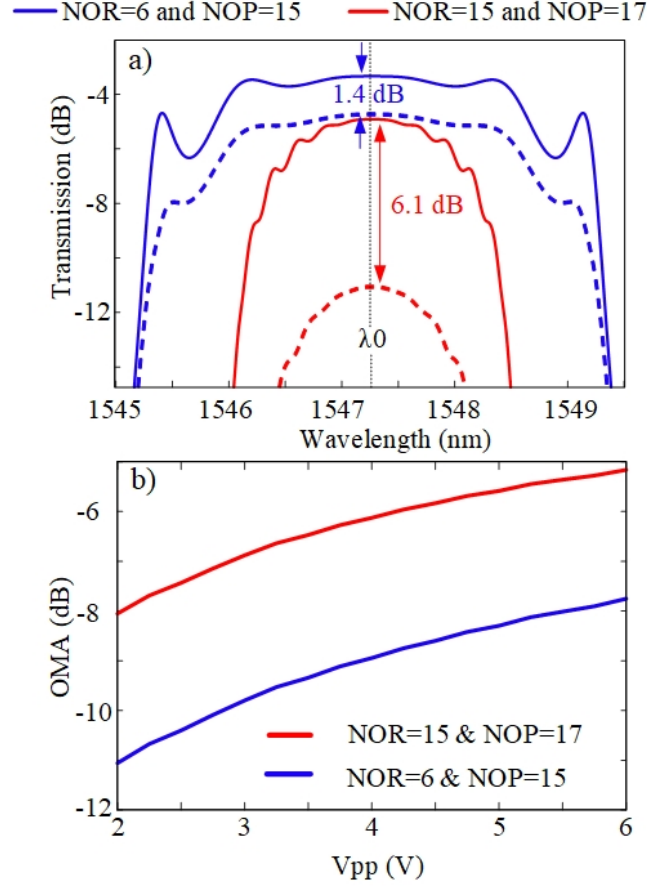


Figure 2.12 – a) Static optical modulation calculations for $\text{NOR} = 6$ and $\text{NOP} = 15$ (blue curves); and for $\text{NOR} = 15$ and $\text{NOP} = 17$ (black curves), b) OMA as a function of voltage for these two designs. In (a), dashed-line and solid-line show off and on states, respectively.

factor by using larger NOPs. Fig. 2.13 (a) and (b) zoom on the OMA spectrum of both designs and show the impact of temperature change. For IBGs in silicon waveguides, typical peak wavelength shift with temperature is $\Delta\lambda/\Delta T = 80 \text{ pm}/^\circ\text{C}$ [21]. A 3-dB reduction of operating OMA, therefore, leads to a temperature operating range of $\Delta T \simeq \pm 12.5^\circ\text{C}$ and $\Delta T \simeq \pm 25^\circ\text{C}$ for the two designs as shown in Fig. 2.13. For comparison, a single resonator MRM can tolerate only a few kelvins of temperature variations [21].

2.4 Dynamic response

In this section, we develop a dynamic model of BGR-MZMs to examine their frequency response. The model is based on the time-dependent coupled-mode equations (see for example [127]) that take into account the response of the resonating structure. The differential equation set is solved using FDTD in MatLab [128]. Because of memory limitation, we numerically investigate only the second design that has a shorter length with $\text{NOP} = 15$ and $\text{NOR} = 6$. The IBG starts at $z = 0$ and ends

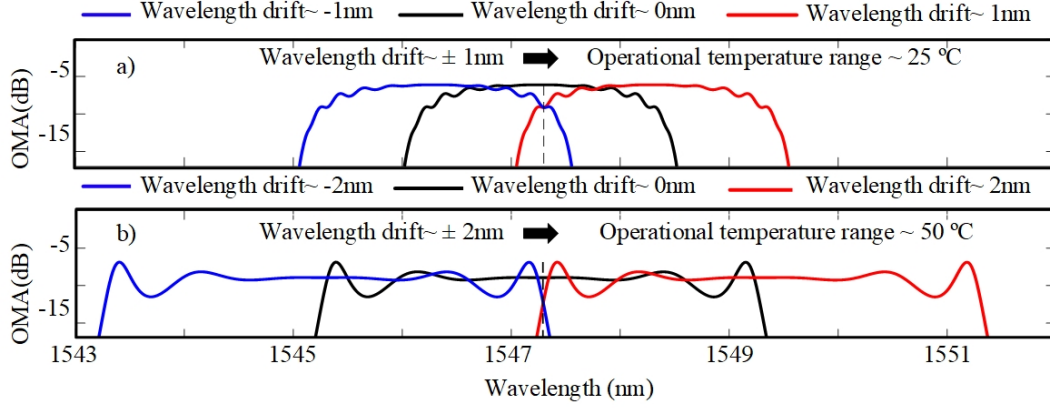


Figure 2.13 – OMA spectra calculated for a) NOR = 15 and NOP = 17 (black line), and b) NOR = 6 and NOP = 15 (black line). In (a), OMA calculated with temperature variations of $\Delta T = -12.5^\circ\text{C}$ (blue line) and $\Delta T = 12.5^\circ\text{C}$ (red line) are also plotted. In (b), OMA calculated with temperature variations of $\Delta T = -25^\circ\text{C}$ (blue line) and $\Delta T = 25^\circ\text{C}$ (red line) are also plotted.

at $z = L$. The phase shifts are located at $z = L/12, 3L/12, 5L/12, 7L/12, 9L/12, 11L/12$. We write the input signal as $E_{cw} = E_0 \exp(i(\beta z - \omega t))$. The equations representing the propagation of the envelopes of the forward and backward propagating mode fields (F and B , respectively), in the waveguide section with a Bragg grating structure (BGS) and in the sections where the waveguide is uniform to create a phase-shift segment (PSS), are as follow,

$$BGS \begin{cases} \frac{\partial F}{\partial z} + \frac{n_{eff}(t)}{c} \frac{\partial F}{\partial t} = i\kappa B \exp(-i2\Delta\beta z) \\ \frac{\partial B}{\partial z} - \frac{n_{eff}(t)}{c} \frac{\partial B}{\partial t} = -i\kappa F \exp(i2\Delta\beta z) \end{cases} \quad (2.13)$$

$$PSS \begin{cases} \frac{\partial F}{\partial z} + \frac{n_{eff}(t)}{c} \frac{\partial F}{\partial t} = 0 \\ \frac{\partial B}{\partial z} - \frac{n_{eff}(t)}{c} \frac{\partial B}{\partial t} = 0 \end{cases} \quad (2.14)$$

where c is the speed of light in vacuum. Also, $n_{eff}(t)$ is the waveguide effective index described as $n_{eff}(t) = n_{eff} - \Delta n_{eff}(t)$ where n_{eff} is effective index of unperturbed waveguide and $\Delta n_{eff}(t)$ is the time-dependent perturbation resulting from the applied voltage as represented in Fig. 2.4. Eq. 2.13 and Eq. 2.14 can be rewritten using normalized parameters,

$$BGS \begin{cases} \frac{\partial F}{\partial T} = -\frac{1}{\eta(T)} \left[\frac{\partial F}{\partial Z} - i\kappa L B \exp(-i2\Delta\beta(T)LZ) \right] \\ \frac{\partial B}{\partial T} = \frac{1}{\eta(T)} \left[\frac{\partial B}{\partial Z} + i\kappa L F \exp(i2\Delta\beta(T)LZ) \right] \end{cases} \quad (2.15)$$

$$PSS \begin{cases} \frac{\partial F}{\partial T} = -\frac{1}{\eta(T)} \frac{\partial F}{\partial Z} \\ \frac{\partial B}{\partial T} = \frac{1}{\eta(T)} \frac{\partial B}{\partial Z} \end{cases} \quad (2.16)$$

where

$$Z = \frac{1}{L}z \quad (2.17)$$

$$T = \frac{c}{Ln_{eff}}t \quad (2.18)$$

$$\eta(T) = \frac{n_{eff} - \Delta n_{eff}(t)}{n_{eff}} \quad (2.19)$$

$$\Delta\beta(T) = \frac{2\pi}{\lambda} (n_{eff} - \Delta n_{eff}(t)) - \frac{\pi}{\Lambda} \quad (2.20)$$

The FDTD method is used to solve Eq. 2.15 and Eq. 2.16 [128]. We take discrete values for Z and T : $j\Delta Z$ and $n\Delta T$, where j and n are integers. $\Delta Z = 1.3 \times 10^{-4}$ is considered, corresponding to node number of 7320. We define the Courant number as $\Gamma = \Delta T / \Delta Z$. Courant number should be between 0 and 1 to achieve a convergence [128]. Considering $\Gamma = 0.5$, ΔT is 6.5×10^{-5} . The discretized forms of Eq. 2.15 and Eq. 2.16 are as follow,

$$BGS \begin{cases} F_j^{n+1} = F_j^n - \frac{\Delta T}{\eta^n} \times \left[\frac{F_j^n - F_{j-1}^n}{\Delta Z} - i\kappa L B_j^n \exp(-i2\Delta\beta^n L \Delta Z j) \right] \\ B_j^{n+1} = B_j^n + \frac{\Delta T}{\eta^n} \times \left[\frac{B_{j+1}^n - B_j^n}{\Delta Z} + i\kappa L F_j^{n+1} \exp(+i2\Delta\beta^n L \Delta Z j) \right] \end{cases} \quad (2.21)$$

$$PSS \begin{cases} F_j^{n+1} = F_j^n - \frac{\Delta T}{\eta^n} \left[\frac{F_j^n - F_{j-1}^n}{\Delta Z} \right] \\ B_j^{n+1} = B_j^n + \frac{\Delta T}{\eta^n} \left[\frac{B_{j+1}^n - B_j^n}{\Delta Z} \right] \end{cases} \quad (2.22)$$

where F_j^n is $F(n\Delta T, j\Delta Z)$. The same definition holds true for B_j^n . At $Z = 0$ (or $j = 1$), the forward field is equal to $1/\sqrt{2}$ of the CW beam and the backward field should be continuous. Also, at $Z = 1$ (or $j = 7320$), the forward field must be continuous and the backward field is equal to zero. Therefore, the boundary condition for each IBG are introduced as,

$$F(0, T) = E_0/\sqrt{2} \quad , \quad \left. \frac{\partial F(Z, T)}{\partial Z} \right|_{Z=1} = 0 \quad (2.23)$$

$$\left. \frac{\partial B(Z, T)}{\partial Z} \right|_{Z=0} = 0 \quad , \quad B(1, T) = 0 \quad (2.24)$$

We first calculate the steady state condition of Eq. 2.21 and Eq. 2.22 using initial values of $F_1^1 = 1$, $F_{j \neq 1}^1 = 0$, and $B_j^1 = 0$. The transient time is around 20 ps as shown in Fig. 2.14 (a). The steady state values of the nodes are illustrated in Fig. 2.14 (b) where six peaks appear, corresponding to the six coupled resonators.

We use pseudorandom binary bit sequence 2^5-1 as input of the simulation. Fig. 2.15 shows the time response of the BGR-MZM at bitrates of 30 Gb/s, 70 Gb/s, and 110 Gb/s; and their respective

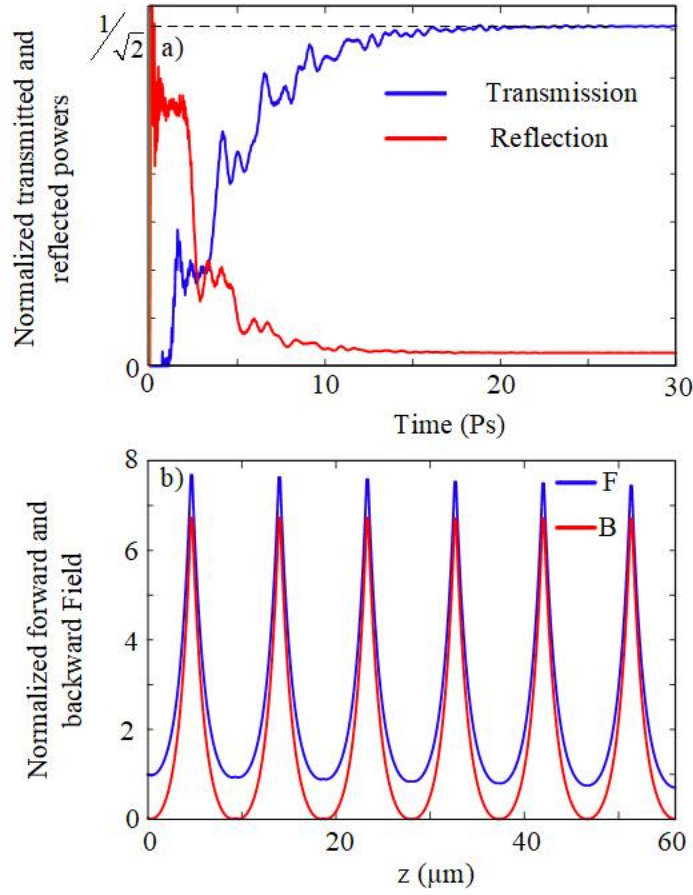


Figure 2.14 – a) Transient time of the FDTD model at λ_0 normalized to E_0 , b) normalized steady state value of each node for the forward and backward fields at λ_0 .

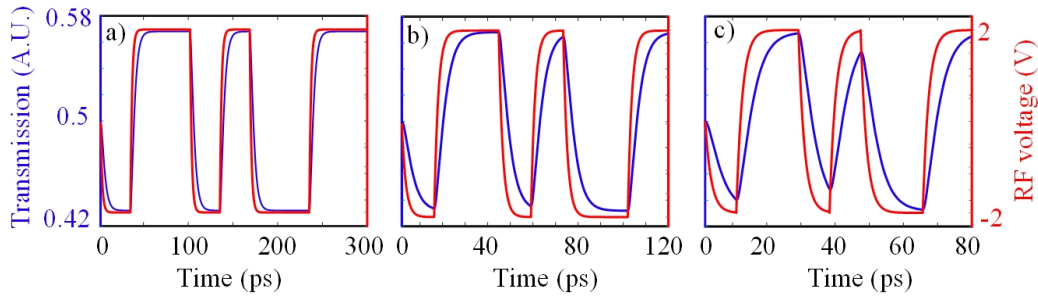


Figure 2.15 – Time response of BRG-MZM for a) 30 Gb/s, b) 70 Gb/s, and c) 110 Gb/s when applying RF voltage of $4 V_{pp}$ on each arm at the reverse voltage of -2 V and at λ_0 .

eye diagrams are plotted in Fig. 2.16 when applying RF voltage of $4 V_{pp}$ on each arm at the reverse voltage of -2 V and at λ_0 . Note that the calculated eye diagrams are noiseless and therefore the quality factor of eye diagram would be further reduced in the presence of noise.

The EO bandwidth of the BGR-MZM is limited by the electrical and optical dynamics that are usually quantified using the RC time constant and the quality factor of the Bragg grating filter (or

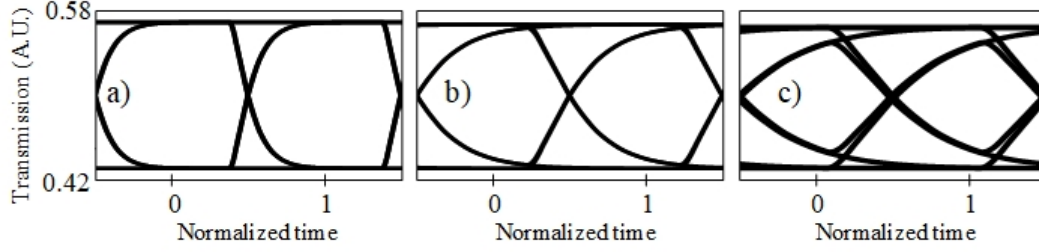


Figure 2.16 – Eye diagrams calculated for BGR-MZM operated at (a) 30 Gb/s, (b) 70 Gb/s (c) 110 Gb/s.

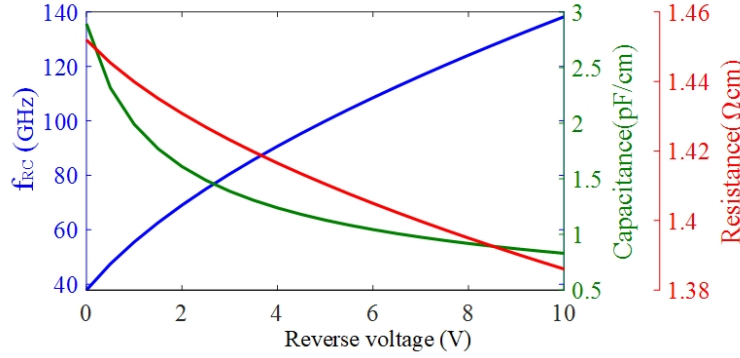


Figure 2.17 – Capacitance (blue) and resistance (red) of p-n junction as a function of reverse voltage. The resulting electrical cut-off frequency (black) is also shown.

the photon lifetime, τ). The EO 3-dB cutoff frequency, f_C , of the small signal response of BGR-MZM is estimated by

$$\frac{1}{f_C^2} = \frac{1}{f_{RC}^2} + \frac{1}{f_\tau^2} \quad (2.25)$$

where f_{RC} represents the cutoff frequency of the RC circuit modeling a reverse biased p-n junction, and f_τ is the optical cutoff frequency, given by $f_\tau = 1/(2\pi\tau)$. The resistance and capacitance of the p-n junction are modeled as in Ref. [125] and are shown as a function of reverse bias in Fig. 2.17. The junction capacitance and resistance are equal to 1.6 pF/cm and 1.4 Ωcm at $V_{bias} = -2$ V, corresponding to $f_{RC} = 69$ GHz.

The EO cutoff frequency is estimated by injecting an ultra-short electrical pulse and calculating the transmitted optical pulse using the full dynamic model described above (see Fig. 2.18). Then, we take the Fourier transform of the time response to extract the EO frequency response. Fig. 2.19 illustrates the EO response of the grating structure, showing that f_C is 41 GHz. Considering Eq. 2.25, f_τ is calculated to be 50 GHz, which corresponds to $\tau = 3.1$ ps. Fig. 2.20 also displays the dynamic OMA as a function of bitrate. The blue dot markers are the OMA values calculated with the full dynamic model at various bitrates while the line is a guide to the eye. As indicated, OMA sharply reduces after 3-dB EO bandwidth ($f_C = 41$ GHz) because of the dynamic power penalty.

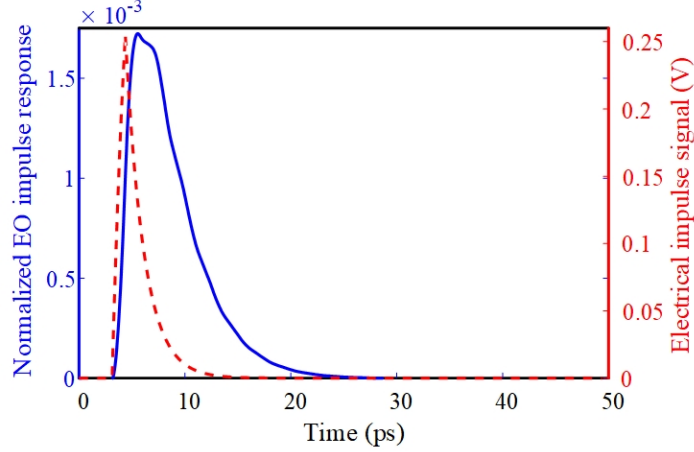


Figure 2.18 – Normalized EO impulse response.

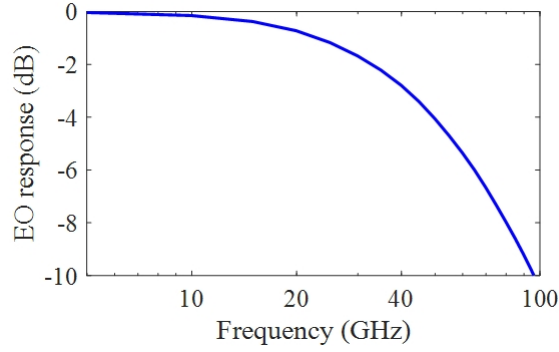


Figure 2.19 – Small-signal EO response of BGR-MZM.

2.5 Characterization of MZM assisted by Bragg grating resonators

Based on the modeling discussed in the previous sections, we now present experimental results of the MZM assisted by Bragg grating resonators. In the following section, we discuss the modulator structure and design. Then, we report the modulator performance considering modulation efficiency, loss, EO bandwidth, optical bandwidth (or modulation stability). Finally, we present the large-signal performance of the modulator through evaluating Bit error rate at different modulation speeds for a wide range of operating wavelengths.

2.5.1 Design and modulator structure

Figure 2.21 (a) shows the modulator schematic. In section 2.3, we discussed how to engineer the IBGR slow-light effect, taking into account the tradeoff between efficiency and stability. The key idea is to ensure that the resonance optical bandwidth remains large by employing cavities with a low-quality factor. The required phase modulation is then obtained by cascading such resonators. The modulator offers a compact footprint and low power consumption (similar to MRM). It also presents

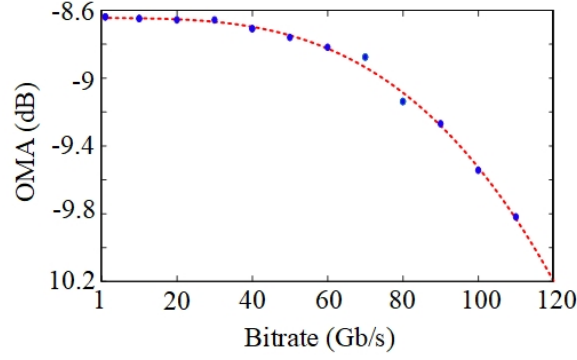


Figure 2.20 – OMA as a function of bitrate.

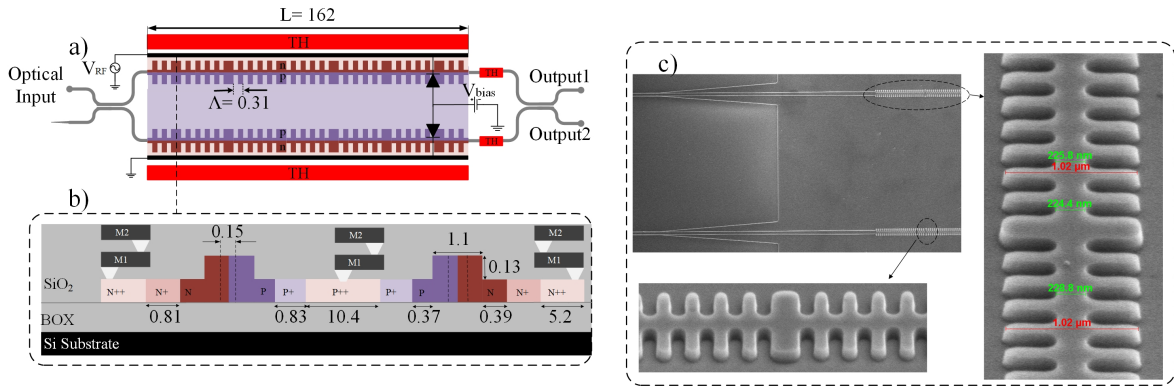


Figure 2.21 – a) Modulator schematic, b) modulator cross-section, c) SEM picture of the two arms with their resonators. (Dimensions in a) and b) are in μm).

a stable operation and a high EO bandwidth (similar to conventional MZM), achieving a balance in the performance. An IBGR, with a uniform period of $\Lambda = 300 \text{ nm}$ and six-coupled resonators, is placed in each arm of the MZM. Each resonator consists of a phase-shifted section with 45 grating periods on each side. The Bragg gratings consist of sidewall corrugations with a duty cycle of 50% in a ridge waveguide having an average width of 625 nm, a ridge height of 220 nm and a slab height of 90 nm. The maximum and minimum widths are 1100 nm and 150 nm, respectively. Such ultra-large corrugations allow us to keep the number of grating periods low, resulting in a short phase shifter length. Fig. 2.21 (b) shows the symmetric lateral p-n junctions and the three doping levels used to minimize optical loss and keep the resistance low.

Because of fabrication imperfections, four thermal elements are included in the design to adjust the modulator. We placed two thermal elements on top of the integrated Bragg grating resonators (IBGRs) to match their stopbands. In each arm, we also put a thermal element to bias the modulator at the quadrature point. Also, we placed an on-chip 50Ω load between RF pads for impedance matching. The modulator was fabricated in a multi-project wafer run using a standard 193-nm lithography process at the IME (AMF) A*STAR with a silicon layer thickness of 220 nm and a $2 \mu\text{m}$ buried oxide. Fig. 2.21 (c) shows SEM pictures of parts of the fabricated modulator.

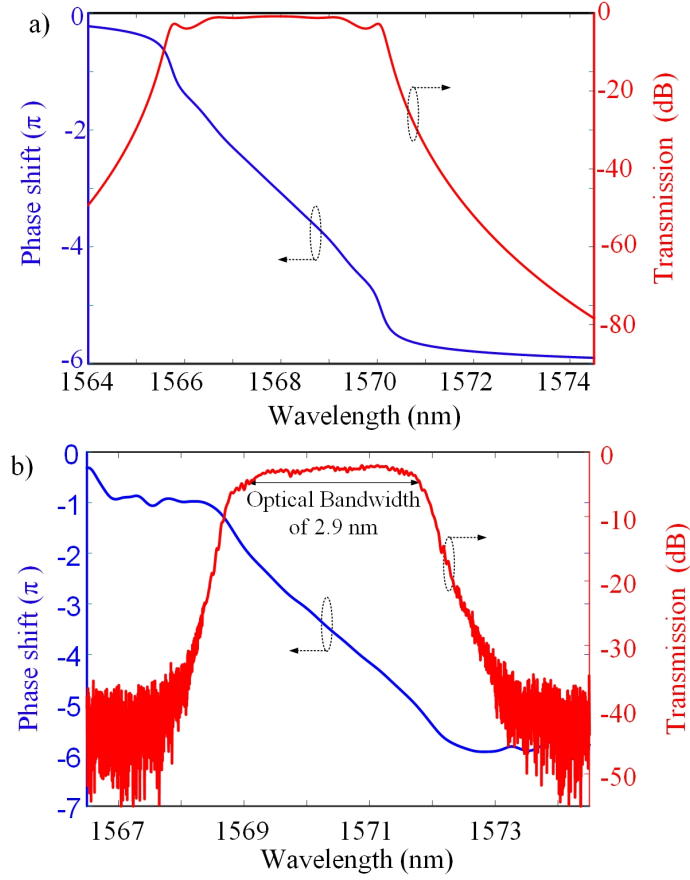


Figure 2.22 – a) Simulated transmission amplitude and phase responses of the IBGR b) Transmission amplitude and phase responses of the IBGR measured with a LUNA OVA.

2.5.2 Transmission spectrum

Figure 2.22 (a) illustrates the simulated transmission amplitude and phase of the IBGR close to the resonant peak. The simulated resonant peak has a bandwidth of 4 nm; however, the measured spectrum (in Fig. 2.22 (b)) shows only a 2.9 nm bandwidth. This difference can be explained by fabrication errors that result in the resonators of the IBG structure not being perfectly matched, *i.e.*, not having the exact same central wavelength. The MZI response also shows that the quadrature point at $\lambda_0 = 1570$ nm is obtained by applying a voltage of 1.9 V to the heater of the bottom arm. The extinction ratio (ER) of the MZI structure is 28 dB.

2.5.3 Modulation Efficiency

The phase-shifted IBGs are operated in transmission as phase modulators, and therefore they must be placed into a MZI to produce amplitude modulation. Assuming ideal directional couplers, the MZI output is given by Eq. 2.10. The modulation efficiency can be evaluated by the typical figure of merit ($V_\pi \times L$) and the required energy per bit.

The on-chip $50\text{-}\Omega$ termination does not allow us to measure the large-signal V_π . That is because, when applying DC voltages to RF pads, the DC current passing through the termination causes a change in the temperature of the chip, resulting in an unwanted shift in the optical spectrum. Therefore, to avoid heating caused by large-signal $V_\pi \times L$, we provide an estimation of V_π by applying a small signal at a low frequency; and we assume that the variation of phase as a function of voltage is linear around the bias point. Using this approach, the modulator records a small-signal $V_\pi \times L$ of 0.18 V.cm . For the purpose of comparison, we perform a similar measurement on a conventional MZM that has been fabricated with the same manufacturing process. Note that the p-n junctions of both modulators are identical. The conventional MZM is characterized by a small-signal $V_\pi \times L$ of 1.27 V.cm . This shows that the IBGR structure provides an enhancement factor of $\gamma = 7$, or, in other words, this means that the length of its phase shifters can be seven times shorter to obtain the same phase shift.

In order to compare our structure with the other Bragg-grating-based MZMs [25] and [26], we refer to delay-bandwidth product (or γ -bandwidth product). Note that a larger enhancement factor means a larger delay. Reference [25] reported a γ -bandwidth product of 2.6 nm (enhancement factor of 2 and optical bandwidth of 1.3 nm); also reference [26] demonstrated two γ -bandwidth products of 12 nm (enhancement factor of 3 and optical bandwidth of 4 nm) and 4.8 nm (enhancement factor of 6 and optical bandwidth of 0.6 nm). Our modulator provides the enhancement factor of 7 while the optical bandwidth is 2.9 nm , recording a γ -bandwidth product of 20.3 nm . Furthermore, our modulator has much more compact footprint ($L = 162\text{ }\mu\text{m}$) compared to references [25] ($L = 500\text{ }\mu\text{m}$), and [26] ($L = 2000\text{ }\mu\text{m}$).

The energy consumption per bit of the modulator for the OOK modulation format is calculated by $E_b = CV_{pp}^2/4$. The p-n junction model illustrated in 2.17 shows that the capacitance of the p-n junctions at the reverse bias (V_{bias}) of 1.5 V is 1.7 pF/cm [125]. Considering a $162\text{ }\mu\text{m}$ phase shifter length, the total capacitance is 27.5 fF . As a result, the estimated power consumption is 84 fJ/bit .

2.5.4 Loss

The total on-chip loss is 22.5 dB , of which 17 dB comes from the un-optimized grating couplers and fiber arrays, 1 dB from the two 3-dB adiabatic couplers, 2.5 dB propagation loss from 1 cm -long routing waveguide, and 2 dB from the modulator (*i.e.*, propagation loss of 123 dB/cm for IBGRs).

2.5.5 EO Bandwidth

Figure 2.23 shows EO bandwidth of the modulator at V_{bias} of -1 V measured with the PNA Microwave Network Analyzer (Agilent N5227A $10\text{ MHz} - 67\text{ GHz}$). The 3-dB bandwidth is about 28 GHz for different operational wavelengths. The EO bandwidth is usually described by considering the photon lifetime of the IBGR, $f_\tau = 1/(2\pi\tau)$, and the RC time constant of the p-n junction, $f_{RC} = 1/(2\pi RC)$. The 3-dB EO bandwidth of the modulator is therefore calculated using Eq. 2.25. The RC time constant of the modulator modeled in Fig. 2.17 is equal to 2.8 ps for V_{bias} of -1 V , resulting in cut-off frequency

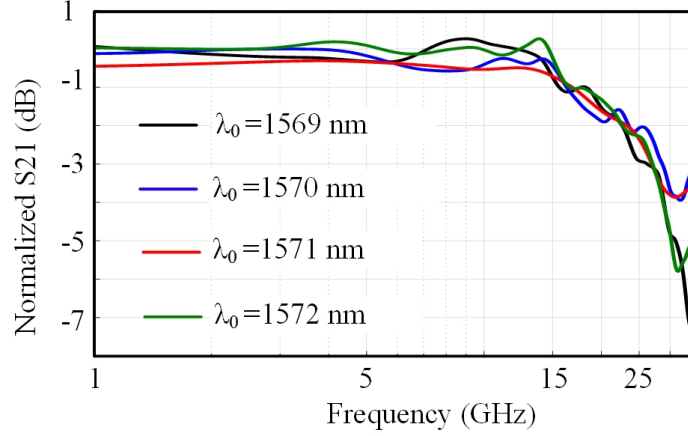


Figure 2.23 – Measured EO scattering parameter S21 for different operational wavelengths at a reverse bias of 1V.

of $f_{RC} = 55$ GHz. From the measured EO bandwidth and the calculated f_{RC} , we estimate f_{τ} of 32.5 GHz, which corresponds to a photon lifetime (τ) of approximately 5 ps. Fig. 2.23 also shows that the small-signal bandwidth of the modulator is similar over a wavelength range of 3 nm, which should reduce the modulator sensitivity to the temperature variations compared to usual RBMs.

2.5.6 Optical modulation amplitude (OMA) and modulator stability

To evaluate the quality of the modulated signal, we measured the OMA of the modulator. The OMA is computed using $OMA = P_1 - P_0$, where P_1 and P_0 are output powers corresponding to bit “1” and bit “0”, respectively. Fig. 2.24 displays the OMA spectra for different bitrates measured on a commercial optical receiver (SHF 41211 C) that has an internal RF amplifier. Fig. 2.24 shows that the modulator exhibits good performance in terms of OMA over a wavelength range of 3.5 nm. Considering a typical resonant shift of 80 pm/°C [21], the operating temperature range of the modulator is estimated to be larger than 40 °C. Compared to single-resonator modulators such as MRM, the requirement on the thermal control is significantly relaxed, leading to reduced cost and control-circuit complexity.

2.5.7 Large-signal performance

The modulator performance was evaluated with an OOK modulation format using the setup shown in Fig. 2.25. We first generate a pseudo-random bit sequence with a length of $2^{31}-1$ using a bit pattern generator (BPG) (SHF 12103 A). Next, the signal is amplified by a 30 GHz bandwidth RF amplifier (SHF 807), resulting in a peak-to-peak modulation voltage of 3.5 V on each arm of the modulator.

The input laser signal, with a power of 15 dBm goes through a polarization controller (PC) to improve fiber-to-chip coupling in the fundamental TE mode. After modulation, the signal is amplified by two stages of erbium-doped fiber amplifier (EDFA) and tunable optical bandpass filter (TOBP). An

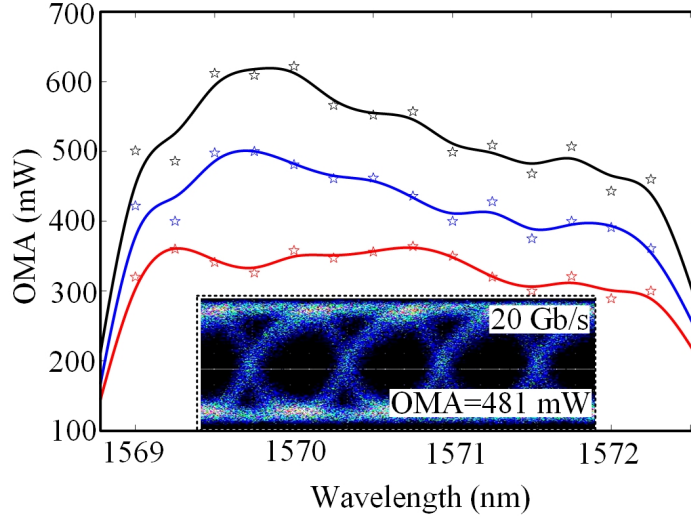


Figure 2.24 – OMA spectra measured for bitrates of 10 Gb/s (black curve), 20 Gb/s (blue curve), and 30 Gb/s (red curve) at a V_{bias} of -1.5 V. Symbols are experimental measurements, the curves are guides for the eye. The inset is the eye diagram for a bitrate of 20 Gb/s.

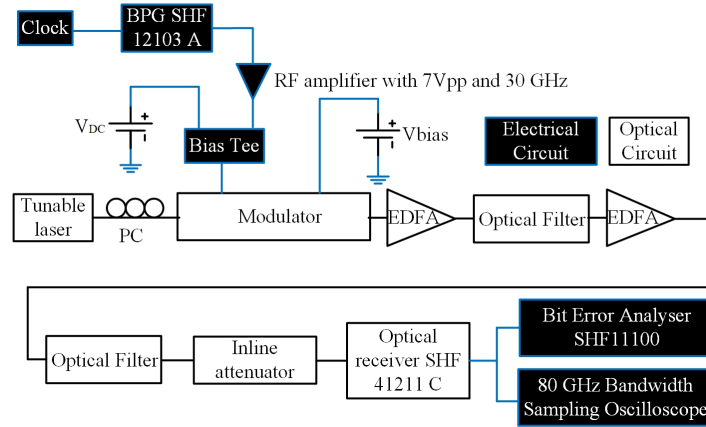


Figure 2.25 – Setup used to measure OMA, BER, and eye diagram.

inline attenuator controls the signal power at the optical receiver (SHF 41211 - 32 GHz). We use an 80 GHz bandwidth sampling oscilloscope and a bit-error-rate analyzer (SHF 11100 B) to respectively capture the eye-diagrams and measure the BER. Note that all of the results are obtained without digital signal processing (DSP).

The inset of Fig. 2.24 shows the eye diagram of the modulated signal at 20 Gb/s. BER curves, measured as a function of the received power at λ_0 of 1570 nm and V_{bias} of -1.5 V, are shown in Fig. 2.26. Assuming a 7% FEC threshold, the modulator provides error-free operation up to 30 Gb/s. Fig. 2.27 shows the measured BER as a function of wavelength for different modulation speeds, clearly showing that the modulator can be operated over a wavelength range of 3.5 nm with a BER below the 7% FEC threshold. This bandwidth should provide an operating temperature range $> 40^\circ\text{C}$ as

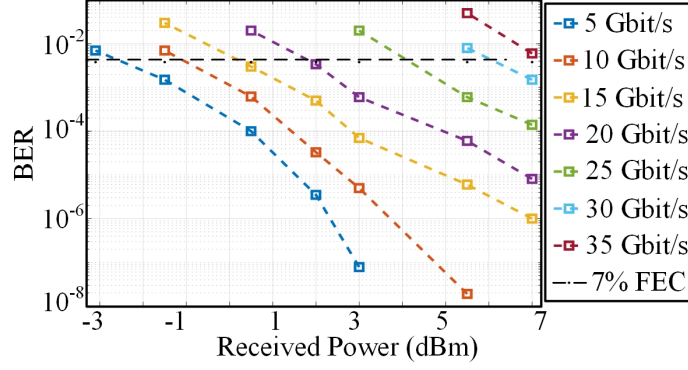


Figure 2.26 – BER as a function of the received power for different bitrates. Results are measured at V_{bias} of -1.5 V and λ_0 of 1570 nm.

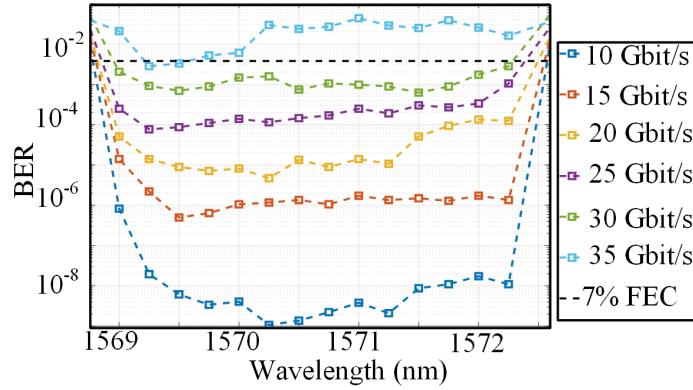


Figure 2.27 – BER vs. wavelength for different bitrates at V_{bias} of -1.5 V.

previously discussed.

2.6 Conclusion

We proposed a novel SiP modulator design based on a resonant structure with coupled cavities that uses the slow-light effect to improve the modulation efficiency and the operating temperature range simultaneously. The key idea is to use an IBG structure operated in transmission as a phase modulator. When inserted in a MZI structure, the resonance enhancement of the phase modulation allows a reduction of the phase shifter length, which improves efficiency in comparison to conventional MZM. Also, the cavities are designed with a low-quality factor to widen the optical bandwidth and significantly increase the tolerance to thermal variations (up to $\Delta T = \pm 25$ K) when compared to modulators based on the use of micro rings. Despite cascading many resonators, the modulator size is remarkably compact due to the use of Bragg gratings with a large photonic band gap. By solving the time-dependent coupled mode equations, we numerically investigated the dynamics of this modulator that exhibits an EO 3-dB cutoff frequency of 41 GHz for the specific design considered.

Furthermore, we experimentally demonstrated this modulator: an MZM assisted by coupled resonators in an IBG structure. The modulator significantly improves modulation efficiency and footprint. The results are obtained using low-quality-factor resonators in order to have an operating range of several nanometers. The use of coupled resonators provides more degrees of freedom for optimization and leads to significant improvement over previous demonstrations. This modulator is thus characterized by a low power consumption (84 fJ/bit), an improved modulation efficiency (small-signal $V_\pi \times L = 0.18$ V.cm), and a compact footprint ($L = 162$ μm). The BER measurement shows that the modulator can be operated up to 30 Gb/s below the 7% FEC threshold and that it should be stable over a temperature range larger than $\Delta T > 40$ °C.

These results show the demonstrated modulator is promising for low-power, high-speed optical interconnects. The demonstrated modulator with cascaded resonator waveguides could also be adopted in other 1D photonic crystal structures with stronger dielectric corrugations to achieve a higher delay-bandwidth product and a smaller footprint, but these devices would face the challenge of implementation using UV lithography [129].

Chapter 3

Efficiency-speed tradeoff in slow-light silicon photonic modulators

Résumé- Le but de ce chapitre est double. Tout d'abord, nous discutons du compromis efficacité-vitesse dans les modulateurs photoniques au silicium (SiP) à lumière lente (SL). Pour cela, un modèle complet de la réponse électro-optique (EO) des modulateurs Mach-Zehnder à lumière lente (SL-MZM) et à électrodes localisées est présenté. La validité du modèle est vérifiée en le comparant à des expériences. Notre analyse montre que le ralentissement de l'onde optique permet d'améliorer l'efficacité en augmentant le temps d'interaction entre l'onde optique et la tension uniforme sur les électrodes localisées, mais au prix d'une limitation de la bande passante EO. Ensuite, nous étudions les SL-MZM avec des électrodes à ondes progressives (TW) dont l'interaction dynamique est prédite à l'aide d'un modèle de circuit distribué. Ayant été résolu par la méthode du domaine temporel à différence finie (FDTD), le modèle montre que les TW SL-MZM sont capables d'améliorer à la fois l'efficacité et la vitesse lorsque l'effet SL est optimisé. Nous comparons également les SL-MZM avec les MZM conventionnels (C-MZM) en considérant une valeur de mérite (FOM) qui combine des paramètres clés tels que l'efficacité, les pertes et la bande passante EO. Nous montrons que la perte supplémentaire des guides d'ondes SL a un impact significatif sur le choix du type de modulation préféré à différentes vitesses de transmission. Le deuxième objectif de ce chapitre est d'examiner différentes stratégies de conception pour réduire le V_{π} des C-MZM pour répondre aux exigences du pilote CMOS en utilisant 1) un déphaseur plus long, 2) des densités de dopage plus élevées, et 3) l'effet SL. De ces trois stratégies, il a été démontré que l'effet SL offre les meilleures performances globales. En effet, seul l'effet SL offre une amélioration simultanée de V_{π} , de l'encombrement et de la bande passante EO ; les autres approches fournissent une réduction de V_{π} , mais au prix d'une vitesse réduite ou d'un encombrement plus important (voire des deux).

Abstract- The purpose of this chapter is twofold. First, we discuss the efficiency-speed tradeoff in slow-light (SL) silicon photonic (SiP) modulators. For this, a comprehensive model for the electro-optic (EO) response of lumped-electrode SL Mach-Zehnder modulators (SL-MZMs) is presented. The

model accuracy is verified by comparing it to experiments. Our analysis shows that slowing down the optical wave helps to enhance efficiency by increasing the interaction time between the optical wave and the uniform voltage across lumped electrodes, but at the cost of limiting the EO bandwidth. Then, we investigate SL-MZMs with traveling-wave (TW) electrodes whose dynamic interaction is predicted using a distributed circuit model. Having been solved by the finite-difference time-domain (FDTD) method, the model shows that TW SL-MZMs are capable of improving both efficiency and speed under an optimized SL effect. We also compare SL-MZMs with conventional MZMs (C-MZM) considering a figure of merit (FOM) that combines key parameters such as efficiency, loss, and EO bandwidth. We show that the additional loss of SL waveguides significantly impacts the preferred modulator choice at different baudrates. The second aim of this chapter is to examine different design strategies to reduce V_π of C-MZMs in order to meet the requirement of CMOS driver using 1) a longer phase shifter, 2) higher doping densities, and 3) the SL effect. It is shown that the SL effect provides the best overall performance among the three. Indeed, only the SL effect offers simultaneous improvement in V_π , footprint, and EO bandwidth; the other approaches provide V_π reduction but at the cost of reduced speed or enlarged footprint (or even both).

3.1 Introduction

Silicon modulators are one of the key components needed to provide cost-effective and energy-efficient photonic integration of optical transceivers. Tremendous efforts have recently been dedicated to improving the performance of SiP modulators. Notwithstanding, three fundamental trade-offs still exist between: efficiency-stability, efficiency-speed, and efficiency-loss. The efficiency of modulators is described by either their V_π or power consumption in energy per bit.

Among SiP modulators, MZMs loaded with TW electrodes are preferred devices in commercial optical systems because of their stability and high-speed operation. However, they are generally energy-hungry and have a large footprint. In contrast, resonator-based modulators, for example, micro-ring modulators (MRMs), offer a highly efficient operation with energy consumption of only a few femtojoule per bit and a compact footprint. However, MRMs are unstable and sensitive to the operational wavelength. Moreover, their speed is limited by the photon lifetime of their cavities.

SL-MZMs recently demonstrated outstanding potential to improve SiP modulator efficiency and stability, simultaneously. Indeed, slowing down the optical waves can enable significant modulation enhancement over a large optical bandwidth while offering an operating condition insensitive to temperature fluctuations. For instance, using 2-D photonic crystal waveguides loaded into an MZM, Ref. [74] reports a group index of about 10 over the whole C-band with a phase shifter length of 200 μm . In Ref. [23], micro-ring resonators are used to slow down optical waves inside an MZM and the authors report an operating temperature range of 54 $^\circ\text{C}$ with a compact phase shifter length of 110 μm and an enhancement factor of $\gamma = 8$. Here, the enhancement factor is defined as $\gamma = n_{g,SL}/n_g$, where $n_{g,SL}$ and $n_g \simeq 3.8$ are the group indices of SL waveguides and simple waveguides, respectively. In Ref. [25], an MZM based on 1-D photonic crystal (Bragg grating) waveguides was proposed. This modulator is characterized by a group index of 8 over an optical bandwidth of 1.3 nm with a footprint length of 500 μm . In chapter 2, we also demonstrated an MZM assisted by Bragg grating resonators which achieved $\gamma = 7$ over an optical bandwidth of 3.5 nm (equivalent to an operating temperature range of 40 $^\circ\text{C}$) with a phase shifter length of 162 μm .

Although SL-MZMs are capable of enhancing both efficiency and stability, their operating speed is typically limited. Conventional SiP modulators (such as MRMs and MZMs) are characterized by an efficiency-speed tradeoff: modulation efficiency is enhanced either by increasing p-n junction capacitance or photon lifetime at the cost of compromised EO bandwidth. In the case of SL-MZMs, because of their short phase shifter, they are typically implemented with lumped electrodes and their speed is restricted not only by the RC time constant but also by the interaction time between the optical signal and the uniform voltage along electrodes [130, 131]. This interaction time is increased by the low optical group velocity. The SL effect therefore imposes an intrinsic restriction on the modulator speed. Studies show that specially designed TW electrodes can mitigate this issue. For example, in Ref. [132], a SL-MZM combined with meander-line electrodes was proposed to compensate for the velocity mismatch between RF and optical waves.

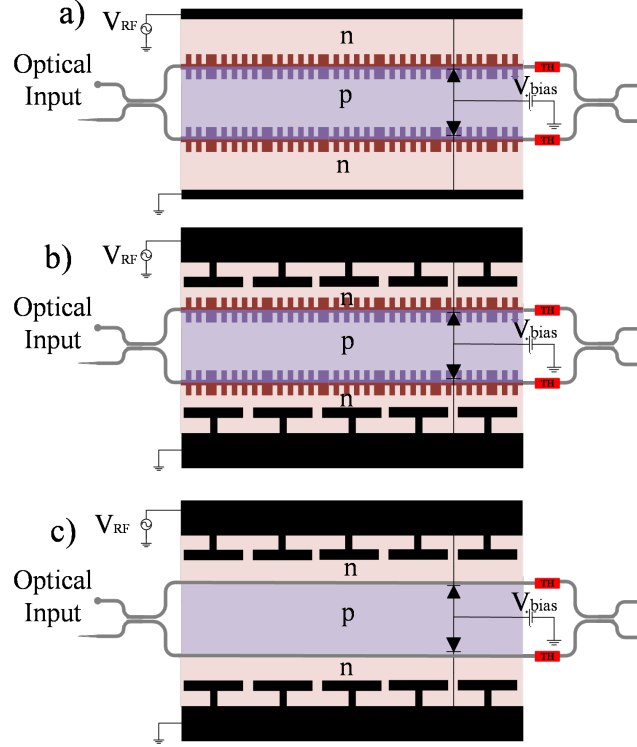


Figure 3.1 – Schematic of a SL-MZM based on Bragg grating resonators and a) lumped electrodes, and b) TW electrodes. A C-MZM with TW electrodes is shown in c).

In order to investigate the efficiency-speed tradeoff in SL-MZMs, a deeper understanding of the dynamic interaction between electrical and optical waves in SL-MZMs is required. Many efforts have been dedicated to modeling lumped-electrode modulators [130, 133–135], and TW MZMs [125, 136–138]; however, none of these previous models incorporated the SL effect. In this chapter, we present and experimentally validate a dynamic model for SL-MZMs combined either with lumped electrodes or with TW electrodes. Such a model is currently missing from the literature. We investigate the EO response of SL-MZMs in comparison to C-MZMs considering efficiency, loss, and EO bandwidth.

The rest of this chapter is organized as follows. In the next section, we first develop a model to predict the EO response of lumped-electrode SL-MZMs, as shown in Fig. 3.1 (a). We validate the model with experimental measurement. Thereafter, we expand the model for SL-MZMs to include TW electrodes as illustrated in Fig. 3.1 (b). The model is obtained by solving the coupled equations of TW electrodes using the FDTD method. Afterwards, we compare the three modulators: lumped-electrode SL-MZM, TW SL-MZM, and C-MZM shown in Fig. 3.1 (c). We consider the EO bandwidth and a FOM that combines performance indicators such as efficiency, loss, and EO bandwidth. Finally, we examine and discuss three design strategies to reduce V_π of MZMs: increasing the phase shifter length (IPSE), increasing doping density (IDD) of p-n junctions, and using the SL effect.

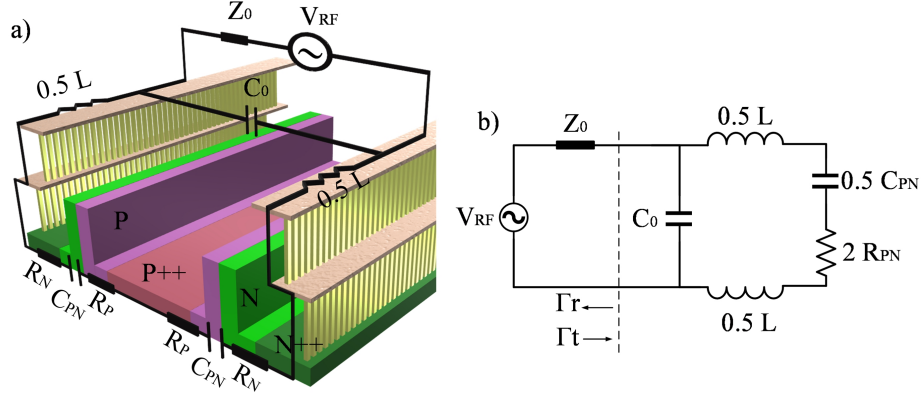


Figure 3.2 – a) Schematic of a single-drive push-pull MZM with lumped electrodes. b) Equivalent RF circuit model.

3.2 SL-MZMs with lumped electrodes

3.2.1 EO model

In this section, we develop a general model of the EO response of lumped-electrode SL-MZMs with analysis of both RF circuit and optical waveguide. The model can be employed for SL-MZMs based on different passive structures. Our case study is the lumped-electrode SL-MZM based on Bragg grating resonators (BGRs) (shown in Fig. 3.1 (a)).

RF analysis: An equivalent electrical circuit for a loaded transmission line (TML) is required to calculate the effective RF power applied on p-n junctions. Fig. 3.2 shows the cross-section of the modulator operated with the single-drive push-pull configuration, as well as its equivalent electrical circuit. The impedance mismatch between the TML and the RF source introduces a RF transmission coefficient (T_{TML}) as

$$T_{TML}(\omega) = \frac{2 \left[\left(j\omega L + 2R_{PN} + 2(j\omega C_{PN})^{-1} \right)^{-1} + j\omega C_0 \right]^{-1}}{\left[\left(j\omega L + 2R_{PN} + 2(j\omega C_{PN})^{-1} \right)^{-1} + j\omega C_0 \right]^{-1} + Z_0} \quad (3.1)$$

where C_{PN} and R_{PN} are capacitance and series resistance of a single p-n junction, respectively. L represents the electrode inductance. C_0 is the pad parasitic capacitance. The characteristic impedance of the source is represented by Z_0 . After that, the effective voltage (V_{eff}) on each p-n junction as a function of the source (V_{RF}) is calculated as

$$\begin{aligned} V_{eff}(\omega) &= \frac{1}{2} \frac{2/j\omega C_{PN}}{j\omega L + 2R_{PN} + 2/j\omega C_{PN}} T_{TML}(\omega) V_{RF}(\omega) \\ &= T_{Circuit}(\omega) T_{TML}(\omega) V_{RF}(\omega) \end{aligned} \quad (3.2)$$

Optical analysis: In this step, we derive an expression of the optical phase shift, produced by carrier depletion in the p-n junction, as a function of the effective voltage. The changes in the effective index

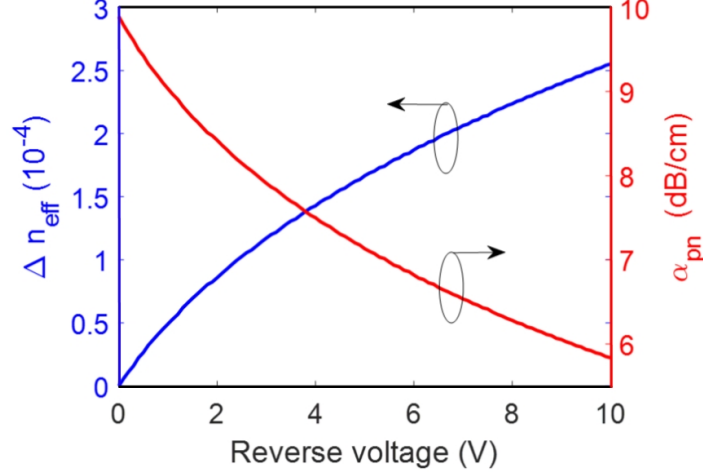


Figure 3.3 – The changes in the refractive index and the p-n junction absorption loss as a function of reverse voltage for a simple waveguide.

and the absorption loss due to the applied voltage is given as

$$\Delta n_{eff}(V(\omega)) = \frac{\iint_S E^*(x, y) \Delta n(x, y, V(\omega)) E(x, y) dx dy}{\iint_S E^*(x, y) E(x, y) dx dy} \quad (3.3)$$

$$\Delta \alpha_{eff}(V(\omega)) = \frac{\iint_S E^*(x, y) \Delta \alpha(x, y, V(\omega)) E(x, y) dx dy}{\iint_S E^*(x, y) E(x, y) dx dy} \quad (3.4)$$

where E is the mode electrical field, and Δn and $\Delta \alpha$ are described as

$$\Delta n(x, y, V) = -3.64 \times 10^{-10} \lambda^2 \Delta N_D(x, y, V) - 3.51 \times 10^{-10} \lambda^2 \Delta N_A^{0.8}(x, y, V) \quad (3.5)$$

$$\Delta \alpha(x, y, V) = 3.52 \times 10^{-6} \lambda^2 \Delta N_D(x, y, V) + 2.4 \times 10^{-6} \lambda^2 \Delta N_A(x, y, V) \quad (3.6)$$

where λ is the optical wavelength, and ΔN_A and ΔN_D are the carrier densities of holes and electrons, respectively. We simulate the electrical field for the fundamental optical waveguide mode in a rib waveguide using Lumerical-Mode. Afterward, we numerically compute the integrals in Eq. 3.3 using MatLab to calculate the changes in the refractive index as a function of the effective voltage, as shown in Fig. 3.3 (blue line) [21, 125].

For a given phase shift, SL-MZMs require shorter phase shifter length (L_{SL-MZM}) compared to conventional MZMs. Considering that, the partial derivative of the phase shift ($\delta \Delta \varphi$) is calculated along a very small length of the electrode (δL_{SL-MZM}) as

$$\delta \Delta \varphi(V(t)) = k_0 \times \Delta n(V(t)) \times \delta L_{SL-MZM} \quad (3.7)$$

where k_0 is equal to $2\pi/\lambda$. Considering that light speed is constant along the waveguide, δL_{SL-MZM} can be expressed as

$$\delta L_{SL-MZM} = \left(\frac{c}{\gamma n_g} \right) \times \delta t \quad (3.8)$$

where c is the light speed in free space. Finally, the total phase shift along the electrode is computed as

$$\Delta\varphi(V(t)) = k_0 \frac{c}{\gamma n_g} \int_{t-t_0}^t \Delta n_{eff}(V(t)) dt, \quad t_0 = \frac{\gamma n_g L_{SL-MZM}}{c} \quad (3.9)$$

Equation 3.9 gives the phase shift in the time domain that is rewritten and solved in the frequency domain as

$$\Delta\varphi(V(\omega)) = k_0 \frac{c}{\gamma n_g} \mathbf{F} [\Delta n_{eff}(V(t)) * u(t) - \Delta n_{eff}(V(t)) * u(t - t_0)] \quad (3.10)$$

$$\Delta\varphi(V(\omega)) = k_0 \frac{c}{\gamma n_g} \left[\Delta n_{eff}(V(\omega)) \times \left(\frac{1}{j\omega} + \pi\delta(\omega) \right) - \Delta n_{eff}(V(\omega)) \times \left(\frac{1}{j\omega} + \pi\delta(\omega) \right) \times e^{-j\omega t_0} \right] \quad (3.11)$$

$$\Delta\varphi(V(\omega)) = k_0 \frac{c}{\gamma n_g} (1 - e^{-j\omega t_0}) \times \left[\Delta n_{eff}(V(\omega)) \times \left(\frac{1}{j\omega} + \pi\delta(\omega) \right) \right] \quad (3.12)$$

Equation 3.12 represents a direct expression of the phase shift as a function of the refractive index change in the frequency domain.

The amplitude response of MZMs at the quadrature point is given as

$$|S_{21}(\omega)|^2 = \mathbf{F} \left[e^{-\alpha L_{SL-MZM}} \cos^2 \left(\frac{\Delta\varphi(V, t) - \pi/2}{2} \right) \right] \quad (3.13)$$

$$|S_{21}(\omega)|^2 = \mathbf{F} \left[\frac{e^{-\alpha L_{SL-MZM}}}{2} (1 + \cos(\Delta\varphi(V, t) - \pi/2)) \right] \quad (3.14)$$

$$|S_{21}(\omega)|^2 = \mathbf{F} \left[\frac{e^{-\alpha L_{SL-MZM}}}{2} (1 + \sin(\Delta\varphi(V, t))) \right] \quad (3.15)$$

By excluding the DC component, the frequency response, S_{21} , of SL-MZMs is derived as

$$|S_{21}(\omega)|^2 = \frac{e^{-\alpha L_{SL-MZM}}}{2} \mathbf{F} \{ \sin(\mathbf{F}^{-1}[\Delta\varphi(V, \omega)]) \} \quad (3.16)$$

where F and F^{-1} represent the Fourier- and inverse-Fourier transform, respectively, and α is the attenuation coefficient.

3.2.2 Model validation

The parameters of the lumped electrode, such as C_0 , R_{PN} , C_{PN} , L , can be estimated using the measured S_{11} that is an all-electrical process. Indeed, these parameters can be extracted with curve fitting of the measured S_{11} and the back reflection formula of the TML, which is equal to $R_{TML} = T_{TML} - 1$. In addition to that, there are numerical models to estimate their values. Under the reverse-bias operation, the capacitance and the series resistance of a p-n junction have been modeled

in [125, 133], as shown in Fig. 2.17. The per-unit-length inductance of coplanar strip (CPS) is also approximated as [139],

$$L [H/m] = \begin{cases} \frac{120}{V_{RF}} \ln \left(2 \frac{1+\sqrt{K}}{1-\sqrt{K}} \right) & \frac{1}{\sqrt{2}} \leq K \leq 1 \\ \frac{120\pi^2}{V_{RF} \ln \left[\frac{2(1+\sqrt{K'})}{(1-\sqrt{K'})} \right]} & 0 \leq K \leq \frac{1}{\sqrt{2}} \end{cases} \quad (3.17)$$

$$K = \frac{s_{TML}}{s_{TML} + 2w_{TML}}, \quad K' = \sqrt{1 - K^2} \quad (3.18)$$

where s_{TML} and w_{TML} are the distance between two metals and the width of the metals in a CPS, respectively. Moreover, C_0 is estimated to be around 26 fF [134]. All parameters with their vales that have been used in the simulation of lumped-electrode SL-MZM are listed in Table 3.1.

Table 3.1 – A list of the parameters used in the simulation of lumped-electrode SL-MZM

Parameters	Notation	Values
Electrode inductance [nH]	L	0.167
Pad parasitic capacitance [fF]	C_0	26
Impedance characteristic of the source [Ω]	Z_0	50
p-n junction capacitance [pF/cm]	C_{PN}	Fig. 2.17
p-n junction resistance [Ω .cm]	R_{PN}	Fig. 2.17
Doping for n-dopants [cm^{-3}]	N_D	3×10^{17}
Doping for p-dopants [cm^{-3}]	N_A	5×10^{17}
Group index	ng	3.8
Loss per enhancement factor for SL-MZMs [dB/cm]	α_{SL-MZM}	17.5
Loss for the C-MZM [dB/cm]	α_{C-MZM}	12.3
Optical wavelength [nm]	λ	1550

We verify our model using measurement results of the MZM assisted by BGRs reported in section 2.5.5. The modulator demonstrates an enhancement factor of $\gamma = 7$ over an optical bandwidth of about $\Delta\lambda_{BW} = 3.5$ nm with a phase shifter length of $L_{SL-MZM} = 162$ μm . The colored dashed lines in Fig. 3.4 show the measured S21 for different operational wavelengths with 3-dB bandwidths close to 28 GHz at a reverse bias of 1 V. The solid black line in Fig. 3.4 illustrates the EO response of the SL-MZM predicted by our model, showing a good agreement with the measurement. We also perform a large-signal analysis and plot the optical eye diagram in Fig. 3.5 (a). These simulations considered a peak-to-peak voltage of 3.5 V on each arm, a reverse bias voltage of 1.5 V, an operational wavelength of 1570 nm, and a modulation speed of 20 Gb/s. Comparing it with Fig. 3.5 (b), the model provides a satisfactory estimation of the measured eye diagram reported in section 2.5.7.

3.2.3 EO bandwidth of SL modulators with lumped electrodes

After obtaining a reliable model, we perform an analysis to understand the impact of the enhancement factor and the bias voltage on the EO bandwidth of lumped-electrode SL-MZMs. Fig. 3.6 shows

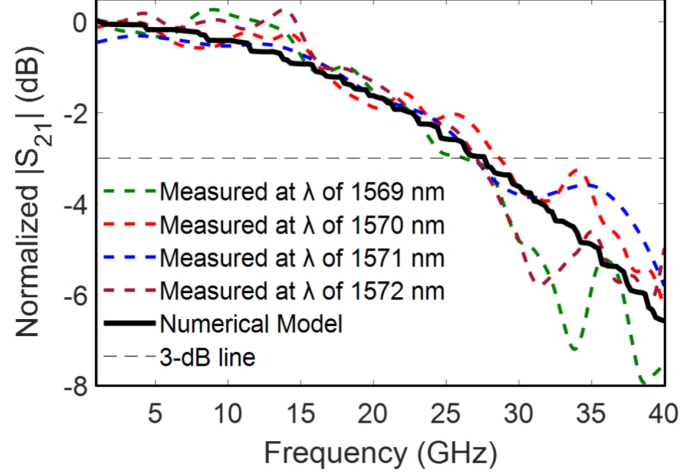


Figure 3.4 – Normalized S_{21} of SL-MZM with lumped electrodes ($\gamma = 7$, $V_{bias} = -1$ V and $L_{SL-MZM} = 162 \mu\text{m}$). Dash-colored lines are measurement results for different operational wavelengths. The solid black line is the EO response predicted by the model.

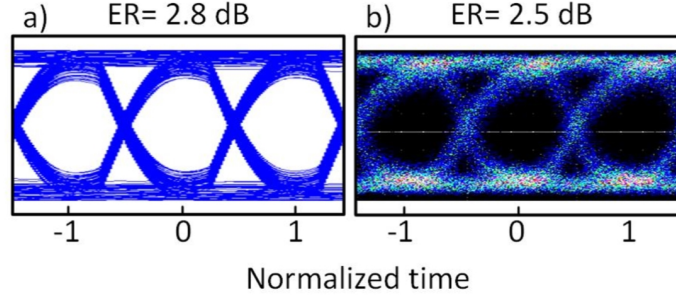


Figure 3.5 – Eye diagram of SL-MZM with lumped electrodes at 20 Gb/s a) simulation b) measurement with $V_{pp} = 3.5$ V on each arm, $V_{bias} = 1.5$ V and $\lambda_0 = 1570$ nm.

the EO bandwidth of SL-MZMs with a phase shifter length of $L_{SL-MZM} = 162 \mu\text{m}$ as a function of the reverse bias (V_{bias}) for different enhancement factors. As expected, the EO bandwidth increases as V_{bias} becomes larger; however, the increase is inversely related to the enhancement factor. In other words, as V_{bias} changes from 0 V to -20 V, the increase for $\gamma = 3$ is 33 GHz, whereas it is 3.1 GHz for $\gamma = 13$. Indeed, if a strong SL effect is exploited, the EO bandwidth saturates as it becomes limited by the interaction time. It is also seen that for larger enhancement factors, the EO bandwidth saturates at lower V_{bias} ; *i.e.*, the saturation voltage is 10 V for $\gamma = 7$, whereas it is 6 V for $\gamma = 10$.

3.2.4 Comparing SL-MZMs to C-MZMs

We compare the performance of SL-MZMs with lumped electrodes to a C-MZM with TW electrodes, by considering the EO bandwidth as well as a FOM introduced in [140]. In Ref. [61], an MZMs with TW electrodes was designed and demonstrated for operation above 400 Gb/s. This modulator is characterized by a $V_{\pi} \simeq 7$ V, a phase shifter length of $L_{C-MZM} = 4.8$ mm, and an insertion loss of 12.3 dB/cm, including the propagation loss (2.5 dB/cm) and the absorption loss (9.8 dB/cm). Utilizing

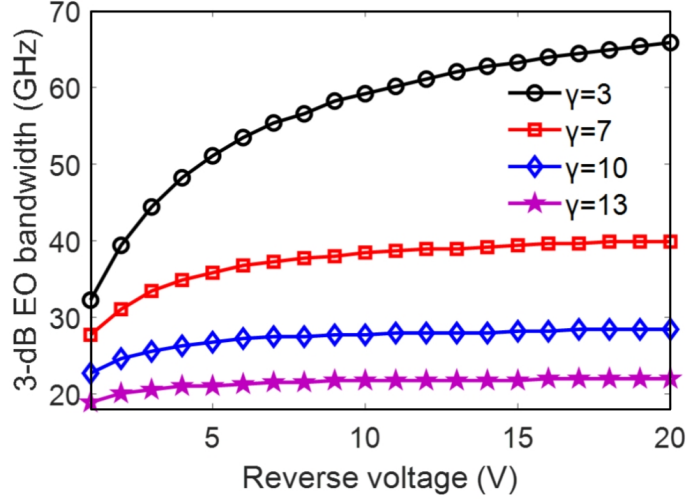


Figure 3.6 – The EO bandwidth as a function of reverse voltage for different enhancement factors and $L_{SL-MZM} = 162 \mu\text{m}$.

the time-domain model reported in [125], we estimate this MZM EO bandwidth as 15.8 GHz at V_{bias} of -1 V. We choose this modulator as a reference in our analysis.

SL-MZMs are typically characterized by high insertion loss of more than 100 dB/cm, which is caused by the highly structured passive SL waveguides that generate loss through sidewall roughness and lithographic inaccuracies. This loss typically scales with group index. We reported an insertion loss of 123 dB/cm for our MZM assisted by BGRs with $\gamma = 7$ in section 2.5.4. In [141, 142], it is shown that the propagation loss in SL waveguides scales linearly with γ and, therefore, we assume in our assessment that the proportionality factor is 17.5 dB/cm (*e.g.*, $\alpha_{SL-MZM} = 35$ dB/cm for $\gamma = 2$).

To make a fair comparison, we consider an operating condition under which both modulators (SL-MZMs and the C-MZM) possess similar V_π . To this end, the phase-shifter length of the C-MZM must be equal to the length of SL-MZMs multiplied by the enhancement factor, as expressed in Eq. 3.19 or, in the following analysis, $L_{C-MZM} = 4.8$ mm and $L_{SL-MZM} = 4.8/\gamma$ mm. Also, note that we set $V_{bias} = -1$ V for all calculations.

$$L_{C-MZM} = L_{SL-MZM} \times \gamma \quad (3.19)$$

EO bandwidth

The calculated EO bandwidth of the SL-MZMs with lumped electrodes and the C-MZM with TW electrodes, under the condition of Eq. 3.19, are shown in Fig. 3.7. As mentioned previously, the EO bandwidth of the C-MZM is 15.8 GHz, while the “SL-MZM” with lumped electrode and no SL effect ($\gamma = 1$ and $L_{SL-MZM} = 4.8$ mm) provides only a 6 GHz bandwidth. When slowing down the light ($\gamma > 1$), the EO bandwidth first improves and then saturates. Up to $\gamma = 5$ ($L_{SL-MZM} = 960 \mu\text{m}$), the EO bandwidth is increased to 9 GHz and, thereafter, it remains almost unchanged. Indeed,

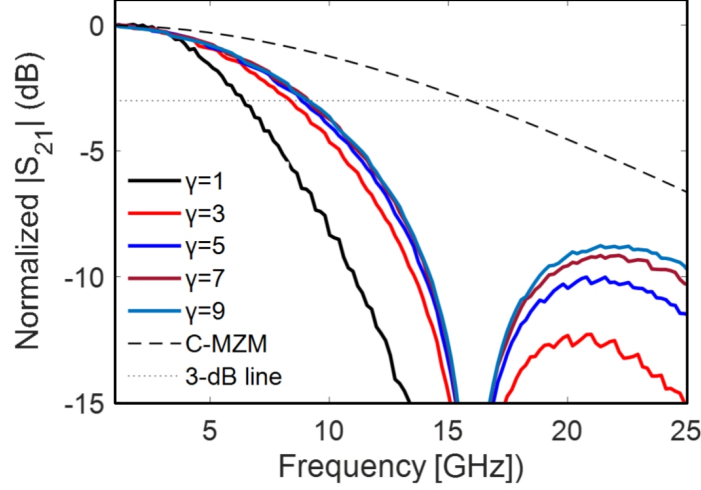


Figure 3.7 – Normalized S21 for SL-MZMs with lumped electrodes and the C-MZM. $L_{C-MZM} = 4.8$ mm, $L_{SL-MZM} = 4.8/\gamma$ mm, and $V_{bias} = -1$ V.

larger enhancement factors ($\gamma \geq 5$) allow a reduction in the phase shifter length and, consequently, a decrease in the RC time constant; however, this comes at the cost of an increase in the interaction time. The reduction in the RC constant and the increase in the interaction time compensate each other, resulting in an EO bandwidth that remains fixed.

It is also observed in Fig. 3.7 that the C-MZM offers an EO response with a smooth roll-off, which is a key advantage to operate modulators at much larger baudrate than their EO bandwidth. In the present case, the 10-dB bandwidth is 33 GHz for the C-MZM, whereas it is only 14.5 GHz for SL-MZM with $\gamma = 9$ ($L_{SL-MZM} = 533 \mu\text{m}$). Note that the small fluctuation in the results in Fig. 3.7 comes from numerical errors associated with FFT and IFFT operations.

FOM

A SiP modulator FOM grouping efficiency, loss, and EO bandwidth was derived in [140]. A classical FOM is $FOM = V_\pi \times \alpha \times L_{PS}$, where L_{PS} is the phase shifter length. This FOM is derived considering the static transmission power penalty (TPP) generated by the modulation loss and the propagation loss. In addition to this static TPP, a dynamic TPP occurs due to intersymbol interference (ISI) resulting from the finite EO bandwidth. The impact of ISI is particularly important when modulators operate at baudrate exceeding their EO bandwidth. The classical aforementioned FOM does not take this into account. In Ref. [140], it was theoretically shown that the normalized optical modulation amplitude (OMA) is a more reliable means to represent the dynamic and static TPPs. From the definition of OMA, the authors add another term to the FOM, that is now as expressed as

$$FOM = V_\pi \alpha L_{PS} \frac{M - 1}{1 - \frac{M}{2} \cdot \exp\left(-4.43 \frac{BW_{EO}^2}{BR^2}\right)} \quad (3.20)$$

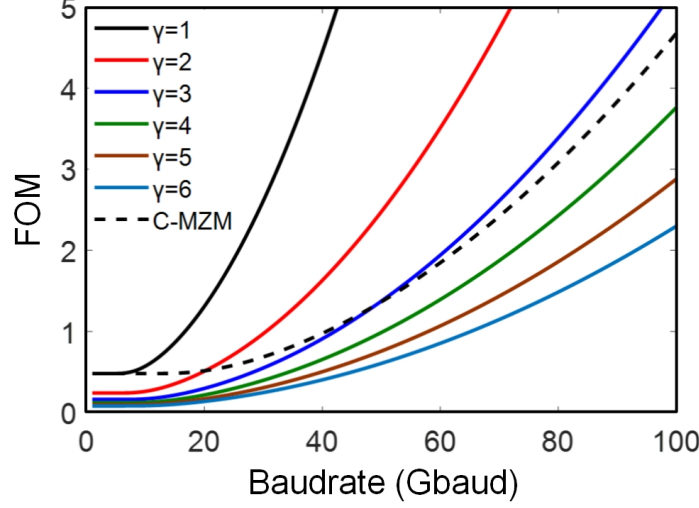


Figure 3.8 – FOM for OOK modulation format ($M = 2$), without considering loss ($\alpha = 1$ dB/cm for both cases), as a function of baudrate for lumped-electrode SL-MZMs and the C-MZM. $L_{C-MZM} = 4.8$ mm, $L_{SL-MZM} = 4.8/\gamma$ mm, and $V_{bias} = -1$ V.

where BW_{EO} is the EO bandwidth, BR the target baudrate, and M is the modulation level of the modulation format. For future discussion, note that smaller FOM indicates better performance.

We carry out our FOM analysis with and without loss in order to examine its impact on the performance of SL-MZMs. Fig. 3.8 illustrates the FOM for the C-MZM (dash line) and lumped-electrode SL-MZMs (solid lines) with different γ as a function of baudrate without including loss ($\alpha = 1$ dB/cm for both cases). As depicted, lumped-electrode SL-MZMs demonstrate superior performance if the light is slowed down enough ($\gamma \geq 4$). Indeed, larger enhancement factors ($\gamma \geq 4$) make phase shifter more compact ($L_{SL-MZM} \leq 1.2$ mm), which leads to a drastic reduction in the FOM's value. Including the excess loss due to the SL waveguide in the evaluation has an important impact in the lumped-electrode SL-MZMs FOM, as shown in Fig. 3.9 (*i.e.*, $\alpha_{C-MZM} = 12.5$ dB/cm for C-MZM and $\alpha_{SL-MZM} = 17.5 \times \gamma$ dB/cm). The SL-MZM no longer presents a better performance, even with strong SL effects. The two FOMs are diverging rapidly for baudrates > 20 Gbaud and, for example, at baudrate of 80 Gbaud, the FOM_{C-MZM} is 8.7, whereas the FOM_{SL-MZM} is 36 under with $\gamma = 9$ ($L_{SL-MZM} = 533$ μ m).

3.2.5 Discussion: lumped-electrode SL-MZMs vs. C-MZMs

The C-MZM offers a larger EO bandwidth than lumped-electrode SL-MZMs (under the condition of Eq. 3.19). Furthermore, the EO response of C-MZM is more suitable to push the operation to high baudrate due to its smooth frequency response roll-off. As a result, lumped-electrode SL-MZMs enhance efficiency but at the cost of reduced speed. These modulators therefore do not present a solution to the efficiency-speed tradeoff. One way to improve the performance of SL-MZMs is to optimize their passive structures and the fabrication processes to reduce the excess loss of SL

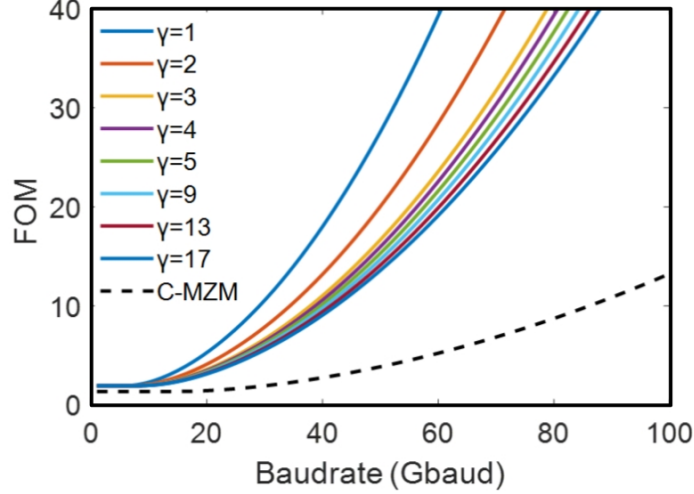


Figure 3.9 – FOM for OOK modulation format ($M = 2$), considering loss ($\alpha_{C-MZM} = 12.5$ dB/cm for C-MZM and $\alpha_{SL-MZM} = 17.5 \times \gamma$ dB/cm), as a function of baudrate for lumped-electrode SL-MZMs and the C-MZM. $L_{C-MZM} = 4.8$ mm, $L_{SL-MZM} = 4.8/\gamma$ mm, and $V_{bias} = -1$ V.

waveguides, which is out of the scope of this paper. Another way is to manipulate the electrodes in order to improve the EO bandwidth, which will be discussed in the following section.

3.3 SL-MZMs with TW electrodes

In this section, we investigate SL-MZMs with TW electrodes (Fig. 3.1 (b)) and examine whether TW electrodes enable SL-MZMs to address the efficiency-speed tradeoff and present an improved performance compared to C-MZMs.

3.3.1 Small signal model for TW SL-MZMs

In Ref. [125], a comprehensive time-domain model for C-MZMs with TW electrodes is reported. We now expand this model such that it also incorporates the SL effect. The model is based on coupled propagation equations of the forward and backward RF waves along the TML. The forward and backward RF waves along the TML whose the coupled equations are given as

$$\frac{\partial V_F(z,t)}{\partial z} + K_0 \frac{\partial V_F(z,t)}{\partial t} = -K_1 [V_F(z,t) + V_R(z,t) - V_j(z,t)] - K_2 V_{con}(z,t) - K_3 \frac{\partial V_R(z,t)}{\partial z} \quad (3.21)$$

$$\frac{\partial V_R(z,t)}{\partial z} - K_0 \frac{\partial V_R(z,t)}{\partial t} = K_1 [V_F(z,t) + V_R(z,t) - V_j(z,t)] - K_2 V_{con}(z,t) - K_3 \frac{\partial V_F(z,t)}{\partial z} \quad (3.22)$$

where V_F and V_R are the forward and the backward voltages, respectively, and the other terms are described as

$$K_0 = \frac{1}{2} \left[Z_{unload} C_U + \frac{L_U}{Z_{unload}} \right], K_1 = \frac{Z_{unload}}{2R_{PN}}, K_2 = \frac{1}{2}, K_3 = \left[Z_{unload} C_U - \frac{L_U}{Z_{unload}} \right] \approx 0 \quad (3.23)$$

$$V_j(z, t) = V_F(z, t) + V_R(z, t) - R_{PN}C_{PN} \frac{\partial V_j(z, t)}{\partial t} \quad (3.24)$$

$$V_{con}(z, t) = Z_{con}(t) * \left[\frac{V_R(z, t) - V_F(z, t)}{Z_{unload}} \right] \quad (3.25)$$

where Z_{unload} , C_U , and L_U represent the characteristic impedance, capacitance, and inductance of the unloaded TML, respectively. $Z_{con}(t)$ is the inverse Fourier transform of $Z_{con}(f)$ that represents the frequency-dependent conductor impedance [125, 137]. Using the first-order difference approximation, Eq. 3.21, Eq. 3.22, and Eq. 3.24 are rewritten as

$$\begin{aligned} \frac{V_F(z+1, t) - V_F(z, t)}{\Delta z_{RF}} + K_0 \frac{V_F(z, t+1) - V_F(z, t)}{\Delta t} = \\ -K_1 [V_F(z, t) + V_R(z, t) - V_j(z, t)] - K_2 V_{con}(z, t) \end{aligned} \quad (3.26)$$

$$\begin{aligned} \frac{V_R(z+1, t) - V_R(z, t)}{\Delta z_{RF}} - K_0 \frac{V_R(z, t+1) - V_R(z, t)}{\Delta t} = \\ K_1 [V_F(z, t) + V_R(z, t) - V_j(z, t)] - K_2 V_{con}(z, t) \end{aligned} \quad (3.27)$$

$$V_j(z, t+1) = \frac{V_F(z, t) + V_R(z, t)}{\Delta t + R_{PN}C_{PN}} + \frac{R_{PN}C_{PN}}{\Delta t + R_{PN}C_{PN}} V_j(z, t) \quad (3.28)$$

where Δz_{RF} and Δt are the RF mesh size and the time step, respectively. Also, the optical field is numerically described as [125, 143]

$$\begin{aligned} E_F(z, t) = \exp \{ [-\Delta\alpha(z - \Delta z_{Opt}, t - \Delta t)/2 \\ - i\Delta\beta(z - \Delta z_{Opt}, t - \Delta t)] \Delta z_{Opt} \} E_F(z - \Delta z_{Opt}, t - \Delta t) \end{aligned} \quad (3.29)$$

where $\Delta\alpha$ and $\Delta\beta$ represent the changes in the attenuation coefficient (shown in Fig. 3.3 with a red line) and the propagation constant because of the applying voltage, respectively. Δz_{Opt} is the optical mesh size and is equal to $\Delta z_{Opt} = V_{g,SL} \times \Delta t$, where $V_{g,SL} = c/\gamma/n_g$ is the optical group velocity in the SL waveguide. In order to consider the velocity mismatch in the simulation, the following conditions between optical mesh size, RF mesh size, and time step should be satisfied.

$$\Delta z_{RF} = \frac{n_g \gamma}{n_{RF}} \Delta z_{Opt}, \quad \Delta t = \frac{n_g \gamma}{C} \Delta z_{Opt} \quad (3.30)$$

where n_{RF} is the RF index, which is equal to around 2.7 for T-shaped-extensions TW electrodes [62].

Figure 3.10 shows the EO response of a TW SL-MZM with a fixed phase shifter length of 1 mm for different enhancement factors. As can be seen, the TW MZM with no SL effect ($\gamma = 1$) provides an EO bandwidth of about 40 GHz, while the TW SL-MZM with $\gamma = 5$ presents a bandwidth of around 20 GHz. This reduction in the EO bandwidth comes from the increased velocity mismatch between the electrical and optical signals when the light is slowed down. All parameters with their values that have been used in the simulation of TW SL-MZM are listed in Table 3.2.

3.3.2 Comparing TW SL-MZMs with C-MZMs

In this section, similarly to the section 3.2.4, we compare a TW SL-MZM to the C-MZM considering the EO bandwidth and the FOM. As was done previously, the respective lengths of the MZM structures are chosen in accordance to Eq. 3.19.

Table 3.2 – A list of the parameters used in the simulation of TW SL-MZM

Parameters	Notation	Values
Impedance characteristic of the source [Ω]	Z_0	50
Characteristic impedance of the unloaded TML [Ω]	Z_{unload}	50
Capacitance of the TW electrode [pF/cm]	C_U	1.30
Inductance of the TW electrode [nH/cm]	L_U	6.33
p-n junction capacitance [pF/cm]	C_{PN}	Fig. 2.17
p-n junction resistance [Ω .cm]	R_{PN}	Fig. 2.17
Doping for n-dopants [cm^{-3}]	N_D	3×10^{17}
Doping for p-dopants [cm^{-3}]	N_A	5×10^{17}
Group index	ng	3.8
Loss per enhancement factor for SL-MZMs [dB/cm]	α_{SL-MZM}	17.5
Loss for the C-MZM [dB/cm]	α_{C-MZM}	12.3
Optical wavelength [nm]	λ	1550

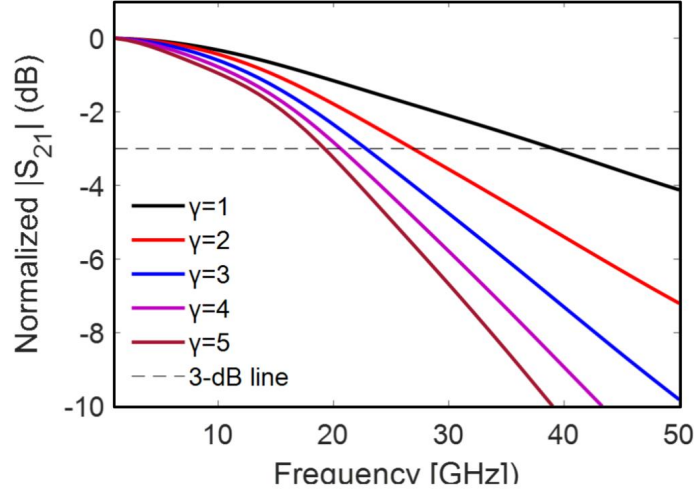


Figure 3.10 – EO response of SL-MZMs combined with TW electrodes with $L_{SL-MZM} = 1$ mm at a reverse bias of 1 V.

EO bandwidth

Figure 3.11 shows the EO bandwidth estimated for lumped-electrode SL-MZMs and TW SL-MZMs as a function of the enhancement factor. We also plot the 3-dB bandwidth of the C-MZM as a reference value (black dash line). As can be seen, the TW SL-MZM offers a larger EO bandwidth compared to C-MZM in a specific range of the enhancement factor. In this range, TW SL-MZM require shorter electrodes to operate with the same V_π , which leads to a reduction in the RF attenuation. The small length and the reasonable SL effect ($\gamma \simeq 9$) also limit the EO velocity mismatch.

Figure 3.11 also indicates that the EO bandwidth reaches a maximum at an optimum enhancement factor of $\gamma = 9$ ($L_{SL-MZM} = 533 \mu\text{m}$). The optimum γ represents a compromise between the two limiting factors of the EO bandwidth (RF loss and EO velocity mismatch), for $\gamma < 9$ the

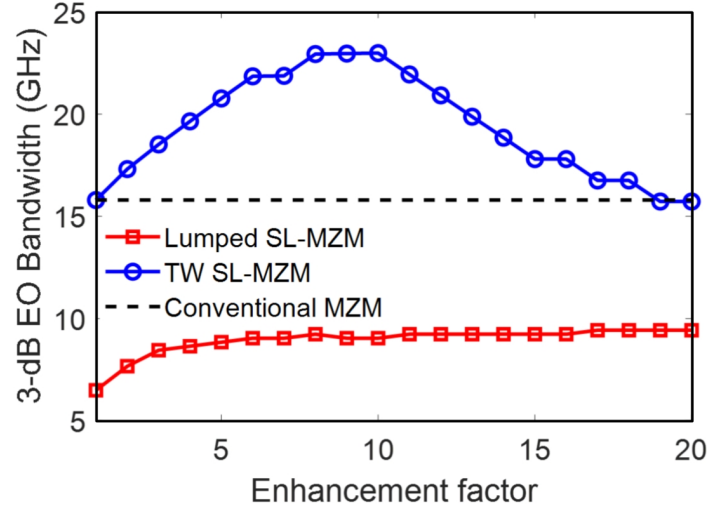


Figure 3.11 – The EO bandwidth as a function of enhancement factor at the reverse voltages of 1 V. $L_{C-MZM} = 4.8$ mm and $L_{SL-MZM} = 4.8/\gamma$ mm.

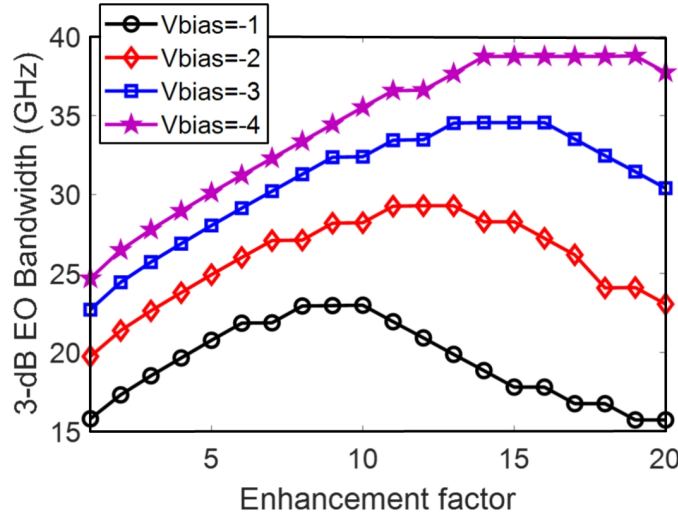


Figure 3.12 – EO bandwidth of SL-MZMs with TW electrodes as a function of the enhancement factor for different V_{bias} . $L_{C-MZM} = 4.8$ mm and $L_{SL-MZM} = 4.8/\gamma$ mm.

EO bandwidth is limited by the RF loss and while its limited by the EO velocity mismatch $\gamma > 9$. Indeed, the group velocity of the optical wave is reduced by the enhancement factor, whereas the RF group velocity remains the same. The difference in traveling time therefore increases as $L_{C-MZM} \times (n_g - n_{RF}/\gamma) / c$, which contributes to limiting the EO bandwidth in larger enhancement factors. In Fig. 3.12, we examine the EO bandwidth for different V_{bias} , showing that the optimum γ is voltage-dependent and shifts to larger value with increasing V_{bias} , *i.e.*, the optimum values are $\gamma = 9, 12, 14$, and 16 at $V_{bias} = -1$ V, -2 V, -3 V, and -4 V, respectively.

Finally, Fig. 3.11 illustrates that the substitution of lumped electrodes by TW electrodes allows a significant improvement in the EO bandwidth of SL-MZMs. For example, at $\gamma = 9$ ($L_{SL-MZM} = 533$

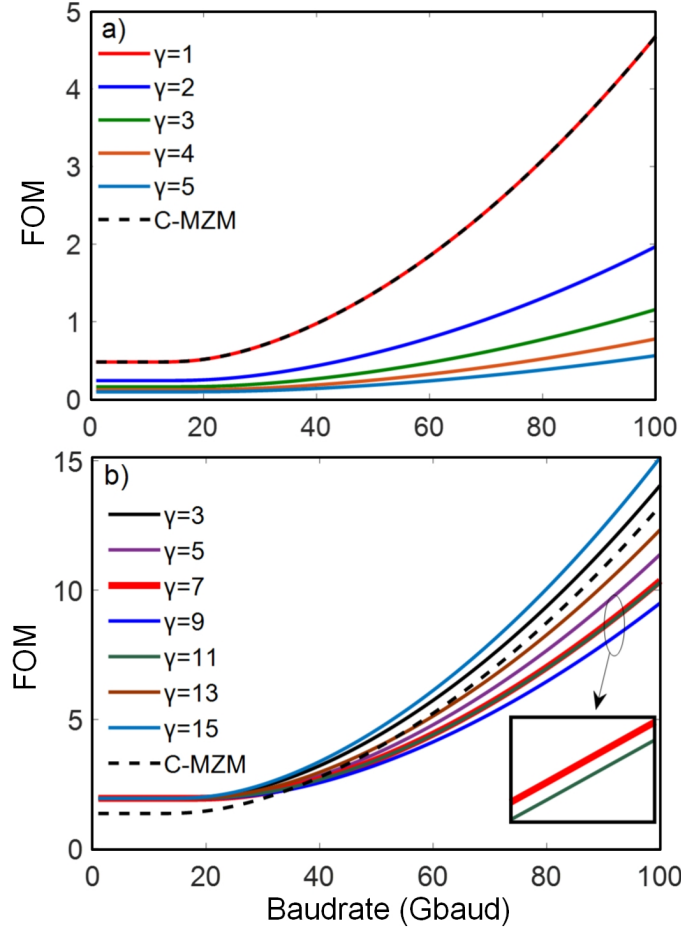


Figure 3.13 – FOM for OOK modulation format ($M = 2$) a) without b) with considering loss of the SL waveguides as a function of baudrate for TW SL-MZM and the C-MZM. $L_{C-MZM} = 4.8$ mm, $L_{SL-MZM} = 4.8/\gamma$ mm, and $V_{bias} = -1$ V.

μm), the TW SL-MZM offers a 23 GHz bandwidth, while it is only 9 GHz for the lumped-electrode SL-MZM.

FOM

We evaluate the FOM expressed in Eq. 3.20 for the TW SL-MZMs and the C-MZM. Fig 3.13 (a) shows the results without including loss in the analysis ($\alpha = 1$ dB/cm for both cases). The TW SL-MZM, for all γ , outperforms the C-MZM in terms of efficiency and EO bandwidth. This is because the TW SL-MZM requires a shorter length for the same V_π (e.g., $L_{SL-MZM} = 0.96$ mm at $\gamma = 5$ vs. $L_{C-MZM} = 4.8$ mm), and provides a larger EO bandwidth (for example, $f_{SL-MZM} = 20.7$ GHz at $\gamma = 5$ vs. $f_{C-MZM} = 15.8$ GHz).

In Fig. 3.13 (b), showing both FOMs in the presence of the loss, when the light is not slowed down enough ($\gamma = 3$) or is slowed down too much ($\gamma = 15$), the C-MZM still outperforms TW SL-

MZMs at all baudrates. The reason is that for $\gamma = 3$, the long length of the phase shifter results in a high RF loss; and for $\gamma = 15$, the velocity mismatch between the RF and optical waves is too large. On the other hand, if the light speed is reduced by factors of 5 to 13 ($5 \leq \gamma \leq 13$), the best modulator depends on the target speed (baudrate); for example, considering $\gamma = 9$, the C-MZM operates better at lower speed (< 35 Gbaud), while it is the TW SL-MZM for higher speed (> 35 Gbaud). Indeed, for baudrates below 35 Gbaud, the additional loss associated with SL waveguides does not allow the total TPP of the SL-MZM to become smaller than the one of the C-MZM. On the other hand, for high-speed operations (> 35 Gbaud), the EO bandwidth is the determining factor to minimize the total TPP, and thus the TW SL-MZM demonstrates superior performance.

Finally, Fig. 3.13 (b) shows that the optimum γ defined in the previous section ($\gamma = 9$), demonstrates the lowest FOM for high baudrates in this case as well. Considering now a modulation speed of 100 Gbaud, which is being targeted for designing the next generation of SiP transmitters, the C-MZM presents the FOM of 13.25, whereas the TW SL-MZM reduces this value by 3.75, *i.e.*, $\text{FOM}_{\text{SL-MZM}} = 9.5$.

3.3.3 Discussion: TW SL-MZMs vs. C-MZMs

TW SL-MZMs can exhibit significant improvement in both efficiency and speed. At the optimum enhancement factor, they improve the EO bandwidth by 7.5 GHz due to their much reduced length for the same V_π . Therefore, SL-MZMs with TW electrodes offers a solution to the efficiency-speed tradeoff. As shown in Fig. 3.13 (b), the TW SL-MZM under an optimum design is a promising candidate to substitute the C-MZM. Indeed, despite the additional loss associated with SL waveguides, TW SL-MZMs reduces the total TPPs compared to C-MZMs because of their large EO bandwidth.

3.4 V_π reduction in silicon photonic modulators

Due to constraints in CMOS drivers and electrical interfaces, the required swing voltage for driving SiP modulators should be as low as possible. Indeed, implementation of CMOS drivers with swing voltages of more than 2.5 V is very challenging because of the reliability concerns although there are some demonstrations on co-design SiP modulators with a high-swing CMOS driver [39, 144, 145]. In addition, the high RF propagation loss at high-speed operations (> 50 Gbaud) is an important limitation to bandwidth scaling that can be somewhat relaxed by a reduction in the electrical power budget. It is therefore of high interest to reduce the energy per bit consumption (E_b) of SiP modulators, which scales with the peak-to-peak voltage (*i.e.*, $E_b \propto V_{pp}^2$).

Improvement in SiP modulators V_π requirements is thus necessary for high-performance integration system. The C-MZM in our study was characterized by a V_π of 7 V with a length of $L_{PS} = 4.8$ mm, which is not compatible with current CMOS drivers. For example, in [48], the authors have reported a modulator driver with a peak-to-peak voltage of 2.5 V using a partially depleted SOI 45-

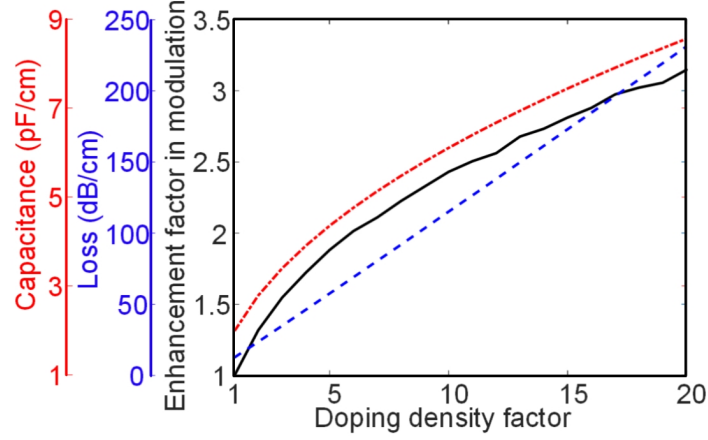


Figure 3.14 – Phase modulation multiplication factor, total loss, and RC constant of a simple p-n junction as a function of the normalized doping density factor (a normalized doping density factor of 5 means doping concentrations of $5 \times N_A$ and $5 \times N_D$ with $N_A = 5 \times 10^{17} \text{ cm}^{-3}$ and $N_D = 3 \times 10^{17} \text{ cm}^{-3}$).

nm process. In order to meet this voltage range, the aforementioned V_π should reduce by a factor of 3 (*i.e.*, $V_\pi = 2.33\text{V}$). Three design strategies are examined below.

3.4.1 Design strategies to reduce V_π

Increasing phase shifter length (IPSL)

Considering the phase shift equation ($\pi = k_0 \times \Delta n(V_\pi) \times L_{C-MZM}$), the easiest way to reduce the V_π is to make phase shifters longer. According to the index variation versus the applied voltage shown in Fig. 3.3, the C-MZM will offer a V_π of 2.33 V if its length increases by a factor of about two (*i.e.*, $L_{C-MZM} = 10 \text{ mm}$).

Increasing doping density (IDD)

Increasing the doing level allows an enhancement in the efficiency of phase shifters. Our studied devices (the lumped-electrode SL-MZM and the C-MZM) have been fabricated under an estimated doping concentrations of $N_A = 5 \times 10^{17} \text{ cm}^{-3}$ and $N_D = 3 \times 10^{17} \text{ cm}^{-3}$ for holes and electrons, respectively. When the doping level increases, Fig. 3.14 shows that an enhancement in the phase modulation is achieved but at the cost of significantly higher loss. Also, higher doping levels results in larger junction capacitance, leading to significantly increasing the microwave propagation loss of the TML, therefore dramatically limiting the EO bandwidth of TW MZMs. According to Fig. 3.14, in order to reduce the V_π from 7 V to 2.33 V, the doping density of the C-MZM with TW electrodes should increase by a factor of 6, which would increase the phase modulation by a factor of 2 (*i.e.*, $N_A = 30 \times 10^{17} \text{ cm}^{-3}$ and $N_D = 18 \times 10^{17} \text{ cm}^{-3}$).

Slow-light effect

As discussed in this paper, the SL effect is another means to decrease the V_π . According to the phase shift equation ($\pi = k_0 \times \Delta n(V_\pi) \times \gamma \times L_{SL-MZM}$), a SL-MZM loaded by TW electrode with an optimized enhancement factor of $\gamma = 12$ and a phase shifter length of $L_{SL-MZM} = 833 \mu\text{m}$ offers a V_π of 2.33 V.

3.4.2 Discussion

Table 3.3 compares the performance characteristics of these various approaches considering EO bandwidth, loss, and phase shifter length. As shown, the IPSL is not an effective way to lessen the V_π because it leads to a significantly reduced bandwidth. Indeed, with exploiting this approach, the EO bandwidth shrinks due to the RF loss, moreover the footprint is increased. The IDD approach provides a low V_π of 2.33 V with the same phase shifter length as the C-MZM, but at the cost of introducing a significant loss (33 dB) mainly originated by the absorption loss of p-n junctions, as well as a dramatically shrunk EO bandwidth due to the heavy doping that increases the conductor loss and the dielectric loss considerably, resulting in increased RF loss. On the other side, the SL-MZM combined with TW electrodes is capable of reducing V_π from 7 V to 2.33 V, improving the EO bandwidth from 15.8 GHz to 17.6 GHz, as well as shortening the phase shifter from 4.8 mm to 833 μm . Compared to the IDD scheme, the SL design also offers a better compromise on loss (17 dB vs. 33 dB). Finally, we examine the three approaches considering the FOM expressed in Eq. 3.20. The simulation results are shown in Fig. 3.15. As can be seen, the SL approach presents the optimum FOM compared to the other approaches. For example, at the 80 Gbaud, the FOM's values are 35.34, 238.5, and 21 for the IPSL, the IDD, and the SL effect approaches, respectively.

Table 3.3 – Comparing different design strategies based on their operating parameters

	Reference MZM [61]	IPSL	IDD	SL effect
V_π (V)	7	2.33	2.33	2.33
EO bandwidth (GHz)	15.8	11.8	6.9	17.6
Phase shifter length (mm)	4.8	10	4.8	0.833
Loss (dB)	5.9	12.3	33	17

Recently, the IDD approach was used to bring down $V_\pi \times L$ of SiP C-MZMs [42]. However, according to our assessment, using the SL waveguide with an optimized enhancement factor is a better solution for this purpose. As discussed, the SL approach not only improves significantly efficiency under a stable operation but also provides a larger EO bandwidth. On the other hand, the slight improvement in the efficiency using the IDD approach is provided at the expense of a dramatic reduction in EO bandwidth and severe increment in the absorption loss of p-n junctions.

The next generation of the integrated SiP platform should leverage TW SL-MZMs to enable a new class of SiP transmitters that feature best-in-class performance in key parameters such as

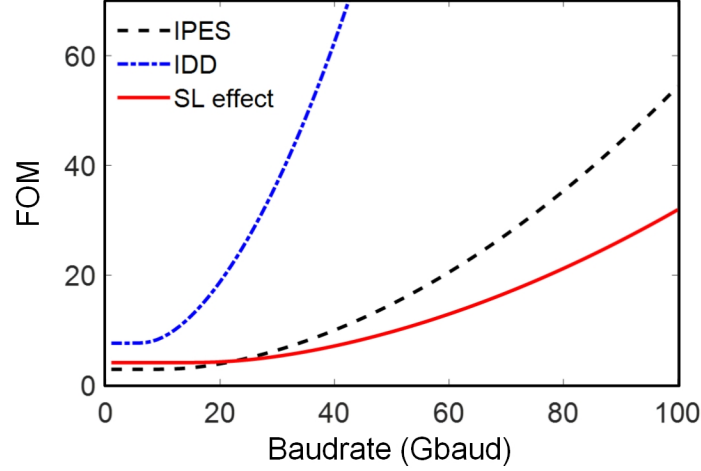


Figure 3.15 – FOM of the different approaches for V_π reduction through phase modulation enhancement as a function of baudrate.

high stability, low power budget, high EO bandwidth, and compact footprint. These modulators are capable of providing a very low V_π (< 2.5 V) with a compact phase shifter length (< 1 mm). Therefore, the requirements on the RF amplification and the thermal control are significantly relaxed, leading to reduced cost and complexity of control circuits and CMOS drivers. The additional loss associated with SL waveguides can be compensated by high-performance optical amplifiers.

3.5 Conclusion

We have presented an investigation of the benefits and tradeoffs of SL-MZMs with either lumped electrodes or TW electrodes. We compared these two SL modulators to the C-MZM through calculation of their EO bandwidth and FOM, the latter being derived from the reduction of the static and dynamic TPPs. To this end, we developed a RLC circuit model to simulate the dynamic behavior of lumped-electrode SL-MZMs. Our model was validated with experimental measurement of an SL-MZM. Key findings are summarized below:

1) Due to the high loss and low bandwidth of the SL waveguides, the lumped-electrode SL-MZMs did not show any performance improvement over C-MZMs. In addition to the RC time constant, the interaction time between the lumped electrodes and the optical signal also limits the modulator speed. Simulations show that a C-MZM with a V_π of 7 V and a phase shifter length of $L_{C-MZM} = 4.8$ mm is characterized by an EO bandwidth of 15.8 GHz, while the lumped-electrode SL-MZM with the same V_π ($L_{SL-MZM} = 4.8/\gamma$ mm) demonstrated a maximum EO bandwidth of 9 GHz.

2) SL-MZMs can offer remarkable benefits when implanted with TW electrodes. In this case, their EO bandwidth reaches 23 GHz at the optimum SL value of $\gamma = 9$ ($L_{SL-MZM} = 533$ μ m). The FOM calculations show that the optimum SL-MZMs can then outperform C-MZMs at high-speed

operations.

3) Furthermore, compared to the other strategies currently considered to reduce V_π of C-MZMs, employing the SL effect is the best-in-performance solution. Compared to the C-MZM, the optimized SL design allowed reducing the V_π from 7 V to 2.33 V, compacting the MZM arm length from 4.8 mm to 833 μm , improving EO bandwidth from 15.8 GHz to 17.6 GHz. These good performances are reached despite the additional loss of waveguides that can be compensated by an optical amplifier. Future progress in the design and fabrication process of SL waveguides should further reduce the propagation loss and make these modulators even more attractive for applications requiring arrays of high-speed, compact and energy efficient modulators.

Chapter 4

DAC-less PAM-4 slow-light silicon photonic modulator providing high efficiency and stability

Résumé- Nous rapportons un modulateur à lumière lente en silicium qui permet une opération PAM à grande vitesse sans l'utilisation d'un convertisseur numérique-analogique (DAC) électrique. Les résonateurs à réseau de Bragg, intégrés dans chaque bras d'un modulateur Mach-Zehnder, améliorent la modulation de phase grâce à un effet de lumière lente. Le signal PAM optique à 4 niveaux est généré en pilotant directement le déphaseur segmenté, que nous avons conçu, avec deux signaux binaires. Ce modulateur a une empreinte ultra-compacte ($L_{SL-MZM} = 570 \mu\text{m}$), une faible consommation d'énergie (73 fJ / bit) et une bande passante électro-optique élevée ($> 40 \text{ GHz}$). Jusqu'à 90 Gb/s sont obtenus en opération sur une bande passante ayant une plage spectrale de l'ordre nanométrique ($\Delta\lambda_{BW} = 2 \text{ nm}$). Comparée à d'autres modulateurs basés sur des résonateurs à basse énergie, tels que les micro-anneaux, cette bande passante d'opération offre une plus grande stabilité avec une plage de température de fonctionnement potentielle de $\Delta T = 50 \text{ }^\circ\text{C}$. Nous examinons également la robustesse de la conception proposée face aux variations de fabrications par des mesures des propriétés spectrales au niveau spatial inter-gauche. Ce modulateur est d'un intérêt particulier pour certaines applications, telles que les communications de données à courte portée qui nécessitent plusieurs modulateurs compacts et écoénergétiques sur une seule puce.

Abstract- We report a slow-light silicon modulator that enables high-speed PAM operation without using an electrical digital-to-analog converter (DAC). Bragg grating resonators, integrated into each arm of a Mach-Zehnder modulator, enhance the phase modulation through the slow light effect. The optical 4-level PAM signal is generated by driving directly the segmented phase shifter design with two binary signals. This modulator presents an ultra-compact footprint ($L_{SL-MZM} = 570 \mu\text{m}$), low energy consumption (73 fJ/bit), large electro-optic bandwidth ($> 40 \text{ GHz}$). Up to 90 Gb/s is achieved over an nm-range spectral operation bandwidth ($\Delta\lambda_{BW} = 2 \text{ nm}$). Compared to other low-

energy resonator-based modulators, such as micro-rings, this operating bandwidth confers higher stability with a potential operating temperature range of $\Delta T = 50$ °C. We further examine the robustness of the proposed design to fabrication variations by measurements of spectral properties across the wafer. This modulator is of particular interest for applications, such as short-range data communications that require multiple compact and energy-efficient modulators on a single chip.

4.1 Introduction

Silicon photonics (SiP) is an enabling technology that leverages advanced CMOS process to manipulate electrons and photons on the same platform [45]. SiP modulators featuring high-speed operation, low power consumption, compact footprint, and stable operation are demanded to address the growing bandwidth requirements of the data centers. For this application, pulse amplitude modulation (PAM) is increasingly considered as one of the best solutions for higher data rates with a good compromise between spectral efficiency and system complexity. The latter results from the intensity-modulation direct-detection nature of the PAM format that simplifies the receiver compared to coherent formats [65]. Consequently, 4-level PAM (PAM-4) is a main contender to accomplish the IEEE 400 Gb/s Ethernet task force [81]. The 400 Gb/s target can be achieved by 25 Gbaud PAM-4 using 8 wavelength channels, or 50 Gbaud PAM-4 using 4 wavelength channels.

Mach-Zehnder modulators (MZMs) with two-segment phase shifters are a popular configuration to generate DAC-less PAM-4, reaching high-speed operation (> 100 Gb/s) [82]. However, due to the weak index modulation created by the plasma dispersion effect in silicon, long phase shifters are required in order to keep V_π low. As a result, MZMs are energy-hungry, have a large footprint, and require traveling-wave electrodes or distributed drivers to reach a high modulation bandwidth.

Resonator-based modulators have been proposed to reduce footprint and energy requirements. Recently, Sun *et al.* developed a micro-ring modulator (MRM) in lateral-vertical PN junctions and achieved a data rate of > 100 Gb/s per wavelength [40]. This modulator features a compact footprint, an energy consumption of 18 fJ/bit for PAM-4, and a 50 GHz electro-optic (EO) bandwidth. This remarkable enhancement in EO bandwidth compared to other MRM demonstrations is gained by using a higher doping level, which leads to a significant increase in absorption loss introduced by PN junctions, which, in turns, results in a reduced photon lifetime (or quality factor). Despite the impressive performance, MRMs have a narrow operating spectral bandwidth (< 0.1 nm). Therefore, temperature fluctuations may cause a large variation in the modulator response; additional feedback circuits are needed to perform the temperature stabilization and lock the resonance wavelength. Moreover, the modulator requires process customization for vertical junctions, which is not widely available. Also, MRMs require pre-distorted driving signals to generate higher order PAM in order to compensate the nonlinearity in the roll-off of the resonator transfer function and achieve equally spaced levels in the optical eye [65].

Slow-light (SL) SiP modulators are another enabling design choice to address the tradeoff between stability and efficiency. Providing that the enhancement in phase modulation occur over a wide optical bandwidth, they are not as sensitive as MRMs to temperature variations. Also, compared to MZMs, they require several times shorter phase shifters and consume significantly less energy per bit. Nevertheless, operation of SL modulators have been mostly reported with OOK formats because of foreseen difficulties in upgrading their designs to generate PAM or QAM. For example, in the case of photonic crystal waveguides (PCW), longer PCW is needed to generate DAC-less PAM

with a segmented configuration (two phase shifters placed in series). These longer PCWs result in higher susceptibility to fabrication imperfections [108]. Although, PCW-based MZM using a parallel configuration is proposed in [146] to generate DAC-less PAM-4 modulation, the performance is limited to 15 Gbaud. In addition to PCWs, cascaded micro ring resonators have been utilized to slow down the optical wave. In this case, PAM signal generation requires a large number of uncoupled ring resonators (more than 20 cavities), whose resonance wavelengths are often different because of fabrication imperfections. Tuning all cavities independently to generate PAM becomes almost impossible due to thermal crosstalk.

In this chapter, we report a new design of a DAC-less PAM-4 SL-MZM based on Bragg grating resonators (BGRs). In section 2.5, we demonstrated an MZM assisted by BGRs for OOK modulation. What makes this design unique is the presence of cascaded coupled cavities, which leads to resonators sharing the same resonating wavelength. Therefore, it is not necessary to tune the cavities independently, which eases the measurement process. Also, since Bragg gratings are 1-D photonic crystals, instead of 2-D, they are inherently less sensitive to fabrication errors compared to PCWs and are routinely fabricated with CMOS compatible fabrication process using UV lithography. Hence, in this paper, we adapt the SL-MZM based on BGRs design reported in section 2.5 for DAC-less generation of PAM-4 optical signal. We experimentally demonstrate that this modulator has the potential to meet the recommendations of the IEEE Ethernet task force since it features compact footprint, low power consumption, and stable operation simultaneously. It is therefore an appropriate choice when a large set of optical modulators need to be integrated in a single photonic chip.

In the following sections, we present the segmented modulator design and characterize the variations of its spectral response across the wafer. We then perform RF and EO bandwidth characterizations of both phase shifters of the modulator. Finally, we present bit-error-rate measurement. Our results show that the modulator is characterized by a phase efficiency of $V_\pi \times L = 0.51$ Vcm, an energy consumption of $E_b = 73$ fJ/bit, and an EO bandwidth of > 40 GHz. The modulator operates up to 90 Gb/s below 20% FEC threshold over an operating wavelength range of $\Delta\lambda_{BW} = 2$ nm.

4.2 Modulator design

Figure 4.1 (a) shows the modulator schematic. Slowing down the optical wave in each arm, BGRs help to enhance the phase modulation. These coupled resonators are designed with a low quality factor in order to achieve the enhancement across a larger spectral bandwidth. In section 2.3, we discussed in detail how to engineer the SL effect using BGRs. Each arm of the MZM is loaded by a BGRs superstructure with a uniform period of $\Lambda = 300$ nm, a duty cycle of 50%, a maximum waveguide width of 1000 nm and minimum waveguide width of 250 nm (corrugations of 375 nm on each side), and 26 coupled resonators. Each resonator consists of a phase-shifted section with 38 grating periods on each side. We loaded the first 15 resonators and the last 10 resonators with PN junctions to introduce the two phase shifter segments placed in series, called “most significant bit

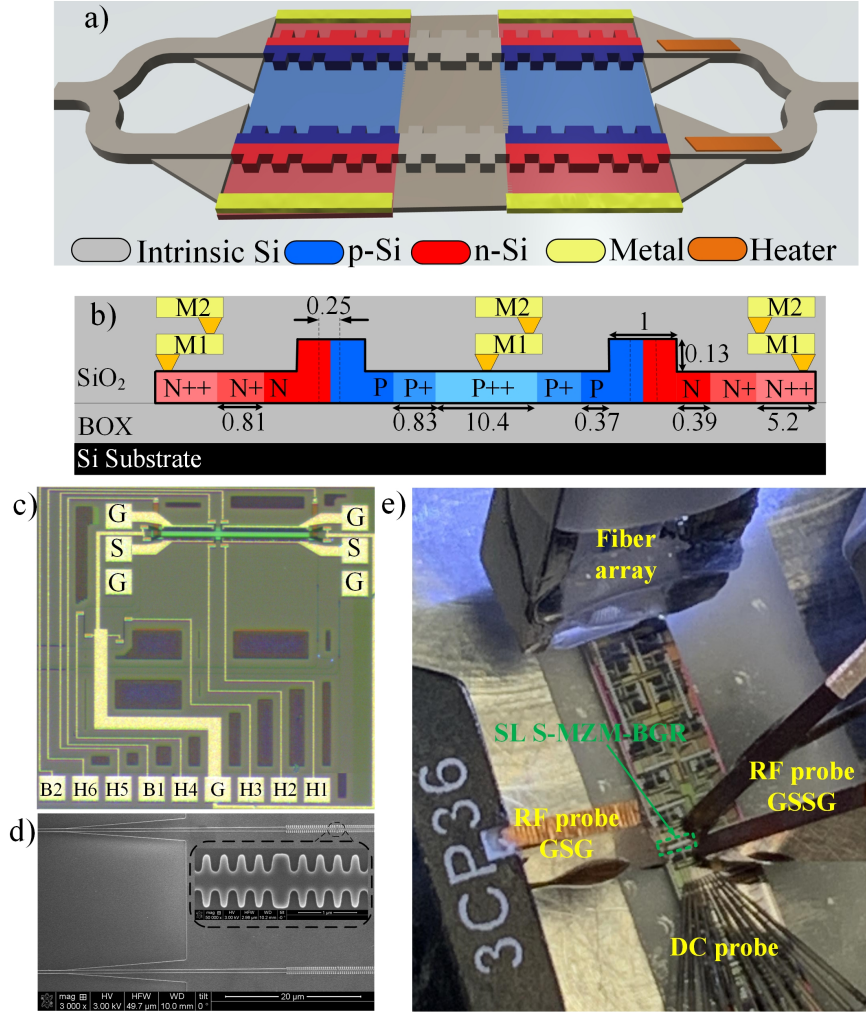


Figure 4.1 – a) Schematic of the DAC-less PAM-4 SL-MZM, b) cross-section of the modulator (the labeled parameters are in μm), c) close view of the fabricated modulator, d) SEM picture of a part of the fabricated modulator (inset is a zoom on the Bragg grating), and e) modulator under the test.

(MSB) segment” and “least significant bit (LSB) segment”, respectively. Note that one cavity remains unloaded in order to separate these two segments. Figure 4.1 (b) illustrates the cross-section of the modulator, showing that the silicon waveguide is formed by the partial etch with a slab height of 90 nm and a ridge height of 220 nm. The lateral PN junction is designed to reach a compromise between absorption loss and EO bandwidth.

Figure 4.1 (c) displays a close view of the fabricated modulator, showing that the modulator is driven using lumped electrode. We placed four thermal elements (labeled H1, H2, H5 and H6) on top of each segment in order to fine-tune the resonance wavelengths of each BGRs segment if necessary. Also, two heaters (labeled H3 and H4) were placed in each arm to set the operating point of the modulator. The modulator operates in the depletion mode (negative bias voltage) under a single-drive push-pull configuration. Pads, labeled B1 and B2, are used for adjusting the bias point

of the LSB and MSB segments, respectively. The modulator was fabricated in a multi-project wafer run using a standard 193 nm lithography process at the IME (AMF) A*STAR with a silicon layer thickness of 220 nm and a 2 μm buried oxide. Figure 4.1 (d) shows an SEM picture of the two arms and the inset shows a close-up view of a cavity in the BGR structure.

4.3 Modulator characterization

4.3.1 Optical spectrum

In order to examine the reliability and repeatability of the passive structure, which is composed of 26 coupled cavities in each arm, we perform measurements of the optical response of the passive structure. We first examine the reflection and transmission of the components to compare the response from the two arms, then we examine the uniformity of the Bragg wavelength and spectral bandwidth across the wafer.

Component-level testing

Figure 4.2 (a) and (b) show the schematic of the test structure. It differs from the modulator structure by the presence of two directional couplers at the input of each arm. Figure 4.2 (a) shows the input and output ports to measure the transmission from the upper Mach-Zehnder arm (blue), lower Mach-Zehnder arm (red) and full structure (black). Figure 4.2 (b) shows the configuration for reflection measurements. Figure 4.2 (c) presents the normalized transmission spectra for the upper arm (blue), the lower arm (red) and the whole structure (black). As depicted, the resonance wavelengths and their bandwidths are almost identical in all three cases, indicating good fabrication uniformity of the resonators between the two arms of a single device. Similarly, figure 4.2 (d) presents the reflected spectra.

Wafer-uniformity testing

To assure repeatability and uniformity of the design over the whole wafer, we picked randomly several dies and examined the resonance wavelength (or Bragg wavelength) and the optical bandwidth. Each die has a size of $3 \times 15.8 \text{ mm}^2$. As indicated in figure 4.3 (a), the resonance wavelength of the BGRs was quite uniform with a value of 1563 nm on average with a standard deviation of 2.5 nm. Figure 4.3 (b) shows the optical bandwidth of the transmission band, having an average of 3.27 nm with a standard deviation of 0.25 nm.

Device-under-test (DUT) spectrum

Figure 4.4 presents the measured characteristic of the modulator structure chosen for RF measurements and data transmission. Figure 4.4 (a) zooms on the transmission and reflection spectra close to the resonance wavelength. The 3.2 nm optical bandwidth, much larger than typical resonating structure, results from the low quality factor cavities. Also, the insertion loss of the modulator is 5.5

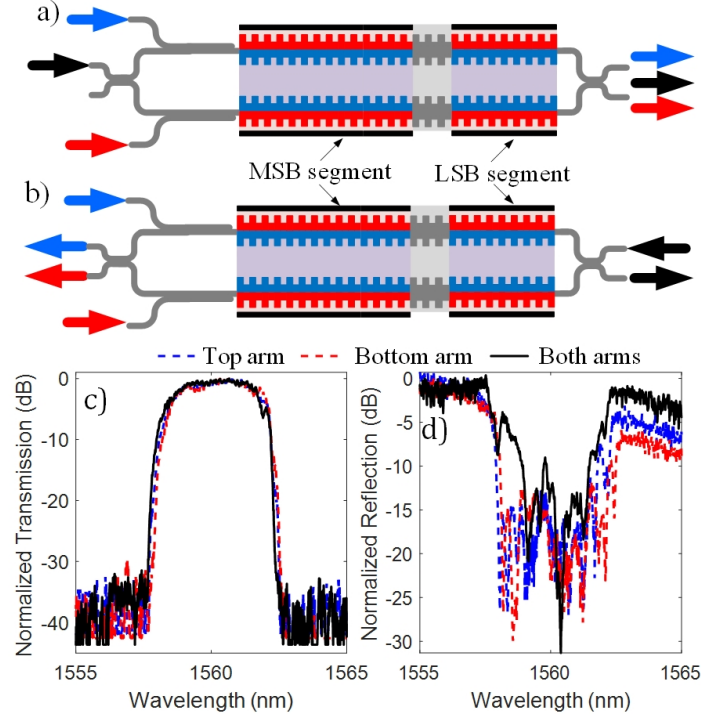


Figure 4.2 – a) and b) are respectively schematics of the test configuration used to measure transmission and reflection of each arms in the test structure; c) and d) are respectively the transmission and reflection spectra of the test structure for different input/output ports.

dB (*i.e.*, propagation loss of 92 dB/cm). This loss is caused by the discontinuity in the waveguide modes and effective indices of the rib waveguide at the start and end of the Bragg grating structure, and by high propagation loss due to sidewall roughness and lithographic inaccuracies in the highly structured waveguide. The loss can be mitigated by improving design, for example through waveguide tapering or grating apodization at the interface between slow and fast regimes, and using fabrication processes with a better resolution. Note that losses are expected to decrease as SiP fabrication processes improve. Figure 4.4 (b) illustrates the transmission through both arms of the modulator structure at the operational wavelength of $\lambda_0 = 1562$ nm when the relative phase is adjusted using the thermal element (heater labeled H3). Results show that the MZI structure provides an extinction ratio of 15 dB. Moreover, about 10 mW of power is needed to set the modulator at the quadrature point. The modulator spectrum at the quadrature point is shown by the green line in figure 4.4 (a).

4.3.2 DC characterization

The output of a MZM incorporating SL elements in its arms is given by,

$$P_{out} = P_{in} \exp(-\alpha L) \cos^2 \left(\frac{\pi}{\lambda} \Delta n_{eff}(V) \gamma L + \frac{\pi}{4} \right) \quad (4.1)$$

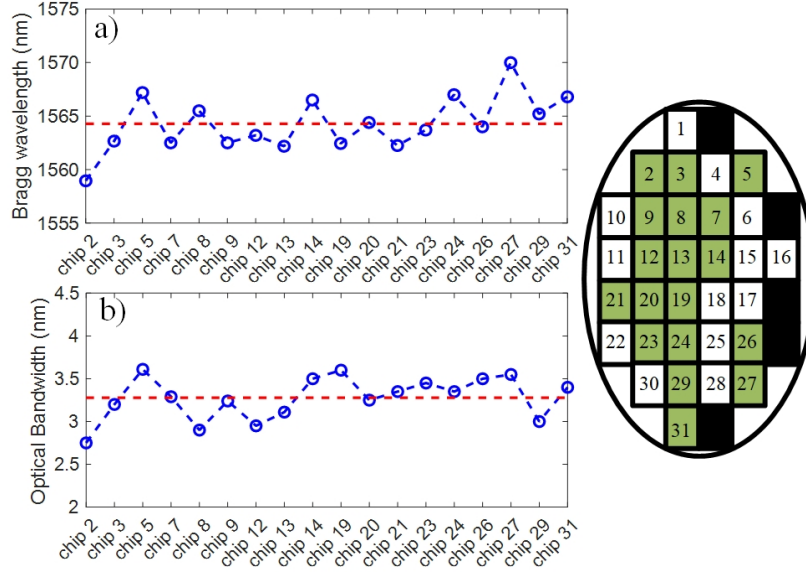


Figure 4.3 – a) Bragg wavelength and b) optical bandwidth of measured on chips from different wafer locations.

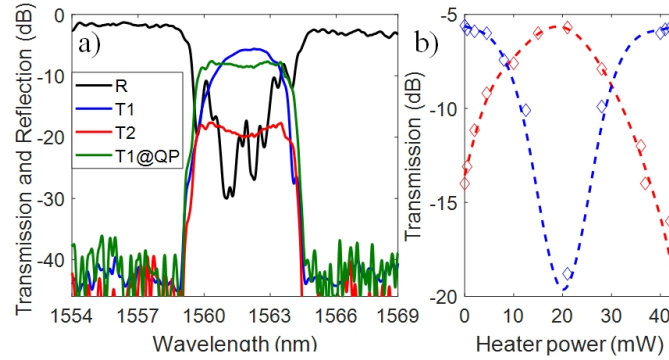


Figure 4.4 – a) Transmission and reflection spectra of the SL-MZM, b) transmission of the two ports of the adiabatic coupler (located at the end of the modulator for recombining optical wave) as a function of the heater power. T1: output power from port1 of the adiabatic coupler, T2: output power from port2 of the adiabatic coupler, T1@QP: Transmission of the port 1 at the quadrature point.

where P_{in} is the input power, α is the propagation loss coefficient, and λ is the operational wavelength. The modulation of the waveguide effective refractive index with applied voltage is Δn_{eff} , while the factor γ is the enhancement factor. The latter represents the phase modulation enhancement produced by the BGRs compared to a simple phase shifter in a rib waveguide with the same length. Modulation efficiency of the SL phase shifter can be described by the typical figure of merit ($V_\pi \times L$ where L is the phase shifter length). The modulator experimentally records a $V_\pi \times L$ of 0.51 Vcm. In order to evaluate the enhancement provided by the SL effect, we compare our SL modulator with a typical MZM fabricated with the same process. The regular MZM is characterized by a $V_\pi \times L$

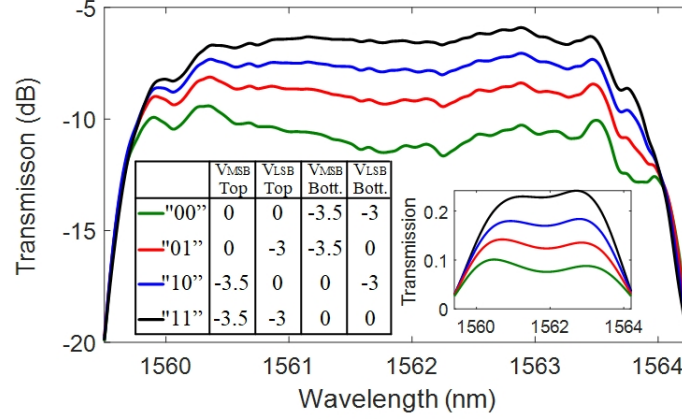


Figure 4.5 – Transmission spectra for different combination of applied voltages (see inset table) to generate four levels (in linear scale in the inset figure).

of 3.15 Vcm, and thus, we find a phase modulation enhancement factor of $\gamma = 6$.

Figure 4.5 shows the transmission spectra at the quadrature point when applying the DC voltages specified in the inset table, to the MSB and LSB segments. Figure 4.5 indicates that the modulator can generate four-level transmission with a total DC extinction ratio (ER) of $\simeq 4.4$ dB over the optical bandwidth. The transmission, displayed in linear scale in the inset of figure 4.5, shows four well-spaced levels. The modulator can therefore be driven in single-drive push-pull configuration using reverse bias and two by RF signals with peak-to-peak voltages of $7 V_{pp}$ and $6 V_{pp}$ applied to the MSB and LSB segments, respectively.

4.3.3 EO bandwidth

We measured S21 using a PNA Microwave Network Analyzer (Agilent N5227A 10 MHz - 67 GHz). We used RF probe with 50- Ω termination, allowing to keep S11 below -15 dB, as shown in figure 4.6 (a) (color dashed lines). Figure 4.6 (a) also reports the RF crosstalk (black line) between the adjacent segments, showing that a slight leakage between the two segments occurs (less than 35 dB over 67 GHz bandwidth), and thus, distortions associated with electrical crosstalk are negligible. Figure 4.6 (b) shows the frequency response of the modulator at the operational wavelength of $\lambda_0 = 1562$ nm. Both segments present a 3-dB EO bandwidth of more than 40 GHz at the zero-voltage bias. As the reverse bias increases, the EO bandwidth only slightly increases, showing that the SL effect imposes a limit on the EO bandwidth. In fact, frequency response of SL modulators with lumped electrodes is restricted by not only RC time constant but also by the SL effect that increases the interaction time between optical wave and uniform RF signals along the electrodes.

Figure 4.6 (c) illustrates the spectra of the 3-dB EO bandwidth, indicating that each segment offers a similar EO response over a wavelength range of $\Delta\lambda_{BW} = 2$ nm. This shows that the modulator should be able to operate with no or little distortion in the presence of temperature fluctuations

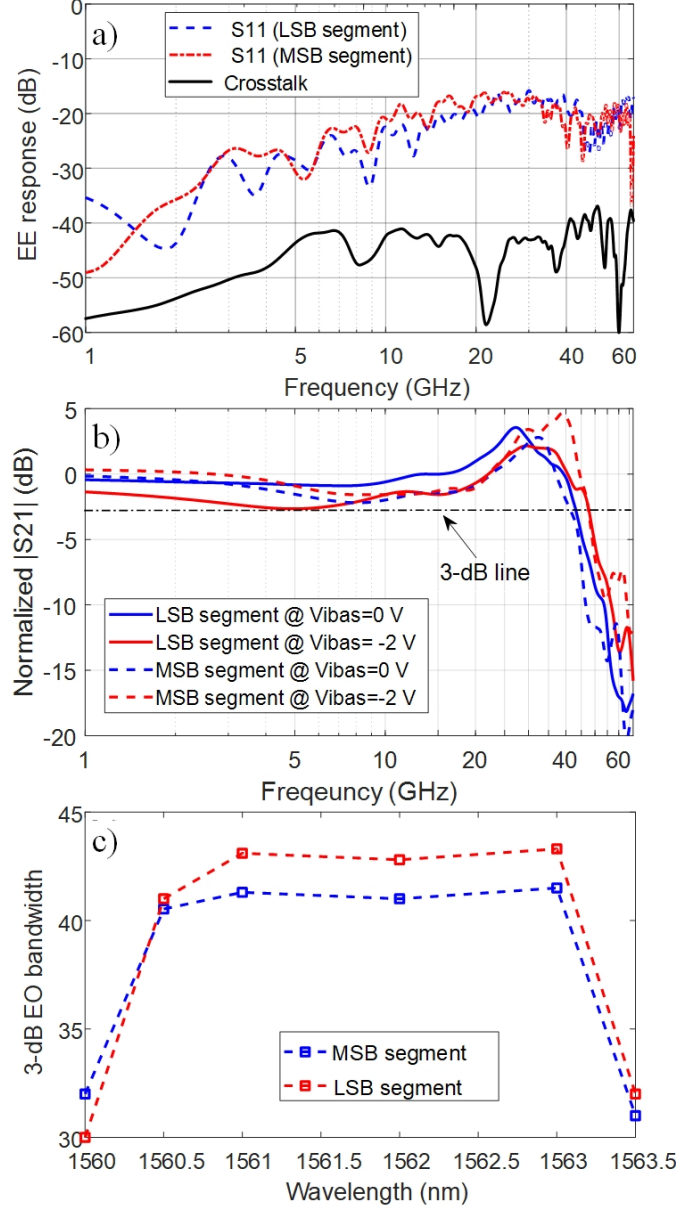


Figure 4.6 – a) S11 of LSB and MSB segments. RF crosstalk between LSB and MSB segments (black) also is shown b) EO responses of MSB and LSB segments for different reverse voltages, c) 3-dB EO bandwidth spectra of MSB and LSB segments.

that shift the spectrum within $\Delta\lambda_{BW} = 2$ nm, which is about one order of magnitude larger than MRMs [40]. This larger operating bandwidth also eliminates the dependence of the frequency response on frequency detuning that causes dynamic nonlinear responses in MRM [21].

4.3.4 High speed characterization

Figure 4.1 (e) displays the device under test (DUT) and figure 4.7 shows the schematic of the measurement setup to evaluate the bit error rate (BER). We first generated a PRBS with a length of $2^{15}-1$

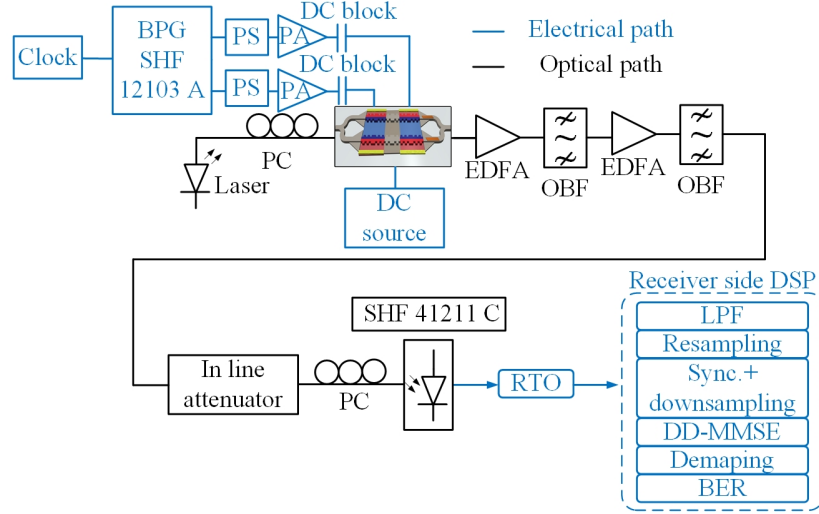


Figure 4.7 – Block diagram of the experimental setup.

using a 56-Gb/s bit pattern generator (SHF 12103 A). Then, we boosted the RF signal applied to the MSB (LSB) segment with an RF amplifier having a bandwidth of 30 GHz (40 GHz) and obtained a peak-to-peak voltage of 7 V_{pp} (6 V_{pp}). Thereafter, we used bias-T (bandwidth of 50 GHz) as DC blocks. In the optical part, we set the laser power to 15 dBm and adjusted the polarization with a polarization controller before coupling the light into the chip. After modulation, the signal was amplified by a two-stage EDFA and each stage is followed by a tunable optical bandpass filter (one of them with a fixed bandwidth of 1 nm and the other one with a tunable bandwidth). The output optical signal was converted to the electrical signal using a photodetector (SHF 41211 with a 32 GHz bandwidth) and then digitalized by a real-time oscilloscope (RTO) with a sampling rate of 80 GSa/s and a bandwidth of 63 GHz. At the receiver side, digital signal processing (DSP) is applied to the signal following the steps shown in figure 4.7. The signal is filtered by a 10th order super Gaussian low pass filter (LPF), resampled, time synchronized, and down-sampled. BER is calculated using a decision-directed minimum mean square error (DD-MMSE) equalizer with a tap number of 2⁴ taps. The signal is de-mapped for BER calculation.

We first evaluate the performance of each segment using OOK modulation. The MSB (LSB) segment operates under a peak-to-peak RF voltage of 3.5 V_{pp} (3 V_{pp}) on each arm. The junction capacitance is 1.7 pF/cm at a reverse bias voltage of 1.5 V. Therefore, the MSB (LSB) segment introduces a total capacitance of 58 fF (38 fF), corresponding to an energy consumption of 170 fJ/bit (85 fJ/bit). Figure 4.8 (a) and (b) shows the BER spectra for MSB and LSB segments, respectively. It is shown that both segments can achieve up to 60 Gb/s with BER below the 20% FEC threshold. As bitrate decreases, the operating wavelength range increases; for example, the operating wavelength range at 45 Gb/s is around $\Delta\lambda_{BW} = 4$ nm, corresponding to an operating temperature range of $\Delta T = 100$ °C assuming a heterogeneously integrated laser with 40 pm/°C wavelength drift between laser and SiP modulators [40].

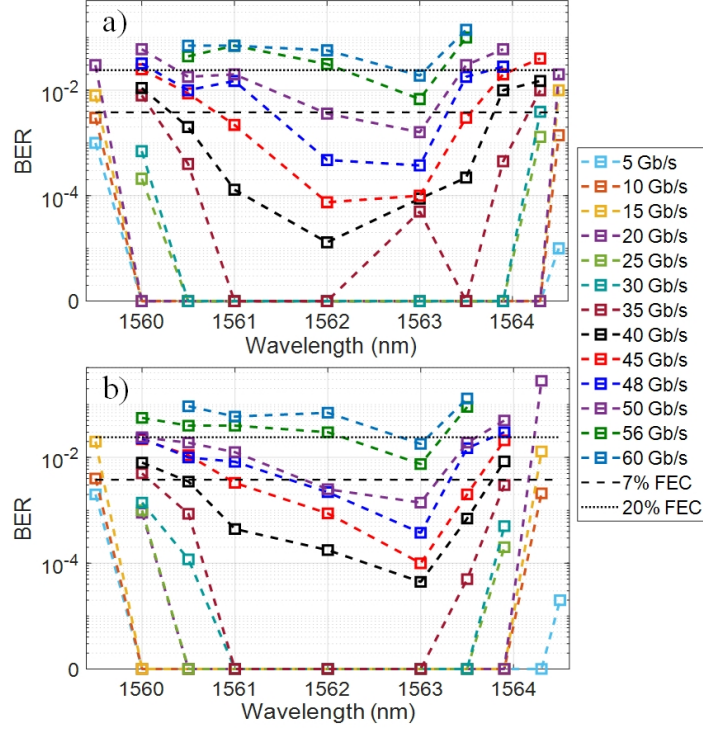


Figure 4.8 – BER spectral measurement when modulating either the a) MSB and b) LSB segments, for OOK modulation at different bitrates. Dashed and dotted lines show 7% and 20% FEC thresholds, respectively.

We then applied the two RF signals to the MSB and LSB segments to generate DAC-less PAM-4. Figure 4.9 illustrates the BER, measured over a $\Delta\lambda_{BW} = 2$ nm optical bandwidth, when the modulator is driven for generating the PAM-4 format at different bitrates. As indicated, the modulator is capable of providing a modulation speed up to 90 Gb/s with BER below the 20% FEC threshold. Figure 4.10 shows histograms of the detected symbols for different bitrates at different operating wavelengths. Note that an operating wavelength range of $\Delta\lambda_{BW} = 2$ nm would correspond to a temperature range of $\Delta T = 50$ °C. The energy consumption for PAM-4 can be calculated using [65]

$$E_b = \frac{CV_{pp}^2}{M^2 \log_2(M)} \sum_{i=0}^{M-1} (M-i) \left(\frac{i}{M-1} \right)^2 \quad (4.2)$$

where, $M = 4$ is the modulation level and C represents the junction capacitance. Using Eq. 4.2, the total energy consumption is estimated to be 73 fJ/bit for PAM-4 format.

Optical-signal-to-noise ratio (OSNR) has a significant impact on maximum speed achieved. One way to improve OSNR is to reduce loss. Several design strategies can help to mitigate this issue. Firstly, using edge coupling can considerably decrease the chip-to-fiber coupling loss. In the present modulator, we use vertical couplers that typically generate a coupling loss of 13 dB (two grating couplers in a back-to-back configuration). State-of-the-art edge couplers offer a back-to-back loss below 2 dB. This 11-dB reduction in the coupling loss would significantly improve the maximum

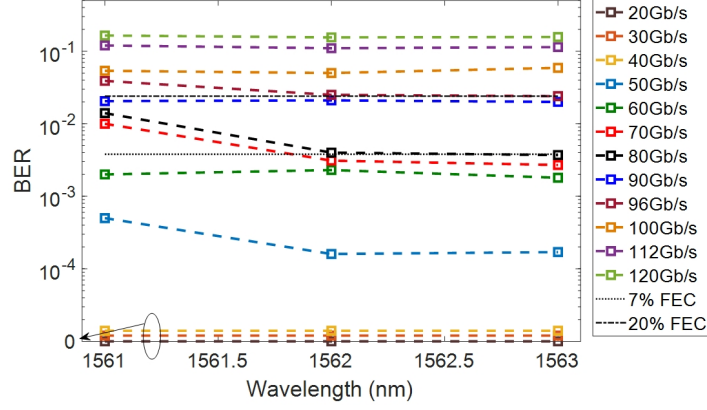


Figure 4.9 – BER spectral measurement of DAC-less SL-MZM for PAM-4 format. Dotted and dash-dotted lines show 7% and 20% FEC thresholds, respectively.

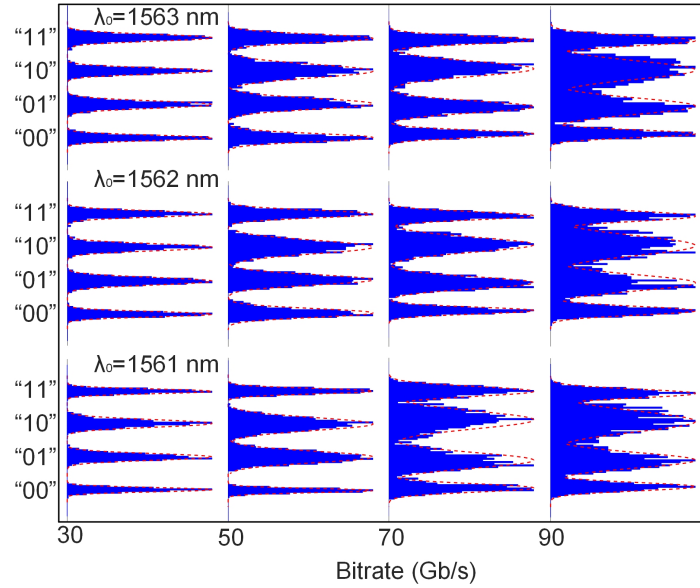


Figure 4.10 – Histograms of detected bits (one sample per symbol) used for BER calculation at different bit rates (30, 50, 70 and 90 Gb/s) and operational wavelengths (1561, 1562 and 1563 nm).

data rate achievable by the modulator. Secondly, as discussed above, gradually adapting the routing waveguide to the slow-light waveguide should also decrease insertion loss. Modulation speed of 100 Gb/s therefore seem within reach for this modulator with PAM-4.

4.4 Conclusion

In this paper, we demonstrated a new design of DAC-less PAM-4 SiP modulators based on the SL effect. BGRs integrated into each arm of a MZM structure slowed down the optical wave, leading to enhancement in the phase modulation, *i.e.*, a factor of 6 in the present case. In contrast to MRMs, this enhancement is achieved over a larger optical bandwidth, resulting in increased stability in per-

formance and enlarged EO bandwidth. The phase modulation enhancement results in a modulator with a compact footprint ($L_{SL-MZM} = 570 \mu\text{m}$) and low power consumption (only 73 fJ/bit). The SL-MZM was characterized by an EO bandwidth of $> 40 \text{ GHz}$ and was operated up to 90 Gb/s over an operating wavelength range of $\Delta\lambda_{BW} = 2 \text{ nm}$. This wavelength range guaranties an operation without any distortion in presence of temperature fluctuations up to $\Delta T = 50 \text{ }^\circ\text{C}$. Therefore, compared to MRM, the requirements on the thermal control are significantly relaxed, leading to reduced cost and complexity of the control circuit. Our DAC-less PAM-4 SL-MZM is clearly capable of addressing the tradeoff not only between efficiency and speed, but also between efficiency and stability.

Chapter 5

Fully integrated designs of SDM transmitters with compact footprint and power-efficient operation

Résumé- Dans ce chapitre, nous proposons des conceptions d'émetteurs SDM à quatre canaux utilisant des modulateurs SiP à lumière lente (SL) intégrés à un multiplexeur modal sur puce. Nous utilisons des modulateurs Mach-Zehnder (MZM) assistés par des résonateurs à réseau de Bragg en cascade (présentés dans la section 2.5) au lieu d'autres modulateurs SiP typiques (MZM conventionnels ou modulateurs à micro-anneau (MRM)). Comme discuté dans la section 2.3.3, les modulateurs SL fournissent un équilibre dans les indicateurs de performance tels que l'efficacité de modulation, la stabilité, l'efficacité énergétique et la vitesse de modulation. En effet, dans ces modulateurs, les résonateurs à réseau de Bragg ralentissent les ondes optiques dans une bande passante optique de l'ordre du nm, améliorant la modulation de phase sur une plage de longueurs d'onde relativement large pour obtenir un fonctionnement plus stable par rapport au modulateur de résonance unique (*e.g.*, MRMs).

Nous concevons un émetteur SDM pour les systèmes à courte portée basé sur des modulateurs SL à deux segments pilotés avec deux signaux binaires (démontré dans la section 4.2). Les deux segments SL sont conçus de telle sorte que la diaphonie RF intra-canal (fuite RF entre les deux déphaseurs série) est minimisée comme décrit dans la section 4.3.3. Entraînés par des électrodes localisées, les modulateurs PAM SL peuvent être situés très près les uns des autres sans souffrir de diaphonie RF inter-canal (diaphonie entre deux modulateurs SL adjacents), permettant une densité de bande passante élevée (vitesse par unité d'encombrement [Gb/s/m²]). Nous plaçons quatre de ces modulateurs PAM en configuration parallèle pour réaliser quatre canaux spatiaux. Nous ciblons également les transmissions de longue distance lors de la conception de modulateurs SL en phase et en quadrature (IQ) intégrés à des électrodes à ondes progressives (TW). Comme expliqué dans la section 3.3, les électrodes TW permettent aux modulateurs SL d'offrir simultanément des opérations à faible V_π et à

grande vitesse. Nous utilisons quatre de ces modulateurs IQ SL en parallèle avec une conception RF minutieuse pour supprimer la diaphonie RF inter-canaux. Les deux modèles (émetteurs SDM basés sur PAM et IQ) présentent une densité de bande passante élevée et une efficacité énergétique élevée.

En outre, nous présentons un modèle complet pour évaluer la pénalité de puissance d'émission totale (TPP) des émetteurs SDM pour les deux scénarios (modulateurs PAM SL et modulateurs IQ SL). Le modèle incorpore des pénalités de puissance dynamiques, initiées par de la compensation DAC et de la pré-distorsion du signal en raison de la bande passante finie des modulateurs SiP, ainsi que des pénalités de puissance statique, résultant de la perte de propagation et de la perte induite par la modulation. Le modèle indique que les deux conceptions fournissent des TPP optimaux.

Enfin, les signaux modulés provenant des modulateurs SL sont multiplexés spatialement par un multiplexeur modal sur puce. Le multiplexeur de mode conçu est composé de trois coupleurs directionnels asymétriques en cascade pour générer des modes d'ordre supérieur (dans ce cas, les modes TE₀, TE₁, TE₂ et TE₃). Nous avons déjà évoqué l'utilisation de cette structure comme séparateur de mode dans la section 1.3.2. En utilisant un mécanisme, ces signaux multiplexés spatialement sont dirigés vers une fibre à coeur elliptique faiblement multimode qui guide les modes mentionnés. Le multiplexeur modal sur puce nous permet de proposer des émetteurs SDM entièrement intégrés.

Abstract- In this chapter, we propose four-channel SDM transmitter designs using slow-light (SL) SiP modulators integrated with an on-chip mode multiplexer. We exploit Mach-Zehnder modulators (MZMs) assisted by cascaded Bragg grating resonators (presented in section 2.5) instead of other typical SiP modulators (conventional MZMs or micro-ring modulators (MRMs)). As discussed in section 2.3.3, SL modulators provide a balance in the performance indicators such as modulation efficiency, stability, power efficiency, and modulation speed. Indeed, in these modulators, Bragg grating resonators slow down optical waves in a nm-range optical bandwidth, enhancing phase modulation over a relatively broad wavelength range to achieve more stable operation compared to single-resonance-based modulators (*e.g.*, MRMs).

We design an SDM transmitter for short-reach systems based on two-segment SL modulators driven with two-binary signals (demonstrated in section 4.2). The two SL segments are engineered in the way that the intra-channel RF crosstalk (RF leakage between the two series phase shifters) will be minimized as discussed in section 4.3.3. Driven by lumped electrodes, PAM SL modulators can be located very close to each other without suffering from inter-channel RF crosstalk (crosstalk between two adjacent SL modulators), allowing high bandwidth density (speed per unit footprint [Gb/s/m²]). We place four of these PAM modulators in parallel configuration to realize four spatial channels. We also target long-haul transmissions in designing in-phase-and-quadrature (IQ) SL modulators integrated with travelling wave (TW) electrodes. As elaborated in section 3.3, TW electrodes enable SL modulators to simultaneously offer low V_π and high-speed operations. We employ four of these IQ SL modulators in parallel with a careful RF engineering to suppress inter-channel RF crosstalk. Both designs (PAM- and IQ-based SDM transmitters) feature high bandwidth density and high power

efficiency.

Furthermore, we present a comprehensive model to evaluate the total transmission power penalty (TPP) of SDM transmitters for both scenarios (PAM SL modulators and IQ SL modulators). The model incorporates dynamic power penalties, initiated by the DAC compensation and pre-distortion of signal due to finite bandwidth of SiP modulators, as well as static power penalties, resulted from propagation loss and modulation loss. The model indicates that both designs offer better TPPs.

Finally, the modulated signals coming from the SL modulators are spatially multiplexed by an on-chip mode multiplexer. The designed mode multiplexer is composed of three cascaded asymmetric directional couplers to generate higher order modes (in the present case TE₀, TE₁, TE₂, and TE₃ modes). We already reported using this structure as a mode splitter in section 1.3.2. Using a mechanism (for example, using 3D polymer waveguide), these spatially multiplexed signals are directed to a few-mode elliptical-core fiber that supports the mentioned modes. Having an on-chip mode multiplexer enables us to propose fully integrated SDM transmitters.

5.1 Introduction

During the last decade, time division multiplexing (TDM), polarization division multiplexing (PDM), wavelength division multiplexing (WDM), and coherent techniques enabled continuous evolution of optical communication systems with the fast growing demand. These techniques push the capacity of single mode fibers (SMFs) close to the Shannon limit, having little possibilities to increase capacity. The potential solution to tackling this limit lies in exploiting space as the last physical dimension for multiplexing data, an approach known as space division multiplexing (SDM). These spatial channels can be realized by multi-core fibers (MCFs), few-mode fibers (FMF), or even a combination of them. The trend toward utilizing SDM/WDM systems necessitates the integration of a large number of optical transmitters. Crucial considerations include footprint, power consumption, modulation speed, and reliability of integrated electro-optic (EO) devices. A solution optimizing all these requirements is desired.

Most existing efforts in SiP modulators for higher-order modulation formats have been focusing on MZMs due to their large optical bandwidth. However, because of the low modulation efficiency of the carrier dispersion effect, long phase shifters with TW electrodes are required, which brings other issues such as large RF loss, power consumption, and footprint. Also, due to the RF crosstalk between the long TW electrodes, these MZMs should be placed far enough from each other, decreasing bandwidth density. MRMs have been proposed to address these issues; however, they are quite sensitive to the operational wavelength so that they need additional complex circuits to achieve thermal stabilization, which consumes a large amount of energy.

In this chapter, we pursue the goal of developing high-performance optical SDM transmitters suited for next-generation high-capacity optical transmission systems: low-power, high-bandwidth, ultra-compact, stable, and fully integrated in SiP. The MZM assisted by coupled Bragg grating resonators increases phase modulation efficiency in each arm using resonators carefully designed to have larger optical bandwidth. This design simultaneously achieves advantages of low-power consumption, compact footprint, and relaxed requirements on the thermal control, leading to a significant reduction in cost and control circuit complexity. Their compact footprint allows for high-density integration for high-capacity SDM transceivers. Furthermore, we design an on-chip mode multiplexer with low crosstalk, broadband response, and compact footprint. This paves the path for a fully integrated SDM transmitter. We also present a system-performance study on SiP modulators via estimating the total transmission power penalty (TPP) in an unamplified link for PAM and QAM operations. It will be shown that SL modulators under an optimized design can simultaneously offer more compact footprint and reduce total TPP (reduced by 10 dB at 100 Gbaud) compared to the convectional MZM presented in Ref. [61].

5.2 Mode multiplexer

5.2.1 Different schemes for mode division multiplexing

Two strategies have been pursued to couple lights from optical chips to SDM fibers (MCFs or FMFs). The first strategy is to couple the modulated signals from optical chips to single mode fibers (SMFs), and then couple them from SMFs to SDM fibers, introducing off-chip mode division multiplexing (MDM). The off-chip MDM might be easier to implement, however at the cost of introducing a bulky transmission setup [90, 147]. The second strategy is to directly couple the lights from optical chips to SDM fibers, employing the on-chip MDM which offers ultra-compact transmitter [148].

In the off-chip MDM, to couple light from SMFs to MCFs, free space coupling and fiber coupling devices are demonstrated. Free space coupling is basically based on lens systems to combine multiples beams [90], offering low crosstalk; however, at the cost of introducing a bulky and sophisticated transmitter. Fiber coupling devices present a relatively more compact and simpler transmitter. This method is based on directly connecting the MCFs to the SMFs, for example, using tapered fiber bundle or multi-core connectors [147]. However, this scheme might suffer from crosstalk. For coupling SMFs to FMFs, other techniques have been proposed such as using phase plates, mirrors, beam splitters, q-plates, and fiber-based approach including photonic lantern, [90, 148–150]. These techniques are essentially based on free-space optics. These approaches feature a good mode selectivity. However, this benefit comes at cost of high insertion loss and cumbersome setups.

On the other hand, the on-chip MDM leveraging SiP technology offers a coupling scheme to FMFs with compact footprint. Last but not least, the on-chip MDM eliminates the need for a cumbersome setup and facilitates the path for a fully EO integrated transmitter. There have been different demonstrations on generating orbital-angular-momentum (OAM) modes [148, 151, 152] and linearly polarized (LP) modes [153].

In the following section as an example, we propose an on-chip mode multiplexer based on cascaded asymmetric directional couplers to generate TE modes (TE₀, TE₁, TE₂, and TE₃). These four spatial channels are guided into a few-mode highly-elliptical-core fiber that was fabricated in COPL [95]. Fig. 5.1 illustrates the mode profiles propagating in the fiber, showing that the fiber supports the expanded shapes of TE mode profiles that propagate in SiP waveguides, which will be discussed in details in section 5.4.1.

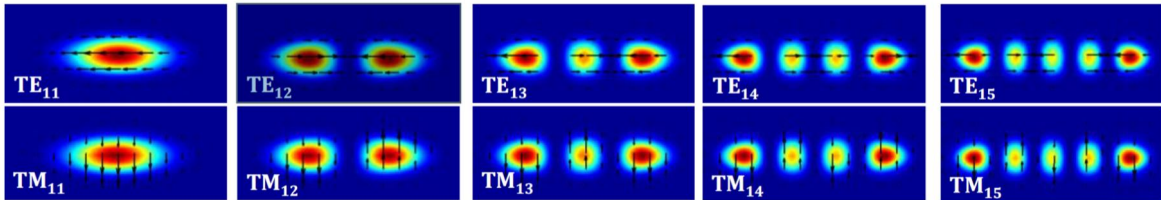


Figure 5.1 – TE and TM modes supported by in the highly-elliptical-core fiber.

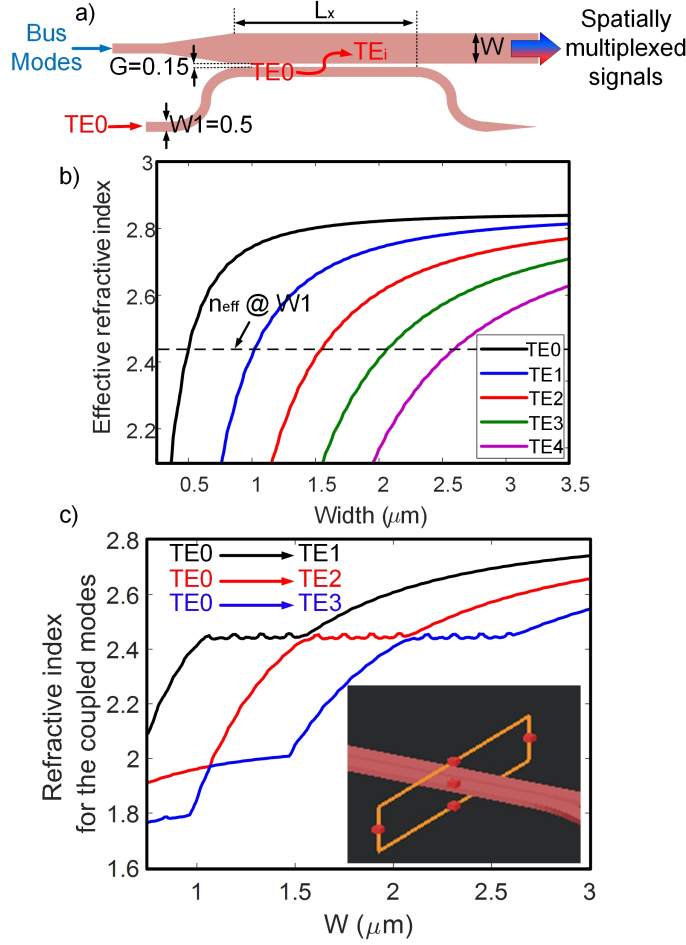


Figure 5.2 – a) Schematic of an asymmetric directional coupler b) effective refractive indices of TE0-TE4 as a function of width of the waveguide (W) c) mode coupling as a function of waveguide width (or super-mode simulation). The inset in (c) shows the simulation area in Lumerical-mode where the simulation area is defined on the cross-section of the coupling area (*i.e.*, including bus waveguide with width of W and the waveguide with width of 500 nm) .

5.2.2 Mode multiplexer design

In the SiP platform, directional couplers are the most common solution for combining and splitting optical powers due to their broadband response and low insertion loss under an optimized design. As shown in Fig. 5.2 (a), the concept of directional couplers can be also utilized to introduce the on-chip multi-mode SDM optical interconnects [154]. Optical powers in the fundamental mode will be entirely coupled to another mode in the bus waveguide if the phase matching, expressed in Eq. 5.1, is satisfied.

$$\beta_1 L_x - \beta_2 L_x = 0 \quad (5.1)$$

where β_1 and β_2 represent propagation constants of the two waveguides, L_x is the coupling length. We designed the asymmetric directional couplers for coupling different modes using Lumerical-Mode and Lumerical-FDTD. Fig. 5.2 (b) presents effective refractive indices of TE0-TE4 as a function

of width of the waveguide (W) as well as the effective index of the waveguide with a width of 500 nm. Fig. 5.2 (c) shows the effective refractive index of the coupled mode as a function of the width of the bus waveguide at $\lambda_0 = 1550$ nm. It shows that, for example, to couple TE0 to TE1 (the black line), the width of the bus waveguide should be $1 \leq W \leq 1.5$. Any chosen width (W) within this range corresponds with a specific coupling length (L_x). We specified the design values using Lumerical-FDTD (listed in Table 5.1) and their simulation results are shown in Fig. 5.3. As indicated, the coupling loss for the three cases is lower than 1 dB in the whole C-band. In addition, a slight power is coupled to undesired modes with crosstalk of less than 30 dB over the C-band. Finally, we cascade these asymmetric directional couplers, as displayed in Fig. 5.4, in order to spatially multiplex optical signals into four spatial channels.

5.3 Silicon photonic modulator designs

5.3.1 PAM transmission

Figure 5.5 shows the schematic of the PAM SL modulators that are proposed for the SDM transmitter targeting short-reach systems. In section 2.3.3, we elaborated the potential of using multiple cascaded low-Q-factor resonators to enhance phase modulation, improve energy efficiency, and offer a stable operation. Each arm of an MZM is loaded by a Bragg grating superstructure with a uniform period of $\Lambda = 300$ nm, a duty cycle of 50%, a minimum width of 250 nm, and a maximum width of 1000 nm. We introduce 30 phase-shifted sections along a uniform Bragg grating superstructure. Then, each resonator consists of a phase-shifted section with 38 grating periods on each side. We loaded the first 17 resonators and the last 12 resonators with PN junctions to introduce the two series segments, called “most significant bit (MSB) segment” and “least significant bit (LSB) segment”, respectively. Therefore, one cavity remains unloaded in order to minimize intra-channel RF crosstalk between these two segments.

As shown in Fig. 5.5, we considered two thermal elements to control the PAM SL modulator. The thermal element, labeled “1”, is utilized for shifting the superstructure’s spectrum if necessary. The other thermal element (labeled “4”) is placed in order to set the operating point of the modulator at the quadrature point. The modulator operates in the depletion mode under a single-drive push-pull configuration. The other two DC connections, labeled “2” and “3”, are used to adjust the bias point of LSB and MSB segments, respectively. Fig. 5.6 (a) illustrates the modulator’s layout designed in Pyxis, showing that the modulator is driven with lumped electrodes. Using lumped electrodes

Table 5.1 – The parameters of the designed directional couplers

	$W_1[\mu m]$	$G[\mu m]$	$W[\mu m]$	$L_x[\mu m]$
TE0 to TE1	0.5	0.15	1.03	32
TE0 to TE2	0.5	0.15	1.565	40
TE0 to TE3	0.5	0.15	2.095	50

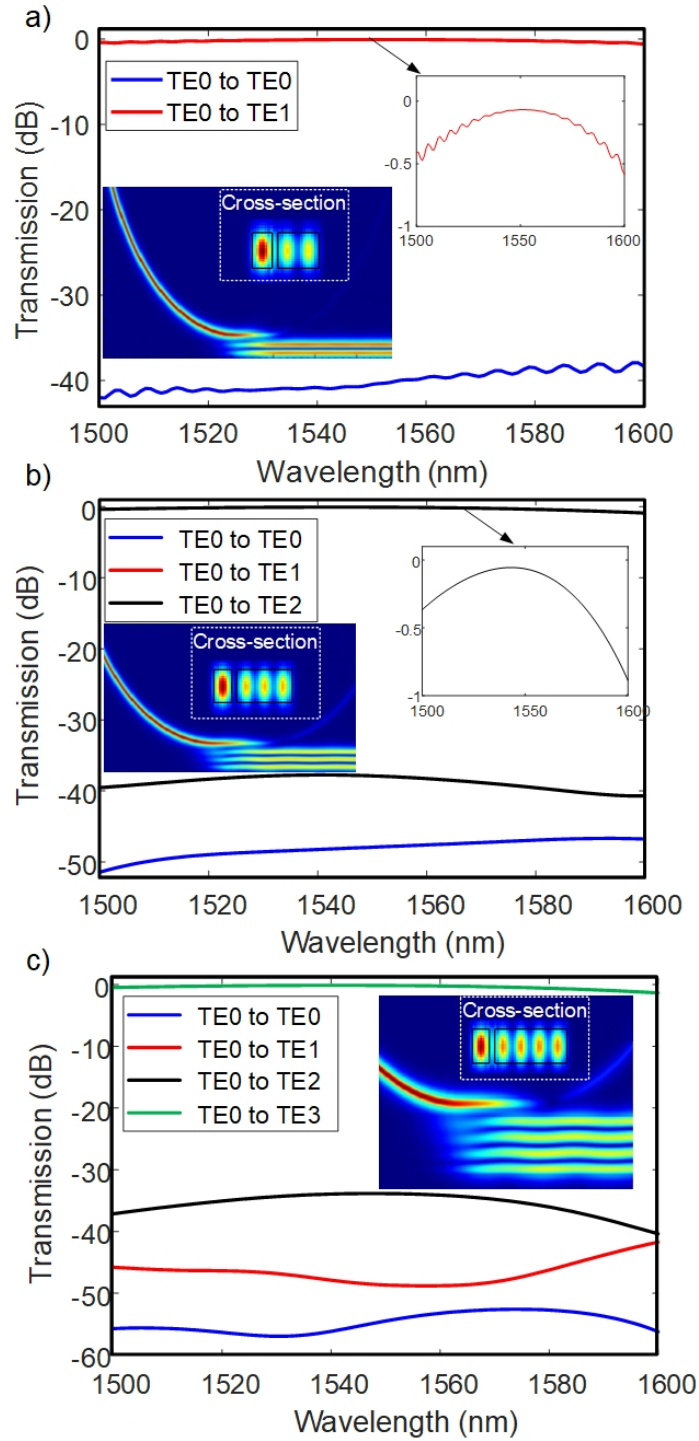


Figure 5.3 – Simulation results of asymmetric directional coupler when designed for coupling a) TE0 into TE1 b) TE0 into TE2 c) TE0 into TE3. The insets show the mode propagation for coupling of each design to desired mode in the bus waveguide as well as their cross-sections. In the simulations, the power monitors are placed after the coupling area plus $20 \mu\text{m}$

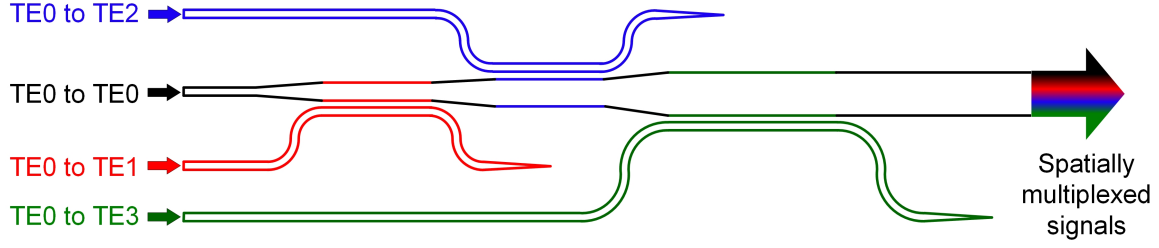


Figure 5.4 – Schematic of the mode multiplexer based on cascaded asymmetric directional couplers.

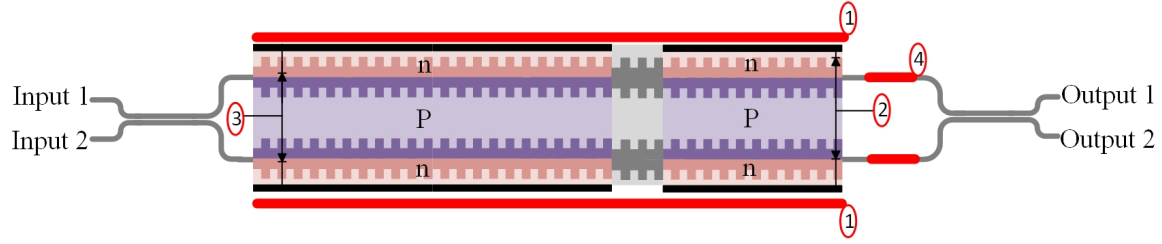


Figure 5.5 – Schematic of PAM SL modulators based on Bragg grating resonators with two segments and four DC elements to set the operating point and bias the modulator

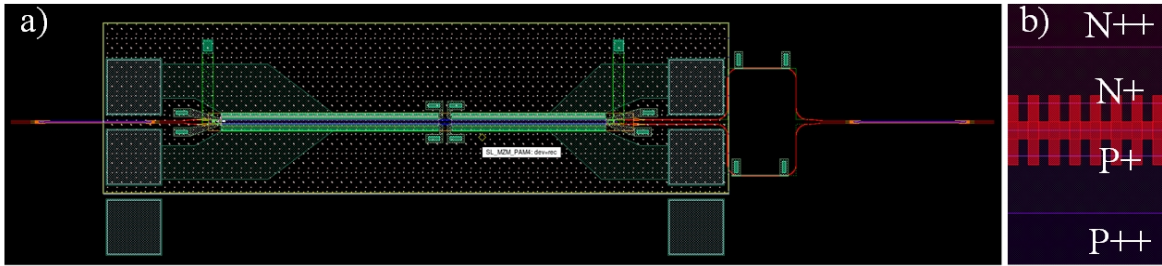


Figure 5.6 – a) Layout of PAM SL modulators designed in Pyxis b) a close view of Bragg grating structure.

enhances power efficiency and eliminates the in-channel RF crosstalk if several of these PAM modulators are placed close to each other, resulting in enhanced bandwidth density.

Figure 5.6 (b) shows a close-up view of the Bragg grating structure loaded with lateral PN junctions. As displayed, compared to our design in section 4.2, we use a four-layer PN junction, instead of six layers, loading the MSB and LSB segments with $P++ | P+ | N+ | N++$ junctions. Although it increases the insertion loss of the modulator, it enables the SL phase shifters to present higher modulation efficiency. In addition, it helps to slightly widen EO bandwidth. Our calculations show that highly doped SL modulators increase phase modulation by 42% compared to that of a normal-doped SL modulator. The extra loss introduced by highly doped PN junctions remains in an acceptable range (additional loss of 1 dB) as the length of the phase shifters is small. In our model, we use the following doping densities: $P++ = 10^{18} \text{ cm}^{-3}$, $N+ = 10^{18} \text{ cm}^{-3}$, $P = 5 \times 10^{17} \text{ cm}^{-3}$, and $N = 3 \times 10^{17} \text{ cm}^{-3}$.

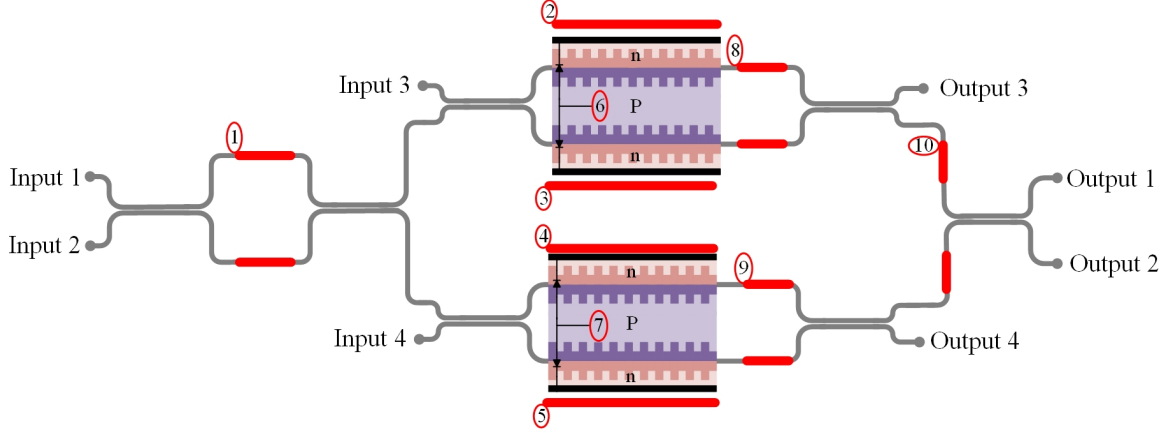


Figure 5.7 – Schematic of IQ SL modulators based on Bragg grating resonators

5.3.2 Coherent transmission

To realize an SDM transmitter for long-haul applications, we design an IQ SL modulator. Fig. 5.7 shows the modulator schematic consisting of the two MZMs assisted by Bragg grating resonators and a Mach-Zehnder interferometer (MZI) to adjust optical power between I and Q branches. As displayed, there are two inputs and two outputs (labeled by "1" and "2") for the whole IQ modulator. In addition, using the input and output labeled "3" ("4"), it is possible to monitor only I branch (Q branch), helping to characterize each modulator individually.

An integrated Bragg grating resonator, with a uniform period of $\Lambda = 300$ nm and thirty-coupled resonators, is placed in each arm of MZMs. Each resonator is composed of a phase-shifted section with 38 grating periods on each side. The Bragg gratings consist of sidewall corrugations with a duty cycle of 50% in a ridge waveguide having an average width of 625 nm, a ridge height of 220 nm and a slab height of 90 nm. The maximum and minimum widths are 1000 nm and 250 nm, respectively.

We employ eight thermal elements to control the IQ SL modulator. The four thermal elements labeled "2", "3", "4", and "5" are placed on top of each segment in order to fine-tune the resonance wavelength of each integrated Bragg grating resonator if required. The heaters labeled "8" and "9" are used to set operating point of the I- and Q-branch of the IQ modulator, respectively. The heater labeled "10" is used to introduce a $\pi/2$ phase shift between I- and Q-modulated signals. Finally, the thermal element labeled "1" is placed in one arm of the MZI to adjust the split power ratio between I- and Q-branch of the IQ modulator. The modulators are driven with the single-drive push-pull configuration using the depletion mode. The two other DC connections, labeled "6" and "7", are utilized to adjust the bias point of I and Q modulators, respectively.

Figure 5.8 (a) shows the modulator layout designed in Pyxis, showing that the modulator is driven with TW electrodes. As discussed in section 3.3, SL modulators are capable of reaching a good compromise between speed and efficiency if integrated with TW electrodes. The TW electrodes are designed based on coplanar stripline (CPS) configuration as illustrated in Fig. 5.9. In order to reduce

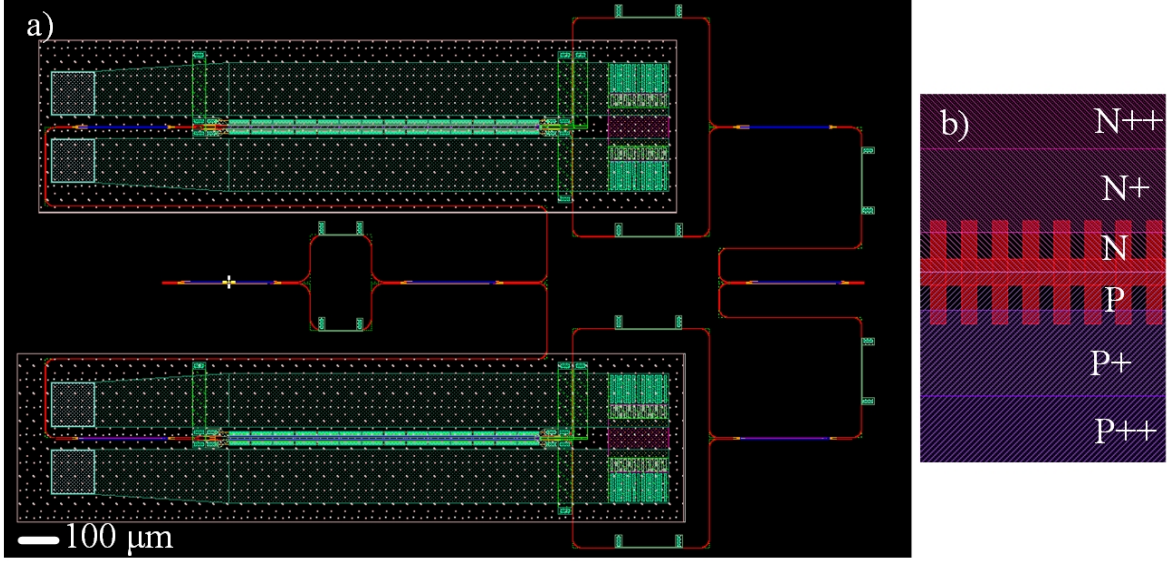


Figure 5.8 – a) Layout of IQ SL modulators designed in Pyxis b) a close view of Bragg grating structure.

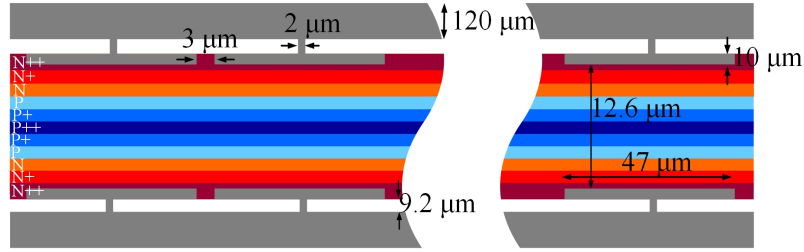


Figure 5.9 – Loaded TW electrode with "T" shaped extensions to increase the RF index

velocity mismatching between RF and optical signals, we add "T" shaped extensions to the CPS transmission line. These extensions introduce an additional metal capacitance while keeping the RF impedance 50Ω . As a result, they help to slow down RF signals, achieving a better match between RF and optical indices. The TW electrodes are terminated with on-chip 50Ω loads. The TW electrode design is explained in details in [61]. Despite the advantage of TW electrodes, the RF crosstalk between two adjacent TW electrodes necessitates a larger distance between these electrodes, losing bandwidth density (speed per unit footprint [Gb/s/m^2]). In [66], it is reported that the minimum distance between TW electrodes with a length of 4 mm should be $800 \mu\text{m}$ to assure possessing a crosstalk of $< -30 \text{ dB}$. The advantage of our IQ SL modulators compared to conventional TW MZMs is that we can place them much closer to each other since their length is several times shorter. In our design, we consider a distance of $400 \mu\text{m}$ between two adjacent TW electrodes.

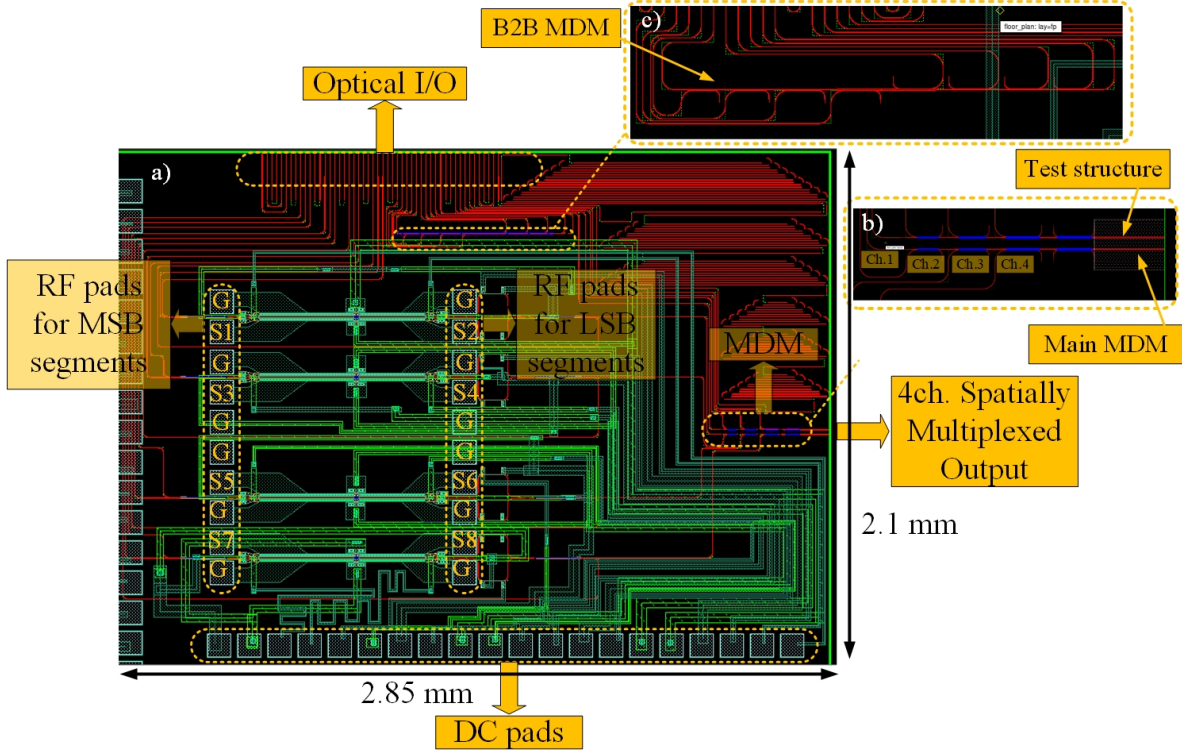


Figure 5.10 – a) Four-channel SDM transmitter based on PAM4 SL modulators, b) a close view of on-chip mode multiplexers, c) a close view of a back-to-back configuration of mode multiplexers

5.4 SDM transmitter designs

5.4.1 PAM transmission

Figure 5.10 (a) shows our design for a four-channel SDM transmitter targeting short-reach systems. It requires a space of $2.85 \times 2.1 \text{ mm}^2$ and consists of four PAM SL modulators described in section 5.3.1 and an on-chip mode multiplexer based on cascaded asymmetric directional couplers discussed in section 5.2.2. We positioned the modulators in a compact footprint ($\simeq 1.1 \times 1.2 \text{ mm}^2$) due to the beneficial attributes related to lumped electrodes. There are two sets of RF pads. The one in left (right) side is connected to MSB (LSB) segments. Each set is composed of 10 pads that can be driven with an RF probe with configuration of "GSGSGSGSGSG", which is commercially available with a fixed pin distance of $125 \mu\text{m}$. Therefore, it is possible to use the full potential of the transmitter without performing RF packaging. Note that due to the lack of on-chip load and in order to keep S11 low, the RF probes should be terminated with 50Ω loads.

There are twenty pads for DC connections. Each channel requires five of them for the MZM control as shown in Fig. 5.5. Note that one pad has been designed as common grounds of the all heaters to save the required space. In the case where DC packaging is not performed, all pads can still be connected with a DC probe with twenty pins.

Total number of optical inputs and outputs (I/Os) is fifty. We put edge couplers for chip-to-fiber light coupling because it offers less coupling loss compared to vertical couplers. The expected improvement is around 11 dB which has a significant impact on optical-signal-to-noise ratio (OSNR). The fifty optical I/Os have been distributed as 12 edge couplers for PAM SL modulators, 10 edge couplers for a back-to-back mode multiplexer, 4 edge couplers for a test mode multiplexer, and the rest used in a back-to-back configuration for different purposes. Using well-spaced routing waveguides, we connected three optical-I/O ports in each channel, named "Input 1", "Input 2", and "output 1" in Fig. 5.5, to the three edge couplers, being able to monitor each channel individually. The other port in Fig. 5.5, labeled "Output 2" is linked to the on-chip mode multiplexer.

The mode multiplexer, shown in Fig. 5.10 (b), is located in the right edge to provide a four-channel spatially multiplexed output. In addition to the main mode multiplexer, we placed a test mode multiplexer with a distance of $20\ \mu\text{m}$ from the main one. This test structure is directly connected to four of the edge couplers, allowing us to recognize the impact of the on-chip MDM on transmitted data. It can be also used to design a post-processing scheme to guide lights from the on-chip mode multiplexer to the highly-elliptical-core fiber. The scheme can be either based on 3D tapered polymer waveguide or based on special lenses. Fig. 5.11 shows profiles of the modes propagating in the fiber and the mode multiplexer (cross-section of the mode multiplexer output). In Lumerical-Mode, the simulation geometry for the mode multiplexer is defined as 16.5 times smaller than that of for the fiber ($3.03 \times 3.03\ \mu\text{m}^2$ vs. $50 \times 50\ \mu\text{m}^2$). As indicated in Fig. 5.11, the shapes of the mode profiles are almost similar; however, their sizes are different. Placing a 3D tapered polymer waveguide between these two components can be a possible solution by which the modes are allowed to be expanded in both horizontal and vertical directions. From the EO integration perspective, it is a desired solution with a potential of offering low coupling loss. The other solution is based on free space optics, using special lenses to magnify the mode size in horizontal and vertical directions as shown in Fig. 5.12. The required magnifications are approximately 27 and 14 in vertical and horizontal directions, respectively. We also placed a back-to-back configuration of the mode multiplexer, displayed in Fig. 5.10 (c), in our layout to evaluate the all-on-chip performance of the mode multiplexer.

5.4.2 Coherent transmission

Figure 5.13 (a) shows our layout for a four-channel SDM transmitter targeting long-haul applications. The required space is $6.1 \times 2.5\ \text{mm}^2$ and it consists of four IQ SL modulators explained in section 5.3.2 and an on-chip mode multiplexer discussed in section 5.2.2. We placed the IQ modulators with enough distance ($= 400\ \mu\text{m}$) from each other to minimize in-channel RF crosstalk. The set of RF pads is located in the top edge of the layout for RF connections. To exploit the full potential of the IQ-based SDM transmitter (exploiting all four spatial channels), an RF carrier should be designed with eight channels and then be connected to RF pads via either flip chip or wire-bonding. The pads are located with a space of $240\ \mu\text{m}$ from the top edge of the chip, well-positioned for RF packaging.

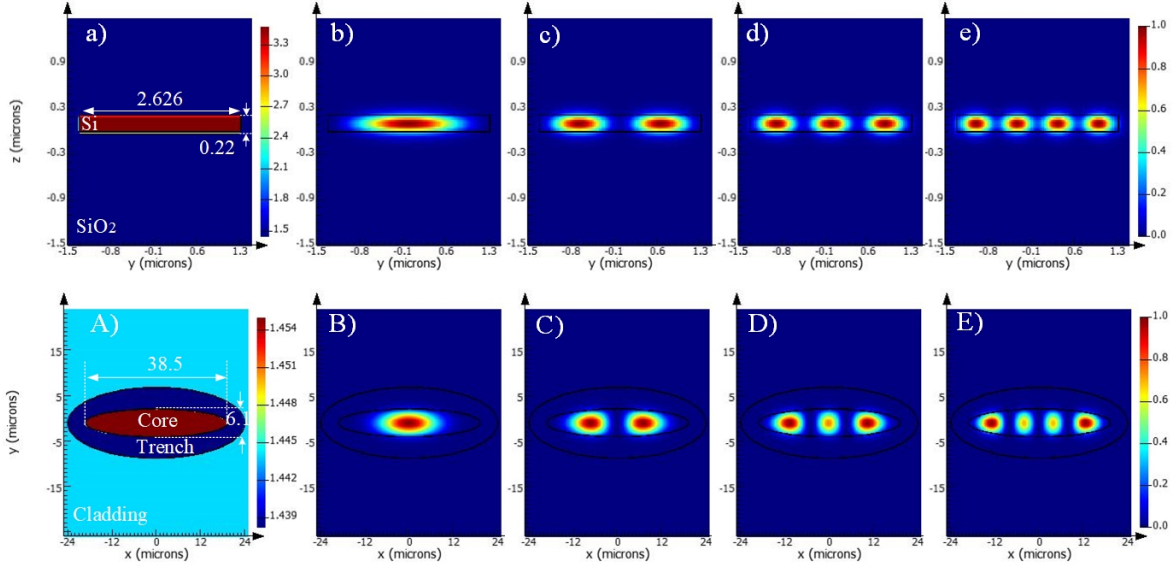


Figure 5.11 – Simulation results of the cross-section of the mode multiplexer output a) index profile, b) TE0 mode profile, c) TE1 mode profile, d) TE2 mode profile, e) TE3 mode profile. The capital letters show the same information for the highly-elliptical-core fiber in [95]

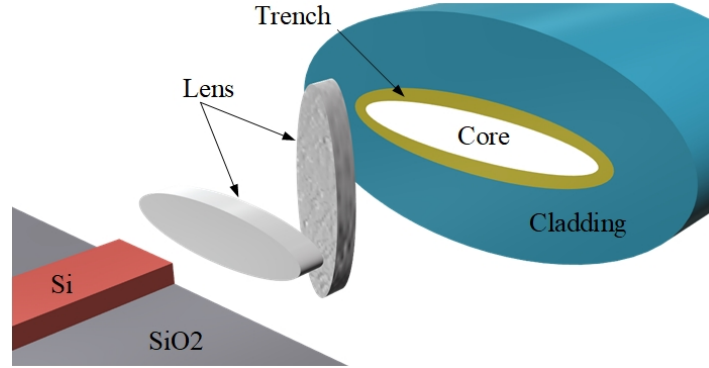


Figure 5.12 – Lens-based coupling scheme between the on-chip mode multiplexer and the highly elliptical core fiber

ing. However, it is still possible to drive two of the channels using two RF probes with a "GSSG" configuration. Note that due to the presence of on-chip 50- Ω loads, RF probes without terminations should be used.

Forty-eight pads are placed in the bottom edge for DC connections. Each channel requires twelve of these pads for setting operating points, fine-tuning the resonance wavelength of each arm, tuning bias points, and adjusting power between I- and Q-branch of IQ modulators (see Fig. 5.7). Note that two pads are used as common grounds for all the heaters.

Sixty-eight edge couplers are employed for optical I/Os. The optical I/Os have been distributed as 28 edge couplers for IQ SL modulators, 10 edge couplers for a back-to-back mode multiplexer, 4

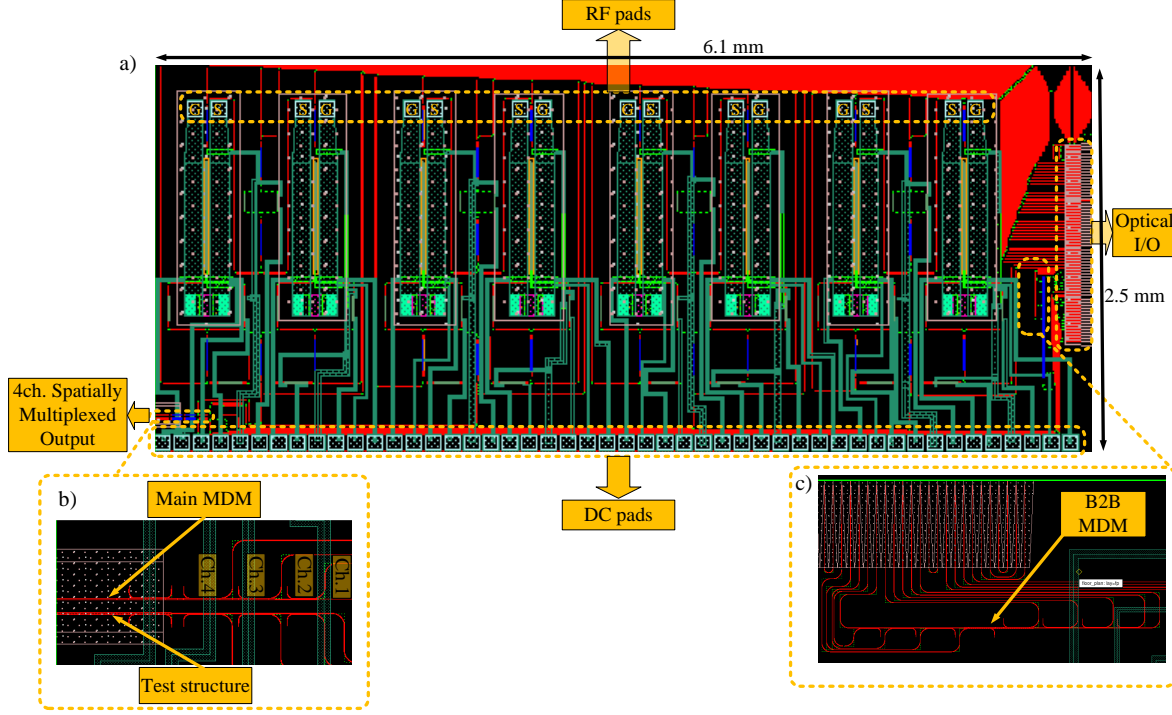


Figure 5.13 – a) Four-channel SDM transmitter based on IQ SL modulators, b) a close view of on-chip mode multiplexers, c) a close view of a back-to-back configuration of mode multiplexers

edge couplers for a test mode multiplexer, and the rest used in a back-to-back configuration. Each channel has eight optical I/O ports (see Fig. 5.7). The port, labeled "Output2" in Fig. 5.7, is linked to the on-chip mode multiplexer while the other ports are connected to the edge couplers.

The mode multiplexer, shown in Fig. 5.13 (b), is placed in the left edge to provide a four-channel spatially multiplexed output. In addition to the main mode multiplexer, similar to our design for the PAM SDM transmitter, we placed two test structures: a test mode multiplexer, shown 5.13 (b), and a back-to-back configuration of the mode multiplexer, displayed in Fig. 5.13 (c). These test structures were discussed in details in the fourth paragraph of section 5.4.1.

5.5 Transmission power penalty of slow-light modulators

We study system-oriented performance of SL modulators by estimating transmission power penalty (TPP) in an unamplified short-reach data links for PAM and coherent transmissions. As briefly mentioned in section 3.2.4, system-level degradations associated with SL modulators can be categorized into two main groups: static TPP and dynamic TPP. The static TPP results from propagation loss, mainly caused by absorption loss of PN junctions, as well as modulation loss, generated by producing less phase modulation than $\Delta\varphi < \pi$ (or a driving voltage of lower than $V_{pp} < V_\pi$). The dynamic TPP is created due to finite bandwidth of optical modulators. The finite bandwidth degrades high-frequency components, resulting in increased rise and fall times, and consequently, less opened eye

diagram in the PAM transmission or closer symbols in the coherent transmission. In the following sections, we evaluate the total TPP in the PAM and coherent transmissions.

5.5.1 PAM transmission

Figure 5.14 shows the block diagram of our model to calculate the total TPP for the PAM transmission at a 50-GBaud modulation speed. We first generate MSB (Fig. 5.14 (b)) and LSB signals. After applying pulse shaping, we assume that number of sample per symbol (SPS) is 5 and the DAC has a bandwidth of 50 GHz (Fig. 5.14 (c) and (d)). Then, we pre-compensate for the bandwidth limitation of the DAC applying a digital filter whose frequency transfer function is inverse of the DAC (Fig. 5.14 (e)). Compensation for the bandwidth limitation of SiP SL modulators requires calculating their EO response (Fig. 5.14 (f)) and pre-distorting signals accordingly (Fig. 5.14 (g)). Basically, in these two mentioned steps, we weaken low-frequency components in order to have a flatten spectrum after taking to account the bandwidth limitations induced by the DAC and SiP modulators up to the target speed. The EO response of SL modulators with lumped electrodes is calculated using the model presented in section 3.2.1. Thereafter, electrical signals are boosted (Fig. 5.14 (h)). The MSB (LSB) signal passes through an RF amplifier with a bandwidth of 30 GHz (50 GHz), a gain of 24 dB (23 dB), a saturated gain of 21 dBm (18 dBm). Note that we use the specs of RF amplifiers that are available in our lab. We set the bias point of the modulator in the reverse domain using a DC voltage of -1.75 V (Fig. 5.14 (i)). Note that we assume the modulator is driven using a single drive push-pull configuration. Finally, we apply the electrical signals to the MSB and LSB segments of the PAM SL SiP modulator described in section 5.3.1. Fig. 5.14 (k) shows the eye diagram of the modulated signal, composed of four distinct levels.

As indicated, even though the considered system is noise-less, the modulated eye diagram is not perfect and eye opening becomes closer compared to that of generated by an ideal system, *i.e.*, a system with no propagation loss, no modulation loss and infinite bandwidth. Hence, we define the total TPP as

$$TPP = 10 \times \log \left(\frac{d}{D} \right) \quad (5.2)$$

where d and D represent eye openings of the optical signal when modulated by non-ideal and ideal systems, respectively. Using Eq. 5.2, the total TPP for the PAM SL modulator designed in section 5.3.1 is calculated to be 6.1 dB. Fig. 5.15 reports the total TPP of SL SiP modulators with different designs, showing that the designed modulator with an enhancement factor of 6 provides almost an optimized TPP. This figure also indicates that optimized TPP is achieved in shorter phase shifter length when employing stronger SL effect (larger γ), resulting in more compact footprint. However, these designs are more susceptible to fabrication imperfections. Hence, in our design presented in section 5.3.1, we did not consider a strong SL effect to reach a compromise.

Figure 5.16 presents the total TPP of the designed PAM SL modulator for different baudrates. The trend in the graph indicates that up to a certain baudrate (60 GBaud), the total TPP remains constant because it is mainly caused by static limiting factors. Whereas, after 60 GBaud, the total

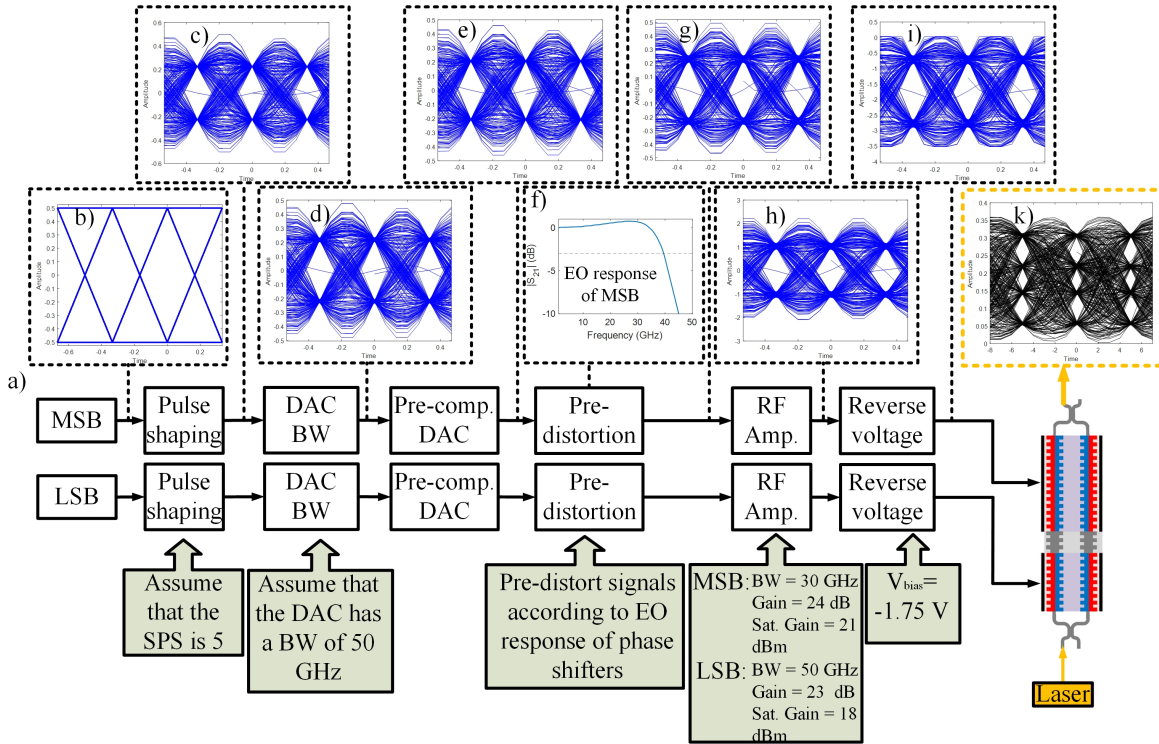


Figure 5.14 – a) Schematic of our model to calculate the total TPP of PAM SL modulators with lumped electrodes at baudrate of 50 GBaud, b) eye diagram of generated data, c) eye diagram of electrical signal after pulse shaping, d) eye diagram of electrical signal after applying bandwidth limitation of DAC, e) eye diagram of electrical signal after pre-compensating the DAC, f) EO response of the MSB segment, g) eye diagram of the pre-distorted signal due to the finite bandwidth of modulator, h) eye diagram of electrical signal after RF amplifier, i) eye diagram of applied signal to the modulator, k) eye diagram of optical modulated signal.

TPP sharply increases because the EO response has a sharp roll-off (see Fig. 5.14 (f)) and the operating speeds are larger than the 3-dB EO bandwidth, which is the dynamic TPP. The sharp roll-off comes from integration of the PAM SL modulator with lumped electrodes as explained in section 3.2.5.

5.5.2 QAM transmission

Figure 5.17 displays the schematic of our model for calculating the total TPP for the QAM transmission at a baudrate of 100 GBaud. We first generate I signal (Fig. 5.17 (b)) and Q signal. Then, we apply pulse shaping (Fig. 5.17 (c)). It is assumed that SPS is 5 and the DAC bandwidth is 50 GHz (Fig. 5.17 (d)). After that, we pre-compensate for the DAC employing a digital filter with a spectrum that is inverse of the DAC spectrum (Fig. 5.17 (e)). Next, similar to the previous section, we compensate for the impact of the finite bandwidth of SiP SL modulators by pre-distorting data with respect to the modulator's EO response (Fig. 5.17 (f) and (g)). We described in details how to calculate the EO response of SL modulators with TW electrodes in section 3.3.1. Thereafter, electrical signals are amplified using RF amplifiers with a bandwidth of 50 GHz, a gain of 23 dB, a saturated gain of 18

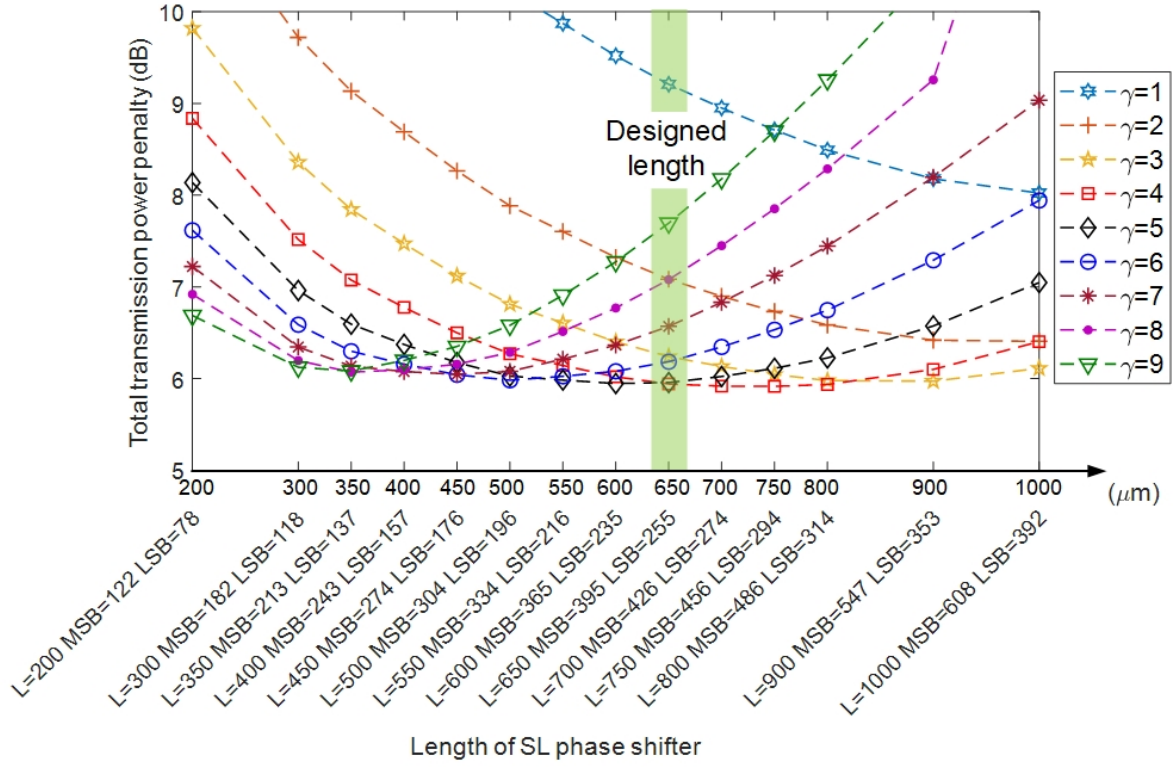


Figure 5.15 – Total transmission power penalty as a function of length of SL phase shifters for different enhancement factors (γ) at baudrate of 50 GBaud for PAM4 format.

dBm (Fig. 5.17 (h)). We adjust the bias point of the modulator in a reverse voltage of -1.25 V (Fig. 5.17 (i)). The modulator is driven under a single drive push-pull configuration. Finally, we apply the electrical signals to the I and Q branches of our IQ SL SiP modulator described in section 5.3.2.

Figure 5.17 (k) shows the constellation diagram of the modulated signal. Fig. 5.17 (m) illustrates the spectra of the electrical signal before and after implementing the pre-distortion as well as the spectrum of the optical modulated signal, clearly showing the impact of pre-distortion on the spectra. Fig. 5.18 shows the constellation diagram of 16- and 64-QAM signals at 100 GBaud in a ideal system (black stars), a system only suffering from the finite bandwidth (red dots), a system suffering from the finite bandwidth and modulation loss (blue dots), and a system suffering from the finite bandwidth, modulation loss, and on-chip propagation loss (yellow dots). This figure clearly shows the contribution of each limiting factor in the total TPP.

The total TPP in the coherent transmission similar to the PAM transmission is calculated using Eq. 5.2, where d and D are the distance between two adjacent points in constellation diagrams with and without presence of impairments from IQ SL modulators (non-ideal and ideal systems), respectively. We assess the total TPP of IQ SL modulators with different designs at baudrate of 50 GBaud. The results are reported in Fig. 5.19, showing that the designed IQ modulator with an

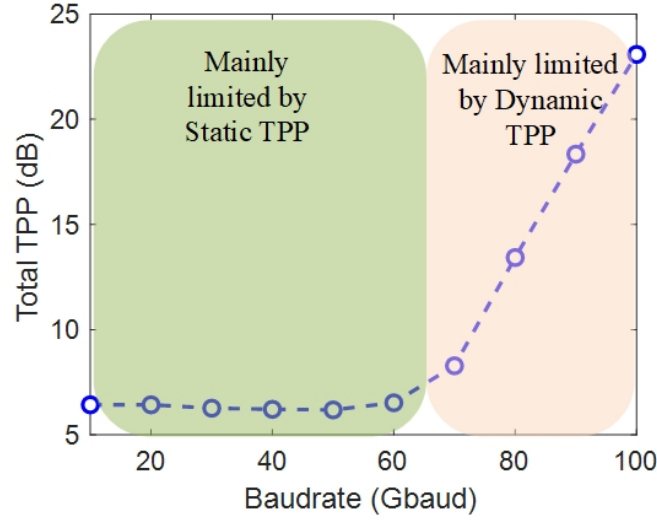


Figure 5.16 – Total transmission power penalty as a function of baudrate for the designed PAM SL modulator introduced in section 5.3.1.

enhancement factor of 6 offers almost an optimized TPP.

Figure 5.20 (a) shows the total TPP as a function of baudrate for the designed IQ SL modulator for different modulation formats (QPSK, 16QAM, and 64QAM). As indicated, the total TPP increases gradually, not sharply, with increasing the modulator speed because the modulator has a EO response with a smooth roll-off (see Fig. 5.17 (f)). The smooth roll-off is a result of integrating the IQ SL modulator with TW electrodes as discussed in section 3.3.3. Furthermore, it is observed that the total TPP is almost similar for all mentioned modulation formats, coming from the way that we define the TPP in Eq. 5.2. To realize the impact of higher modulation format on the performance, we introduce another factor, called probability error factor. This factor is defined as the distance between modulated symbols (d) normalized to the input optical field. Fig. 5.20 (b) presents the probability error factor versus baudrate, showing that the error factor sharply increases for higher-order QAM transmissions.

Slow-light modulators vs. conventional MZMs for QAM transmission

In this section, we aim to compare the designed IQ SL modulator with the conventional MZM reported in [61]. Fig. 5.21 presents the calculated TPPs of IQ SL modulators with an enhancement factor of $\gamma = 6$ (red solid curve) and IQ conventional MZMs (blue solid curve) as a function of their phase shifter length. We mark two spots in these two curves that represent the total TPP of our designed IQ SL modulator (discussed in section 5.3.2) and the reference IQ conventional MZM reported in Ref. [61]. As depicted, the designed SL modulator is capable of offering not only a more compact footprint but also less power penalty in comparison to the reference MZM. As mentioned in section 5.4.2, a four-channel SDM transmitter based on the IQ SL modulators requires a space of $\simeq 5.6 \times 1.7 \text{ mm}^2$, while the one based on conventional modulators needs approximately a $8 \times 6.1 \text{ mm}^2$

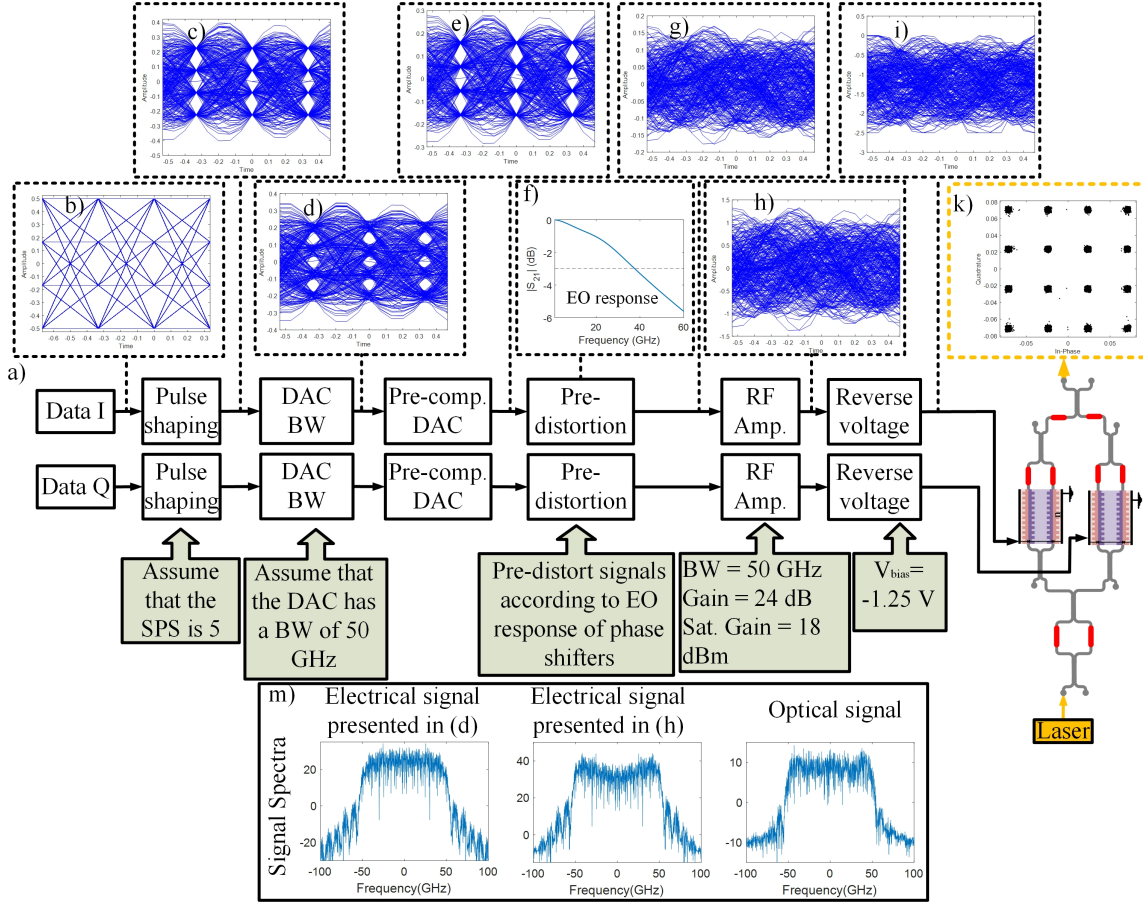


Figure 5.17 – a) Schematic of our model to calculate the total TPP of IQ SL modulators with TW electrodes at a baudrate of 100 GBaud, b) eye diagram of generated data, c) eye diagram of electrical signal after pulse shaping, d) eye diagram of electrical signal after applying bandwidth limitation of DAC, e) eye diagram of electrical signal after pre-compensating the DAC, f) EO response of the modulator, g) eye diagram of the pre-distorted signal due to the finite bandwidth of modulator, h) eye diagram of electrical signal after RF amplifier, i) eye diagram of applied signal to the modulator, k) constellation diagram of optical modulated signal

space [61]. Therefore, operated in the same baudrate, the SL-modulator-based transmitter improves the bandwidth density (speed per unit footprint [Gb/s/m^2]) by a factor of about 5.1 compared to the conventional-MZM-based transmitter. Additionally, the total TPP of the SL-modulator-based transmitter improves by 1.3 dB. To realize the generosity of our conclusion to RF amplifier, we repeat the analysis with a CMOS-compatible RF amplification (peak-to-peak voltage of 2.5 V with bandwidth of 50 GHz), the total TPP increases to 12 dB for our deigned IQ SL modulator and to 13.6 for the reference IQ conventional MZM, again showing 1.4 improvement in the total TPP. As shown, our conclusion is valid regardless of RF amplification.

Figure 5.21 also shows that IQ modulators with a conventional configuration offer the better TPP (7.9 dB) at 50 GBaud when employing a phase shifter with a length of 2.5 mm. Even with the optimized length, conventional MZMs cannot offer a better TPP compared to the proposed SL design

- * Ideal optical modulation
- Impact of finite bandwidth on the modulated signal
- Impact of finite bandwidth and modulation loss on the modulated signal
- Impact of finite bandwidth, modulation loss and on-chip propagation loss on the modulated signal

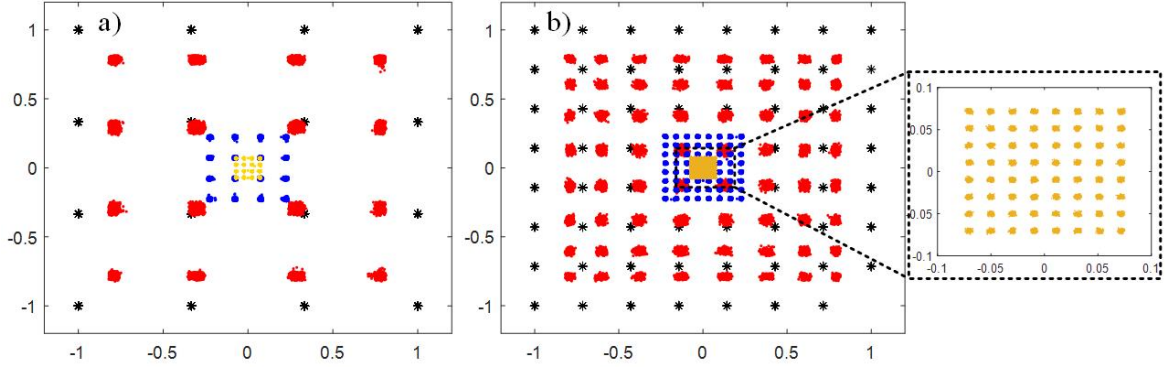


Figure 5.18 – Constellation diagram of modulated IQ signal for different scenarios at a baudrate of 100 GBaud for a) 16 QAM and b) 64 QAM.

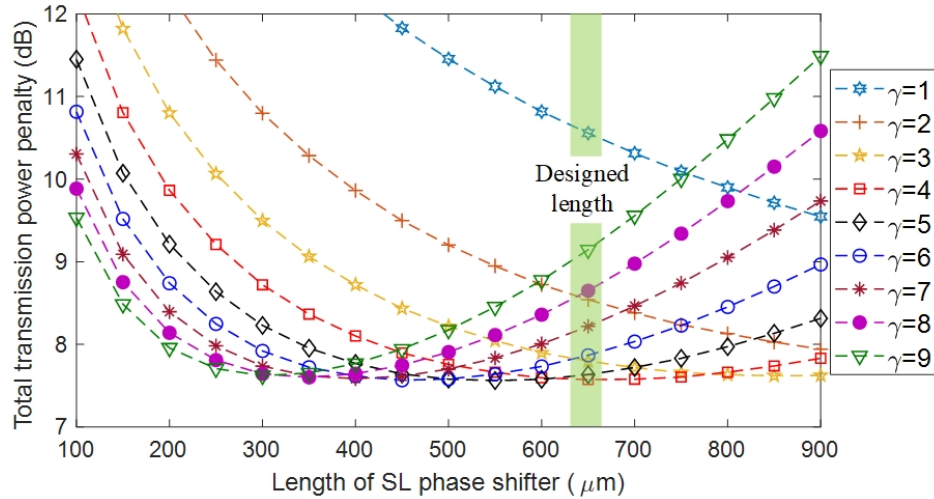


Figure 5.19 – Total transmission power penalty as a function of length of SL phase shifters for different enhancement factors (γ) for the 16 QAM format at a baudrate of 50 GBaud.

for the coherent transmission.

A considerable part of the total TPP of the IQ SL modulator is caused by high propagation loss in the SL waveguide (discussed in section 4.3.1, $\alpha_{SL-MZM} = 92 \text{ dB/cm}$). If propagation loss is improved through design and fabrication, the optimized modulator will demonstrate a significantly better TPP. For example, assuming that the propagation loss in the current SL design ($L_{SL-MZM} = 650 \mu\text{m}$) is reduced from 6 dB to 3 dB, the total TPP improves by 2 dB. The dash red curve in Fig 5.21 shows the total TPP of the improved SL modulator with a propagation loss of $\alpha_{SL-MZM} = 46 \text{ dB/cm}$ including the absorption loss. This improvement can be realized by employing a tapered

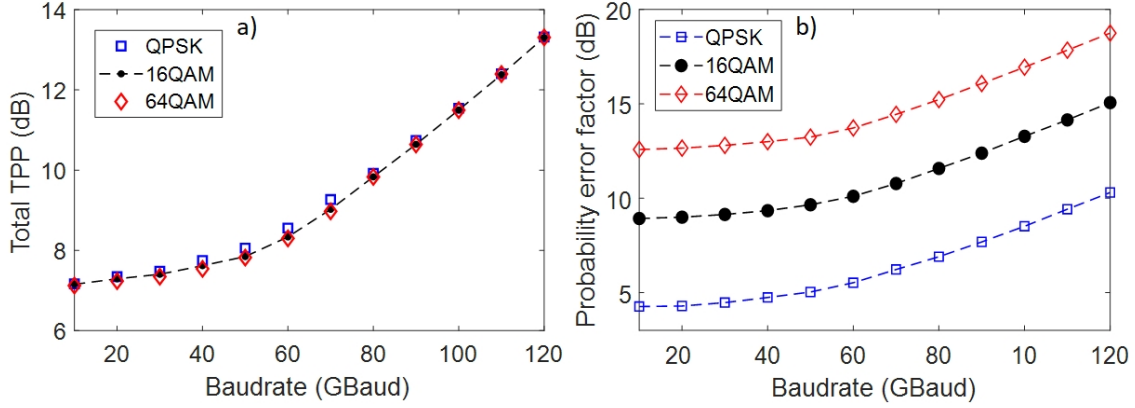


Figure 5.20 – a) Total transmission power penalty and b) probability error factor of the designed IQ SL modulator introduced in section 5.3.2 as a function of baudrate for different modulation formats.

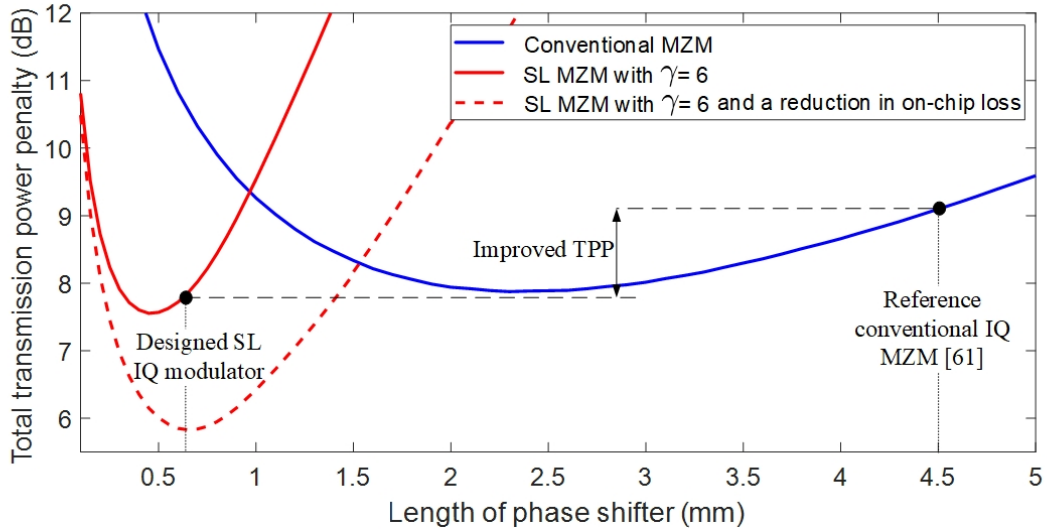


Figure 5.21 – Total transmission power penalty of IQ SL modulators with a γ of 6 (red line) and conventional MZMs (blue line) as a function of phase shifter length at 50 GBaud. The red dash line shows the TPP of an SL-MZM that presents less loss. The dot on the blue line shows the TPP of the reference conventional IQ MZM presented in [61], the dot on the red line represents the TPP of the designed IQ SL MZM, and finally the dot on the red dash line shows the better TPP of the structurally improved IQ SL MZM.

grating structure, for example. The optimized SL modulator would provide a reduction of 3.3 dB in the total TPP compared to conventional MZM reported in [61].

5.6 Conclusion

In this chapter, we proposed two designs of SDM transmitters, for short-reach and long-haul systems, that could be followed by an on-chip mode multiplexer to realize all-silicon transmitters. We

designed the transmitter for short-reach systems based on two-segment SL modulators integrated with lumped electrodes and for long-haul systems using IQ SL modulators integrated with TW electrodes. For both cases, we went through the design processes and the requirements for their measurements. Then, we demonstrated a comprehensive model for assessing the total TPP of SL modulators for both scenarios (PAM SL modulators and IQ SL modulators). We took into account both dynamic TPP and static TPP in our model. The model indicated that both designs offer almost optimized TPPs. We also proposed a design for on-chip mode multiplexers consisting of three cascaded asymmetric directional couplers to generate TE₁, TE₂, and TE₃ modes. Hence, the mode multiplexer creates four spatial channels. The simulation results show that the coupling loss of each mode is less than 1 dB and crosstalk (coupling the power to not desired modes) is also below 30 dB in the whole c-band.

The transmitters will be fabricated through a multi-project wafer run using a standard 193 nm lithography process at the IME (AMF) A*STAR with a silicon layer thickness of 220 nm and a 2 μ m buried oxide.

Conclusion and future works

In this thesis, we pursue the goal of developing high-performance optical transmitters. These transmitters require several modulators integrated into a single chip. These modulators should offer high-speed operation, low energy consumption, compact footprint, and stability simultaneously. Well-known silicon photonic (SiP) modulators, such as micro-ring modulators (MRMs) and Mach-Zehnder modulators (MZMs), do not meet all the aforementioned features. Hence, we start this thesis with exploring innovative SiP modulators that could reach a compromise in the performance. We experimentally demonstrated two novel SiP modulators, one of them based on the mode conversion and the other one based on the slow-light (SL) effect. The SL modulator provided a promising solution; hence, we explored its potential from a system-level perspective. Finally, we propose a vision for four-channel SDM transmitters based on SL modulators.

Our first contribution was to demonstrate a mode-conversion-based SiP modulator with a half-period offset between sidewall gratings. We experimentally reported a modulator operated in reflection with a low on-chip loss and without a circulator using an asymmetric Bragg grating (ABG) structure in a two-mode waveguide. The reflection operation provides a more efficient performance compared to the one in transmission. The ABG structure results in a contra-directional coupling between two orthogonal modes, in the present case between the incident TE₀ mode and the reflected TE₁ mode. This mode conversion offers an opportunity to introduce a device at the modulator input (asymmetric Y-junction or asymmetric directional couplers) as a mode splitter. The whole device therefore act similarly to an on-chip circulator. The modulator in the first demonstration, loaded with lateral junctions, had a low power consumption of 150 fJ/bit and operated with a BER below the 7% FEC threshold up to 30 Gb/s. In the second demonstration, we reported a mode-conversion based SiP modulator that takes advantage of both lateral and interleaved p-n junctions to enhance phase modulation. The modulator gained a 67% improvement in the phase modulation compared to the lateral one. The modulator operated up to 55 Gb/s with BER below the 20% FEC threshold showing great potential for high speed, low cost, compact ($L = 290 \mu\text{m}$), and power efficient (226 fJ/bit) transmissions. At the present case, the performance is limited by delay time introduced by the high corrugations of the Bragg grating structure. With optimizing the Bragg structure, it should be possible to improve the modulation speed. Also, the modulator performance also is sensitive to the operating point, similar to MRMs.

Employing strong corrugations helps to achieve a sharp response in the edge of the modulator spectrum even with a small length, resulting in high extinction ration. Nevertheless, it introduces higher insertion loss and larger delay time, which in turn limits the EO bandwidth of the modulator. For future works, Optimizing grating strength is critical to reach a compromise in the mentioned criteria. Furthermore, considering the fact that the optical modes are symmetric with respect to center of the waveguide, it is possible to exploit n-p-n junctions, instead of p-n junctions. Such n-p-n junctions introduce two parallel depletion regions along the waveguide, instead of one, resulting in an enhanced modal overlap, and thus, an improved phase modulation. Nevertheless, such a doping configuration is quite challenging for the standard CMOS manufacture. We propose segmented n-p-n junctions to meet the all the standards; however, having a low resistance introduced by n-p-n junction would still be an issue.

As the second contribution, we demonstrated a slow-light (SL) SiP modulator: a Mach-Zehnder modulator (MZM) assisted by coupled Bragg grating resonators (BGRs). We presented a design improving the tradeoff between optical bandwidth and power consumption, reaching a compromise between the large optical bandwidth of conventional MZMs and the high modulation efficiency of micro-ring modulators (MRMs). We employed cavities with low Q factors to improve optical bandwidth. The required phase modulation is then achieved by cascading several of these resonators along the waveguide, each resonator providing a fraction of the total required phase shift. We designed BGRs with large grating corrugations to obtain high photonic bandgaps. With these gratings, a large number of resonators can be placed in series, while keeping the overall footprint quite small. A comprehensive models in the frequency domain as well as the time domain for BGRs were presented that enabled us to carefully engineer the SL effect using BGRs. The SL modulator was experimentally characterized by a low power consumption (84 fJ/bit), an improved modulation efficiency (small-signal $V_\pi \times L = 0.18$ V.cm), and a compact footprint ($L = 162$ μ m). The modulator operated up to 30 Gb/s below the 7% FEC threshold over a temperature range larger than $\Delta T > 40$ °C.

According to our assessment, a big part of TPP introduced by SL modulators is caused by high propagation loss (static TPP). Reduction in the insertion loss can boost their performance significantly. Hence, it is important to study different design strategies in order to reduce the insertion loss of MZMs assisted by BGRs.

In our third contribution, we studied SL modulators considering the fundamental tradeoffs in SiP modulators. We assessed the performance of SL modulators compared to conventional MZMs taking into account electro-optic (OE) bandwidth and a FOM. The FOM examines key parameters such as efficiency, loss, and speed. To this end, we first modeled the EO behavior of SL modulators with lumped electrodes and TW electrodes. The model for lumped SL modulators showed that in addition to the RC time constant, the interaction time between the uniform voltage along electrodes and optical signals imposes a limitation on the modulator's speed. The FOM calculations indicated that the total transmission power penalty (TPP) associated with lumped SL modulators never becomes smaller than that of in the reference MZM. Next, we showed that the change in the type of

electrodes (replacing lumped electrodes by TW electrodes) enabled SL modulators to achieve a significant improvement in the EO bandwidth. This improvement allows SL modulators to outperform the reference MZM at high-speed operations. Finally, we discussed different design strategies to reduce V_π of conventional MZMs. It was shown that the SL effect offers the best-in-performance solution.

As discussed in this chapter, replacing lumped electrode by TW electrodes enables SL modulators to simultaneously reduce V_π and increase EO bandwidth, improving bandwidth-efficiency tradeoff. This shows the importance of driving schemes in SL modulators. A novel driving scheme that is exclusively designed for SL modulator can boost the performance of this modulator even more. With the current TW electrode, a considerable part of RF powers is dissipated upon the resistance terminator. Hence, An innovative design for driving SL modulators is desired.

Our fourth contribution was to demonstrate an SL SiP modulator to generate PAM4 without the need for digital-to-analog converters (DACs). Superstructural BGRs are carefully designed and loaded into each arm of an MZM to slow down the optical wave, resulting in enhancement in the phase modulation, an enhancement factor of $\gamma = 6$. This enhancement is offered over a larger optical bandwidth, which in turn results in enhanced stability and enlarged EO bandwidth. Due to the phase modulation enhancement, the modulator had a compact footprint and presented a low power consumption (only 73 fJ/bit). The modulator was experimentally characterized by an EO bandwidth of > 40 GHz and was operated up to 90 Gb/s over an operating wavelength range of $\Delta\lambda_{BW} = 2$ nm, corresponding to an operating tempeture range of $\Delta T = 50$ °C. The DAC-less PAM-4 SL modulator is capable of improving the tradeoff not only between efficiency and speed, but also between efficiency and stability. This indicates a promising solution for the next generation of 400 Gb/s SiP transmitters featuring low cost, high bandwidth density and less complexity for the thermal control circuit.

In the last contribution, we designed all-silicon SDM transmitters based on SL modulators followed by an on-chip mode multiplexer. The design features high bandwidth density, high power efficiency, and relatively stable operation. We aimed both short-reach and long-haul systems in designing PAM and IQ SL modulators, respectively. We employed MZMs assisted by cascaded BGRs as SL modulators. In short-reach transmissions, power budget and cost (power efficiency and footprint) outweigh all other criteria in importance; hence, we loaded SL modulators with lumped electrodes. Whereas, long-haul transmissions require high-performance modulators with low V_π and large EO bandwidth; thus, we integrated SL modulators with TW electrodes. We placed four of these IQ/PAM SL modulators in parallel configuration to realize four spatial channels after passing through the on-chip mode multiplexer. We also evaluated the total transmission power penalty (TPP) of these SDM transmitters through a comprehensive model. The model composed of both the dynamic TPP and the static TPP. Moreover, we designed a mode multiplexer based on three cascaded asymmetric directional couplers to generate higher order modes (in the present case TE₀, TE₁, TE₂, and TE₃ modes), featuring compact footprint, low insertion loss and low crosstalk.

For the future, there are two important aspects that should be studied in order to realize a full SDM transmission. 1) A post-processing scheme to guide lights from the on-chip mode multiplexer to the highly-elliptical-core fiber is vital for realizing the SDM transmission. We propose using 3D tapered polymer waveguide or designing special lenses in this case. 2) As the number of RF and DC inputs increases, RF and DC packagings reveal their importance. RF chip carrier with minimum crosstalk between RF signal paths has to be realized to reach the full potential of SDM transmitters.

Publication list

- 1 W. Shi, S. LaRochelle, **O. Jafari**, "OPTICAL PHASE MODULATOR AND OPTICAL MODULATOR", United States patent application US 16/978,785. 2020 Dec 31.
- 2 **O. Jafari**, H. Sepehrian, W. Shi, and S. LaRochelle, "High-Efficiency Silicon Photonic Modulator Using Coupled Bragg Grating Resonators", Journal of Lightwave Technology, 37(9), 2065-2075, 2019.
- 3 **O. Jafari**, W. Shi, and S. LaRochelle, "Mach-Zehnder Silicon Photonic Modulator Assisted by Phase-Shifted Bragg Gratings", IEEE Photonics Technology Letters, 32(8), 445-448, 2020.
- 4 **O. Jafari**, W. Shi, and S. LaRochelle, "Efficiency-speed tradeoff in slow-light silicon photonic modulators", IEEE Journal of Selected Topics in Quantum Electronics, 27(3), 2020.
- 5 **O. Jafari**, S. Zhalepour, W. Shi, and S. LaRochelle, "Mode-conversion-based Silicon photonic modulator loaded by a combination of lateral and interleaved p-n junctions", OSA Photonic Research, 9(4), 2021.
- 6 **O. Jafari**, S. Zhalepour, W. Shi, and S. LaRochelle, "Highly efficient DAC-less PAM-4 silicon photonic modulator with stable operation", Journal of Lightwave Technology, accepted.
- 7 **O. Jafari**, H. Sepehrian, W. Shi, and S. LaRochelle "Silicon Photonic Modulator based on Coupled Bragg Grating Resonators used as Phase Shifters", Optical Fiber Communication Conference (OFC), 2018.
- 8 **O. Jafari**, W. Shi, and S. LaRochelle. "Silicon Photonic Modulator Using Coupled Bragg Grating Resonators in a Mach-Zehnder structure", Conference on Lasers and Electro-Optics (CLEO), 2019.
- 9 **O. Jafari**, W. Shi, and S. LaRochelle, "Silicon Photonic Modulator using Mode Conversion with Asymmetric Sidewall Bragg Gratings", 2018 IEEE International Conference on Group IV Photonics (GFP). IEEE, 2018.
- 10 **O. Jafari**, J. Lin, W. Shi, and S. LaRochelle, "Mode-conversion-based silicon photonic modulator using asymmetric Bragg grating and Y-branch", European Conference on Optical Communication (ECOC), 2019.

- 11 **O. Jafari**, S. Zhalehpour, W. Shi, and S. LaRochelle, "Silicon photonic modulator based on asymmetric Bragg grating waveguides loaded by a combination of lateral and interleaved p-n junctions", OSA Advanced Photonics Congress, 2020.
- 12 **O. Jafari**, W. Shi, and S. LaRochelle, "A model for electro-optic response of slow-light silicon photonic modulators with lumped electrodes" IEEE Photonics conference (IPC), 2020.
- 13 **O. Jafari**, W. Shi, and S. LaRochelle, "Silicon photonic modulator loaded by NPN junctions", Photonics North Conference, 2020.
- 14 **O. Jafari**, S. Zhalepour, W. Shi, and S. LaRochelle, "DAC-Less PAM-4 Slow-Light Silicon Photonic Modulator Assisted by Coupled Bragg Grating Resonators", Optical Fiber Communications Conference (OFC), 2021.
- 15 M. Hasan, **O. Jafari**, X. Guan, L. A. Rusch, S. Larochelle, and T. Hall. "Integrated optical SSB modulation/frequency shifting using cascaded silicon MZM", IEEE Photonics Technology Letters. 2020.
- 16 D. Charron, J. St-Yves, **O. Jafari**, S. LaRochelle, W. Shi, "Subwavelength-grating contradirectional couplers for large stopband filters", Optics letters, 43(4), 895-898, 2018.

Bibliography

- [1] M. R. Tan, P. Rosenberg, W. V. Sorin, B. Wang, S. Mathai, G. Panotopoulos, and G. Rankin, "Universal Photonic Interconnect for Data Centers," *Journal of Lightwave Technology*, vol. 36, no. 2, pp. 175–180, 2018.
- [2] K. I. Kitayama, A. Hiramatsu, M. Fukui, T. Tsuritani, N. Yamanaka, S. Okamoto, M. Jinno, and M. Koga, "Photonic network vision 2020 - Toward smart photonic cloud," *Journal of Lightwave Technology*, vol. 32, no. 16, pp. 2760–2770, 2014.
- [3] C. Kachris and I. Tomkos, "A Survey on Optical Interconnects for Data Centers," *IEEE Communications Surveys & Tutorials*, vol. 14, no. 4, pp. 1021–1036, 2012.
- [4] S. Sakr, A. Liu, D. M. Batista, and M. Alomari, "A Survey of Large Scale Data Management Approaches in Cloud Environments," *IEEE Communications Surveys & Tutorials*, vol. 13, no. 3, pp. 311–336, 2011.
- [5] K. I. Sato, "Realization and Application of Large-Scale Fast Optical Circuit Switch for Data Center Networking," *Journal of Lightwave Technology*, vol. 36, no. 7, pp. 1411–1419, 2018.
- [6] T. Tekin, N. Pleros, R. Pitwon, and A. Hakansson, *Optical interconnects for data centers*. Woodhead Publishing, 2016.
- [7] M. Imran, P. Landais, M. Collier, and K. Katrinis, "A data center network featuring low latency and energy efficiency based on all optical core interconnect," in *2015 17th International Conference on Transparent Optical Networks (ICTON)*, pp. 1–4, IEEE, Jul 2015.
- [8] D. Lee, "Scaling Networks in Large Data Centers," in *Optical Fiber Communication Conference/National Fiber Optic Engineers Conference 2011*, (Washington, D.C.), p. OWU1, OSA, mar 2011.
- [9] "Vision and roadmap: Routing telecom and data centers toward efficient energy use," https://www1.eere.energy.gov/manufacturing/datacenters/pdfs/vision_and_roadmap.pdf.
- [10] M. Tan, P. Rosenberg, W. Sorin, S. Mathai, G. Panotopoulos, and G. Rankin, "Universal Photonic Interconnect for Data Centers," in *Optical Fiber Communication Conference*, vol. 36, (Washington, D.C.), p. Tu2B.4, OSA, 2017.

- [11] M. Hochberg, N. C. Harris, Ran Ding, Yi Zhang, A. Novack, Zhe Xuan, and T. Baehr-Jones, "Silicon Photonics: The Next Fabless Semiconductor Industry," *IEEE Solid-State Circuits Magazine*, vol. 5, no. 1, pp. 48–58, 2013.
- [12] T. Baehr-Jones, T. Pinguet, P. Lo Guo-Qiang, S. Danziger, D. Prather, and M. Hochberg, "Myths and rumours of silicon photonics," *Nature Photonics*, vol. 6, pp. 206–208, Apr 2012.
- [13] A. Spott, J. Peters, M. L. Davenport, E. J. Stanton, C. D. Merritt, W. W. Bewley, I. Vurgaftman, C. S. Kim, J. R. Meyer, J. Kirch, L. J. Mawst, D. Botez, and J. E. Bowers, "Quantum cascade laser on silicon," *Optica*, vol. 3, p. 545, May 2016.
- [14] H. Rong, R. Jones, A. Liu, O. Cohen, D. Hak, A. Fang, and M. Paniccia, "A continuous-wave Raman silicon laser," *Nature*, vol. 433, pp. 725–728, Feb 2005.
- [15] D. Liang and J. E. Bowers, "Recent progress in lasers on silicon," *Nature Photonics*, vol. 4, pp. 511–517, Aug 2010.
- [16] M. Ahmadi, L. Bodiou, W. Shi, and S. LaRochelle, "Comprehensive modeling and design of raman lasers on soi for mid-infrared application," *Journal of Lightwave Technology*, 2020.
- [17] Q. Xu, B. Schmidt, S. Pradhan, and M. Lipson, "Micrometre-scale silicon electro-optic modulator," *Nature*, vol. 435, pp. 325–327, May 2005.
- [18] M. Caverley, X. Wang, K. Murray, N. A. Jaeger, and L. Chrostowski, "Silicon-on-Insulator Modulators Using a Quarter-Wave Phase-Shifted Bragg Grating," *IEEE Photonics Technology Letters*, vol. 27, pp. 2331–2334, Nov 2015.
- [19] J. Sun, M. Sakib, J. Driscoll, R. Kumar, and H. Jayatilleka, "A 128 Gb / s PAM4 Silicon Microring Modulator," *Optical Fiber Communication Conference*, vol. 1, p. Th4A.7, 2018.
- [20] K. Bédard, A. D. Simard, B. Filion, Y. Painchaud, L. A. Rusch, and S. LaRochelle, "Dual phase-shift Bragg grating silicon photonic modulator operating up to 60 Gb/s," *Optics Express*, vol. 24, no. 3, p. 2413, 2016.
- [21] R. Dubé-Demers, S. LaRochelle, and W. Shi, "Ultrafast pulse-amplitude modulation with a femtojoule silicon photonic modulator," *Optica*, vol. 3, no. 6, pp. 622–627, 2016.
- [22] Q. Xu, S. Manipatruni, B. Schmidt, J. Shakya, and M. Lipson, "12.5 Gbit/s carrier-injection-based silicon micro-ring silicon modulators," *Optics Express*, vol. 15, no. 2, pp. 430–436, 2007.
- [23] S. Romero-García, A. Moscoso-Mártir, S. S. Azadeh, J. Müller, B. Shen, F. Merget, and J. Witzens, "High-speed resonantly enhanced silicon photonics modulator with a large operating temperature range," *Optics Letters*, vol. 42, no. 1, pp. 81–84, 2017.
- [24] G. T. Reed, G. Mashanovich, F. Y. Gardes, and D. J. Thomson, "Silicon optical modulators," *Nature Photonics*, vol. 4, pp. 518–526, Aug 2010.

- [25] A. Brimont, D. J. Thomson, F. Y. Gardes, J. M. Fedeli, G. T. Reed, J. Martí, and P. Sanchis, "High-contrast 40 Gb/s operation of a 500 μm long silicon carrier-depletion slow wave modulator," *Optics Letters*, vol. 37, no. 17, pp. 3504–3506, 2012.
- [26] R. Hosseini, L. Mirzoyan, and K. Jamshidi, "Energy consumption enhancement of reverse-biased silicon-based Mach-zehnder modulators using corrugated slow light waveguides," *IEEE Photonics Journal*, vol. 10, no. 1, pp. 1–7, 2018.
- [27] M. Feng, J. Wang, R. Zhou, Q. Sun, H. Gao, Y. Zhou, J. Liu, Y. Huang, S. Zhang, M. Ikeda, H. Wang, Y. Zhang, Y. Wang, and H. Yang, "On-Chip Integration of GaN-Based Laser, Modulator, and Photodetector Grown on Si," *IEEE Journal of Selected Topics in Quantum Electronics*, vol. 24, pp. 1–5, Nov 2018.
- [28] H. Qiu, J. Jiang, P. Yu, T. Dai, J. Yang, H. Yu, and X. Jiang, "Silicon band-rejection and band-pass filter based on asymmetric Bragg sidewall gratings in a multimode waveguide," *Optics Letters*, vol. 41, p. 2450, Jun 2016.
- [29] D. Charron, J. St-Yves, O. Jafari, S. LaRochelle, and W. Shi, "Subwavelength-grating contradi-rectional couplers for large stopband filters," *Optics letters*, vol. 43, no. 4, pp. 895–898, 2018.
- [30] Q. Han, M. Ménard, and W. Shi, "Silicon nitride arrayed waveguide grating with a waveguide superlattice," in *2020 Conference on Lasers and Electro-Optics (CLEO)*, pp. 1–2, IEEE, 2020.
- [31] Q. Han, J. St-Yves, Y. Chen, M. Ménard, and W. Shi, "Polarization-insensitive silicon nitride arrayed waveguide grating," *Optics letters*, vol. 44, no. 16, pp. 3976–3979, 2019.
- [32] P. C. Eng, S. Song, and B. Ping, "State-of-the-art photodetectors for optoelectronic integration at telecommunication wavelength," *Nanophotonics*, vol. 4, pp. 277–302, Jan 2015.
- [33] M. N. N. Sakib, J. Sun, R. Kumar, J. Driscoll, and H. Rong, "Demonstration of a 50 Gb/s all-silicon waveguide photodetector for photonic integration," in *Conference on Lasers and Electro-Optics*, (Washington, D.C.), p. JTh5A.7, OSA, May 2018.
- [34] B. W. Jia, K. H. Tan, W. K. Loke, S. Wicaksono, K. H. Lee, and S. F. Yoon, "Monolithic Integration of InSb Photodetector on Silicon for Mid-Infrared Silicon Photonics," *ACS Photonics*, vol. 5, pp. 1512–1520, Apr 2018.
- [35] C. Shang, Y. Wan, D. Jung, J. Norman, M. Kennedy, D. Liang, C. Zhang, A. C. Gossard, J. E. Bowers, A. C. Gossard, J. E. Bowers, J. E. Bowers, and J. E. Bowers, "Quantum dot micro-lasers integrated with photodetectors and optical amplifiers on (001) Si via waveguide coupling," in *Conference on Lasers and Electro-Optics*, (Washington, D.C.), p. SM2I.6, OSA, May 2018.
- [36] M. Casalino, "Design of Resonant Cavity-Enhanced Schottky Graphene/Silicon Photodetectors at 1550 nm," *Journal of Lightwave Technology*, vol. 36, pp. 1766–1774, May 2018.

- [37] R. A. Soref and J. P. Lorenzo, "Single-crystal silicon: a new material for 1.3 and 1.6 μm integrated-optical components," *Electronics Letters*, vol. 21, pp. 953–954, October 1985.
- [38] H. Li, G. Balamurugan, T. Kim, M. N. Sakib, R. Kumar, H. Rong, J. Jaussi, and B. Casper, "A 3-d-integrated silicon photonic microring-based 112-gb/s pam-4 transmitter with nonlinear equalization and thermal control," *IEEE Journal of Solid-State Circuits*, 2020.
- [39] B. Casper, G. Balamurugan, H. Rong, H. Li, H. Jayatilleka, J. Jaussi, J. Driscoll, J. Sun, M. Sakib, and R. Kumar, "A 112 Gb/s PAM4 Silicon Photonics Transmitter With Microring Modulator and CMOS Driver," *Journal of Lightwave Technology*, vol. 38, no. 1, pp. 131–138, 2020.
- [40] J. Sun, R. Kumar, M. Sakib, J. B. Driscoll, H. Jayatilleka, and H. Rong, "A 128 Gb/s PAM4 Silicon Microring Modulator With Integrated Thermo-Optic Resonance Tuning," *Journal of Lightwave Technology*, vol. 37, no. 1, pp. 110–115, 2019.
- [41] S. Fatholouloumi, K. Nguyen, H. Mahalingam, M. Sakib, Z. Li, C. Seibert, M. Montazeri, J. Chen, J. K. Doyle, H. Jayatilleka, *et al.*, "1.6 tbps silicon photonics integrated circuit for co-packaged optical-io switch applications," in *Optical Fiber Communication Conference*, pp. T3H–1, Optical Society of America, 2020.
- [42] E. Timurdogan, Z. Su, R.-J. Shiue, M. J. Byrd, C. V. Poulton, K. Jabon, C. DeRose, B. R. Moss, E. S. Hosseini, I. Duzevik, M. Whitson, R. P. Millman, D. A. Atlas, and M. R. Watts, "400G Silicon Photonics Integrated Circuit Transceiver Chipsets for CPO, OBO, and Pluggable Modules," in *Optical Fiber Communication Conference (OFC)*, (Washington, D.C.), p. T3H.2, OSA, 2020.
- [43] E. Maniloff, S. Gareau, and M. Moyer, "400g and beyond: Coherent evolution to high-capacity inter data center links," in *2019 Optical Fiber Communications Conference and Exhibition (OFC)*, pp. 1–3, IEEE, 2019.
- [44] "http://www.yole.fr,"
- [45] T. Liljeberg, "Silicon photonics and the future of optical connectivity in the data center," in *6th IEEE Photonics Society Optical Interconnects Conference, OI 2017*, pp. 1–2, Institute of Electrical and Electronics Engineers Inc., 2017.
- [46] Z. Zhou, B. Yin, and J. Michel, "On-chip light sources for silicon photonics," *Light: Science & Applications*, vol. 4, no. 11, p. e358, 2015.
- [47] L. Chrostowski and M. E. Hochberg, *Silicon photonics design*. Cambridge University Press, 2015.
- [48] V. Stojanović, R. J. Ram, M. Popović, S. Lin, S. Moazeni, M. Wade, C. Sun, L. Alloatti, A. Atabaki, F. Pavanello, N. Mehta, and P. Bhargava, "Monolithic silicon-photonics platforms in state-of-the-art CMOS SOI processes [Invited]," *Optics Express*, vol. 26, no. 10, pp. 13106–13121, 2018.

- [49] N. Feilchenfeld, F. Anderson, T. Barwicz, S. Chilstedt, Y. Ding, J. Ellis-Monaghan, D. Gill, C. Hedges, J. Hofrichter, F. Horst, *et al.*, “An integrated silicon photonics technology for o-band datacom,” in *2015 IEEE International Electron Devices Meeting (IEDM)*, pp. 25–7, IEEE, 2015.
- [50] M. Zhang, C. Wang, X. Chen, M. Bertrand, A. Shams-Ansari, S. Chandrasekhar, P. Winzer, M. Lončar, and M. Lončar, “Ultra-High Bandwidth Integrated Lithium Niobate Modulators with Record-Low V_π ,” in *Optical Fiber Communication Conference Postdeadline Papers*, (Washington, D.C.), p. Th4A.5, OSA, Mar 2018.
- [51] C. Wang, M. Zhang, X. Chen, M. Bertrand, A. Shams-Ansari, S. Chandrasekhar, P. Winzer, M. Lončar, P. Winzer, and M. Lončar, “100-GHz Low Voltage Integrated Lithium Niobate Modulators,” in *Conference on Lasers and Electro-Optics*, (Washington, D.C.), p. SM3B.4, OSA, May 2018.
- [52] C. Wang, M. Zhang, B. Stern, M. Lipson, and M. Lončar, “Nanophotonic lithium niobate electro-optic modulators,” *Optics Express*, vol. 26, p. 1547, Jan 2018.
- [53] R. Walker, “High-speed III-V semiconductor intensity modulators,” *IEEE Journal of Quantum Electronics*, vol. 27, pp. 654–667, Mar 1991.
- [54] T. Hiraki, T. Aihara, K. Hasebe, K. Takeda, T. Fujii, T. Kakitsuka, T. Tsuchizawa, H. Fukuda, and S. Matsuo, “Heterogeneously integrated III–V/Si MOS capacitor Mach–Zehnder modulator,” *Nature Photonics*, vol. 11, pp. 482–485, Jul 2017.
- [55] S. A. Baig, J. L. Boland, D. A. Damry, H. H. Tan, C. Jagadish, H. J. Joyce, and M. B. Johnston, “An Ultrafast Switchable Terahertz Polarization Modulator Based on III–V Semiconductor Nanowires,” *Nano Letters*, vol. 17, pp. 2603–2610, Apr 2017.
- [56] V. Lal, P. Studenkov, T. Frost, H. Tsai, B. Behnia, J. Osenbach, S. Wolf, R. Going, S. Porto, R. Maher, *et al.*, “1.6 tbps coherent 2-channel transceiver using a monolithic tx/rx in p and single sig asic,” in *Optical Fiber Communication Conference*, pp. M3A–2, Optical Society of America, 2020.
- [57] A. Chen and E. Murphy, *Broadband optical modulators: science, technology, and applications*. CRC press, 2011.
- [58] F. Eltes, J. Fompeyrine, and S. Abel, “Ultra-efficient optical switching based on a large pockels effect embedded in silicon photonics,” in *Optical Fiber Communication Conference*, pp. W1H–4, Optical Society of America, 2020.
- [59] R. Soref and B. Bennett, “Electrooptical effects in silicon,” *IEEE Journal of Quantum Electronics*, vol. 23, pp. 123–129, Jan 1987.

- [60] W. S. Sasan Zhalehpour, Jiachuan Lin, Mengqi Guo, Hassan Sepehrian, Zhuhong Zhang, Leslie A. Rusch, "All-Silicon IQ Modulator for 100 GBaud 32QAM Transmissions," *Optical Fiber Communication Conference Postdeadline Papers*, vol. Th4A.5, 2019.
- [61] H. Sepehrian, J. Lin, L. A. Rusch, and W. Shi, "Silicon Photonic IQ Modulators for 400 Gb/s and Beyond," *Journal of Lightwave Technology*, vol. 37, no. 13, pp. 3078–3086, 2019.
- [62] D. Patel, S. Ghosh, M. Chagnon, A. Samani, V. Veerasubramanian, M. Osman, and D. V. Plant, "Design, analysis, and transmission system performance of a 41 GHz silicon photonic modulator," *Optics Express*, vol. 23, no. 11, pp. 14263–14287, 2015.
- [63] D. Patel, A. Samani, V. Veerasubramanian, S. Ghosh, and D. V. Plant, "Silicon Photonic Segmented Modulator-Based Electro-Optic DAC for 100 Gb/s PAM-4 Generation," *IEEE Photonics Technology Letters*, vol. 27, pp. 2433–2436, Dec 2015.
- [64] A. Samani, V. Veerasubramanian, E. El-Fiky, D. Patel, and D. V. Plant, "A Silicon Photonic PAM-4 Modulator Based on Dual-Parallel Mach–Zehnder Interferometers," *IEEE Photonics Journal*, vol. 8, pp. 1–10, Feb 2016.
- [65] W. Shi, Y. Xu, H. Sepehrian, S. LaRochelle, and L. Rusch, "Silicon photonic modulators for PAM transmissions," *Journal of Optics*, Jun 2018.
- [66] L. Jiang, X. Chen, K. Kim, G. de Valicourt, Z. R. Huang, and P. Dong, "Electro-Optic Crosstalk in Parallel Silicon Photonic Mach-Zehnder Modulators," *Journal of Lightwave Technology*, vol. 36, pp. 1713–1720, May 2018.
- [67] P. Ji, J. Gao, W. Xu, Y. Sun, W. He, and H. Wu, "Electronic-Photonic Integrated Circuit Design and Crosstalk Modeling for a High Density Multi-Lane MZM Array," in *2018 IEEE International Symposium on Circuits and Systems (ISCAS)*, pp. 1–5, IEEE, May 2018.
- [68] M. Watts, W. Zortman, D. Trotter, R. Young, and A. Lentine, "Low-Voltage, Compact, Depletion-Mode, Silicon Mach–Zehnder Modulator," *IEEE Journal of Selected Topics in Quantum Electronics*, vol. 16, no. 1, pp. 159–164, 2010.
- [69] Z. Yong, W. D. Sacher, Y. Huang, J. C. Mikkelsen, Y. Yang, X. Luo, P. Dumais, D. Goodwill, H. Bahrami, P. G.-Q. Lo, *et al.*, "U-shaped pn junctions for efficient silicon mach-zehnder and microring modulators in the o-band," *Optics express*, vol. 25, no. 7, pp. 8425–8439, 2017.
- [70] M. Webster, C. Appel, P. Gothoskar, S. Sunder, B. Dama, and K. Shastri, "Silicon Photonic Modulator Based on a MOS-Capacitor and a CMOS Driver," in *2014 IEEE Compound Semiconductor Integrated Circuit Symposium (CSICS)*, pp. 1–4, IEEE, Oct 2014.
- [71] M. Webster, P. Gothoskar, V. Patel, D. Piede, S. Anderson, R. Tummid, D. Adams, C. Appel, P. Metz, S. Sunder, B. Dama, and K. Shastri, "An efficient MOS-capacitor based silicon modulator and CMOS drivers for optical transmitters," in *11th International Conference on Group IV Photonics (GFP)*, pp. 1–2, IEEE, Aug 2014.

- [72] C. A. Barrios, V. R. D. Almeida, and M. Lipson, “Low-Power-Consumption Short-Length and High-Modulation-Depth Silicon Electrooptic Modulator,” vol. 21, no. 4, pp. 1089–1098, 2003.
- [73] A. D. Simard and S. LaRochelle, “A Dynamic Model of Silicon Bragg Grating Modulators,” *IEEE Journal of Selected Topics in Quantum Electronics*, vol. 22, no. 6, pp. 107–115, 2016.
- [74] Y. Terada, K. Kondo, R. Abe, and T. Baba, “Full C-band Si photonic crystal waveguide modulator,” *Optics Letters*, vol. 42, no. 24, pp. 5110–5112, 2017.
- [75] T. Tatebe, T. Baba, Y. Hinakura, and Y. Terada, “Si Photonic Crystal Slow-Light Modulators with Periodic p–n Junctions,” *Journal of Lightwave Technology*, vol. 35, no. 9, pp. 1684–1692, 2017.
- [76] T. Baba, H. C. Nguyen, N. Yazawa, Y. Terada, S. Hashimoto, and T. Watanabe, “Slow-light Mach–Zehnder modulators based on Si photonic crystals,” *Science and Technology of Advanced Materials*, vol. 15, no. 2, p. 024602, 2014.
- [77] M. Passoni, D. Gerace, L. O’Faolain, and L. C. Andreani, “Slow light with interleaved p–n junction to enhance performance of integrated Mach-Zehnder silicon modulators,” *Nanophotonics*, vol. 8, no. 9, pp. 1485–1494, 2019.
- [78] C. Sciancalepore, K. Hassan, T. Ferrotti, J. Harduin, H. Duprez, S. Menezo, and B. Ben Bakir, “Low-loss adiabatically-tapered high-contrast gratings for slow-wave modulators on SOI,” in *High Contrast Metastructures IV*, vol. 9372, p. 93720G, SPIE, 2015.
- [79] R. Hosseini, L. Mirzoyan, and K. Jamshidi, “Energy Consumption Enhancement of Reverse-Biased Silicon-Based Mach–Zehnder Modulators Using Corrugated Slow Light Waveguides,” *IEEE Photonics Journal*, vol. 10, no. 1, pp. 1–7, 2018.
- [80] O. Jafari, W. Shi, and S. LaRochelle, “Mach-Zehnder Silicon Photonic Modulator Assisted by Phase-Shifted Bragg Gratings,” *IEEE Photonics Technology Letters*, vol. 32, no. 8, pp. 445–448, 2020.
- [81] “IEEE P802.3bs 400 Gb/s Ethernet Task Force.”
- [82] A. Samani, D. Patel, M. Chagnon, E. El-Fiky, R. Li, M. Jacques, N. Abadía, V. Veerasubramanian, and D. V. Plant, “Experimental parametric study of 128 Gb/s PAM-4 transmission system using a multi-electrode silicon photonic Mach Zehnder modulator,” *Optics Express*, vol. 25, p. 13252, Jun 2017.
- [83] A. Simard, B. Filion, D. Patel, D. Plant, and S. LaRochelle, “Segmented silicon mzm for pam-8 transmissions at 114 gb/s with binary signaling,” *Optics express*, vol. 24, no. 17, pp. 19467–19472, 2016.

- [84] T. N. Huynh, N. Dupuis, R. Rimolo-Donadio, J. E. Proesel, D. M. Gill, C. W. Baks, A. V. Rylyakov, C. L. Schow, W. M. Green, and B. G. Lee, "Flexible transmitter employing silicon-segmented mach-zehnder modulator with 32-nm cmos distributed driver," *Journal of Lightwave Technology*, vol. 34, no. 22, pp. 5129–5136, 2016.
- [85] R. Dubé-Demers, S. LaRochelle, and W. Shi, "Low-power DAC-less PAM-4 transmitter using a cascaded microring modulator," *Optics Letters*, vol. 41, p. 5369, Nov 2016.
- [86] T. Mizuno and Y. Miyamoto, "High-capacity dense space division multiplexing transmission," *Optical Fiber Technology*, vol. 35, pp. 108–117, 2017.
- [87] P. J. Winzer, "Scaling optical fiber networks: Challenges and solutions," *Optics and Photonics News*, vol. 26, no. 3, pp. 28–35, 2015.
- [88] P. J. Winzer, R. Ryf, and S. Randel, *Optical Fiber Telecommunications VIB: Chapter 10. Spatial Multiplexing Using Multiple-Input Multiple-Output Signal Processing*. Elsevier Inc. Chapters, 2013.
- [89] D. J. Richardson, J. M. Fini, and L. E. Nelson, "Space-division multiplexing in optical fibres," *Nature Photonics*, vol. 7, pp. 354–362, May 2013.
- [90] G. M. Saridis, D. Alexandropoulos, G. Zervas, and D. Simeonidou, "Survey and Evaluation of Space Division Multiplexing: From Technologies to Optical Networks," *IEEE Communications Surveys & Tutorials*, vol. 17, no. 4, pp. 2136–2156, 2015.
- [91] K. Nakajima, P. Sillard, D. Richardson, M.-J. Li, R.-J. Essiambre, and S. Matsuo, "Transmission media for an SDM-based optical communication system," *IEEE Communications Magazine*, vol. 53, pp. 44–51, Feb 2015.
- [92] H. Yuan, M. Furdek, A. Muhammad, A. Saljoghei, L. Wosinska, and G. Zervas, "Space-division multiplexing in data center networks: on multi-core fiber solutions and crosstalk-suppressed resource allocation," *Journal of Optical Communications and Networking*, vol. 10, no. 4, pp. 272–288, 2018.
- [93] K. Saitoh and S. Matsuo, "Multicore fibers for large capacity transmission," *Nanophotonics*, vol. 2, no. 5-6, pp. 441–454, 2013.
- [94] J. H. Chang, A. Corsi, L. A. Rusch, and S. LaRochelle, "Design analysis of oam fibers using particle swarm optimization algorithm," *Journal of Lightwave Technology*, vol. 38, no. 4, pp. 846–856, 2019.
- [95] A. Corsi, J. H. Chang, R. Wang, L. Wang, L. A. Rusch, and S. LaRochelle, "Highly elliptical core fiber with stress-induced birefringence for mode multiplexing," *Optics Letters*, vol. 45, no. 10, pp. 2822–2825, 2020.

- [96] R. H. Nejad, M. Banawan, and L. A. Rusch, "Crosstalk aware oam mode selection for space division multiplexed optical networks," in *2020 IEEE Photonics Conference (IPC)*, pp. 1–2, IEEE.
- [97] M. Streshinsky, A. Ayazi, Z. Xuan, A. E.-J. Lim, G.-Q. Lo, T. Baehr-Jones, and M. Hochberg, "Highly linear silicon traveling wave Mach-Zehnder carrier depletion modulator based on differential drive," *Optics Express*, vol. 21, no. 3, pp. 3818–3825, 2013.
- [98] O. Jafari, H. Sepehrian, S. LaRochelle, and W. Shi, "High-Efficiency Silicon Photonic Modulator Using Coupled Bragg Grating Resonators," *Journal of Lightwave Technology*, vol. 37, no. 9, pp. 2065–2075, 2019.
- [99] N. N. Klimov, S. Mittal, M. Berger, and Z. Ahmed, "On-chip silicon waveguide Bragg grating photonic temperature sensor," *Optics Letters*, vol. 40, p. 3934, Sep 2015.
- [100] J. Luo and A. K.-Y. Jen, "Highly Efficient Organic Electrooptic Materials and Their Hybrid Systems for Advanced Photonic Devices," *IEEE Journal of Selected Topics in Quantum Electronics*, vol. 19, no. 6, pp. 42–53, 2013.
- [101] M. Streshinsky, R. Ding, Y. Liu, A. Novack, Y. Yang, Y. Ma, X. Tu, E. K. S. Chee, A. E.-J. Lim, P. G.-Q. Lo, T. Baehr-Jones, and M. Hochberg, "Low power 50 Gb/s silicon traveling wave Mach-Zehnder modulator near 1300 nm," *Optics Express*, vol. 21, no. 25, p. 30350, 2013.
- [102] A. Samani, M. Chagnon, D. Patel, V. Veerasubramanian, S. Ghosh, M. Osman, Q. Zhong, and D. V. Plant, "A Low-Voltage 35-GHz Silicon Photonic Modulator-Enabled 112-Gb/s Transmission System," *IEEE Photonics Journal*, vol. 7, no. 3, pp. 1–13, 2015.
- [103] Po Dong, Xiang Liu, S. Chandrasekhar, L. L. Buhl, R. Aroca, and Young-Kai Chen, "Monolithic silicon photonic integrated circuits for compact 100+Gb/s coherent optical receivers and transmitters," *IEEE Journal of Selected Topics in Quantum Electronics*, vol. 20, no. 4, pp. 150–157, 2014.
- [104] X. Zheng, E. Chang, P. Amberg, I. Shubin, J. Lexau, F. Liu, H. Thacker, S. S. Djordjevic, S. Lin, Y. Luo, J. Yao, J.-H. Lee, K. Raj, R. Ho, J. E. Cunningham, and A. V. Krishnamoorthy, "A high-speed, tunable silicon photonic ring modulator integrated with ultra-efficient active wavelength control," *Optics Express*, vol. 22, no. 10, pp. 12628–12633, 2014.
- [105] R. Li, D. Patel, A. Samani, E. El-Fiky, Z. Xing, M. Sowailam, Q. Zhong, and D. V. Plant, "An 80 Gb/s Silicon Photonic Modulator Based on the Principle of Overlapped Resonances," *IEEE Photonics Journal*, vol. 9, no. 3, pp. 1–11, 2017.
- [106] J. Cardenas, P. A. Morton, J. B. Khurgin, A. Griffith, C. B. Poitras, K. Preston, and M. Lipson, "Linearized silicon modulator based on a ring assisted Mach Zehnder inteferometer," *Optics Express*, vol. 21, no. 19, p. 22549, 2013.

- [107] H. C. Nguyen, N. Yazawa, S. Hashimoto, S. Otsuka, and T. Baba, "Sub-100 μm Photonic Crystal Si Optical Modulators: Spectral, Athermal, and High-Speed Performance," *IEEE Journal of Selected Topics in Quantum Electronics*, vol. 19, pp. 127–137, Nov 2013.
- [108] D. Pergande, T. M. Geppert, A. von Rhein, S. L. Schweizer, R. B. Wehrspohn, S. Moretton, and A. Lambrecht, "Miniature infrared gas sensors using photonic crystals," *Journal of Applied Physics*, vol. 109, p. 083117, Apr 2011.
- [109] A. K. Goyal, H. S. Dutta, and S. Pal, "Recent advances and progress in photonic crystal-based gas sensors," *Journal of Physics D: Applied Physics*, vol. 50, p. 203001, May 2017.
- [110] Xu Wang, M. Caverley, J. Flueckiger, Yun Wang, N. A. F. Jaeger, and L. Chrostowski, "Silicon photonic Bragg grating modulators," in *2014 IEEE Photonics Conference*, pp. 190–191, IEEE, Dec 2014.
- [111] K. Bédard, A. D. Simard, B. Filion, Y. Painchaud, L. A. Rusch, and S. LaRochelle, "Transmission of 50 Gb/s with a Dual Phase-Shift Bragg Grating Silicon Photonic Modulator," in *Optical Fiber Communication Conference*, (Washington, D.C.), p. Th3J.7, OSA, Mar 2016.
- [112] M. Burla, L. R. Cortés, M. Li, X. Wang, L. Chrostowski, and J. Azaña, "Integrated waveguide Bragg gratings for microwave photonics signal processing," *Optics Express*, vol. 21, p. 25120, Oct 2013.
- [113] A. D. Simard, N. Belhadj, Y. Painchaud, and S. LaRochelle, "Apodized Silicon-on-Insulator Bragg Gratings," *IEEE Photonics Technology Letters*, vol. 24, pp. 1033–1035, Jun 2012.
- [114] M. Burla, L. R. Cortes, M. Li, X. Wang, L. Chrostowski, and J. Azana, "On-chip ultra-wideband microwave photonic phase shifter and true time delay line based on a single phase-shifted waveguide Bragg grating," in *2013 IEEE International Topical Meeting on Microwave Photonics (MWP)*, pp. 92–95, IEEE, Oct 2013.
- [115] T. Baba, "Slow light in photonic crystals," *Nature Photonics*, vol. 2, no. 8, pp. 465–473, 2008.
- [116] K. McGarvey-Lechable, T. Hamidfar, D. Patel, L. Xu, D. V. Plant, and P. Bianucci, "Slow light in mass-produced, dispersion-engineered photonic crystal ring resonators," *Optics Express*, vol. 25, no. 4, p. 3916, 2017.
- [117] C. Xiang, M. L. Davenport, J. B. Khurgin, P. A. Morton, and J. E. Bowers, "Low-Loss Continuously Tunable Optical True Time Delay Based on Si₃N₄ Ring Resonators," *IEEE Journal of Selected Topics in Quantum Electronics*, vol. 24, no. 4, pp. 1–9, 2018.
- [118] X. Wang, L. Zhou, R. Li, J. Xie, L. Lu, K. Wu, and J. Chen, "Continuously tunable ultra-thin silicon waveguide optical delay line," *Optica*, vol. 4, no. 5, p. 507, 2017.

- [119] J.-W. Dong, X.-D. Chen, H. Zhu, Y. Wang, and X. Zhang, "Valley photonic crystals for control of spin and topology," *Nature Materials*, vol. 16, no. 3, pp. 298–302, 2017.
- [120] S. Mahmoodian, K. Prindal-Nielsen, I. Söllner, S. Stobbe, and P. Lodahl, "Engineering chiral light-matter interaction in photonic crystal waveguides with slow light," *Optical Materials Express*, vol. 7, no. 1, p. 43, 2017.
- [121] L. Jiang and Z. R. Huang, "Integrated Cascaded Bragg Gratings for On-Chip Optical Delay Lines," *IEEE Photonics Technology Letters*, vol. 30, no. 5, pp. 499–502, 2018.
- [122] W. Shi, V. Veerasubramanian, D. Patel, and D. V. Plant, "Tunable nanophotonic delay lines using linearly chirped contradirectional couplers with uniform Bragg gratings," *Optics Letters*, vol. 39, no. 3, p. 701, 2014.
- [123] Z. Zhang, G. I. Ng, T. Hu, H. Qiu, X. Guo, M. S. Rouified, C. Liu, and H. Wang, "Electromagnetically induced transparency-like effect in microring-Bragg gratings based coupling resonant system," *Optics Express*, vol. 24, no. 22, p. 25665, 2016.
- [124] A. Yariv, P. Yeh, and A. Yariv, *Photonics : optical electronics in modern communications*. Oxford University Press, Inc., 2006.
- [125] H. Bahrami, H. Sepehrian, C. S. Park, L. A. Rusch, and W. Shi, "Time-Domain Large-Signal Modeling of Traveling-Wave Modulators on SOI," *Journal of Lightwave Technology*, vol. 34, no. 11, pp. 2812–2823, 2016.
- [126] X. Wang, *Silicon photonic waveguide Bragg gratings*. PhD thesis, University of British Columbia, 2013.
- [127] J. Lauzon, S. LaRochelle, and F. Ouellette, "Numerical analysis of all-optical switching of a fiber Bragg grating induced by a short-detuned pump pulse," *Optics Communications*, vol. 92, no. 4-6, pp. 233–239, 1992.
- [128] E. Kalnay, *Atmospheric modeling, data assimilation, and predictability*. Cambridge University Press, 2003.
- [129] A. Shakoor, K. Nozaki, E. Kuramochi, K. Nishiguchi, A. Shinya, and M. Notomi, "Compact 1D-silicon photonic crystal electro-optic modulator operating with ultra-low switching voltage and energy," *Optics Express*, vol. 22, p. 28623, Nov 2014.
- [130] X. Li, F. Yang, F. Zhong, Q. Deng, J. Michel, and Z. Zhou, "Single-drive high-speed lumped depletion-type modulators toward 10 fJ/bit energy consumption," *Photonics Research*, vol. 5, no. 2, pp. 134–142, 2017.
- [131] S. Sharif Azadeh, J. Nojić, A. Moscoso-Mártir, F. Merget, and J. Witzens, "Power-efficient lumped-element meandered silicon Mach-Zehnder modulators," *Silicon Photonics XV*, vol. 11285, p. 10, 2020.

- [132] Y. Hinakura, Y. Terada, H. Arai, and T. Baba, "Electro-optic phase matching in a Si photonic crystal slow light modulator using meander-line electrodes," *Optics Express*, vol. 26, no. 9, pp. 11538–11545, 2018.
- [133] R. Dube-Demers, J. St-Yves, A. Bois, Q. Zhong, M. Caverley, Y. Wang, L. Chrostowski, S. Larochelle, D. V. Plant, and W. Shi, "Analytical Modeling of Silicon Microring and Microdisk Modulators with Electrical and Optical Dynamics," *Journal of Lightwave Technology*, vol. 33, no. 20, pp. 4240–4252, 2015.
- [134] H. Yu, M. Pantouvaki, J. Van Campenhout, D. Korn, K. Komorowska, P. Dumon, Y. Li, P. Verheyen, P. Absil, L. Alloatti, D. Hillerkuss, J. Leuthold, R. Baets, and W. Bogaerts, "Performance tradeoff between lateral and interdigitated doping patterns for high speed carrier-depletion based silicon modulators," *Optics Express*, vol. 20, p. 12926, Jun 2012.
- [135] D. Samara-Rubio, U. D. Keil, L. Liao, T. Franck, A. Liu, D. W. Hodge, D. Rubin, and R. Cohen, "Customized drive electronics to extend silicon optical modulators to 4 Gb/s," *Journal of Lightwave Technology*, vol. 23, no. 12, pp. 4305–4314, 2005.
- [136] G. L. Li, P. K. L. Yu, and T. G. B. Mason, "Analysis of Segmented Traveling-Wave Optical Modulators," *Journal of Lightwave Technology*, vol. 22, no. 7, pp. 1789–1796, 2004.
- [137] F. Cappelluti and G. Ghione, "Self-consistent time-domain large-signal model of high-speed traveling-wave electroabsorption modulators," *IEEE Transactions on Microwave Theory and Techniques*, vol. 51, no. 4, pp. 1096–1104, 2003.
- [138] H. Yu and W. Bogaerts, "An equivalent circuit model of the traveling wave electrode for carrier-depletion-based silicon optical modulators," *Journal of Lightwave Technology*, vol. 30, no. 11, pp. 1602–1609, 2012.
- [139] C. R. Paul, *Inductance : loop and partial*. Wiley, 2010.
- [140] H. Sepehrian, A. Yekani, W. Shi, and L. A. Rusch, "Assessing performance of silicon photonic modulators for pulse amplitude modulation," *IEEE Journal of Selected Topics in Quantum Electronics*, vol. 24, no. 6, pp. 1–10, 2018.
- [141] S. Hughes, L. Ramunno, J. F. Young, and J. E. Sipe, "Extrinsic Optical Scattering Loss in Photonic Crystal Waveguides: Role of Fabrication Disorder and Photon Group Velocity," *Physical Review Letters*, vol. 94, no. 3, pp. 033903–6, 2005.
- [142] C. Monat, B. Corcoran, M. Ebinali-Heidari, C. Grillet, B. J. Eggleton, T. P. White, L. O’Faolain, and T. F. Krauss, "Slow light enhancement of nonlinear effects in silicon engineered photonic crystal waveguides," *Optics Express*, vol. 17, no. 4, pp. 2944–2953, 2009.

- [143] K. Kiziloglu, N. Dagli, G. L. Matthaei, and S. I. Long, "Experimental Analysis of Transmission Line Parameters in High-Speed Gaas Digital Circuit Interconnects," *IEEE Transactions on Microwave Theory and Techniques*, vol. 39, no. 8, pp. 1361–1367, 1991.
- [144] N. Qi, X. Xiao, S. Hu, X. Li, H. Li, L. Liu, Z. Li, N. Wu, and P. Y. Chiang, "Co-Design and Demonstration of a 25-Gb/s Silicon-Photonic Mach-Zehnder Modulator with a CMOS-Based High-Swing Driver," *IEEE Journal of Selected Topics in Quantum Electronics*, vol. 22, no. 6, pp. 131–140, 2016.
- [145] H. Sepehrian, A. Yekani, L. A. Rusch, and W. Shi, "CMOS-Photonics Codesign of an Integrated DAC-Less PAM-4 Silicon Photonic Transmitter," *IEEE Transactions on Circuits and Systems I: Regular Papers*, vol. 63, pp. 2158–2168, Dec 2016.
- [146] K. Hojo, Y. Terada, N. Yazawa, T. Watanabe, and T. Baba, "Compact QPSK and PAM Modulators With Si Photonic Crystal Slow-Light Phase Shifters," *IEEE Photonics Technology Letters*, vol. 28, pp. 1438–1441, Jul 2016.
- [147] P. M. Krummrich, "Spatial multiplexing for high capacity transport," *Optical Fiber Technology*, vol. 17, pp. 480–489, Oct 2011.
- [148] Y. Chen, Z. Lin, S. Bélanger-de Villers, L. A. Rusch, and W. Shi, "Wdm-compatible polarization-diverse oam generator and multiplexer in silicon photonics," *IEEE Journal of Selected Topics in Quantum Electronics*, vol. 26, no. 2, pp. 1–7, 2019.
- [149] V. Sleiffer, Y. Jung, V. Veljanovski, R. Van Uden, M. Kushnerov, H. Chen, B. Inan, L. G. Nielsen, Y. Sun, D. J. Richardson, *et al.*, "73.7 tb/s (96 x 3 x 256-gb/s) mode-division-multiplexed dp-16qam transmission with inline mm-edfa," *Optics Express*, vol. 20, no. 26, pp. B428–B438, 2012.
- [150] R. Ryf, S. Randel, A. H. Gnauck, C. Bolle, A. Sierra, S. Mumtaz, M. Esmaelpour, E. C. Burrows, R.-J. Essiambre, P. J. Winzer, *et al.*, "Mode-division multiplexing over 96 km of few-mode fiber using coherent 6x6 mimo processing," *Journal of Lightwave technology*, vol. 30, no. 4, pp. 521–531, 2011.
- [151] D. Zhang, X. Feng, and Y. Huang, "Encoding and decoding of orbital angular momentum for wireless optical interconnects on chip," *Optics express*, vol. 20, no. 24, pp. 26986–26995, 2012.
- [152] J. Sun, A. Yaacobi, M. Moresco, D. Coolbaugh, and M. R. Watts, "Chip-scale continuously tunable optical orbital angular momentum generator," *arXiv preprint arXiv:1408.3315*, 2014.
- [153] A. M. J. Koonen, Haoshuo Chen, H. P. A. van den Boom, and O. Raz, "Silicon Photonic Integrated Mode Multiplexer and Demultiplexer," *IEEE Photonics Technology Letters*, vol. 24, pp. 1961–1964, Nov 2012.

- [154] J. Wang, S. He, and D. Dai, “On-chip silicon 8-channel hybrid (de)multiplexer enabling simultaneous mode- and polarization-division-multiplexing,” *Laser & Photonics Reviews*, vol. 8, pp. L18–L22, Mar 2014.